

# MATERIALS TESTING AND RESEARCH SOLUTIONS FROM AGILENT

Polymers and Rubbers Application Compendium

The Measure of Confidence



Agilent Technologies

# MATERIALS TESTING AND RESEARCH SOLUTIONS

From the extraction of raw materials through the development, manufacturing and utilization of advanced materials, to material reuse and recycling, Agilent Technologies offers innovative, reliable analytical solutions for your business. Our comprehensive line of instruments for materials testing and research will ensure you consistently and cost-effectively deliver the highest quality finished products and materials.

## Materials market overview

The materials market comprises the industries involved in the extraction of raw minerals from the earth (geosciences, mining and mineralogy) and the subsequent characterization and transformation of those raw minerals into metal alloys, ceramics, glass, and other engineered materials — described collectively as “advanced materials”. These advanced materials are developed with purpose specific characteristics and properties in a wide variety of industries.

Examples of advanced materials include:

- Aero and automotive (metals, composites)
- Polymers and composites
- Glass/ceramics/optics and photonics (lenses and coatings, eyewear)
- Specialty films and surface coatings (paint, adhesives, resins)
- Semiconductor and electronics (LEDs, LCDs, disk drives, thin-film electronics, fuel cells, solar cells)
- Textiles, paper and packaging
- Consumer goods (jewelry, gemstones, cosmetics)
- Construction (cement, architectural glass, metal alloys)



Materials market lifecycle

# SOLUTIONS FOR POLYMERS AND RUBBERS

When accuracy and reliability in measuring the quality and chemical composition of plastics and polymers is critical to your success, choose Agilent.

Agilent molecular spectroscopy products provide the information required for development, QA/QC and to monitor the in-use service of these materials. Laboratory FTIR bench and microscopy systems provide insight into both bulk and detailed structure of polymers and rubber materials. Mobile FTIR spectroscopy affords non-destructive analysis of polymer, composite and rubber-based objects, regardless of location, shape or size.

In addition, Agilent atomic force microscopy (AFM) systems permit the detailed surface characterization of polymers and rubbers at the nanoscale. These high-precision, modular AFM systems offer industry-leading environmental/temperature control and electrical measurement capabilities to keep moving R&D forward. Agilent also offers an innovative, extremely compact field-emission scanning electron microscopy (FE-SEM) system optimized to provide high surface contrast using low-voltage imaging techniques. When mechanical properties characterization at the nanoscale is needed, user friendly Agilent nanoindentation systems ensure unrivaled accuracy and outstanding versatility.

Polymers and rubber are used across industry in an ever widening set of products and subassemblies. As synthesized materials, their properties, performance and longevity are directly related to achieving proper composition and structure. These materials have finite lifetimes, which are directly related to environmental affects, additives and stabilizers and overall usage.

## Agilent solutions

Agilent FTIR spectrometers, microscopes and chemical imaging systems deliver:

- Detailed structural analysis of polymer and rubber based products.
- QA/QC support in the production of polymer and rubber.
- Defect analysis and analysis of layered materials via FTIR microscopy.
- Nondestructive, in situ analysis of polymer and rubber based objects in support of determining effect of use on longevity and performance.
- Handheld FTIR for nondestructive analysis of polymer, composites and rubber in any shape, size or location

Use Agilent LC systems for:

- Investigating very small differences between the chemical structures of polymers
- Analysis of additives in polymers, such as phenolic antioxidants and erucamide slip additives.
- Screening and qualitative identification of antioxidant polymer additives.

Agilent's GPC/SEC portfolio provides:

- High-performance analysis of engineering polymers such as PEEK and polybutylene terephthalate, polyolefins such as polyethylene and polypropylene, low molecular weight resins such as epoxy resins, polyesters and phenolic resins, or elastomers such as styrenebutadiene and natural rubber
- A comprehensive portfolio of GPC/SEC columns and calibrants for polymer analysis.

Agilent AFM and FE-SEM systems facilitate:

- Surface properties characterization in various environments (for example, heat, cold, gases).
- Electrical testing of charged polymers.

Agilent nanoindentation systems enable:

- Indentation and scratch testing of coatings on plastics.
- Mechanical properties characterization of tires, PVC, and polyethylene.

# APPLICATIONS FOR POLYMERS AND RUBBERS

## **SPECTROSCOPY**

### **Fourier Transform Infrared (FTIR) Spectroscopy**

Quantitative Analysis of Copolymers Using the Cary 630 FTIR Spectrometer

Determination of Percent Polyethylene in Polyethylene/Polypropylene Blends Using Cast Film FTIR Techniques

Rapid Identification of O-rings, Seals and Gaskets Using the Handheld Agilent 4100 ExoScan FTIR

A New Approach to Sample Preparation Free Micro ATR FTIR Chemical Imaging of Polymer Laminates

Identification of Contaminants in Vehicle Fuel Tank Caps Using FTIR ATR-Microscopy

Component Failure Analysis of Vehicle Spark Plugs Using FTIR Spectroscopy With a Micro-ATR Large Sample Objective

Material Analysis by Infrared Mapping: A Case Study Using a Multilayer Paint Sample

### ***Analytical Methods for the Agilent Cary 630 FTIR***

Determination of Irganox 3114 in polypropylene by infrared spectroscopy

Determination of percent ethylene in ethylene-propylene statistical copolymers

Determination of Irganox 1010 in polyethylene by infrared spectroscopy

Determination of Irganox 1010 in polypropylene by infrared spectroscopy

Determination of the vinyl content of polyethylene resins

Determination of percent glycerol monostearate in polypropylene by infrared spectroscopy

### **Atomic Force Microscopy (AFM) and Field-Emission Scanning Electron Microscopy (FE-SEM)**

Advanced Atomic Force Microscopy: Exploring Measurements of Local Electric Properties

Agilent 5600LS AFM High-resolution Imaging Molecular-level Understanding of n-Alkanes Self-Assembly onto Graphite

Several Aspects of High Resolution Imaging in Atomic Force Microscopy

Compositional Mapping of Materials with Single-Pass Kelvin Force Microscopy

Atomic Force Microscopy Studies in Various Environments

Young's Modulus of Dielectric 'Low-k' Materials

### **Nanoindentation**

Nanoindentation, Scratch, and Elevated Temperature Testing of Cellulose and PMMA Films

Measuring the Complex Modulus of Polyethylene Using Instrumented Indentation

Complex Shear Modulus of Commercial Gelatin by Instrumented Indentation

# APPLICATIONS FOR POLYMERS AND RUBBERS

## CHROMATOGRAPHY

### Liquid Chromatography (LC)

Sensitive Polymer Analysis using Critical Point Chromatography and ELSD

Fast Analysis of Phenolic Antioxidants and Erucamide Slip Additives in Polypropylene Homopolymer Formulations Using 1200 Rapid Resolution Liquid Chromatography (RRLC) with Rapid Resolution High Throughput (RRHT) Columns and Method Translator

Analysis of Phenolic Antioxidant and Erucamide Slip Additives in Polymer by Rapid-Resolution LC

Developing a UHPLC Method for UV-based Detection and Quantification of Primary Aromatic Amines in Low Concentrations

Determination of Polymer Additives and Migration Products Prevalent in Food Packaging Material

Determination of Phthalate Migration From Toys

Analysis of Bisphenol A Leaching from Baby Feeding Bottles

High Sensitivity Analysis of Phthalates Using HPLC with Low Temperature Evaporative Light Scattering Detection

Agilent 1290 Infinity LC with Agilent Poroshell Columns for Simultaneous Determination of Eight Organic UV Filters

### Gel Permeation Chromatography (GPC)

Stable Baselines in the Analysis of Poly(lactide-co-glycolide) Polymers by GPC with ELSD

Analyze Injection-Molding Polymers on Agilent PLgel 5  $\mu$ m MIXED-C by GPC

Artifact Free Analysis of Lignins by GPC using Agilent PolarGel-M

GPC and Agilent PolarGel-M Columns for the True Representation of Novolac Resins

Analysis of Polysaccharides by GPC Viscometry using the Agilent 390-MDS Multi Detector Suite

Characterization of Block Copolymers Synthesized via Transition Metal Mediated Living Radical Polymerization

Analysis of Biodegradable Polymers by GPC

Analysis of Poly(styrene/butadiene) Copolymers by Conventional Gel Permeation Chromatography on the Agilent PL-GPC 50 Plus

### Size Exclusion Chromatography (SEC)

Size Exclusion Chromatography for the Analysis of Dental Polymers

SEC Analysis of a Water Soluble Copolymer

SEC Analysis of a Acrylamide Copolymer

### GPC/SEC

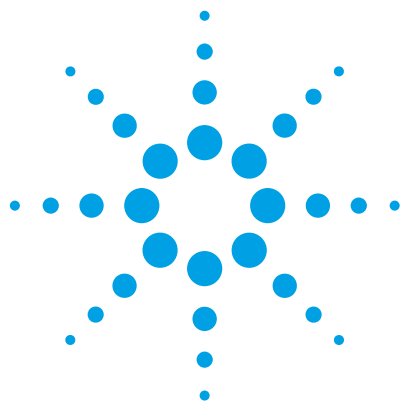
Analysis of biodegradable polymers by GPC/SEC

Analysis of polyolefins by GPC/SEC

Analysis of engineering polymers by GPC/SEC

Analysis of elastomers by GPC/SEC

Low molecular weight resins and prepolymers



# Quantitative analysis of copolymers using the Cary 630 FTIR spectrometer

## Application note

Materials testing and research

### Author

Frank Higgins and Alan Rein

Agilent Technologies  
Danbury, CT, USA



### Introduction

FTIR spectrometers employing attenuated total reflectance (ATR) sampling interfaces are a proven and powerful tool for the analysis of polymeric materials. Because of its unique combination of features and class-leading performance, the new Agilent Cary 630 FTIR spectrometer makes quantitative analysis of polymers especially fast and easy.

In this application note, the amount of key components in two important copolymeric materials are measured — the styrene content in styrene butadiene rubber (SBR) and the ratio of polyethylene to vinyl acetate in polyethylene vinyl acetate (PEVA) polymer. The Cary 630 FTIR equipped with its single reflection Diamond ATR sampling accessory (Figure 1) is used for these measurements.

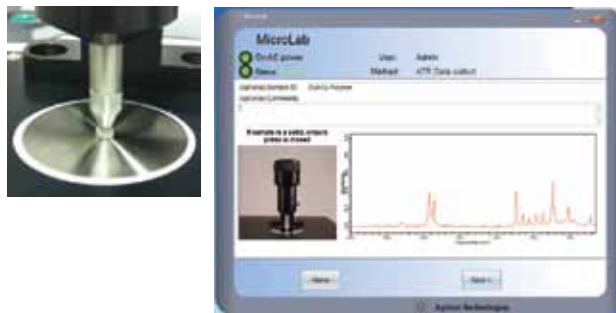


**Figure 1.** Agilent Cary 630 FTIR spectrometer equipped with single reflection Diamond ATR sampling accessory

## Styrene concentration in SBR polymer

Styrene butadiene rubber (SBR) is the most common synthetic rubber material and its main use is in the manufacture of tires, which accounts for nearly 70% of its production. The properties of SBR rubber can be altered by varying the ratio of styrene to butadiene monomers in the manufacturing process. The normal ratio is 3:1 butadiene to styrene (25% styrene). Higher styrene concentrations make the material harder, but less elastic. Most performance industries, such as racing tires and specialty military applications, are requiring more consistent SBR product, which drives the need for better quality assurance and control by both end users and manufacturers.

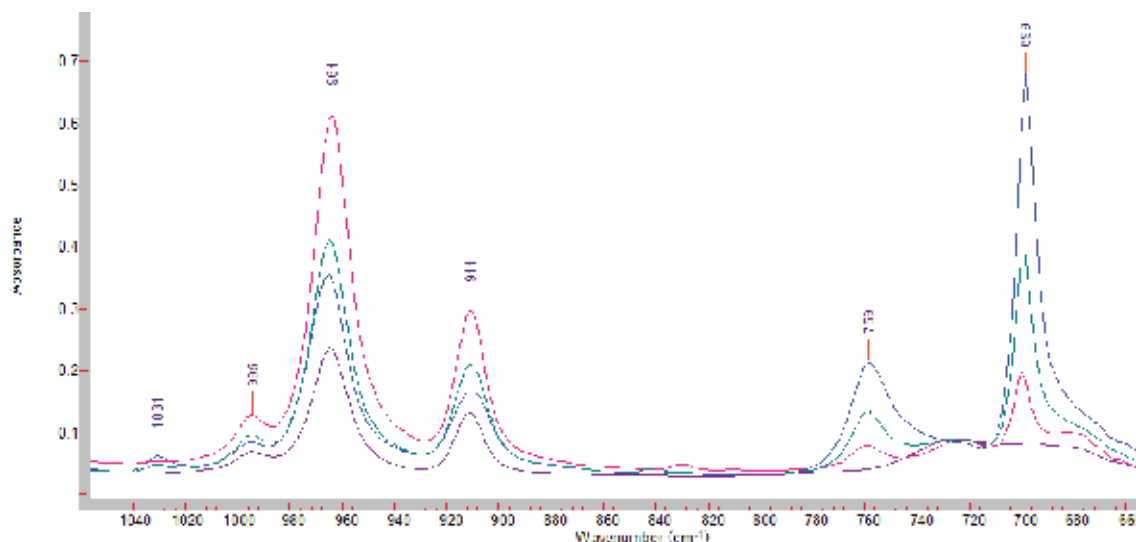
The measurement of a polymer sample by the Cary 630 FTIR equipped with an ATR accessory is extremely straightforward. The polymer material is placed on the diamond crystal and the sample pressure press is rotated downward until adequate pressure is placed on the sample to observe a spectrum in the Cary 630's real-time analysis MicroLab FTIR software (Figure 2). The real-time analysis mode provides instantaneous spectral update and makes it easy for even novice users to get highly repeatable results. The sample press on the Cary 630 is designed so that it cannot be over-tightened, thus protecting the diamond crystal against over-pressure.



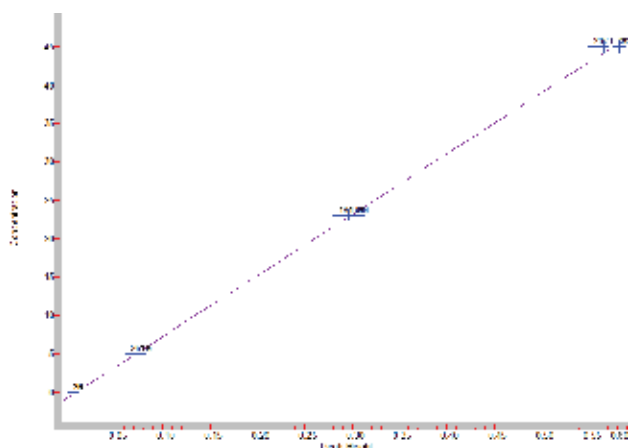
**Figure 2.** Polymer is placed directly on ATR sampling accessory. Uniform, constant pressure is provided by the sample press, ensuring that high quality spectra are obtained. Real-time analysis software provides an immediate indicator of spectral quality

To develop a quantitative FTIR method, four commercial SBR calibration standards, with polystyrene concentrations of 0%, 5%, 23%, and 45%, were measured in triplicate using the Cary 630 FTIR. The spectra reveal the expected polystyrene (PS) absorbance bands (Figure 3) at  $699\text{ cm}^{-1}$ ,  $759\text{ cm}^{-1}$ , and a weaker band at  $1031\text{ cm}^{-1}$ . Spectral bands at  $911\text{ cm}^{-1}$ ,  $964\text{ cm}^{-1}$ , and  $995\text{ cm}^{-1}$  arise from unsaturations (*vinyl* and *trans* CH wag) in polybutadiene, which decrease as the PS bands increase. The exception is the pure polybutadiene, which has far more *cis* unsaturations relative to the other polymers, since it is not cross-linked and in liquid form. The PS absorbance bands appear to follow Beer's Law by increasing proportionately with concentration, and therefore are excellent candidates for quantitative analysis.

The plot of the peak height absorbance for the strongest IR band of PS at  $699\text{ cm}^{-1}$  as a function of concentration indicates great linearity and a strong correlation coefficient of  $R^2=0.999$  in the calibration (Figure 4). Using the linear regression slope and offset from this calibration, a method is added to the MicroLab FTIR software that enables the polystyrene percentage in an unknown sample to be automatically displayed. The limit of detection for the quantitative analysis of PS in SBR is 0.09%, calculated as three times the standard deviation of the 0% replicate data (StDev= 0.03% PS).



**Figure 3.** The FTIR spectra of four SBR rubber standards with increasing polystyrene concentrations: 0% (purple), 5% (red), 23% (green), and 45% (blue)



**Figure 4.** FTIR calibration curve for polystyrene in SBR rubber using the 699  $\text{cm}^{-1}$  peak height absorbance;  $R^2=0.999$ .

## Ratio of polyethylene to vinyl acetate in PEVA

Polyethylene vinyl acetate (PEVA) is very common in everyday products used in the home, sports equipment, industrial and medical applications. In the latter applications, medicines can be mixed in solution with PEVA and then the mixture dried to produce biologically-inert, slow-release plastic implants and transdermal patches.

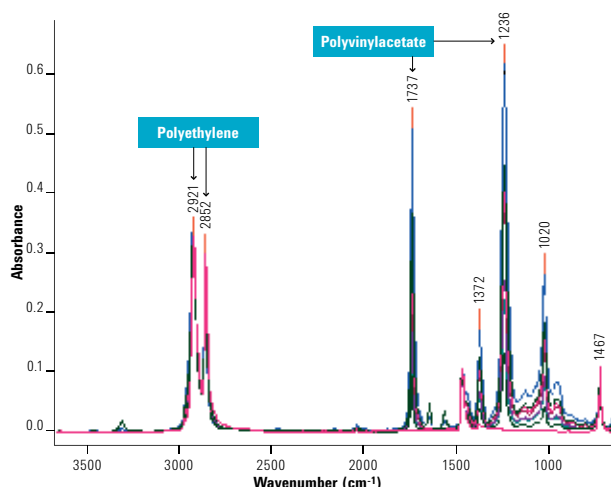
Since the ratio of polyethylene (PE) to vinyl acetate (VA) in PEVA can affect the physical properties of the final product, it is important for manufacturers to have a fast, easy measurement procedure for these components. As in the previous example, the Cary 630 FTIR spectrometer with single reflection diamond ATR is ideal for this measurement.

In this example, seven commercially-available standards of PEVA were measured with the Cary 630 FTIR system. The calibration standards used were:

- Polyethylene, low density (0% vinyl acetate)
- Ethylene/vinyl acetate copolymer #506 (9 wt% vinyl acetate)
- Ethylene/vinyl acetate copolymer #243 (14 wt% vinyl acetate)
- Ethylene/vinyl acetate copolymer #244 (18 wt% vinyl acetate)
- Ethylene/vinyl acetate copolymer #245 (25 wt% vinyl acetate)
- Ethylene/vinyl acetate copolymer #316 (28 wt% vinyl acetate)
- Ethylene/vinyl acetate copolymer #326 (40 wt% vinyl acetate)



The calibration samples were measured with one minute collection times, at a resolution of 4  $\text{cm}^{-1}$ . The FTIR spectra exhibit strong acetate ester carbonyl bands at 1737  $\text{cm}^{-1}$  and an ester C-O stretch band at 1236  $\text{cm}^{-1}$  (Figure 5) arising from polyvinyl acetate (VA). Both of these bands are ideal for quantitative analysis of the VA in the polyethylene (PE) matrix. The characteristic PE absorbance bands are located at 2921  $\text{cm}^{-1}$ , 2852  $\text{cm}^{-1}$ , 1467  $\text{cm}^{-1}$  and 720  $\text{cm}^{-1}$ . The best calibration is obtained by a peak area ratio of the 1236  $\text{cm}^{-1}$  VA absorbance band ratioed to the PE absorbance at 1467  $\text{cm}^{-1}$ . This IR absorbance ratio technique corrects for random variables that may affect the measurement, such as contact pressure or contact area of the polymers on the ATR diamond crystal. This is important since reliable ATR measurements require the sample to make good optical contact with the diamond, and hard, round polymer beads may not contact the whole diamond surface.



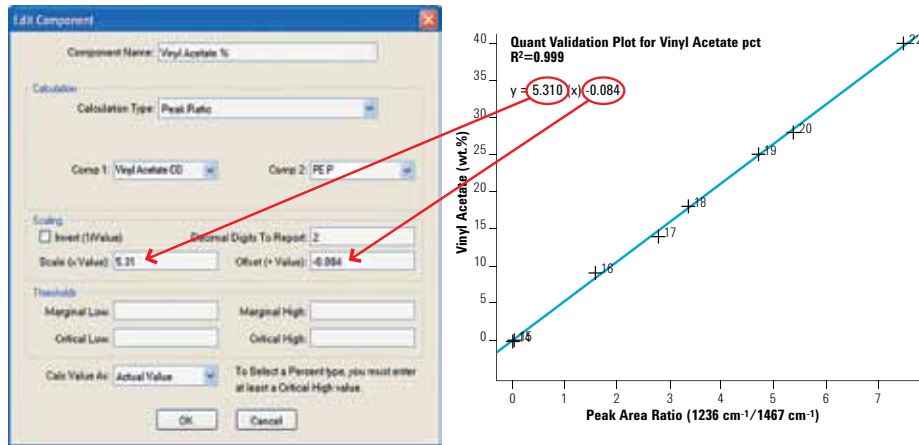
**Figure 5.** Spectral overlay of the calibration standards for polyethylene vinyl acetate). The spectra are all scaled to the polyethylene absorbance. The blue spectrum is 40 wt% VA, and the red spectrum is 0% VA

The resulting linear regression calibration curve from the above peak area ratio is excellent (Figure 6) with a correlation coefficient of  $R^2 = 0.999$ . The slope and offset for the linear regression is easily inserted into the MicroLab FTIR method editor (Figure 6), and the resultant method is now permanently calibrated. To test the robustness of the method, validation standards

were made by diluting (by weight) the 9% VA with the pure PE (0% VA) standards to make 1% and 0.55% VA samples. The polymer validation samples were then dissolved in toluene and heated to 75 °C until all the polymer dissolved. The toluene mixtures were then cast as thin films onto aluminum foil over a 60 °C hotplate and allowed to dry. The resulting polymer validation samples were then measured with the stored method. These validation samples were measured with a much shorter scan time (5 seconds) than the calibration set of spectra (60 seconds). This allows for multiple measurements of incoming raw materials in a very short time; this fast sample analysis is important for quality assurance and quality control (QA/QC) analysis. The speed of this analysis is also a benefit for incoming raw materials analysis in which a batch of PEVA can have some uniformity differences, requiring sampling from multiple areas of the container or on a molded part. The results of this fast analysis (5 second) yield exceptional repeatability and accuracy (Table 1) on the validation samples. A standard deviation of nominally 0.01% VA was obtained with limits of detection (LOD) and limits of quantitation (LOQ) of 0.03 wt% VA and 0.10 wt% VA, respectively. When a sample is run using this calibrated FTIR method, the results can also be displayed in color-coded format (Figure 7), indicating that the sample is in-spec (green), marginal (yellow), or out of spec (red). This enables an operator to get a rapid, visual indicator of the quality of the material.

**Table 1.** VA prediction values from the calibrated VA FTIR method for validation standards at 0.55% VA and 1.00% vinyl acetate in polyethylene. These validation samples were run with only 5 second collection times

Validation sample	0.55% VA	1.00% VA
Rep 1	0.53	0.97
Rep 2	0.54	0.96
Rep 3	0.55	0.96
Rep 4	0.56	0.96
Rep 5	0.55	0.99
Standard deviation	0.0114	0.0130
Average	0.55	0.97



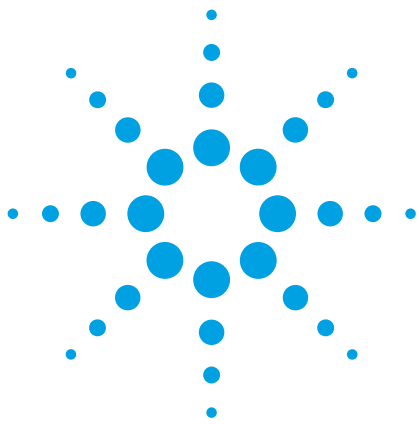
**Figure 6.** The method editor in the MicroLab FTIR software and the calibration plot for VA in PE



**Figure 7.** The result for the 1% VA validation standard — green color indicates an in-spec sample

## Conclusion

The Agilent Cary 630 FTIR equipped with ATR sampling technology is an exceedingly effective spectrometer for analyzing copolymer blends. The combination of its compact size, sampling technology, performance, speed of analysis, and intuitive software enables quantitative methods for polymers to be rapidly developed and deployed in quality assurance and quality control applications. The measurement of both SBR and PEVA copolymers yields highly linear calibrations with excellent quantitative accuracy and reproducibility.



# Determination of percent polyethylene in polyethylene/polypropylene blends using cast film FTIR techniques

## Application note

Energy and chemicals; Materials testing

### Author

Frank Higgins

Agilent Technologies  
Danbury, CT, USA



### Introduction

Polyethylene (PE) is the most common group of thermoplastic polymers due to its low cost and versatile physical properties. PE is blended with polypropylene (PP) to improve physical properties, such as low temperature impact performance. The composition of these blends is important with regard to performance, and the correct mixing of the pure homopolymers (PE and PP) can eliminate the need for costly synthesis of new block copolymers. Knowing the composition of these blends is also critical to the recycling and regeneration of polyolefins in waste and scraps.

In this application note, we demonstrate a method for rapidly determining the PE:PP ratio in blends using the Agilent Cary 630 FTIR spectrometer.



**Agilent Technologies**

## Experimental

Calibration standards of PE/PP blends in the 35–85% PE range were prepared by dissolving different ratios of the polymers in hot (110–120 °C) tetrachloroethylene (perchloroethylene), making a roughly 3% polymer to solvent solution.

The dissolved polymer mixture was then used to cast films on either PTFE coupons or KBr plates for analysis by FTIR. In the case of KBr plates, approximately 0.3 mL of the polymer solution was evenly placed on the plate. The plate was then placed on a ~70 °C hotplate until all the solvent evaporated. The coated KBr plate was allowed to cool and analysis was carried out using the Cary 630 FTIR spectrometer, equipped with a transmission sampling accessory. The ratios of the methyl IR bands (mainly PP) and the methylene CH<sub>2</sub> bands (both PE and PP) were used to accurately measure the weight % PE in the blend. The thickness of the film was controlled to ensure that the strongest absorbance in the 1500–1200 cm<sup>-1</sup> region did not exceed 1.2 absorbance units (AU) and remained in the preferable 0.3–1.0 AU range (Figure 1, Y-axis). Infrared spectra recorded on these salt plate cast films consisted of 74 co-added interferograms measured at 4 cm<sup>-1</sup> resolution. Total measurement time was 30 seconds.

We developed a second, novel procedure for measuring the PE:PP blend ratio. This procedure used the same calibration solutions, but rather than salt plates, the solutions were applied to a smooth piece of PTFE. After drying in an oven at 70–80 °C, the resulting 20–50 μm thick films were easily peeled off the still warm PTFE. These self-supporting polymer cast films were then analyzed by the Cary 630 FTIR equipped with the DialPath (or TumbIR) accessory using the 100 micron pathlength cell. The polymer films easily slide between the cell windows, allowing for convenient repositioning and analysis of multiple areas of the film. This makes finding the optimal thickness (0.3–1 AU) faster, since larger pieces of polymer film can be sampled in many locations. Infrared spectra recorded of these self-supporting films consisted of 74 co-added interferograms measured at 4 cm<sup>-1</sup> resolution. Total measurement time was 30 seconds.

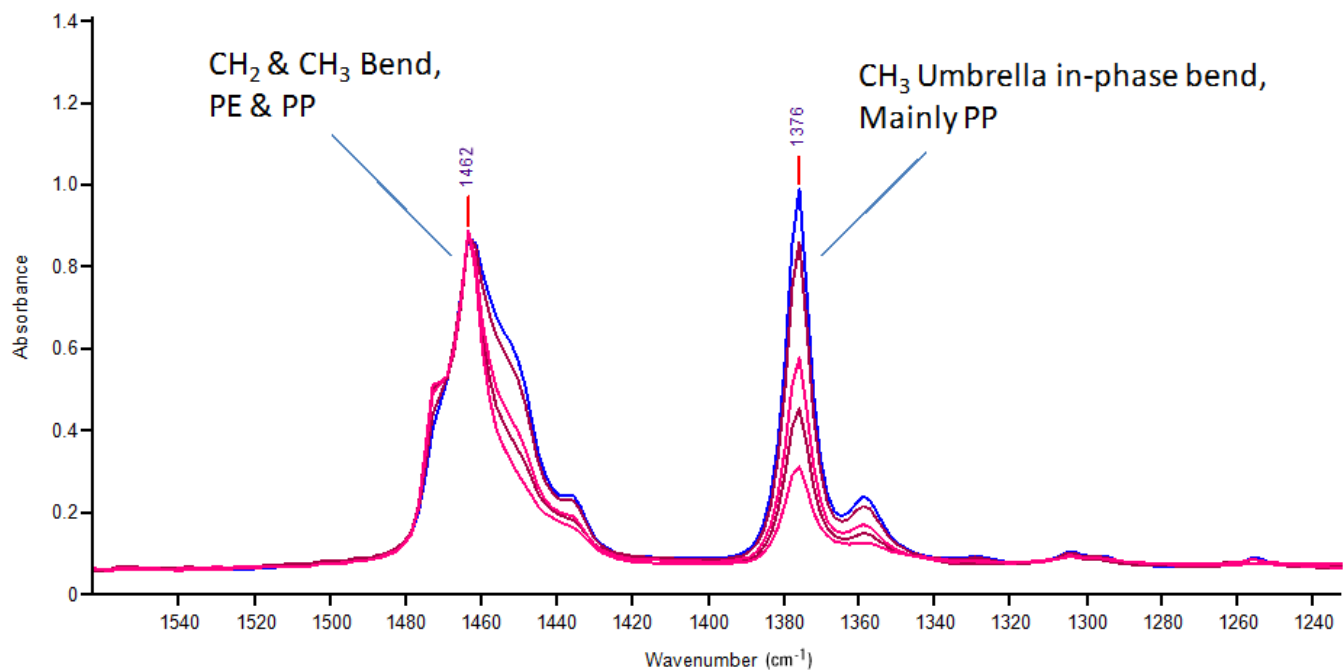
The new DialPath method can be used on the Agilent 4500 and 5500 FTIR spectrometers as well as the Agilent Cary 630 FTIR. The 4500 is a portable, battery operated FTIR spectrometer available with the DialPath technology. The 5500 is a dedicated, benchtop FTIR spectrometer also available with the DialPath sample interface. These instruments have the same reliable performance and patented interferometer technology as the Cary 630 FTIR, but allow for onsite and near line analysis.

A calibrated method was developed and added to the Cary 630 FTIR methods library so that future unknown samples can be analyzed. The method enables an automatic calculation of the PE:PP ratio, and the numerical value and spectra of the unknown is automatically displayed and/or printed.

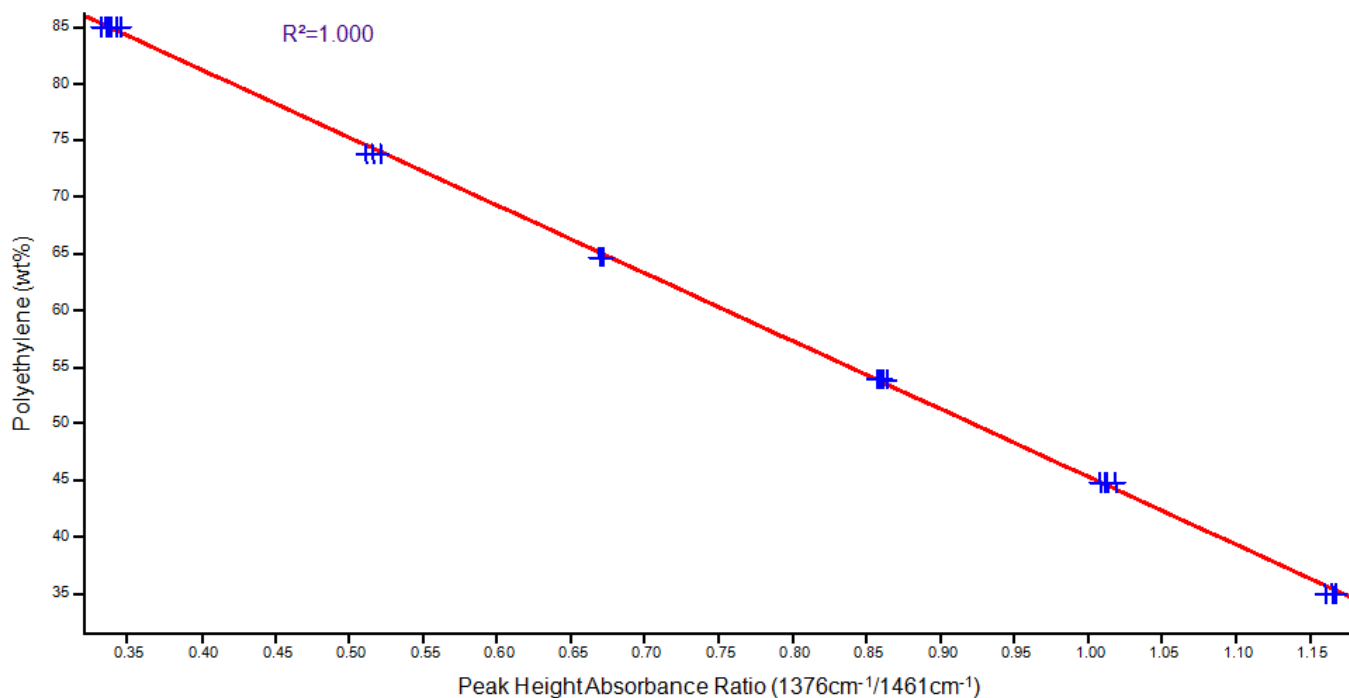
## Results and discussion: PE/PP blend cast film FTIR calibration

The salt plate cast film FTIR procedure is consistent with ASTM D3900-05a (Rubber-Determination of Ethylene Units in Ethylene-Propylene Copolymers (EPM) and in Ethylene-Propylene-Diene Terpolymers (EPDM) by Infrared Spectrometry). To correct for film thickness, the absorbance of a variable component peak (in this case, PP) is measured as a ratio to another matrix peak (in this case, PE). Both the novel PTFE and the original salt plate cast film method use the same peak height ratio of the 1376 cm<sup>-1</sup> to the 1462 cm<sup>-1</sup> bands (Figure 1) to determine composition. The new cast film method, based on the DialPath accessory linear regression calibration plot yields R<sup>2</sup>=1.000 (Figure 2) and the salt plate cast film method yields the identical calibration and R<sup>2</sup> value.

Fringing patterns are sometimes observed when smooth polymer films are measured in the mid infrared region. Fringing appears as a baseline sine wave pattern in the spectra and arises from internal reflection of the IR light inside smooth polymer films. The techniques described in this application note do not produce fringing in the areas of interest by either the salt plate or the DialPath transmission methods. In the latter case, the concave/convex matching cell window design of the DialPath and TumbIR minimizes fringing, while providing an easy to open and clean optical cell with precise pathlength reproducibility.



**Figure 1.** The overlaid aliphatic bend region of the FTIR PE/PP blend calibration spectra. The quantitative method for %PE uses a ratio of the methyl 1376 cm<sup>-1</sup> (mainly PP) to the 1462 cm<sup>-1</sup> (methyl and methylene bend) band.



**Figure 2.** The calibration plot of PE/PP blends prepared as cast films, and analyzed using the Tumbler or DialPath on the Agilent Cary 630 FTIR. The same calibration with traditional transmission compartment (film cast in salt plate) yields similar calibration results. The calibration uses the ratio of the PP band at 1376 cm<sup>-1</sup> to that of the 1462 cm<sup>-1</sup> band in both PE and PP.

## Conclusions

The FTIR analysis of 35–85% PE concentrations in PE/PP blends is now easier than ever using the versatile Agilent Cary 630 FTIR spectrometer. An excellent calibration was developed using the same cast film technique and IR peaks as the ASTM D3900 PE/PP copolymer method. The Cary 630 FTIR standard transmission compartment is used for the measurement of these cast polymer films on salt plates.

A second, novel method has been developed using the Cary 630 FTIR DialPath transmission accessory, which is easier and more versatile, because larger pieces of self-supporting films can be analyzed in a short amount of time. The polymer films can be repositioned and measured in multiple regions without opening the cell, thus allowing the analyst to find the ideal film thickness for the measurement.

Both methods yielded the same excellent calibration and identical  $R^2$  value. The PE:PP calibration is now part of a method that has been added to the Cary 630 FTIR software, allowing the polymer ratio in unknown samples to be instantly calculated and displayed.

**[www.agilent.com/chem](http://www.agilent.com/chem)**

Agilent shall not be liable for errors contained herein or for incidental or consequential damages in connection with the furnishing, performance or use of this material.

Information, descriptions, and specifications in this publication are subject to change without notice.

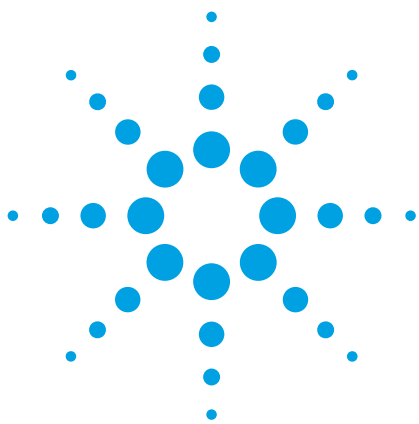
© Agilent Technologies, Inc. 2012

Published January 19, 2012

Publication number: 5990-9785EN



**Agilent Technologies**



# Rapid identification of o-rings, seals and gaskets using the handheld Agilent 4100 ExoScan FTIR

## Application note

### Materials testing

#### Author

John Seelenbinder

Agilent Technologies  
Danbury, CT, USA



## Introduction

In virtually every industrial and chemical plant worldwide, using the correct materials to seal valves, pipes and vessels is critical from both a productivity and safety perspective. Incorrect sealing materials can lead to leaks, loss of product, and equipment downtime, as well as affect worker health or potentially lead to catastrophic failures.

Chemical equipment manufacturers will specify the optimum sealing material for their equipment, but each type of material may have a multitude of different compositions, properties and usages. The material chosen depends on the type of equipment, the specific applications or chemicals that are being processed and the conditions to which the chemicals are being subjected. The result is that there are literally thousands of different o-ring, seals and gaskets available for the chemical, petrochemical and petroleum industries.



**Agilent Technologies**

In manufacturing plants, handheld XRF is being used to ensure that the metals in the chemical equipment have the proper elemental composition for the manufacturing process. Similarly, there is a clear need for a handheld analyzer to ensure that the correct organic based sealing material is positively identified.

Though Near-IR and Raman have some use in this application, many of the o-rings, gaskets and seals are carbon black filled and present a special problem. The Agilent 4100 ExoScan system (Figure 1) equipped with a germanium ATR sample interface provides an excellent solution for identifying these materials, including the difficult-to-analyze carbon black filled examples.



Figure 1. Agilent 4100 ExoScan FTIR system

## Experimental

A series of carbon black filled seals and o-rings were sourced and then analyzed by the 4100 ExoScan FTIR equipped with its novel spherical germanium ATR. This sample interface was chosen for two major reasons:

- The spherical shape of the ATR element results in high quality, reproducible spectral results while at the same time minimizing the pressure exerted on the surface of the sample. This is a non-destructive test (NDT) for measuring a material, that is, the gasket or o-ring is measured without cutting a sample or deforming the surface.
- Germanium is chosen as the ATR material since it has a shorter overall pathlength through the sample due to its higher refractive index and shorter depth

of penetration. Carbon is a nonspecific absorber of IR radiation and if the depth of penetration of IR radiation is too great, the carbon particles will scatter the IR light. This results in a baseline shift in the resultant spectrum, obscuring the characteristic infrared absorbance bands (the IR 'fingerprint') of the sample, making identification of the material less reliable (Figure 2).

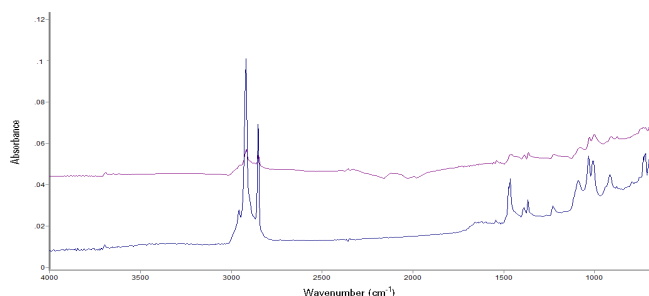


Figure 2. Comparison of carbon black filled elastomeric material recorded using diamond ATR (purple) and germanium ATR (blue). The Ge ATR has a shorter depth of penetration resulting in less scattering from the carbon black particles and less baseline shifting. The fundamental vibrational absorbances are readily visible, when compared to the spectra recorded using the diamond ATR.

Specifically, 14 samples were measured of 9 different seal materials. Samples from different manufactures were measured for 5 of the 9 materials. The following carbon filled sealing materials were measured: fluorosilicone; silicone, viton, EPR/EPDM, neoprene, butyl, kalrez, NBR, polyurethane, and natural rubber. The samples were recorded by lightly pressing against the ATR crystal to ensure contact. The Agilent MicroLab FTIR software has a real-time analysis mode that enables the user to ensure that adequate contact is made between the sample and the ATR element as evidenced by the instantaneous appearance of the desired spectra (Figure 3).

Spectra resulted from a 20 second interferogram co-addition recorded at 8 cm<sup>-1</sup> resolution. The spectra from this group of samples were used to form a reference library in the ExoScan's MicroLab software. Days later, a second set of spectra were recorded from other samples of these materials and searched against the onboard library. The top two hits were reported by the software as well as the degree of similarity (the correlation function).



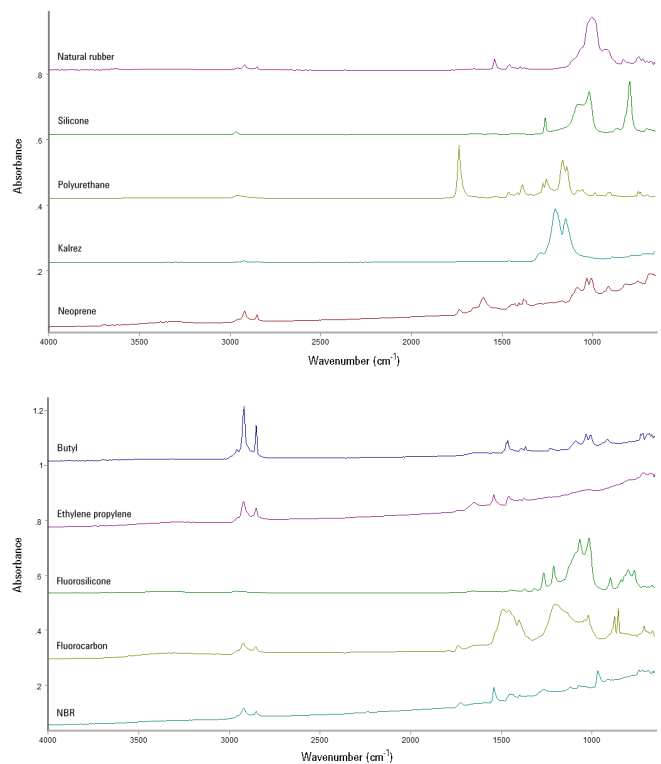


**Figure 3.** Sample is lightly pressed against spherical Ge ATR element (left) and real time display instantly shows that adequate contact is made. Co-addition is initiated and resultant high quality spectrum is searched against onboard spectral library (right).

## Results

High quality spectra (Figures 4 and 5) of the sealing materials were obtained using the previously described procedure. The spectra show clear spectral differentiation based on the class of material and the carbon particles had minimal affect on spectral quality or baseline position. These spectra formed the basis of the onboard library and when the evaluation samples were measured days later, all samples produced the correct first match, and five of the samples produced a close second match from within the same type of material (Table 1).

The spectrum measured from an individual o-ring contains chemical information from both the elastomer material and any fillers used. For this reason, the first match always returns the same brand o-ring. Other o-rings made of the same elastomer may come up as a close second match if the fillers used are similar. Two examples of this in the tested sample set are the silicone and fluorosilicone o-rings. These samples contained very little filler. Their infrared spectra contained information primarily from the elastomer material, and hence both o-rings in these two categories had similar match qualities. By comparison, the NBR sample was highly filled. The two samples of NBR were not close second matches because the amount of filler differed between the two samples.



**Figure 4 and 5.** Spectra of seals were recorded using a 20 second co-addition of interferograms at 8 cm<sup>-1</sup> resolution. The spectra are offset for clarity.

**Table 1.** Library search results for a test set of 14 o-rings matched against an o-ring spectral library. Samples and matches are listed by material (item number). The similarity values are automatically calculated in the MicroLab software and are based on a first derivative normalized dot product correlation.

Sample	1st match	Similarity	2nd match	Similarity
NBR (618316)	NBR (618316)	0.84	Ethylene propylene (618337)	0.21
NBR (618333)	NBR (618333)	0.819	Natural rubber (618332)	0.71
Silicone (618341)	Silicone (618341)	0.977	Silicone (618318)	0.963
Kalrez (618327)	Kalrez (618327)	0.953	Kalrez (618328)	0.951
Viton (618313)	Viton (618313)	0.604	Kalrez (618328)	0.15
Viton (618344)	Viton (618344)	0.71	Viton (618313)	0.1
Neoprene (618325)	Neoprene (618325)	0.55	EPR (618337)	0.14
Fluorosilicone (618311)	Fluorosilicone (618331)	0.95	Fluorosilicone (618319)	0.89
Fluorosilicone (618319)	Fluorosilicone (618319)	0.97	Fluorosilicone (618331)	0.963
Polyurethane (618340)	Polyurethane (618340)	0.955	Kalrez (618328)	0.017
Silicone (618318)	Silicone (618318)	0.976	Silicone (618341)	0.975
EPR (618337)	EPR (618337)	0.5	EPR (618314)	0.37
EPR (618314)	EPR (618314)	0.46	EPR (618337)	0.288
Butyl (618339)	Butyl (618339)	0.47	Neoprene (618315)	0.33

## Conclusion

The Agilent 4100 ExoScan FTIR equipped with spherical Ge ATR is proven to be an effective analyzer for determining and verifying the identify of carbon black filled polymer and elastomeric based seals, gaskets and o-rings used in the chemical industry. These types of materials have traditionally been difficult to analyze by spectroscopic methods such as near-IR and Raman and thus the 4100 ExoScan FTIR system offers a more universal solution for determining the identify of both carbon filled and non carbon filled materials. Other manufacturing industries such as aerospace, food and pharmaceuticals face similar issues.

Because of its performance, size and mobility , the 4100 ExoScan FTIR can be used in both the lab and/or where the sample is located. This means that sealing materials can be examined at the site of use, without having to send them to a lab for measurement and waiting for results. The dedicated MicroLab FTIR software makes the system easy to use, so factory personnel can accurately identify materials. Moreover, this is truly a non-destructive methodology so samples do not need to be cut or otherwise modified for measurement thereby maintaining the integrity of the seal.

[www.agilent.com/chem](http://www.agilent.com/chem)

Agilent shall not be liable for errors contained herein or for incidental or consequential damages in connection with the furnishing, performance or use of this material.

Information, descriptions, and specifications in this publication are subject to change without notice.

© Agilent Technologies, Inc. 2012

Published February 1, 2012

Publication number: 5990-9878EN



**Agilent Technologies**



# A new approach to sample preparation free micro ATR FTIR chemical imaging of polymer laminates

## Application Note

## Materials Testing & Research

### Author

Dr. Mustafa Kansiz  
Agilent Technologies,  
10 Mead Rd, Yarnton,  
Oxfordshire, OX5 1QU, UK

### Abstract

Micro ATR chemical imaging of polymers and in particular polymer laminates typically requires significant application of pressure to ensure good contact between the ATR crystal and the sample. To ensure that such thin samples can withstand the pressure without buckling, elaborate sample preparation procedures are often required to support cross-sectioned materials: embedding of sample in resin, cutting the resin and polishing the contact surface. Such procedures are tedious, require overnight resin curing and carry the added risk of cross-contamination. Presented here is a novel method of ultralow pressure micro ATR FTIR chemical imaging that removes the need for any structural support. This allows samples to be measured "as-is" using direct contact with the ATR crystal. This unique capability is made possible through the use of Agilent's "Live ATR imaging" technique which provides enhanced chemical contrast, and enables the exact moment of contact between the sample and ATR crystal to be determined and provides a visual measure of the quality of contact. Adhesive layers as thin as a few microns can be clearly observed in 50-micron thick polymer laminates without sample preparation.

### Introduction

#### What are polymer laminates and what are they used for?

Polymer laminates are film structures consisting of two or more layers adhered together to make a structure. The polymeric materials forming these laminates have varying thickness—from a few microns to tens of microns. This can influence a variety of properties, such as chemical, mechanical and barrier (e.g., impervious to oxygen and/or moisture) properties.



**Agilent Technologies**

To construct these materials, adhesive (tie) layers are often required between two adjacent but chemical incompatible layers. Typically these incompatibilities are between materials with differing polarities, such as nylon and polyethylene.

The adhesives typically have intermediate polarity or contain functional groups with an affinity to both polar and non-polar layers and hence act as good binding material. Such adhesive layers in laminates can be very thin, e.g., between 2 to 10 microns.

Polymer laminates can range in complexity and thickness from those containing only two layers to more than 10 layers (not including adhesive layers). With total cross-sectional thicknesses ranging from <50 microns to >200 microns, polymer laminates are used in a variety of packaging applications, which are employed in industries such as food and pharmaceuticals.

### **What are the analytical challenges/requirements for polymer laminates?**

With ever increasing manufacturing sophistication enabling more complex and thinner laminate structures to be produced, the analytical challenges to ensure good product quality control, troubleshooting or the reverse engineering of competitive products are also increasing in complexity.

The analytical tools available to analyze such laminates are wide and varied and include a range of optical microscopy techniques, thermal techniques (such as differential scanning calorimetry) and various spectroscopic techniques.

In particular, Fourier Transform Infrared (FTIR) microscopy has proven most useful for the analysis of polymer laminates. This has resulted from the core application of FTIR spectroscopy in the identification and characterization of polymers, combined with the ability to obtain this information from small areas.

When applied to polymer laminate analysis, FTIR microscopy is typically performed in transmission mode and requires that the total sampled thickness be within a certain limit. For polymeric materials, this is typically 10–20 microns. Preparing thinly sliced polymer and polymer laminate materials at a thickness of 10–20 microns presents some challenges. Typically, dedicated (and often expensive) specialized cutting devices such as microtomes are required. Even then, the cut samples are often difficult to handle due to curling or difficulties with static stick. To minimize these effects, samples can be embedded in resin before cutting and microtomed together within the resin support (Figure1). This unfortunately adds another material with a complex IR spectrum to the sample. Once cut, if the sample is flat, it can be placed in a sandwich between infrared transparent windows and sampled in transmission mode. However, because of internal reflections between the front and back surfaces of the sample, “fringing effects” can commonly be observed. This results in a sinusoidal baseline during such measurements.

With these issues and sampling preparation steps aside, transmission FTIR microscopy is a relatively simple technique to obtain spectra from small areas. It does however suffer from one major limitation: spatial resolution is relatively poor, especially when compared to optical microscopy techniques. Typical spatial resolution limits for transmission mode FTIR microscopy are about 10–15 microns.

In comparison to transmission mode, the use of micro attenuated total reflectance (ATR) as the mode of analysis removes the requirement for samples to be a certain thickness, so samples no longer need to be thinly cut. However, as ATR requires intimate contact with the samples, there are still some important sample preparation requirements. Primarily, the sample must be flat and smooth to ensure that there is full and complete contact across the ATR measurement’s field of view. Additionally, and of paramount importance to the detection of ultrathin layers, micro ATR FTIR

microscopy provides for a factor of four spatial resolution enhancement over transmission mode.

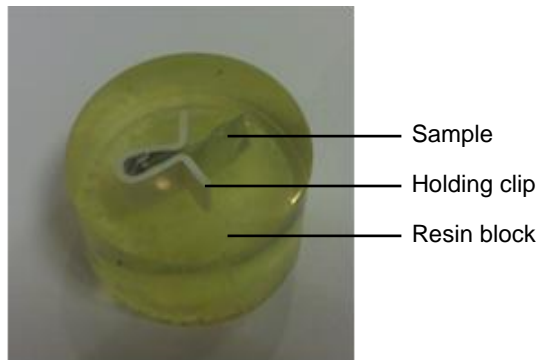
To ensure complete and intimate contact, a significant amount of pressure must be applied between the sample and ATR crystal. Many micro ATR imaging systems rely on indirect methods of ensuring good contact, by using coarse pressure sensors, often with preset pressure levels.

The inability to directly monitor the exact moment and quality of contact in most micro ATR imaging systems is also another factor that requires the use of higher pressures to ensure good contact. For naturally hard materials, the pressures needed to ensure a good contact between the ATR and surface is typically not an issue. However, given samples may have cross-sectional thicknesses of only 50–200 microns, even very slight pressures will cause an unsupported polymer laminate to buckle or deform in a way that prevents good contact.

Therefore, to avoid buckling or other structural distortions of delicate and thin samples under applied ATR pressure, it is mandatory to provide some degree of support. This is most commonly achieved by resin embedding of the sample, followed by cutting and polishing of the surface (Figure 1).

The process of resin embedding is tedious and time consuming (>12 hours), typically consisting of the following steps:

1. Cut a small piece of sample and place it vertically in a holding clamp.
2. Place sample and clamp into a mold and pour in resin to fully cover sample.
3. Allow resin to cure, typically overnight, and then remove the resin-embedded sample from mold.
4. Cut the top surface of resin, so as to expose a cross section of the sample.
5. Polish the cut surface with successively finer and finer lapping paper (from 30 microns to 1 micron).



**Figure 1.** An example of a polymer film, held by a clip and embedded in a resin block

Cutting and polishing also introduces the risk that resin and polishing material may contaminate the sample or complicate the image and spectral interpretation.

Once prepared, resin-embedded samples are brought into contact with the micro ATR and pressure is applied. Often, the levels of pressure applied—even at lower settings—are enough to produce indentations at the surface of the samples, potentially preventing the subsequent analysis of the sample with other analytical techniques. This technique is then potentially destructive.

### **A new approach to “pressure free” micro ATR imaging**

Agilent Technologies has developed a radically new approach that removes the need for resin embedding or any other sample preparation. This enables delicate and thin samples to be measured “as-is”. The new approach hinges upon the fact that the infrared detector in an Agilent FTIR imaging system is a focal plane array (FPA\*) and so affords simultaneous two-dimensional (2-D) data collection. And, most importantly and uniquely, it utilizes the “Live ATR imaging” feature with enhanced chemical contrast to ensure that the minimum pressure necessary for good contact is applied. This results in a non-destructive measurement—a remarkable capability.

Unlike linear array IR detectors, which must be scanned across an area to generate a 2-D image, FPAs provide instantaneous “real-time” imaging of the sample’s surface, as it is in contact with the ATR. Such real-time imaging permits a visual assessment of the quality of sample contact before any data collection.

However, having a 2-D FPA alone does not provide for enough contrast to determine the moment of sample contact with the ATR. To overcome these issues Agilent Technologies has recently developed a unique “Live ATR imaging” mode, which significantly enhances the chemical contrast of the real-time FPA image, so the exact moment of sample contact can be visualized and contact monitored as the pressure is increased.

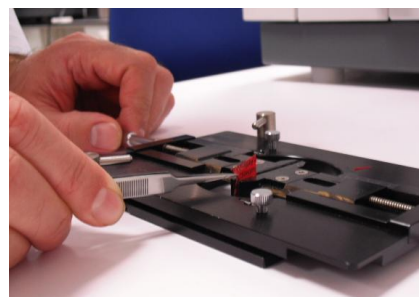
This mode provides for direct and real-time monitoring of the quality of contact (i.e., has the sample made complete contact across the entire field of view), which allows for extremely low levels of pressure to be applied. And it is this extremely low level of pressure that now allows for delicate and thin samples to be mounted, cross-sectioned end on, without any need for sample support using resin.

**Sample measurement with “Live ATR imaging”**

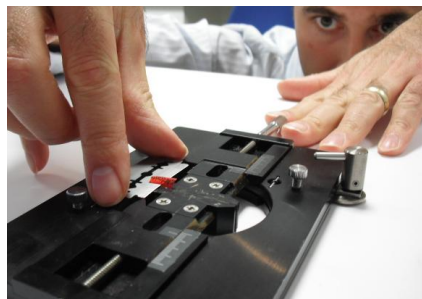
In five simple steps which only take only a few minutes (Figure 2), a sample of polymer laminate (i.e., a sausage wrapper) can be prepared for measurement using “Live ATR imaging”—removing the need to spend hours embedding, cutting, and polishing!



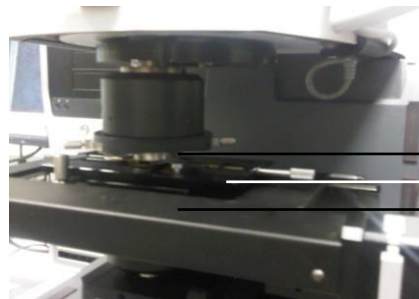
**Step 1.** Cut a small piece of sample.



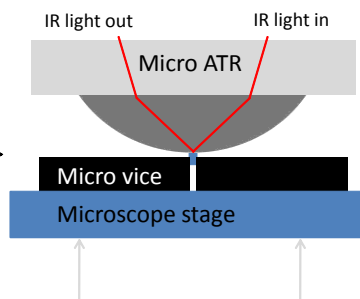
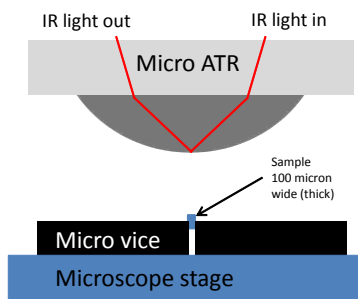
**Step 2.** Place sample into micro-vice.



**Step 3.** Cross-section sample with razor.

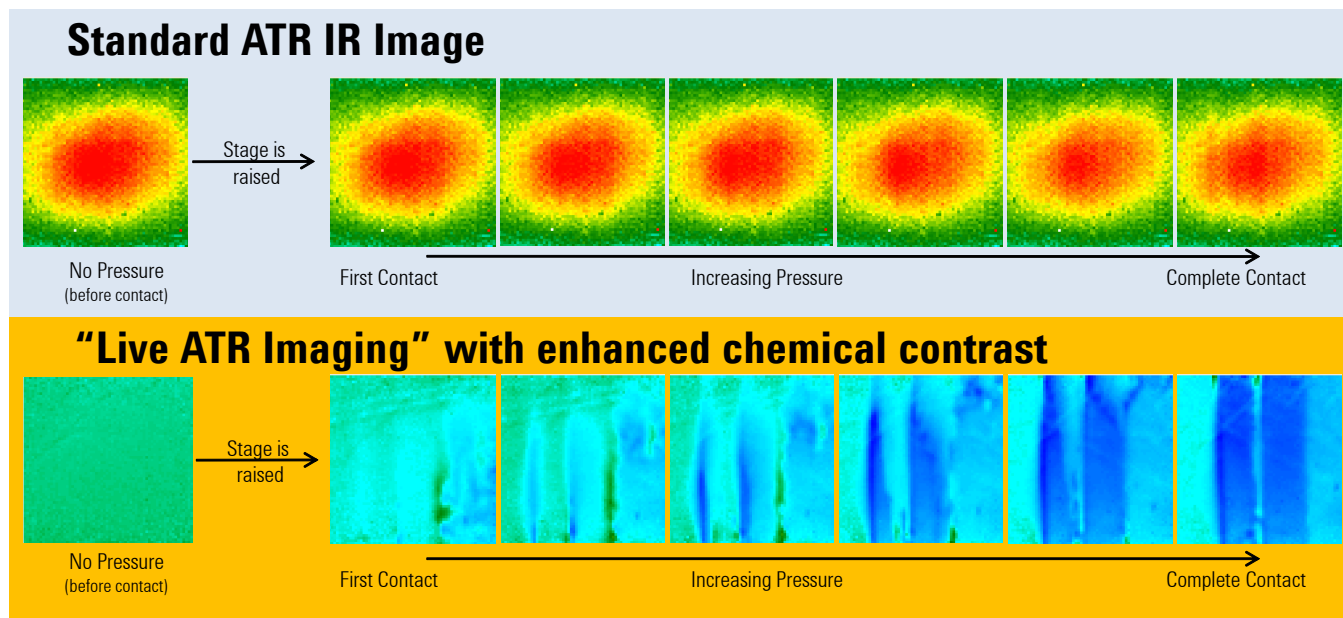


**Step 4.** Place micro-vice onto microscope stage.



**Step 5.** Raise stage to make contact and then collect data.

**Figure 2.** Easy five-step process—from raw sample to data collection—allows sample measurement of polymer laminates to be achieved in minutes using “Live ATR imaging” with enhanced chemical contrast. Note: Micro ATR and sample are drawn to scale



**Figure 3.** Comparison of a standard ATR IR image and Agilent’s “Live ATR imaging” with enhanced chemical contrast—clearly showing the latter can detect first contact of the ATR crystal with the sample and that contact quality can be monitored real-time as the pressure is increased and before any data collection

Figure 3 shows a side-by-side comparison of Agilent’s unique “Live ATR imaging” with enhanced chemical contrast and a standard ATR IR image.

Reviewing the upper series of images, the similarity of all the standard ATR IR images makes it impossible to determine when the ATR crystal makes contact with the sample’s surface or make any reasonable assessment of the quality of the contact as the pressure being applied increases.

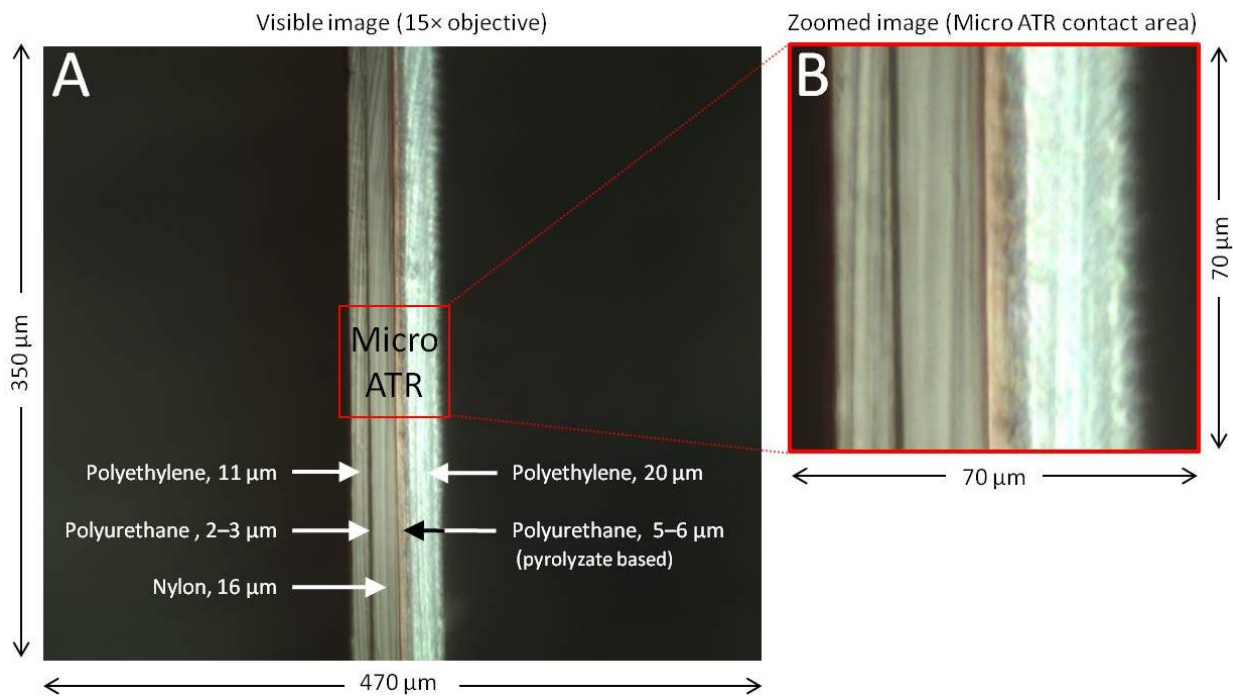
Whereas, as seen in the lower series of images, Agilent’s unique “Live ATR imaging” with enhanced chemical contrast enables real-time monitoring of the sample contact as the sample is being raised and pushed up against the germanium crystal of the Micro ATR. The real-time monitoring allows for a near “pressure free” contact to be made between the sample’s surface and the Micro ATR, this means unsupported cross-sections of ultrathin polymer laminates can be measured directly—even very thin samples of less than 50 microns—without the need for being embedded in resin!

## Results

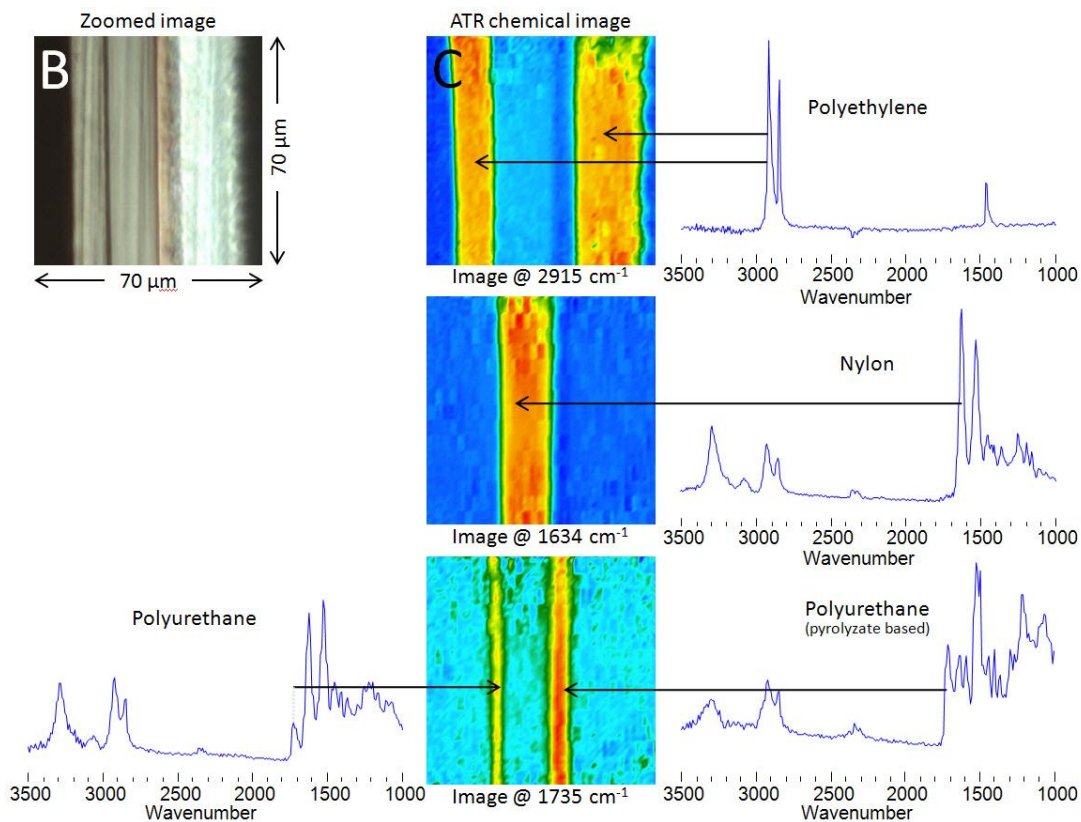
To further demonstrate the capabilities of “Live ATR imaging”, a polymer laminate sample was obtained from the plastic wrapper of a sausage (~55 microns total thickness).

The results below were collected using the following conditions:

FTIR Spectrometer	Agilent Cary 670 FTIR
FTIR Microscope	Agilent Cary 620 FTIR
Focal Plane Array*	64 × 64 MCT
Spectral Resolution	4 cm <sup>-1</sup>
Number of Scans	64 (2 mins)
Spatial Resolution	1.1 microns (pixel size)
Collection mode	Micro ATR (Ge)
Sample Type:	Sausage wrapper



**Figure 4.** Optical images: A—the full field of view visible through microscope, annotated with the chemical composition and approximate thickness of the various layers in the sample; and B—zoomed image corresponding to the contact area of the Micro ATR



**Figure 5.** Identifying layers: B—as per Figure 4, above; and C—three chemical images created with different wavenumbers to highlight the main layers and tie layers with corresponding representative spectra as indicated by the arrows. Note: All spectra are shown in absorbance units, with axes omitted for clarity



A visual inspection of the sample using the standard binocular or internal visible camera revealed the sample to be a polymer film containing three main layers with two adhesive layers (Figure 4).

A summary of the results is presented in Figure 5. This shows how the three main layers are clearly identified: a 16-micron thick layer of nylon sandwiched between two layers of polyethylene, 11 and 20 microns in thickness.

However, as demonstrated, the power of Micro ATR chemical imaging with an Agilent FPA detector is in its ability to measure layers as thin as a few microns. Two tie layers were clearly identified and easily determined as being composed of subtly different polyurethane adhesives. The thinner of the two polyurethane layers was only 2–3 microns across and the pyrolyzate-based layer was thicker at 5–6 microns. The measurement of both these layers would be impossible with any other technique other than micro ATR chemical imaging on the Agilent Cary 620 FTIR chemical imaging system.

## Summary

There are two clear benefits to analyzing polymeric laminates using Agilent's Cary 620 FTIR chemical imaging system:

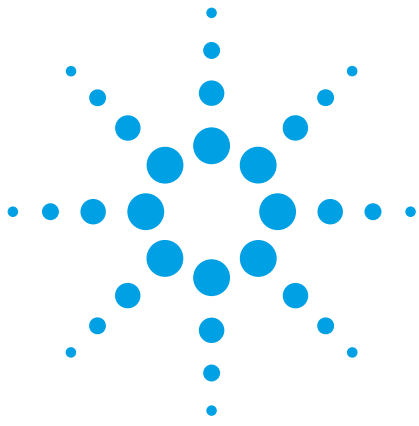
1. Analyze ultra-thin samples without resin embedding

Through the use of Agilent's unique "Live ATR imaging", ultra-thin films of 50 microns or less can be measured as-is with Micro ATR chemical imaging. This avoids the need for any of the traditional and complicated resin embedding requirements. As such, instead of waiting hours for resin to cure and then spending time cutting and then polishing the surface, multiple samples or multiple locations on one sample can be measured in a few minutes.

2. Unrivalled spatial resolution

In combination with the use of a FPA detector\*, Agilent's unique Micro ATR design provides for a pixel size of 1.1 microns that allows ultra-thin adhesive layers as narrow as two microns to be identified. This level of spatial resolution provides unrivalled levels of detail and chemical information to assist in the most complicated and difficult sample measurements.

\*This product is regulated by the U.S. Department of State under the International Traffic in Arms Regulations, 22 CFR 120-130 ("ITAR"). An export license from the U.S. government is therefore required to export this product from the United States, and other ITAR restrictions apply to the shipment, use, service and other aspects of this product and the FTIR instrument in which it is used.



# Identification of contaminants in vehicle fuel tank caps using FTIR ATR-microscopy

## Application note

Materials testing and research

### Authors

Jonah Kirkwood<sup>†</sup> and Mustafa Kansiz<sup>\*</sup>

Agilent Technologies  
<sup>†</sup> Mississauga, ON, Canada  
<sup>\*</sup> Melbourne, Australia



### Introduction

Manufacturers of parts and components to the automotive industry are required to assure the quality of their products, and FTIR spectroscopy is widely used for this purpose. In this example, it was apparent that fuel tank caps were being contaminated by an unknown material during production. The contaminants were ~20–300  $\mu\text{m}$  in size. As the unknown particles were small in size, an FTIR microspectroscopy technique was used to investigate.

## Experimental

### Instrumentation

To perform the analysis of micron-sized contaminants, an Agilent Cary 660 FTIR spectrometer coupled to a Cary 610 FTIR microscope was employed. In order to facilitate direct measurement of the contaminated regions, without any sample preparation, a 'slide-on' germanium micro attenuated total reflectance (ATR) accessory was used. The system enables fast, sensitive and precise microscale direct measurements. The accessory is also available with an optional diamond crystal for the analysis of very hard materials.

### Sample analysis

Minimal sample preparation was required for the analysis. The contaminated regions were simply cut out and placed on a glass slide, which was placed on

the sample stage of the Cary 610 FTIR microscope coupled to a Cary 660 FTIR spectrometer. The system was configured with standard mid-IR components (mid-IR source, KBr beamsplitter, 250 micron narrow band MCT microscope detector) with data collected at  $4\text{ cm}^{-1}$  spectral resolution with 32 co-added scans (10 seconds).

## Results and discussion

A section of the fuel tank cap (distinctive yellow in color) that was free from contamination was sampled by placing the ATR directly onto the sample surface. High quality spectra were acquired in 10 seconds. The contaminants (red specks) were visibly distinct from the fuel cap, so data was collected from the center of one of these sections. The resulting spectra are shown in Figure 1.

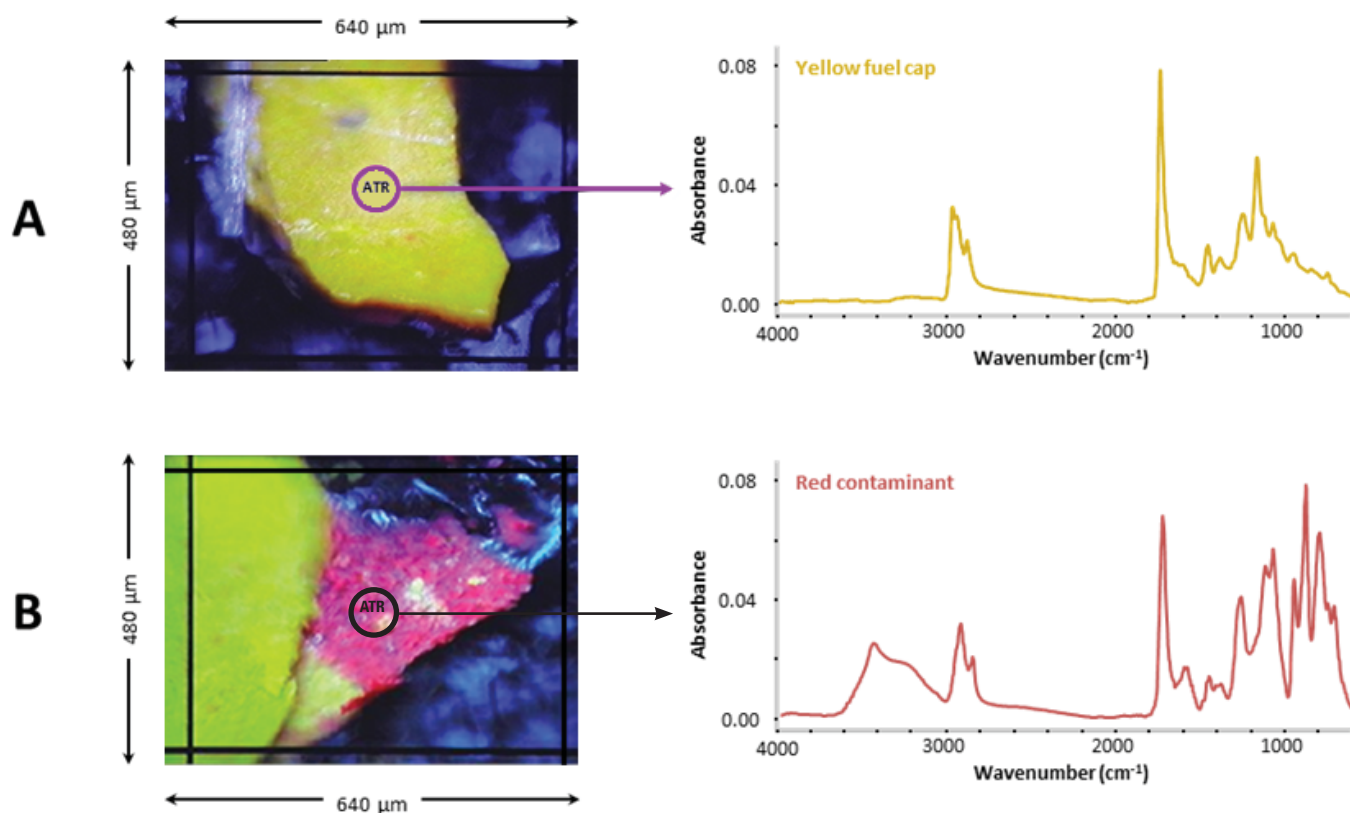


Figure 1. ATR-FTIR analysis of a fuel tank cap. Top: Spectrum measured in a clean section; Bottom: Spectrum measured of a contaminated section

The spectra from the two sections of the fuel tank cap were overlaid using the Agilent Resolutions Pro software so that the data could be visually investigated to see the spectral differences (Figure 2). With just a few simple clicks, the software can subtract the two spectra to isolate the spectral contributions from the contaminant. The next step in the identification process is to search the spectrum against a spectral database using either a custom-built or a commercially-available library.

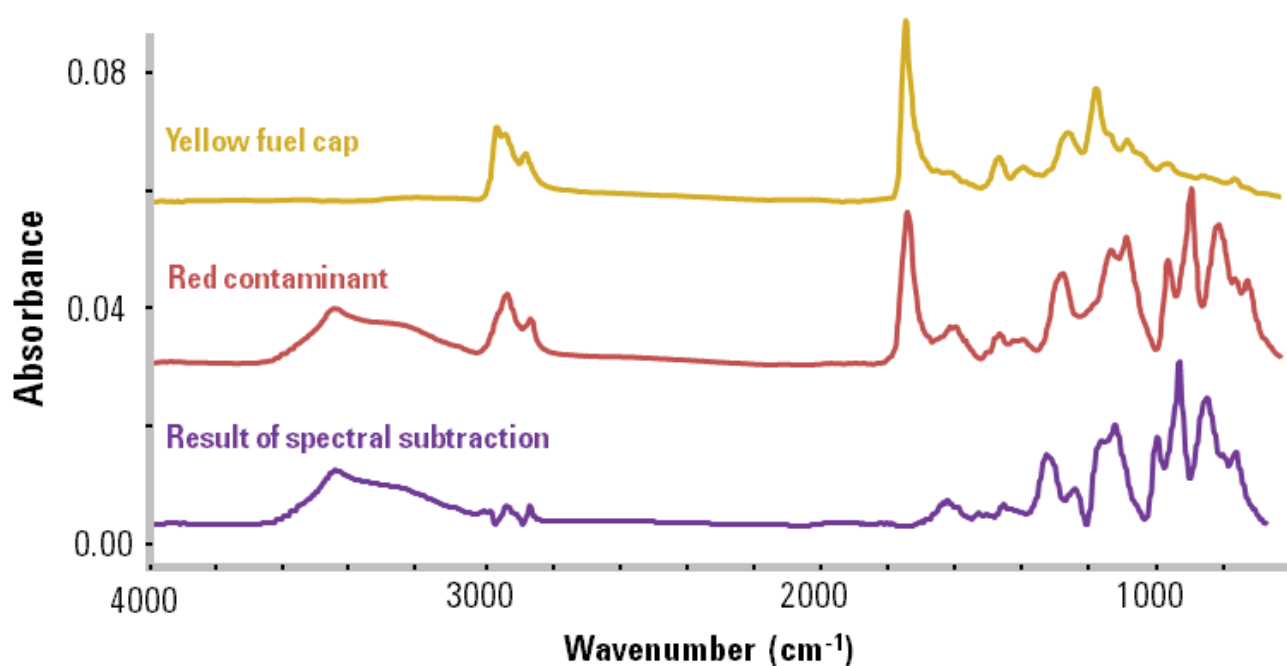


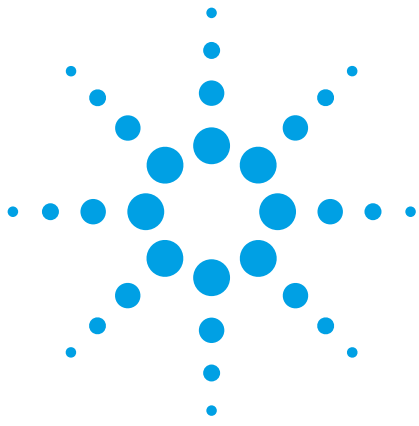
Figure 2. Result (purple) of subtracting the spectrum of a contaminated section (red) of the fuel tank cap from that of a non-contaminated section (yellow)

One of the benefits of using a custom-built library is that it allows the analyst to search against their own proprietary data, at any time. It is also easy to create custom-built libraries, which can be useful for QA/QC applications. However, commercial libraries can provide more advanced data-mining capabilities. The Resolutions Pro software provides direct access to the largest commercially-available FTIR libraries — including a significant number of databases that are dedicated to polymer and materials applications.

As a result of the library search (custom-built or commercial), the contamination was identified to be from the wearing of a red plastic o-ring in a component of the machinery used during manufacturing.

## Conclusions

The study has shown the Agilent Cary 660 FTIR with Cary 610 FTIR microscope fitted with a micro-ATR accessory to be an excellent technique for the identification of the source of contamination in polymeric materials (such as the fuel cap investigated in this instance). Data was collected in 10 seconds and the spectra were compared visually and subtracted to gain a better understanding of the contaminant. A commercially available spectral library search identified the source of the contamination.



# Component failure analysis of vehicle spark plugs using FTIR spectroscopy with a micro-ATR large sample objective

## Application note

Materials testing and research

### Authors

Jonah Kirkwood<sup>†</sup> and Mustafa Kansiz<sup>\*</sup>

Agilent Technologies  
<sup>†</sup> Mississauga, ON, Canada  
<sup>\*</sup> Melbourne, Australia



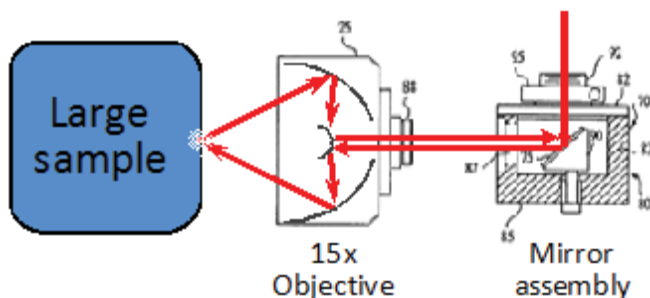
### Introduction

Preventing failure of components or identifying the cause of any failure quickly and reliably is vital across all industries in order to minimize downtime and save money. In this example, the spark plugs of a very large fleet of commercial vehicles began to fail at an unacceptable rate soon after installation. Through simple visual observation, it was apparent that excessive deposits were accumulating on the spark plugs even after low mileage necessitating premature servicing and costly repairs. Clearly corrective measures needed to be implemented.



Agilent Technologies

FTIR is widely used to identify the chemical composition of impurities present in materials, and the traditional approach to this application would be to scrape the surface of the spark plug to try to isolate a small portion from the area of interest. The materials would then be placed under the microscope and spectra would be collected. However, a simpler and completely nondestructive solution uses a micro-ATR FTIR with a large sample objective accessory (see Figure 1). The benefit of this arrangement is that the spark plug samples can be analyzed 'as is', with no intricate sample preparation required.



**Figure 1.** Top: Schematic of the patented Agilent Large Sample Microscope Objective accessory. Bottom: Photograph of the Large Sample Microscope Objective accessory.

## Experimental

### Instrumentation

An Agilent Cary 610 FTIR microscope fitted with a slide-on micro ATR and a Large Sample (LS) Objective accessory was interfaced to an Agilent Cary 660 FTIR spectrometer. The patented large sample microscope objective allows the measurement of unlimited sized samples in reflection or ATR single-point or imaging mode. In this study, the slide-on micro Ge ATR was mounted onto the objective, which points the infrared light out towards the front of the microscope, as indicated in Figure 1.

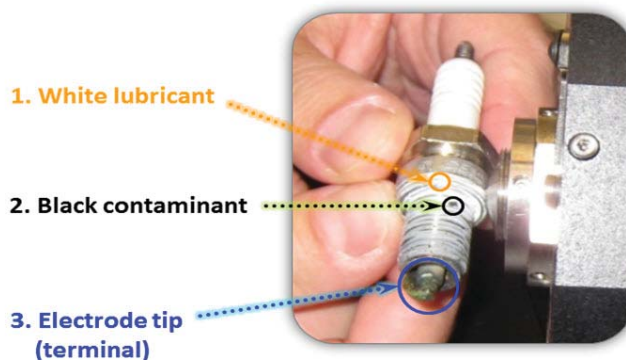
### Sample analysis

No sample preparation was required for the analysis. The spark plug was simply placed against the 90 degree objective of the Cary 610 FTIR microscope. The system was configured with standard mid-IR components (mid-IR source, KBr beamsplitter, 250 micron narrow band MCT microscope detector) with data collected at  $4\text{ cm}^{-1}$  spectral resolution with 16 co-added scans (5 seconds).

## Results and discussion

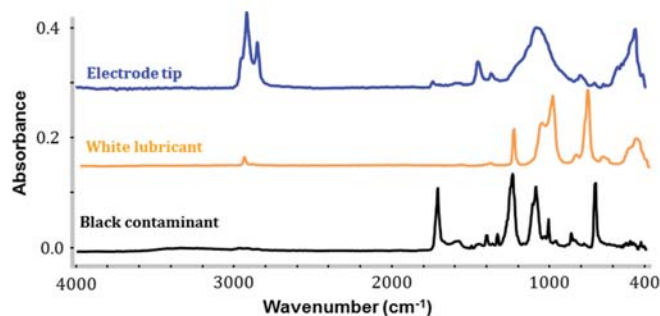
It was clear from zooming in on this spark plug that there were three areas of interest (Figure 2). These included the white lubricant, a potential contaminant (black speck) and the electrode tip with excess deposits.

Figure 2. Side view during ATR analysis of three distinct sampling locations



on a defective spark plug using the Agilent Large Sample Objective

Spectra were collected from each location in 5 seconds each. The spectra were overlaid using the Agilent Resolutions Pro software so that the data could be investigated visually, as shown in Figure 3.



**Figure 3.** FTIR spectra acquired from three sampling locations of a spark plug overlaid using Agilent Resolutions Pro software. Each data set was acquired in 5 seconds.

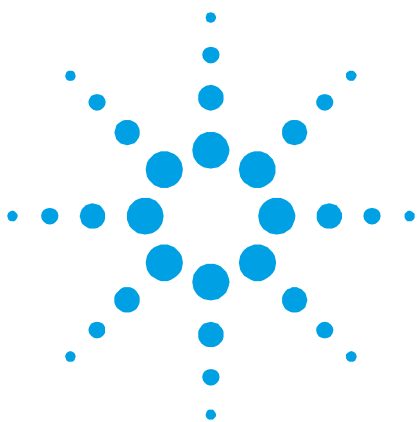
All three spectra of interest were searched against a large commercially available spectral database. The Resolutions Pro software provides direct access to the largest commercially available FTIR libraries, including a significant number of databases that are dedicated to polymer and materials applications. Alternatively, custom-made libraries can be searched.

The results of the search indicated conclusively that the white lubricant was of a silicon polymer based material. The black contaminant was identified as poly(ethylene terephthalate) (PET) with the desposits on the electrode likely to consist of silicone containing oily material.

In this case study, it was likely that the electrode tip deposits were derived from oil and fuel additives, which suggested that fuel and oil were leaking past worn valve guides and piston rings into the combustion chamber, causing hard starting and misfiring. This information enabled corrective action to be taken to prevent further costly repairs and downtime due to damaged vehicle components.

## Conclusion

The Agilent 660 FTIR interfaced to a micro-ATR 610 FTIR microscope with Large Sample Objective accessory is capable of analyzing unlimited sized samples that are difficult to measure using conventional FTIR whilst being nondestructive, hence enabling further analysis via other methods if required. This enabled the direct and rapid analysis of faulty spark plugs that had visible deposits encrusted on the side and center electrodes of the terminal. The use of a commercial spectral library for the identification of unknown contaminants revealed that the deposits were derived from oil and fuel additives. Overall, the method is suitable to resolve component failure issues quickly and efficiently, increasing productivity or reducing downtime in the process, and ultimately saving money.



# Material analysis by infrared mapping: A case study using a multi-layer paint sample

## Application Note

### Author

Dr. Jonah Kirkwood, Dr. John Wilson and Dr. Mustafa Kansiz

Agilent Technologies, Inc.

### Introduction

Agilent's 610 FTIR fourier transform infrared (FTIR) microscopes are routinely used for the analysis of heterogeneous materials. They provide an ability to characterize the spatial distribution of components as well as the ability to identify the specific chemical nature of a sample. Agilent's infrared microscopes can be used on both the microscopic and macroscopic scale using multiple measurement modes including:

- transmission
- reflection
- attenuated total reflectance (ATR)
- grazing angle reflection analysis
- 'large sample' mode using Agilent's large sampling side-port accessory

They are ideal for advanced materials characterization as they are simple to use, provide the best sensitivity and versatility, and can be customized to suit a desired area of analysis. By adding a motorized sample stage to an Agilent Cary 610 FTIR single-element detector microscope system, the capabilities can be extended to include automated infrared mapping analysis.



**Agilent Technologies**



Infrared mapping allows for multiple infrared spectra to be sequentially acquired from different spatially-resolved points on the same sample and provides both spectral and spatial information, thereby facilitating the study of within-sample chemical heterogeneity. Common infrared mapping applications in material sciences include simple material characterization, the analysis of the homogeneity of coating materials, the investigation of multi-layer sample interfaces such as polymer laminates and paint cross-sections, the automated screening of samples for defects or contamination, the characterization of the total reflectance of optical surfaces and other process control applications.

This paper highlights the simplicity and power of Agilent's Agilent Cary 610 infrared mapping microscope for the rapid and automated analysis of a multi-component paint sample.

## **Instrumentation**

The infrared mapping experiment was conducted using a Cary 610 FTIR spectrometer, equipped with a 610 FTIR infrared microscope (containing a 250 micron single-element, narrow-band Mercury Cadmium Telluride detector and a motorized sample stage) operating under Resolutions Pro 5.0 software. A constant flow of dry air was used to purge the system, limiting the contributions from carbon dioxide and atmospheric water vapor.

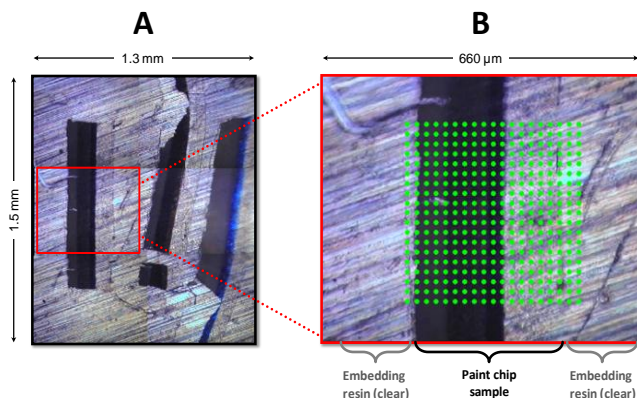
The infrared map was collected in reflection-mode using a pre-loaded grid mapping template that was customized to collect a 19 × 19 grid (totaling 361 spectra) using a 20 μm step size from an area measuring 380 × 380 microns. The infrared spectra were sequentially recorded over the range of 4000–700 cm<sup>-1</sup> at a spectral resolution of 8 cm<sup>-1</sup> by co-adding 16 scans per point (~40 mins for the entire infrared map).

## **Sample preparation**

The paint chip cross sections were prepared from vehicle paint fragments provided by a police forensic laboratory. Samples were mounted in a clear casting polyester resin, and then polished using a 12,000-mesh Micromesh polishing cloth. The embedded paint fragments were microtomed to a thickness of ~10 μm, and the samples transferred to a standard glass microscope slide that was covered with aluminum foil to allow for reflection/absorption analysis.

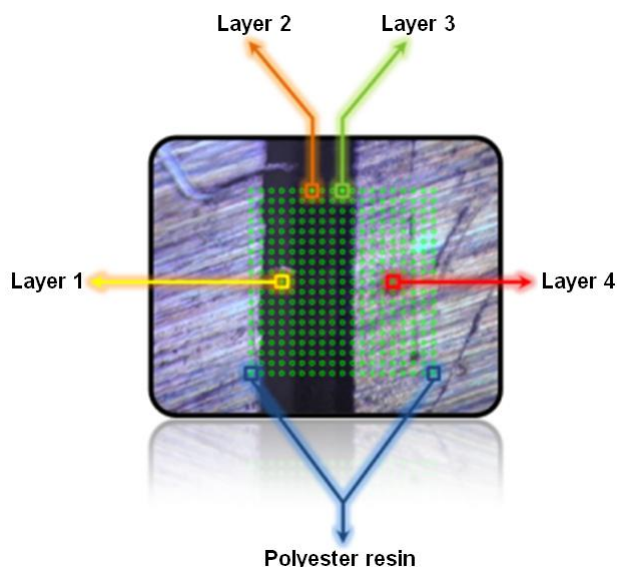
## **Results and discussion**

Infrared mapping using Agilent's Cary 610 FTIR Microscope allows for the automated sequential acquisition of hundreds of high-quality infrared spectra from analytical samples. Using Resolutions Pro software, mapping experiments are extremely flexible. Users can either select individual spectral collection locations themselves or use one of several grid mapping templates that can be customized to a sample, saved and re-applied later. In this experiment, a paint fragment found at an automobile crime scene was embedded in a polymer resin, then microtomed to obtain an appropriate sample thickness. This sample was deposited onto the surface of a reflective infrared support slide which was then placed on the motorized stage of the microscope. A visual image of the paint sample was acquired, followed by the sequential collection of the 361 spectra (19 × 19 grid map; 380 × 380 μm area) using automated infrared mapping. The visual image of the sample and the spectral acquisition locations are shown in Figure 1. Each spectrum in the infrared map results from a spatial resolution of 20 μm.

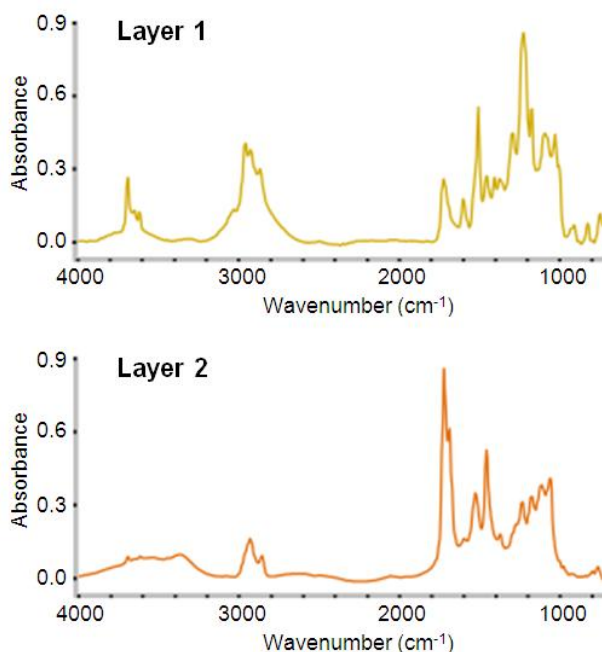


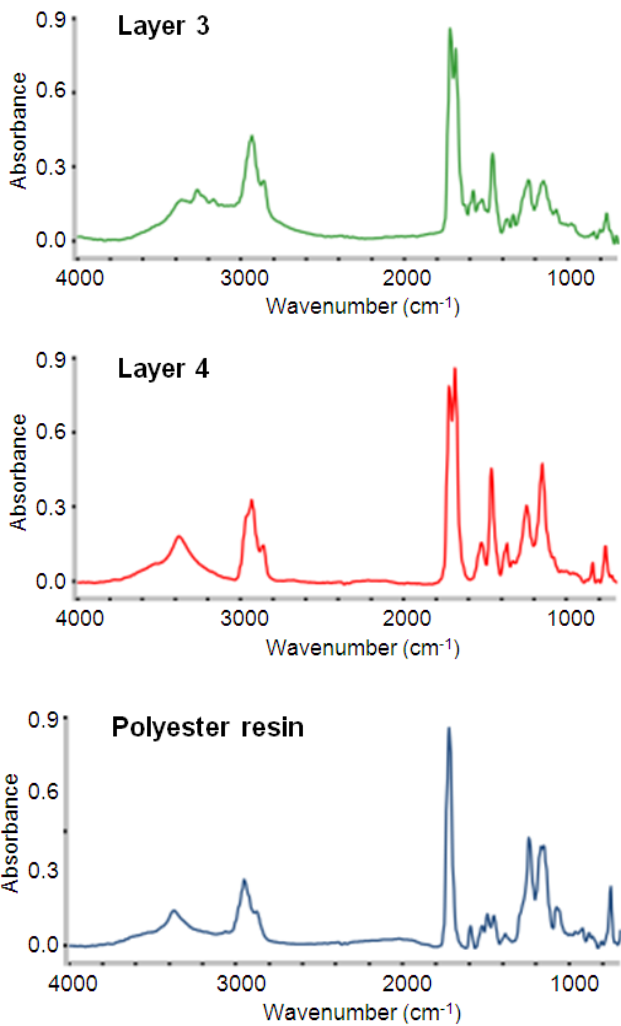
**Figure 1.** (A) Visual image of 3 sections of a paint chip sample (vertical bars), which were embedded into a polyester resin (clear). The reflective aluminum IR-slide upon which the samples are deposited can be seen through the resin. (B) Higher resolution view of a paint chip sample overlaid with the locations of spectral acquisition (represented by the grid of green circles). The overall area of analysis for the spectral map was  $380 \times 380 \mu\text{m}$ , yielding a total of 361 spectra.

The investigation and interpretation of the infrared data was simplified by several intuitive software features. For example, the grid of green circles that is overlaid on the surface of the visual image of the sample can be used to extract spatially resolved data. Simply clicking on a desired sample location (or multiple locations) will fill in the green circle(s) and will display the corresponding IR spectra in the software's 'spectrum' display panel. Spectral peaks of interest can then be compared or used for quantitative analysis, and the selected spectra can be overlaid or stacked to facilitate visual interpretation. Upon cursory visual examination of the forensic evidence in Figure 1, the vertical black strip appeared to be uniform in composition with only minimal variations. However, infrared investigation revealed that the sample is heterogeneous and composed of multiple spatially-resolved vertical layers. Exploratory investigation of the spectra in the map revealed the presence of four chemically distinct layers. In addition, the high spatial resolution of the infrared map allowed for the identification of localized areas with different chemical compositions within the stratified layers. Figure 2 illustrates selected absorbance spectra from the paint chip sample.



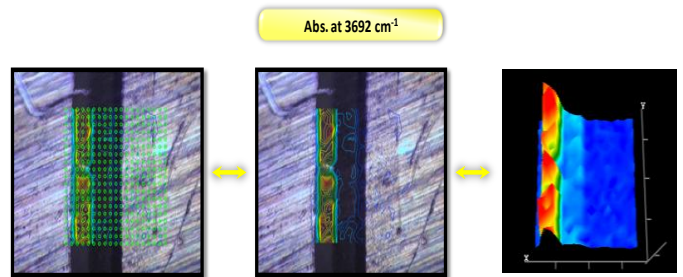
**Figure 2.** Representative FTIR spectra from the four layers of the paint chip sample as well as a spectrum of the embedding resin. Three of the spatially-resolved layers are in the black vertical bar, while one layer is transparent, as is the polyester resin. See layer spectra in the five images below.





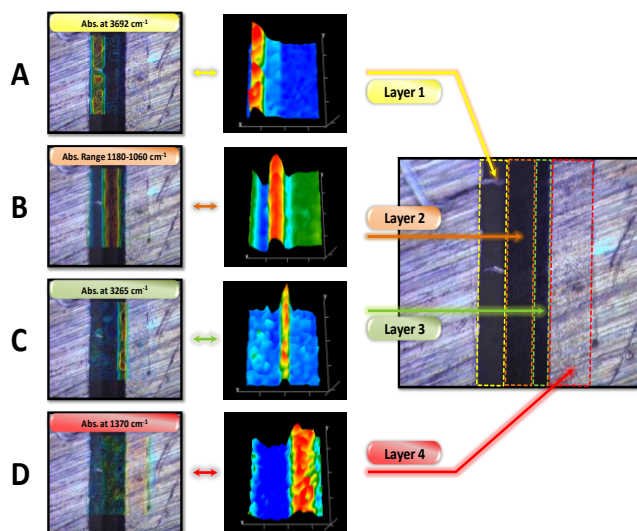
The spectra in Figure 2 are visually distinct and contain sufficient information to allow for the characterization of each individual layer. Based on these spectra, forensic scientists are able to search spectral databases of paint and coating samples to identify the vehicle's make, model, year, and color. In this instance, the ability to detect trace materials in the evidence proved to be very useful in extending the knowledge of the sample's composition far beyond that which could have been obtained by in-bench FTIR experiments or by other analytical techniques.

Without a clear delineation of the layers, it is difficult to study the variations in sample chemistry across the infrared map by using the spectrum display alone. Resolutions Pro software makes it easy to view chemical differences across an entire infrared map of a sample. One means of probing a sample is to generate a feature image based on one or multiple spectral peaks (one or multiple functional groups of interest). A feature image assigns a color to the absorbance value of a selected peak (or spectral region) and plots the intensity across the infrared map to easily view spatially-resolved chemical differences on the visual image of a sample. The color red indicates a high absorbance value, while the color blue indicates a lower absorbance value. Figure 3 shows a feature image generated from a spectral peak that is unique to one layer of the paint chip. It is equally possible to view the feature image without displaying the locations of spectra acquisition, or to view it as a '3D' chemical image as shown in Figure 3.



**Figure 3.** A feature image generated from a spectral peak that is unique to one layer of the paint chip (left), the same feature image shown without the spectral acquisition grid for clarity (center), and the 3-dimensional view of the feature image (right). These images were generated by plotting the intensity of the peak at  $3692\text{ cm}^{-1}$  in the spectrum from each pixel across the entire infrared map.

Advantageously, feature images can be generated in real-time using any spectral range or absorbance peak to provide users with a better understanding of a sample's composition. Figure 4 illustrates the feature images generated from the four chemically distinct paint chip layers.



**Figure 4.** Feature images based on spectral peaks that are unique to each layer in the four-layer paint chip sample. The feature image in 'A' is based on the absorbance of the peak centered at  $3692\text{ cm}^{-1}$ , which is primarily found in layer 1 of the paint chip; while the feature image in 'B' was generated from the absorbance peaks between  $1180\text{--}1060\text{ cm}^{-1}$ , which are largely found in the second layer; 'C' shows the spatial distribution of the absorbance peak centered at  $3265\text{ cm}^{-1}$ ; while 'D' shows the feature image of the clear coating layer of the paint sample based on the absorbance at  $1370\text{ cm}^{-1}$ . Legend for feature images: red = high intensity, green = medium intensity, blue = low intensity.

The chemical image display of the infrared mapping software was particularly useful to highlight the clear external coating of the paint sample, designated by layer 4 in Figure 4D. Depending on the visible contrast of a sample, it is occasionally easier to view the distribution of a selected spectral peak (or range) in different feature image views. From the feature images it is a simple task to estimate the approximate width of each stratified vertical layer; layer 1 is  $\sim 80\text{ }\mu\text{m}$ , layer 2 is  $\sim 80\text{ }\mu\text{m}$ , layer 3 is  $\sim 40\text{ }\mu\text{m}$ , while layer 4 is  $\sim 120\text{ }\mu\text{m}$ . It is equally possible to probe the heterogeneity within each layer for an improved characterization of the sample. For example, layer 1 in Figure 4A is not uniform in chemical composition and has a number of visible defects that can also be observed in the visible and feature images. With Resolutions Pro software, it is simple to investigate the chemical differences between adjacent spectra by displaying spectra simultaneously. However, for a more in-depth understanding of the samples' heterogeneity on the

micro-scale, a higher spatial resolution infrared image would be required.

An alternate approach to acquiring IR spectra with a significantly higher spatial resolution involves the use of an infrared imaging system equipped with a focal plane array (FPA\*) detector. An FPA-FTIR system would provide a superior means of investigating the subtle chemical differences found in each layer of the paint sample. Unlike infrared mapping using a single-element detector, an FPA\* detector collects hundreds to thousands of spectra simultaneously within seconds, thereby providing dramatic savings in spectral acquisition time compared to infrared mapping techniques that perform sequential data collection. In practical terms, this infrared map required  $\sim 40$  minutes acquisition time to collect 361 spectra for the area of  $380 \times 380\text{ }\mu\text{m}$  using a  $20\text{ }\mu\text{m}$  spatial resolution; comparatively, Agilent's  $128 \times 128$  FPA-FTIR system could acquire over 16,000 spectra with an identical signal-to-noise ratio from an area of  $700 \times 700\text{ }\mu\text{m}$  within a few seconds using an even higher spatial resolution of  $5.5\text{ }\mu\text{m}$  per spectrum.

In addition, Agilent's FPA-FTIR imaging spectrometers have a number of easily user-changeable spatial resolution modes including:  $1.1\text{ }\mu\text{m}$  (ATR Analysis),  $5.5\text{ }\mu\text{m}$ ,  $11\text{ }\mu\text{m}$ ,  $22\text{ }\mu\text{m}$  and even larger sizes with pixel binning or macro imaging (for example,  $>40\text{ }\mu\text{m}$ ). FPA-FTIR analysis would involve the same minimal sample preparation and could be used to reveal even the smallest features of the forensic evidence sample.

While this experiment focused on the characterization of a sample obtained from a crime scene, the application of FTIR microscopy and mapping in paint analysis extends far beyond forensic applications. They are commonly used for the characterization of historical art works, and for the development of conservation and preservation strategies for paintings and photographs. FTIR microscopy and mapping are equally important in the QC analysis of raw materials used in the manufacture of paints and inks, and are routinely applied to the analysis of resins, pigments, solvents and additives.

## Conclusion

Agilent's Cary 610 FTIR Microscope provides the ability to collect high quality chemical information from multi-layer samples with a high spatial resolution. It provides an excellent means of probing a sample's chemistry as it can be used to visualize the relative distribution of specific components across a sample area of several centimeters. In this experiment, a  $380 \times 380 \mu\text{m}$  infrared map was automatically collected using a pre-defined acquisition grid to investigate the chemical heterogeneity of a paint chip sample. Four chemically distinct layers were resolved in the forensic evidence, including a miniscule layer measuring  $\sim 40 \mu\text{m}$ .

Feature images also were used to highlight each layer within the infrared map and to probe localized areas with varying chemical compositions within the stratified layers. The rapid nature and the simplicity of automated infrared mapping make it a key technique for the advanced characterization of material and polymer samples.

## References

\*This product is regulated by the U.S. Department of State under the International Traffic in Arms Regulations, 22 CFR 120-130 ("ITAR"). An export license from the U.S. government is therefore required to export this product from the United States, and other ITAR restrictions apply to the shipment, use, service and other aspects of this product and the FTIR instrument in which it is used.

[www.agilent.com/chem](http://www.agilent.com/chem)

© Agilent Technologies, Inc., 2009, 2011  
Published March, 2011  
Publication Number SI-02255



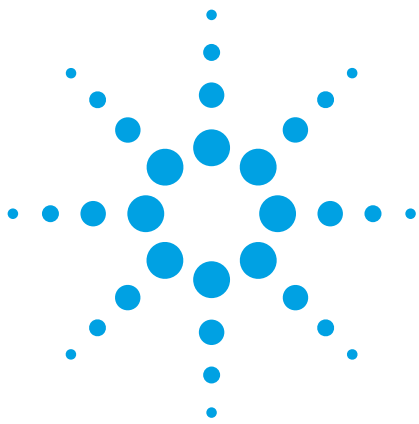
**Agilent Technologies**

## APPLICATIONS FOR POLYMERS AND RUBBERS

### Analytical Methods for the Agilent Cary 630 FTIR

Production of polymers is a tricky process – small variations in the process can have a significant effect on the producer's bottom line. For example, the additives that influence polymer properties must be incorporated at just the right level to produce a profitable resin – too much of the expensive additive increases the production cost of the polymer but too little leaves the resin unsuitable for the customer's applications. Likewise, variations in polymer composition such as incorrect incorporation of ethylene into ethylene-propylene copolymers or changes in molecular weight distribution of polyethylene can lower the market value since it must be sold as out-of-specification product. Therefore, laboratories need fast, sure methods to monitor these processes to keep producing the right product all of the time. The Agilent 630 FTIR using the following methods are the perfect solution for your process control needs.





# Determination of Irganox 3114 in polypropylene by infrared spectroscopy

## Analytical method

Polymers

### Authors

Dr. Wayne Collins\*, John Seelenbinder† and Frank Higgins†

Agilent Technologies  
\* Wilmington, DE, USA  
† Danbury, CT, USA



### Scope

This method is for the determination of Irganox 3114 and chemically identical antioxidants in polypropylene where the additive package is known. The method utilizes a characteristic carbonyl band associated with the additive that is common in many other additives. Therefore, the total additive package must be known to confirm that other additives present do not contain bands that would interfere with the measurement. The method is typically used for process control of additive addition and is not recommended for filled or pigmented resins. The sample must be pressed into a film or coupon prior to the analysis.



**Agilent Technologies**

## Summary

An analytically representative sample of the polypropylene resin is molded into a 0.5 to 0.7 mm thickness film. Molding conditions are not important to the results obtained by this method, as long as the resin is not subjected to temperatures of more than 250 °C for more than 2 to 3 minutes, and the films have a smooth, consistent surface. The film is placed in the infrared spectrometer to obtain the spectrum at 4 wavenumber resolution or better. Using the Agilent DialPath or TumbIIR accessories, the film or coupon can be inserted into the infrared beam path between the top and bottom crystals (Figure 1). Both these accessories are unique to Agilent and provide a revolutionary new way to measure thin polymer films or liquids. The horizontal mounting provides a simple, fast and reproducible mechanism to mount the sample by simply laying it down flat and rotating the crystal into position, eliminating errors and providing accurate and reliable answers — fast! The absorbance of the additive's carbonyl band is measured at 1696 cm<sup>-1</sup> and the absorbance is measured for the reference polypropylene band at 4062 cm<sup>-1</sup> to provide a path length or film thickness correction. To obtain the additive concentration in the sample, the ratio of the additive band to the reference band is substituted into a linear regression calibration equation constructed from measurements of prepared standards with known concentrations of additive. Triplicate films are averaged to obtain a result.



**Figure 1.** The Agilent DialPath transmission cell used for polymer analysis of coupons or films

## Apparatus

- Data is obtained using an Agilent Cary 630 FTIR spectrometer equipped with a DialPath or TumbIIR sample interface with a 1000 μm path length. Equivalent FTIR spectrometers, such as the mobile or portable Agilent 5500/4500 Series FTIR, can also be used.
- Film micrometer — capable of measuring 0.5–0.7 mm thickness.
- Hydraulic press — with heated platens capable of maintaining 200 °C and a ram force of 40,000 pounds.
- Chase mold — to control thickness.
- Aluminum sheet — 0.051–0.178 mm thick.
- Scissors.

## Calibration

Standards were prepared by blending known amounts of Irganox 3114 with polypropylene powder, and compounding under a nitrogen blanket until thoroughly mixed.

To perform the calibration, prepare and analyze at least three films for each standard resin in accordance with the requirements of this method. Perform a linear least squares regression of the concentration of the analyte versus normalized absorbance using all data points; do not include the origin as a data point.

$$\text{Wt\% Irganox 3114} = M \times (A_{1696}/A_{4062}) + N$$

Where:

Wt% Irganox = Weight % of Irganox 3114 in the polypropylene

$A_{1696}$  = Absorbance area of the Irganox 3114 band at 1696 cm<sup>-1</sup>

$A_{4062}$  = Absorbance area of the polypropylene reference band at 4062 cm<sup>-1</sup>

M = Calibration constant

N = Intercept



The calibration curve obtained for the determination of Irganox 3114 in polypropylene in this study is shown in Figure 2.

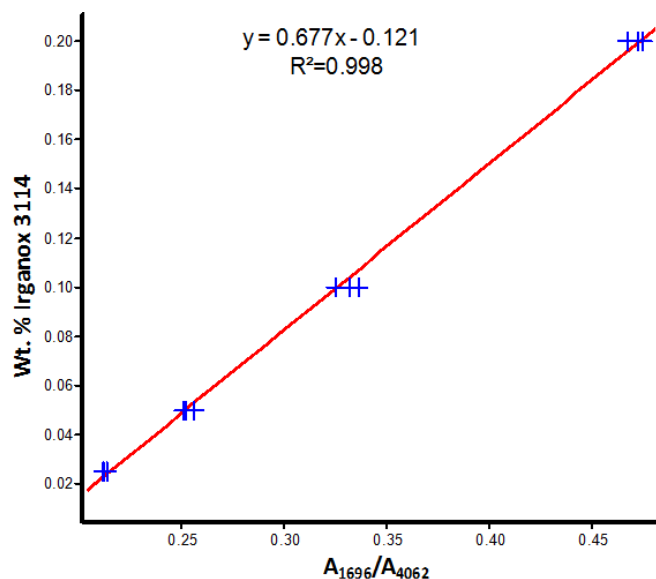


Figure 2. Calibration curve for wt% Irganox 3114 in polypropylene

## Procedure

### Sample preparation

Molding techniques and conditions used to prepare the sample do not significantly influence the results, as long as the resin is not subjected to temperatures of more than 250 °C for more than 2 to 3 minutes, and the prepared films have a smooth, consistent surface. A typical preparation procedure is as follows:

Obtain a representative sample of the resin to be analyzed; statistical sampling techniques are recommended (cone and quarter technique, chute splitter, rotary splitter, roto-riffler, and so forth). Place the chase mold on a sheet of aluminum and slightly overfill each cavity in the chase with the resin. Another sheet of aluminum is placed on top and the stack is carefully placed in the press with the platens heated to 200 °C. The press is closed to apply minimal force for 1 or 2 minutes while the sample melts. The force is increased to at least 25,000 pounds, held for approximately 30 seconds, and released. The stack is then removed from the press and allowed to cool on the benchtop. The aluminum sheet is stripped from the

chase and the films are pushed from the cavities and trimmed to remove the flash. Examine the sample for surface defects and check to ensure that the thickness is between 0.5 and 0.7 mm. Samples with defects or thickness outside of the range are discarded; at least three suitable films are required for the analysis.

### Operating conditions

The infrared spectrometer should be turned on for at least 15 minutes prior to analysis. The resolution should be set to at least 4 wavenumbers.

Collect for a minimum of 30 seconds (74 scans) for each of the triplicate film samples.

### Method configuration

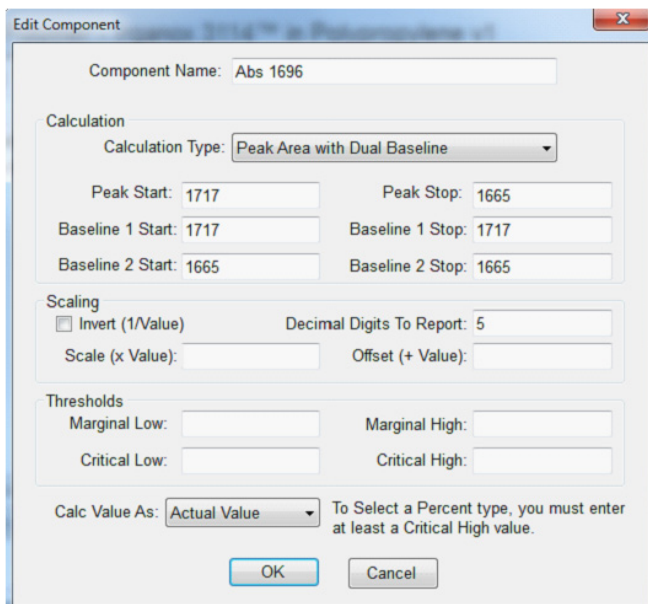
To determine the additive concentration, measure the area under the absorbance band for Irganox 3114 at 1696  $\text{cm}^{-1}$  relative to a baseline drawn between 1717 and 1665  $\text{cm}^{-1}$ . The specified peak areas and baseline points can easily be set in an Agilent MicroLab PC FTIR software method. Each peak measurement is called a component and the baseline limits are easily set as shown in Figure 3. The peak type of 'Peak Area with Dual Baseline' is first set. Then parameters for measurement of the area under the reference polypropylene absorbance band at 4062  $\text{cm}^{-1}$  relative to a baseline drawn between 4097 and 4010  $\text{cm}^{-1}$  (Figure 4) are set. The component is further configured to report the absorbance value to five decimal places as shown in Figures 3 and 4.

A ratio of the analyte band absorbance to the reference band is used for this analysis.

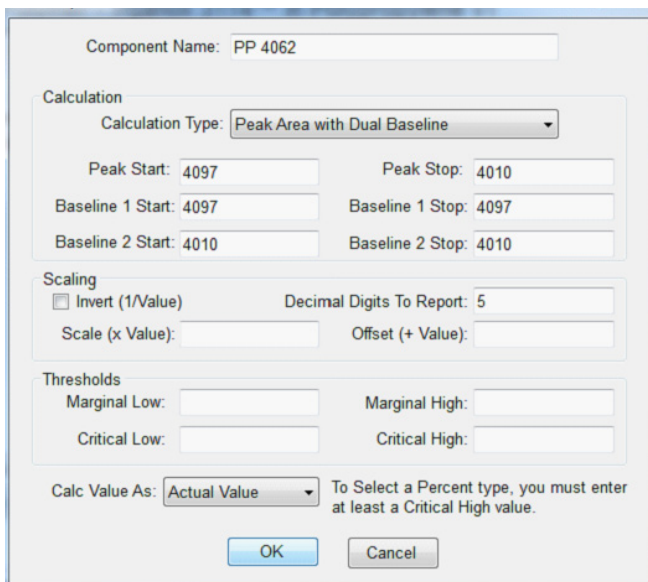
$$\text{Wt\% Irganox 3114} = M \times (A_{1696}/A_{4062}) + N$$

with M and N as determined in the the Calibration section.

The MicroLab PC FTIR software makes the peak ratio calculation easy to set up. Simply edit the method by selecting the 'Peak Ratio' calculation type and the peak components that are to be ratioed (Figure 5).



**Figure 3.** The Irganox 3114 peak area absorbance (component) measurement at 1696  $\text{cm}^{-1}$  in the MicroLab PC FTIR software. The peak start and stop refers to the area under the peak to be integrated. Single point baselines should be set up with the same baseline start and stop points.



**Figure 4.** The polypropylene reference peak component addition in the MicroLab PC FTIR software

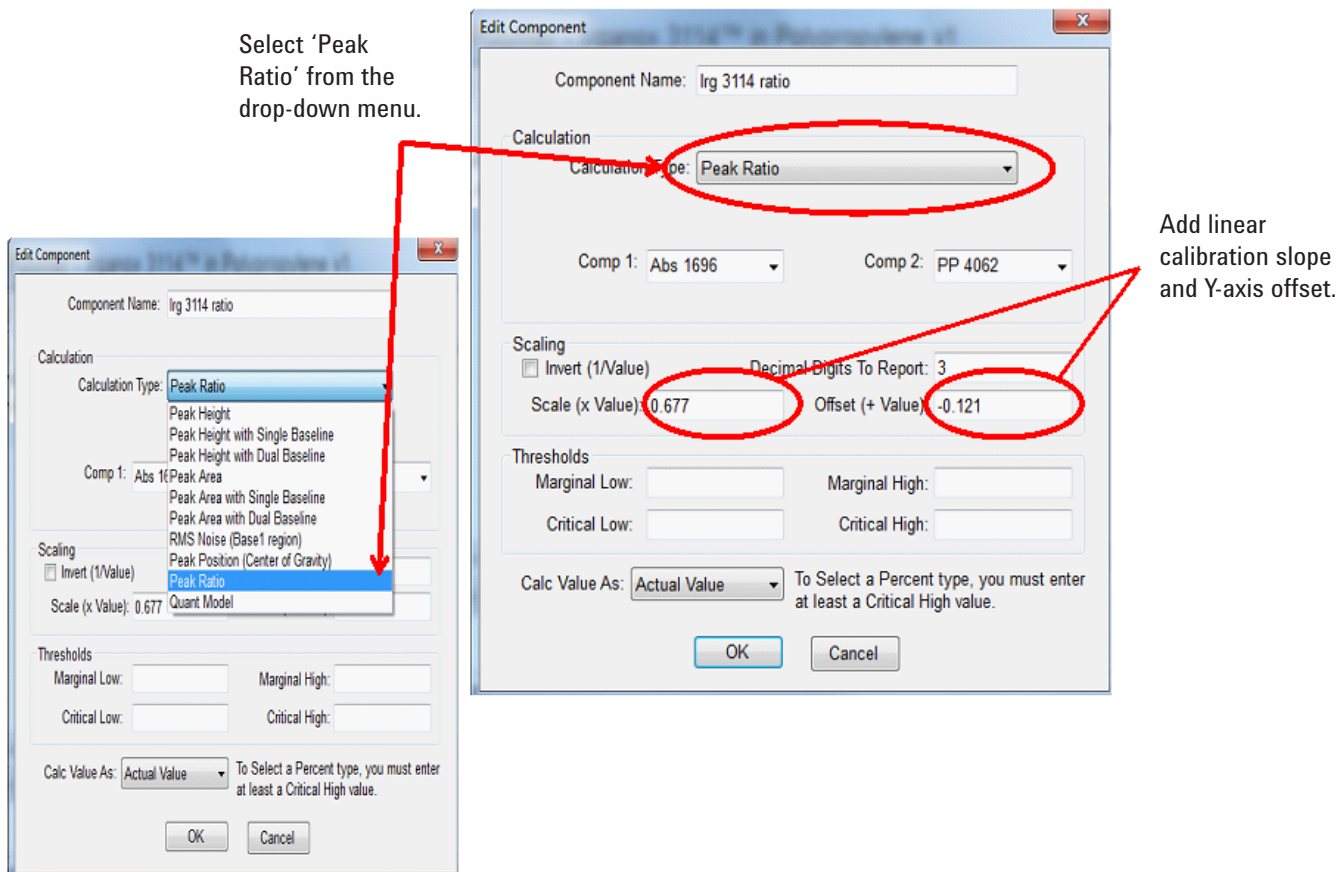
## Analysis

With the ratio defined, the new method is ready to be used to obtain at least triplicate measurements of each calibration standard. Unknown polymer coupons should also be run with a minimum of three measurements around the coupon. This process is made simple and convenient with the DialPath or TumbIIR transmission cells. Users can see the exact point of measurement in real time, and quickly reposition the sample for the replicate measurements.

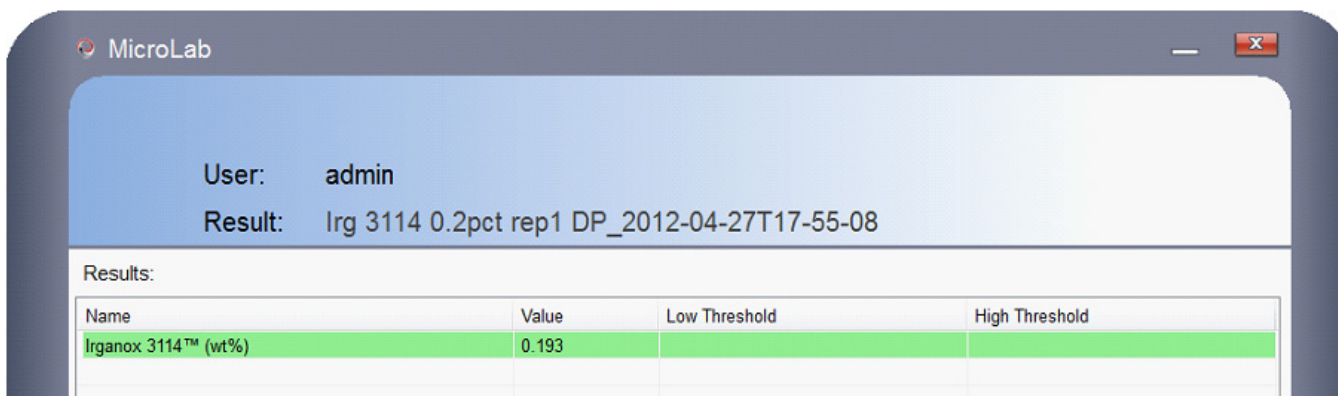
Plot the values measured for the ratio relative to the Irganox 3114 concentration (Figure 2), and insert the slope and offset values back into the method as shown in Figure 5. Once the slope and offset values have been entered, the MicroLab PC FTIR software method will report the Irganox 3114 concentration.

The MicroLab PC software method, Polymer — Irganox 3114 in Polypropylene v1, includes the calibration data from Figure 2. This calibrated method is available with the Agilent 5500 and 4500 Series DialPath or TumbIIR FTIR spectrometers, as well as the Cary 630 FTIR spectrometers. This method and software performs all the calculations automatically and reports the final value as wt% Irganox 3114 (Figure 6).

The values obtained from triplicate determinations should be averaged to give the final reported concentration.



**Figure 5.** The peak ratio component addition in the MicroLab PC FTIR software. After plotting the calibration data, the resulting linear regression line's slope is entered in the 'Scale' field and the Y-axis offset in the 'Offset' field.

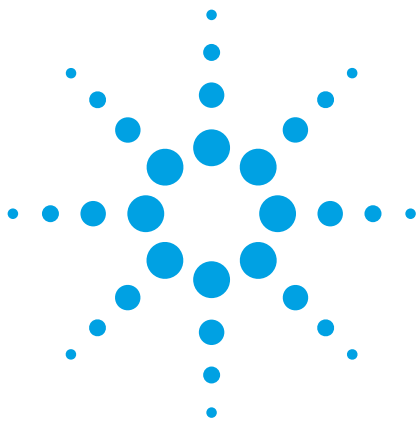


**Figure 6.** The MicroLab PC FTIR software prediction result for a 0.2 wt% Irganox 3114 in polypropylene sample

## Conclusion

This analytical method demonstrates how the Agilent Cary 630 FTIR can be used to easily and accurately measure polymer thin films. The unique sampling capabilities of the DialPath and TumbIIR provide a

simple mechanism to mount your sample, while the step-by-step method-driven software with color-coded, actionable results guides you through your analysis to ensure that your samples are measured with minimum effort and highest accuracy.



# Determination of percent ethylene in ethylene-propylene statistical copolymers

Analytical method

Polymers

## Authors

Dr. Wayne Collins\*, John Seelenbinder† and Frank Higgins†

Agilent Technologies  
\* Wilmington, DE, USA  
† Danbury, CT, USA



## Scope

This method is for the determination of the statistical or randomly distributed ethylene content of ethylene-propylene copolymers. The determination is specific for ethylene and cannot be applied for the quantitation of other comonomers. The method has been validated over the range of 0.3 to 3.5% statistical content and can be used for either powder or pellet samples. Certain sorbitol-based clarifiers have been found to interfere with the determination and therefore a correction factor is necessary for resins containing these additives. This method is generally not recommended for quantitation of ethylene in filled or pigmented resins.



**Agilent Technologies**

## Summary

This method describes a procedure for measuring the statistical ethylene contents in ethylene-propylene statistical copolymers. The procedure utilizes an absorption band at  $733\text{ cm}^{-1}$  associated with statistically distributed ethylene for a Beer's Law type calculation.

An analytically representative sample of the copolymer resin is molded into a film of thickness between 0.5 and 0.7 mm. Molding conditions are not important to the results obtained by this method, as long as the resin is not subjected to temperatures of more than  $250\text{ }^{\circ}\text{C}$  for more than 2 to 3 minutes, and the films have a smooth, consistent surface. The sample is placed in the infrared spectrometer and the spectrum is obtained at a resolution of 4 wavenumbers or better. Using the Agilent DialPath or TumbIIR accessories, the film or coupon can be inserted into the infrared beam path between the top and bottom crystals (Figure 1). Both these accessories are unique to Agilent and provide a revolutionary new way to measure thin polymer films or liquids. The horizontal mounting provides a simple, fast and reproducible mechanism to mount the sample by simply laying it down flat and rotating the crystal into position, eliminating errors and providing accurate and reliable answers — fast! The peak height of the absorbance band at  $733\text{ cm}^{-1}$  is determined relative to a baseline drawn between  $759$  and  $703\text{ cm}^{-1}$ . This value is divided by the peak height of the absorbance band at  $1044\text{ cm}^{-1}$  relative to a baseline drawn between  $1068$  and  $949\text{ cm}^{-1}$  to give the normalized absorbance at each wavenumber. The random ethylene concentrations can then be determined by comparing these values with a linear regression equation of normalized absorbance versus ethylene content for a set of standards of known ethylene content as determined by  $\text{C}^{13}$  nuclear magnetic resonance spectroscopy (NMR), which is a primary analytical technique. At least three separate films are analyzed and averaged for each sample analyzed.



**Figure 1.** The Agilent DialPath transmission cell used for polymer analysis of coupons or films

## Apparatus

- Data is obtained using an Agilent Cary 630 FTIR spectrometer equipped with a DialPath or TumbIIR sample interface with a  $1000\text{ }\mu\text{m}$  path length. Equivalent FTIR spectrometers, such as the mobile or portable Agilent 5500/4500 Series FTIR, can also be used.
- Hydraulic press — with heated platens capable of maintaining  $200\text{ }^{\circ}\text{C}$  and a ram force of 25,000 pounds.
- Chase mold — to control thickness (optional).
- Aluminum sheet —  $0.05\text{--}0.18\text{ mm}$  thick.

## Calibration

Standards are prepared by measuring the statistical ethylene content of a series of copolymers covering the desired range using by NMR, which is a primary analytical technique. To perform the calibration, prepare and analyze at least three films for each standard resin in accordance with the requirements of this method. All absorbance values should be less than 1.6 units. Perform a linear least squares regression of the concentration of the analyte versus normalized absorbance using all data points; do not include the

origin as a data point. Divide the peak height of the statistical ethylene absorbance band by the peak height of the reference polypropylene absorbance band to normalize the result. The calibration equation obtained for the standards used in this study is:

$$\% \text{ Stat. ethylene} = M \times (A_{733}/A_{1044}) + N$$

Where:

% Stat. ethylene = Weight % of statistically distributed ethylene incorporated into the copolymer

$A_{733}$  = Peak height of absorbance band of statistical ethylene band at  $733 \text{ cm}^{-1}$

$A_{1044}$  = Peak height of absorbance band of polypropylene reference at  $1044 \text{ cm}^{-1}$

M = Calibration constant

N = Intercept

The calibration curve for the determination of statistical ethylene in ethylene-propylene copolymers for the standards used in this study is shown in Figure 2.

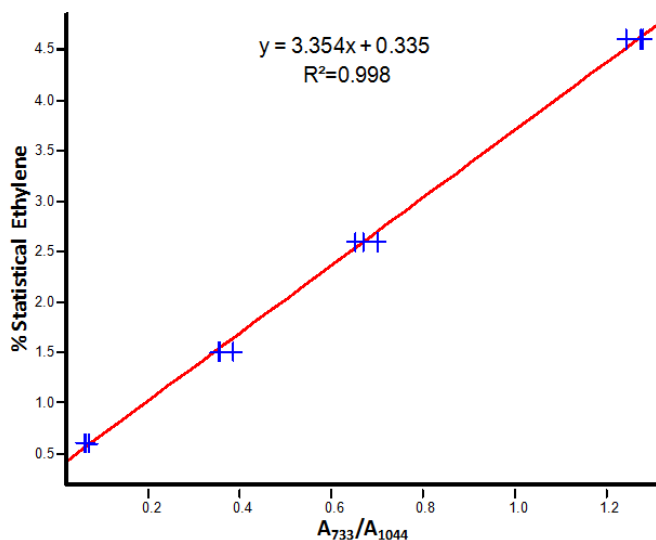


Figure 2. Calibration curve for % statistical ethylene in polypropylene

## Procedure

### Sample preparation

Obtain a representative sample of the resin to be analyzed; statistical sampling techniques are recommended (cone and quarter technique, chute splitter, rotary splitter, roto-riffler, and so forth). Molding conditions are not important to the results obtained by this method, as long as the resin is not subjected to temperatures of more than  $250 \text{ }^{\circ}\text{C}$  for more than 2 to 3 minutes. A typical technique for preparation of these films is as follows:

Place the chase mold on a sheet of aluminum and slightly overfill each cavity in the chase with the resin. Another sheet of aluminum is placed on top and the stack is carefully placed in the press with the platens heated to  $200 \text{ }^{\circ}\text{C}$ . The press is closed to apply minimal force for 1 or 2 minutes while the sample melts. The force is increased to at least 25,000 pounds, held for approximately 30 seconds and released. The stack is then removed from the press and allowed to cool on the benchtop or in a cold press. The aluminum sheet is stripped from the chase and the films are pushed from the cavities and trimmed to remove the flash.

Once the samples are prepared, each sample is examined for surface defects and checked to ensure that the thickness is between 0.5 and 0.7 mm. Samples with defects or thickness outside of the range are discarded; at least three suitable films are required for the analysis.

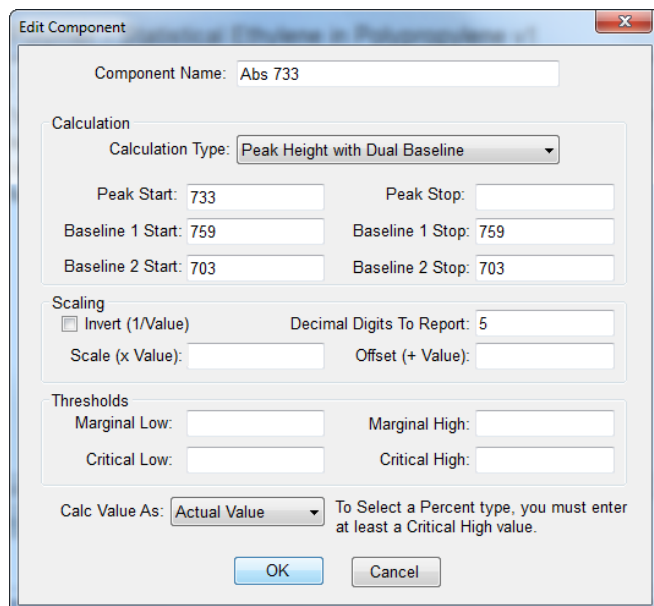
### Operating conditions

The infrared spectrometer should be turned on for at least 15 minutes prior to analysis. The resolution should be set to at least 4 wavenumbers.

Collect for a minimum of 30 seconds (74 scans) for each of the triplicate film samples.

## Method configuration

To determine the statistical ethylene concentration, measure the peak height absorbance for statistical ethylene at 733 cm<sup>-1</sup>, measured by a vertical intersecting line to a baseline drawn between 759 and 703 cm<sup>-1</sup>. The specified peak height and baseline points can easily be set in an Agilent MicroLab PC FTIR software method. Each peak measurement is called a component and the baseline limits are easily set as shown in Figure 3. The peak type of 'Peak Height with Dual Baseline' is first set. Then parameters for measurement of the peak height polypropylene absorbance band at 1044 cm<sup>-1</sup> relative to a baseline drawn between 1068 and 949 cm<sup>-1</sup> (Figure 4) are set. The 'Peak Stop' field is left blank for peak height measurements. The component is further configured to report the absorbance value to five decimal places as shown in Figures 3 and 4.

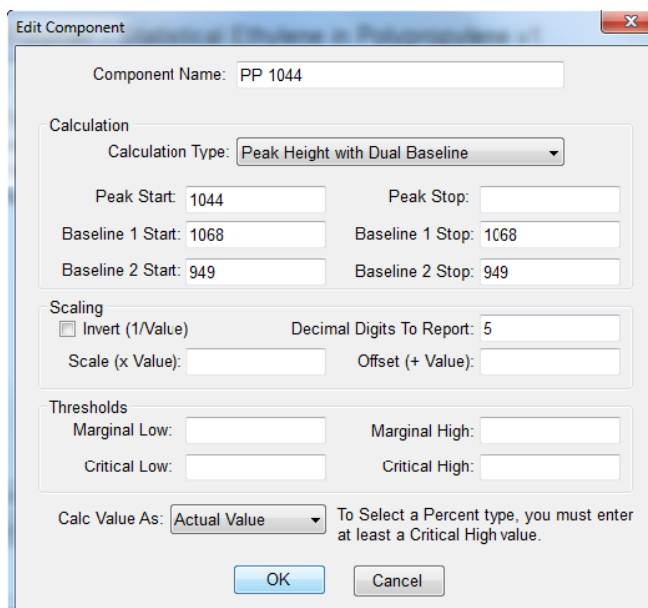


**Figure 3.** The statistical ethylene peak height absorbance (component) measurement at 733 cm<sup>-1</sup> in the MicroLab PC FTIR software. The peak start refers to the peak maxima position from which the peak height is measured. Single point baselines should be set up with the same baseline start and stop points.

A ratio of the analyte band absorbance to the reference band is used for this analysis.

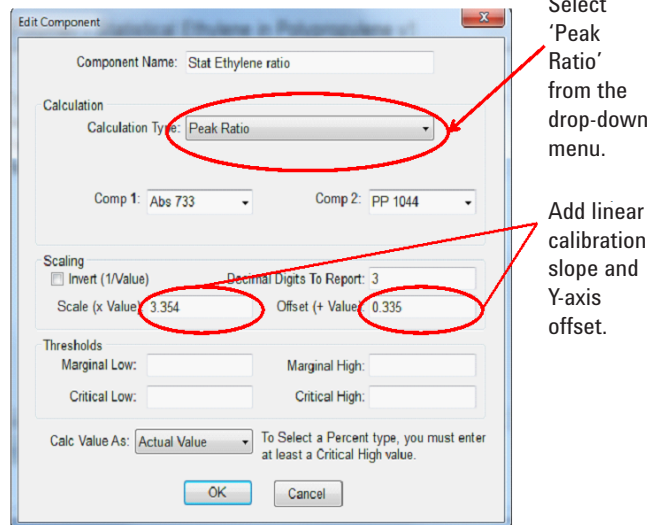
$$\% C_2 \text{ (stat.)} = M_s \times (A_{733}/A_{1044}) + N$$

with M and N as determined in the the Calibration section.



**Figure 4.** The polypropylene reference peak component addition in the MicroLab PC FTIR software

The MicroLab PC FTIR software makes the peak ratio calculation easy to set up. Simply edit the method by selecting the 'Peak Ratio' calculation type and the peak components that are to be ratioed (Figure 5).



**Figure 5.** The peak ratio component addition in the MicroLab PC FTIR software. After plotting the calibration data, the resulting linear regression line's slope is entered in the 'Scale' field and the Y-axis offset in the 'Offset' field.

## Analysis

The specimen is placed in the sample compartment and the spectrum is recorded; a typical spectrum is shown in Figure 6. The presence of an absorption band at  $695\text{ cm}^{-1}$  suggests that the resin contains a sorbitol-based clarifier that can interfere with the statistical ethylene measurement at  $733\text{ cm}^{-1}$ . If the presence of this clarifier is confirmed, the statistical ethylene measurement must be corrected to compensate for the absorbance of the clarifier. Certain anti-acid additives can also have an effect on the measurement but are usually ignored since these compounds are present at very low concentrations.

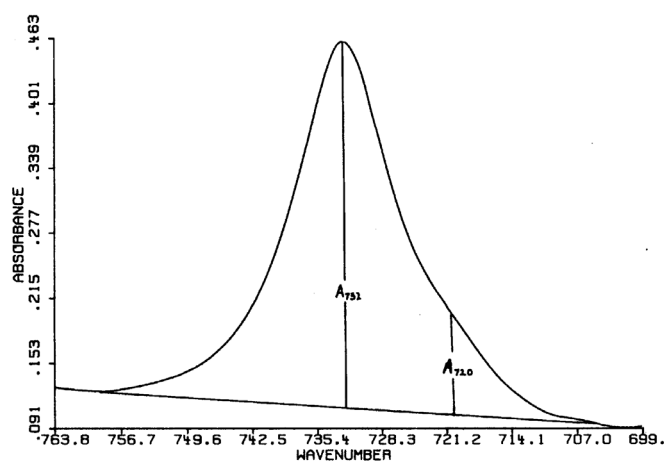


Figure 6. Typical absorption bands for statistical and block ethylene

With the ratio defined from the Method Configuration section, the new method is ready to be used to obtain at least triplicate measurements of each calibration standard. Unknown polymer coupons should also be run with a minimum of three measurements around the coupon. This process is made simple and convenient with the DialPath or TumbIIR transmission cells. Users

can see the exact point of measurement in real time, and quickly reposition the sample for the replicate measurements.

Plot the values measured for the ratio relative to the statistical ethylene concentration (Figure 2), and insert the slope and offset values back into the method as shown in Figure 5. Once the slope and offset values have been entered, the MicroLab PC FTIR software method will report the statistical ethylene concentration.

The MicroLab PC method, Polymer – Statistical Ethylene in Polypropylene v1, includes the calibration data from Figure 2. This calibrated method is available with the Agilent 5500 and 4500 Series DialPath or TumbIIR FTIR spectrometers, as well as the Cary 630 FTIR spectrometers. This method and software performs all the calculations automatically and reports the final value as % statistical ethylene (Figure 7).

The values obtained from triplicate determinations should be averaged to give the final reported concentration.

## Conclusion

This analytical method demonstrates how the Agilent Cary 630 FTIR can be used to easily and accurately measure polymer thin films. The unique sampling capabilities of the DialPath and TumbIIR provide a simple mechanism to mount your sample, while the step-by-step method-driven software with color-coded, actionable results guides you through your analysis to ensure that your samples are measured with minimum effort and highest accuracy.

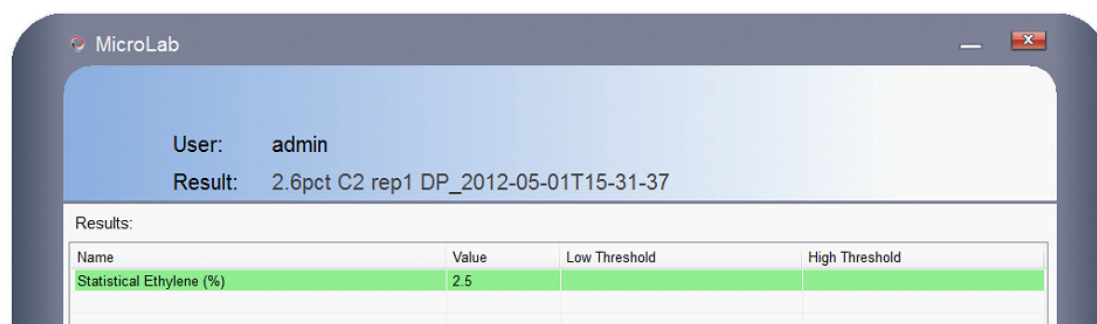


Figure 7. The MicroLab PC software prediction result for a 2.6% statistical ethylene in polypropylene sample





# Determination of Irganox 1010 in polyethylene by infrared spectroscopy

## Analytical method

Polymers

### Authors

Dr. Wayne Collins\*, John Seelenbinder† and Frank Higgins†

Agilent Technologies  
\* Wilmington, DE, USA  
† Danbury, CT, USA



### Scope

This method is for the determination of Irganox 1010 and chemically identical antioxidants in polyethylene where the additive package is known. The method utilizes a characteristic ester carbonyl band associated with the additive that is common in many other additives. Therefore, the total additive package must be known to confirm that other additives present do not contain bands that would interfere with the measurement. The method is typically used for process control of additive addition and is not recommended for filled or pigmented resins. The sample must be pressed into a film or coupon prior to the analysis.

## Summary

An analytically representative sample of the polyethylene resin is molded into a 0.5 to 0.7 mm thickness film. Molding conditions are not important to the results obtained by this method, as long as the resin is not subjected to temperatures of more than 250 °C for more than 2 to 3 minutes, and the films have a smooth, consistent surface. The film is placed in the infrared spectrometer to obtain the spectrum at 4 wavenumber resolution or better. Using the Agilent DialPath or TumbIIR accessories, the film or coupon can be inserted into the infrared beam path between the top and bottom crystals (Figure 1). Both these accessories are unique to Agilent and provide a revolutionary new way to measure thin polymer films or liquids. The horizontal mounting provides a simple, fast and reproducible mechanism to mount the sample by simply laying it down flat and rotating the crystal into position, eliminating errors and providing accurate and reliable answers — fast! The absorbance of the additive band is measured at 1745 cm<sup>-1</sup> and the absorbance is measured for the reference band at 2019 cm<sup>-1</sup> to provide a path length or film thickness correction. To obtain the additive concentration in the sample, the ratio of the additive band to the reference band is substituted into a linear regression calibration equation constructed from measurements of prepared standards with known concentrations of additive. Triplicate films are averaged to obtain a result.



**Figure 1.** The Agilent DialPath transmission cell used for polymer analysis of coupons or films

## Apparatus

- Data is obtained using an Agilent Cary 630 FTIR spectrometer equipped with a DialPath or TumbIIR sample interface with a 1000 μm path length. Equivalent FTIR spectrometers, such as the mobile or portable Agilent 5500/4500 Series FTIR, can also be used.
- Film micrometer — capable of measuring 0.5–0.7 mm thickness.
- Hydraulic press — with heated platens capable of maintaining 200 °C and a ram force of 40,000 pounds.
- Chase mold — to control thickness.
- Aluminum sheet — 0.051–0.178 mm thick.
- Scissors.

## Calibration

Standards are prepared by blending known amounts of Irganox 1010 with polyethylene powder, and compounding under a nitrogen blanket until thoroughly mixed.

To perform the calibration, prepare and analyze at least three films for each standard resin in accordance with the requirements of this method. Perform a linear least squares regression of the concentration of the analyte versus normalized absorbance using all data points; do not include the origin as a data point.

$$\text{Wt\% Irganox 1010} = M \times (A_{1745}/A_{2019}) + N$$

Where:

Wt% Irganox = Weight % of Irganox 1010 in the polyethylene

$A_{1745}$  = Absorbance of Irganox 1010 at 1745 cm<sup>-1</sup>

$A_{2019}$  = Absorbance of polyethylene reference band at 2019 cm<sup>-1</sup>

M = Calibration constant

N = Intercept

The calibration curve for the determination of Irganox 1010 in polyethylene for the standards used in this study is shown in Figure 2.

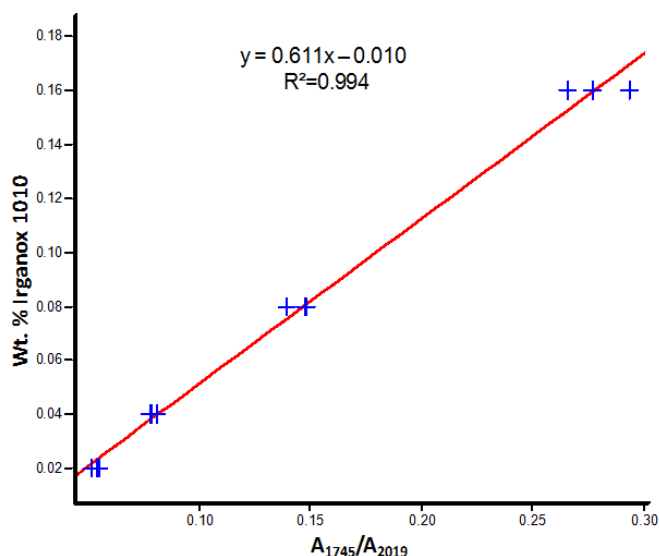


Figure 2. Calibration curve for wt% Irganox 1010 in polyethylene

## Procedure

### Sample preparation

Molding techniques and conditions used to prepare the sample do not significantly influence the results, as long as the resin is not subjected to temperatures of more than 250 °C for more than 2 to 3 minutes, and the prepared films have a smooth, consistent surface. A typical preparation procedure is as follows:

Obtain a representative sample of the resin to be analyzed; statistical sampling techniques are recommended (cone and quarter technique, chute splitter, rotary splitter, roto-riffler, and so forth). Place the chase mold on a sheet of aluminum and slightly overfill each cavity in the chase with the resin. Another sheet of aluminum is placed on top and the stack is carefully placed in the press with the platens heated to 200 °C. The press is closed to apply minimal force for 1 or 2 minutes while the sample melts. The force is increased to at least 25,000 pounds, held for approximately 30 seconds, and released. The stack is then removed from the press and allowed to cool on the benchtop. The aluminum sheet is stripped from the chase and the films are pushed from the cavities and

trimmed to remove the flash. Examine the sample for surface defects and check to ensure that the thickness is between 0.5 and 0.7 mm. Samples with defects or thickness outside of the range are discarded; at least three suitable films are required for the analysis.

### Operating conditions

The infrared spectrometer should be turned on for at least 15 minutes prior to analysis. The resolution should be set to at least 4 wavenumbers.

Collect for a minimum of 30 seconds (70 scans) for each of the triplicate film samples.

### Method configuration

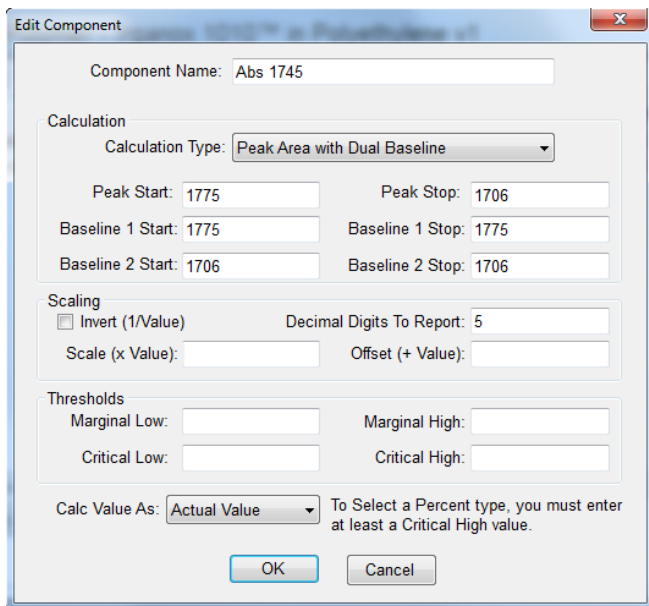
To determine the additive concentration, measure the area under the absorbance band for Irganox 1010 at 1745 cm<sup>-1</sup> relative to a baseline drawn between 1775 and 1706 cm<sup>-1</sup>. The specified peak areas and baseline points can easily be set in an Agilent MicroLab PC FTIR software method. Each peak measurement is called a component and the baseline limits are easily set as shown in Figure 3. The peak type of 'Peak Area with Duel Baseline' is first set. Then parameters for measurement of the area under the reference polyethylene absorbance band at 2019 cm<sup>-1</sup> relative to a baseline drawn between 2108 and 1981 cm<sup>-1</sup> (Figure 4) are set. The component is further configured to report the absorbance value to five decimal places as shown in Figures 3 and 4.

A ratio of the analyte band absorbance to the reference band is used for this analysis.

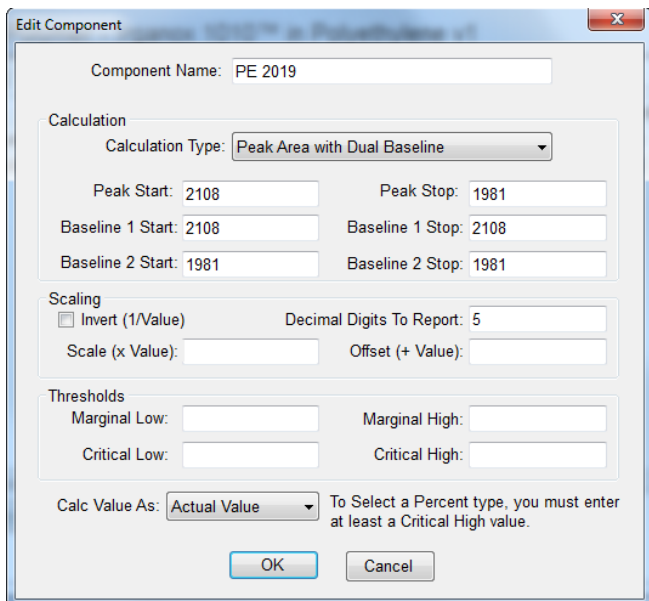
$$\text{Wt}\% \text{ Irganox 1010} = M \times (A_{1745}/A_{2019}) + N$$

with M and N as determined in the the Calibration section.

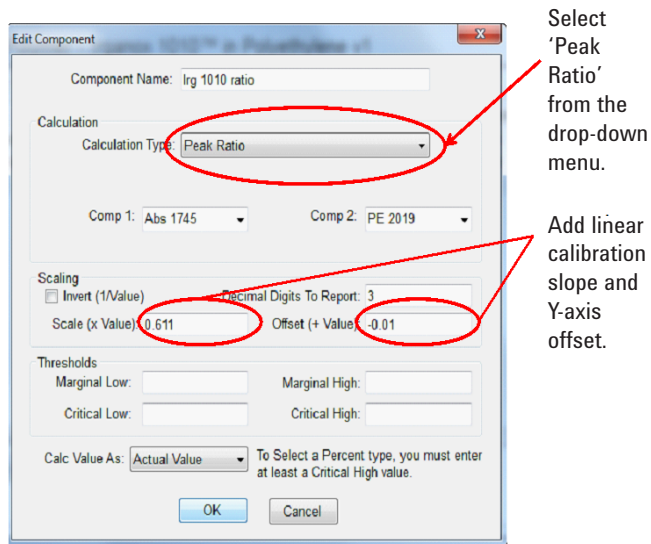
The MicroLab PC FTIR software makes the peak ratio calculation easy to set up. Simply edit the method by selecting the 'Peak Ratio' calculation type and the peak components that are to be ratioed (Figure 5).



**Figure 3.** The Irganox 1010 peak area absorbance (component) measurement at 1745 cm<sup>-1</sup> in the MicroLab PC FTIR software. The peak start and stop refers to the area under the peak to be integrated. Single point baselines should be set up with the same baseline start and stop points.



**Figure 4.** The polyethylene reference peak component addition in the MicroLab PC FTIR software



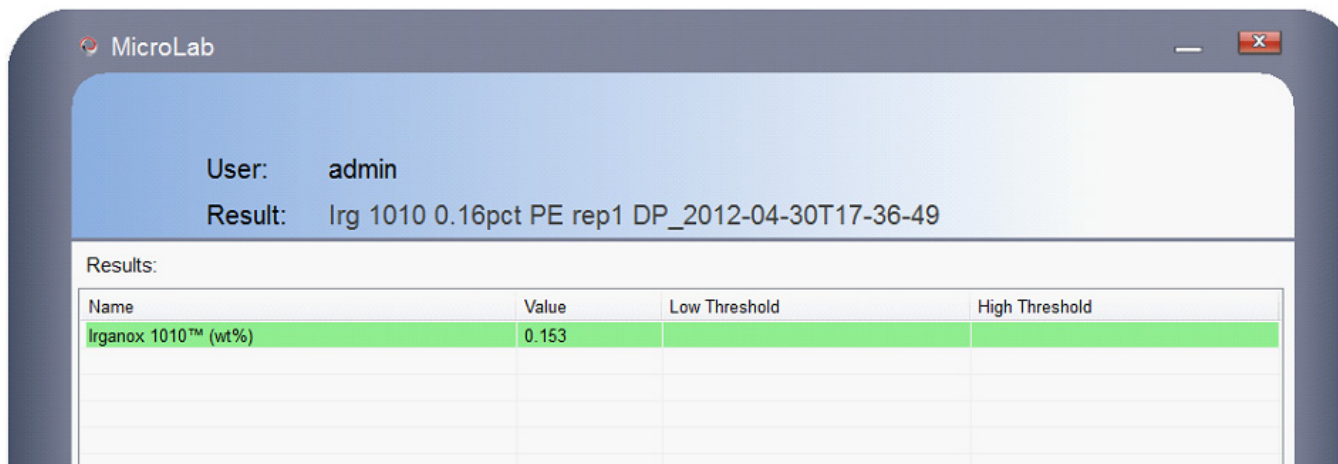
**Figure 5.** The peak ratio component addition in the MicroLab PC FTIR software. After plotting the calibration data, the resulting linear regression line's slope is entered in the 'Scale' field and the Y-axis offset in the 'Offset' field.

## Analysis

With the ratio defined, the new method is ready to be used to obtain at least triplicate measurements of each calibration standard. Unknown polymer coupons should also be run with a minimum of three measurements around the coupon. This process is made simple and convenient with the DialPath or TumbIIR transmission cells. Users can see the exact point of measurement in real time, and quickly reposition the sample for the replicate measurements.

Plot the values measured for the ratio relative to the Irganox 1010 concentration (Figure 2), and insert the slope and offset values back into the method as shown in Figure 5. Once the slope and offset values have been entered, the MicroLab PC FTIR software method will report the Irganox 1010 concentration.

The MicroLab PC software method, Polymer — Irganox 1010 in Polyethylene v1, includes the calibration data from Figure 2. This calibrated method is available with the Agilent 5500 and 4500 Series DialPath or TumbIIR FTIR spectrometers, as well as the Cary 630 FTIR spectrometers. This method and software performs all the calculations automatically and reports the final value as wt% Irganox 1010 (Figure 6).

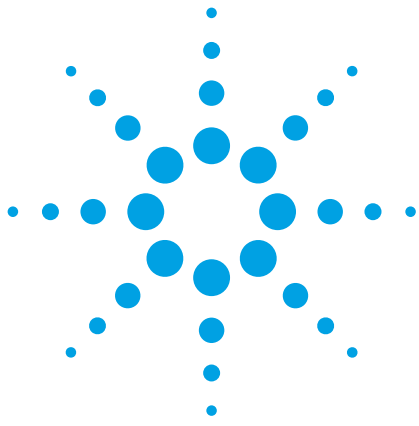


**Figure 6.** The MicroLab PC FTIR software prediction result for a 0.16 wt% Irganox 1010 in polyethylene sample

The values obtained from triplicate determinations should be averaged to give the final reported concentration.

## Conclusion

This analytical method demonstrates how the Agilent Cary 630 FTIR can be used to easily and accurately measure polymer thin films. The unique sampling capabilities of the DialPath and TumbIIR provide a simple mechanism to mount your sample, while the step-by-step method-driven software with color-coded, actionable results guides you through your analysis to ensure that your samples are measured with minimum effort and highest accuracy.



# Determination of Irganox 1010 in polypropylene by infrared spectroscopy

## Analytical method

Polymers

### Authors

Dr. Wayne Collins\*, John Seelenbinder† and Frank Higgins†

Agilent Technologies  
\* Wilmington, DE, USA  
† Danbury, CT, USA



### Scope

This method is for the determination of Irganox 1010 and chemically identical antioxidants in polypropylene where the additive package is known. The method utilizes a characteristic ester carbonyl band associated with the additive that is common in many other additives. Therefore, the total additive package must be known to confirm that other additives present do not contain bands that would interfere with the measurement. The method is typically used for process control of additive addition and is not recommended for filled or pigmented resins. The sample must be pressed into a film or coupon prior to the analysis.



**Agilent Technologies**

## Summary

An analytically representative sample of the polypropylene resin is molded into a 0.5 to 0.7 mm thickness film. Molding conditions are not important to the results obtained by this method, as long as the resin is not subjected to temperatures of more than 250 °C for more than 2 to 3 minutes, and the films have a smooth, consistent surface. The film is placed in the infrared spectrometer to obtain the spectrum at 4 wavenumber resolution or better. Using the Agilent DialPath or TumbIIR accessories, the film or coupon can be inserted into the infrared beam path between the top and bottom crystals (Figure 1). Both these accessories are unique to Agilent and provide a revolutionary new way to measure thin polymer films or liquids. The horizontal mounting provides a simple, fast and reproducible mechanism to mount the sample by simply laying it down flat and rotating the crystal into position, eliminating errors and providing accurate and reliable answers — fast! The absorbance of the additive band is measured at 1745 cm<sup>-1</sup> and the absorbance is measured for the reference polypropylene band at 4062 cm<sup>-1</sup> to provide a path length or film thickness correction. To obtain the additive concentration in the sample, the ratio of the additive band to the reference band is substituted into a linear regression calibration equation constructed from measurements of prepared standards with known concentrations of additive. Triplicate films are averaged to obtain a result.



**Figure 1.** The Agilent DialPath transmission cell used for polymer analysis of coupons or films

## Apparatus

- Data is obtained using an Agilent Cary 630 FTIR spectrometer equipped with a DialPath or TumbIIR sample interface with a 1000 μm path length. Equivalent FTIR spectrometers, such as the mobile or portable Agilent 5500/4500 Series FTIR, can also be used.
- Film micrometer — capable of measuring 0.5–0.7 mm thickness.
- Hydraulic press — with heated platens capable of maintaining 200 °C and a ram force of 40,000 pounds.
- Chase mold — to control thickness.
- Aluminum sheet — 0.051–0.178 mm thick.
- Scissors.

## Calibration

Standards are prepared by blending known amounts of Irganox 1010 with polypropylene powder, and compounding under a nitrogen blanket until thoroughly mixed.

To perform the calibration, prepare and analyze at least three films for each standard resin in accordance with the requirements of this method. Perform a linear least squares regression of the concentration of the analyte versus normalized absorbance using all data points; do not include the origin as a data point.

$$\text{Wt\% Irganox 1010} = M \times (A_{1745}/A_{4062}) + N$$

Where:

Wt% Irganox = Weight % of Irganox 1010 in the polypropylene

$A_{1745}$  = Absorbance of Irganox 1010 at 1745 cm<sup>-1</sup>

$A_{4062}$  = Absorbance of polypropylene reference band at 4062 cm<sup>-1</sup>

M = Calibration constant

N = Intercept

The calibration curve for the determination of Irganox 1010 in polypropylene for the standards used in this study is shown in Figure 2.

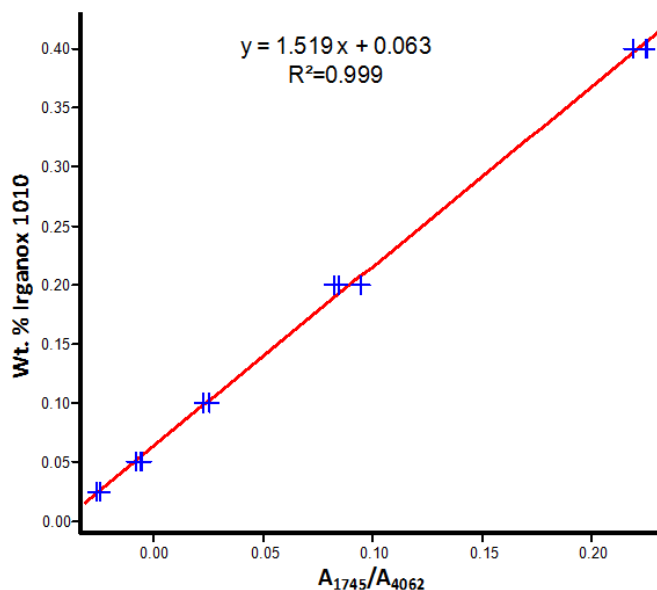


Figure 2. Calibration curve for wt% Irganox 1010 in polypropylene

## Procedure

### Sample preparation

Molding techniques and conditions used to prepare the sample do not significantly influence the results, as long as the resin is not subjected to temperatures of more than 250 °C for more than 2 to 3 minutes, and the prepared films have a smooth, consistent surface. A typical preparation procedure is as follows:

Obtain a representative sample of the resin to be analyzed; statistical sampling techniques are recommended (cone and quarter technique, chute splitter, rotary splitter, roto-riffler, and so forth). Place the chase mold on a sheet of aluminum and slightly overfill each cavity in the chase with the resin. Another sheet of aluminum is placed on top and the stack is carefully placed in the press with the platens heated to 200 °C. The press is closed to apply minimal force for 1 or 2 minutes while the sample melts. The force is increased to at least 25,000 pounds, held for approximately 30 seconds, and released. The stack is then removed from the press and allowed to cool on the benchtop. The aluminum sheet is stripped from the

chase and the films are pushed from the cavities and trimmed to remove the flash. Examine the sample for surface defects and check to ensure that the thickness is between 0.5 and 0.7 mm. Samples with defects or thickness outside of the range are discarded; at least three suitable films are required for the analysis.

### Operating conditions

The infrared spectrometer should be turned on for at least 15 minutes prior to analysis. The resolution should be set to at least 4 wavenumbers.

Collect for a minimum of 30 seconds (70 scans) for each of the triplicate film samples.

### Method configuration

To determine the additive concentration, measure the area under the absorbance band for Irganox 1010 at 1745 cm<sup>-1</sup> relative to a baseline drawn between 1775 and 1721 cm<sup>-1</sup>. The specified peak areas and baseline points can easily be set in an Agilent MicroLab PC FTIR software method. Each peak measurement is called a component and the baseline limits are easily set as shown in Figure 3. The peak type of 'Peak Area with Dual Baseline' is first set. Then parameters for measurement of the area under the reference polypropylene absorbance band at 4062 cm<sup>-1</sup> relative to a baseline drawn between 4097 and 4010 cm<sup>-1</sup> (Figure 4) are set. The component is further configured to report the absorbance value to five decimal places as shown in Figures 3 and 4.

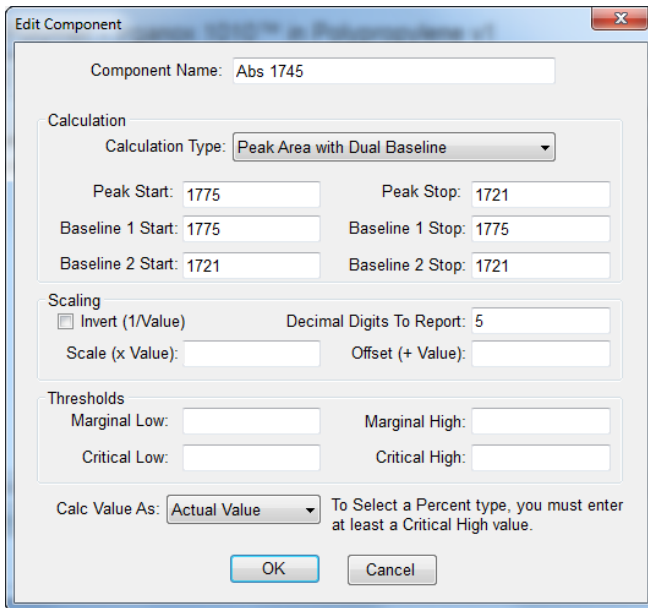
A ratio of the analyte band absorbance to the reference band is used for this analysis.

$$\text{Wt}\% \text{ Irganox 1010} = M \times (A_{1745}/A_{4062}) + N$$

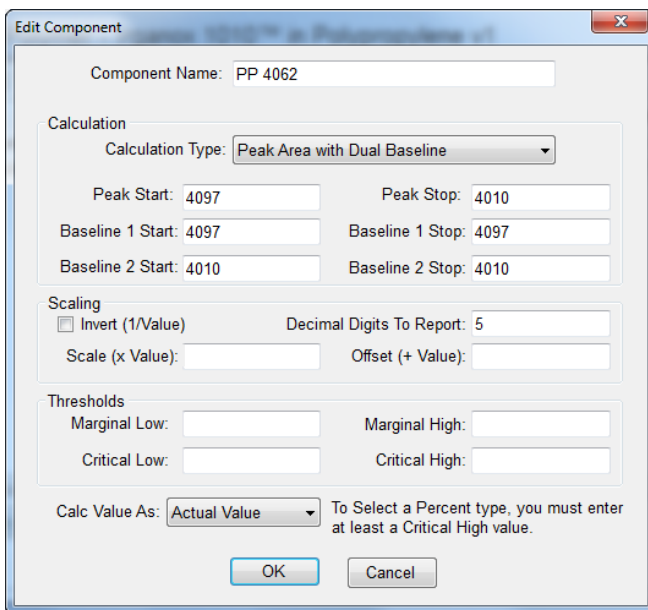
with M and N as determined in the the Calibration section.

The MicroLab PC FTIR software makes the peak ratio calculation easy to set up. Simply edit the method by selecting the 'Peak Ratio' calculation type and the peak components that are to be ratioed (Figure 5).

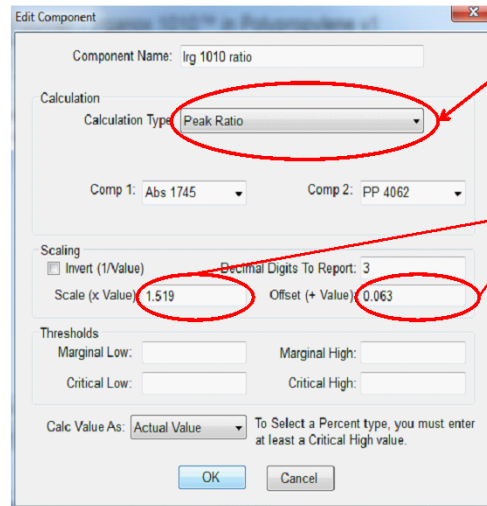




**Figure 3.** The Irganox 1010 peak area absorbance (component) measurement at 1745 cm<sup>-1</sup> in the MicroLab PC FTIR software. The peak start and stop refers to the area under the peak to be integrated. Single point baselines should be set up with the same baseline start and stop points.



**Figure 4.** The polypropylene reference peak component addition in the MicroLab PC FTIR software



Select 'Peak Ratio' from the drop-down menu.  
Add linear calibration slope and Y-axis offset.

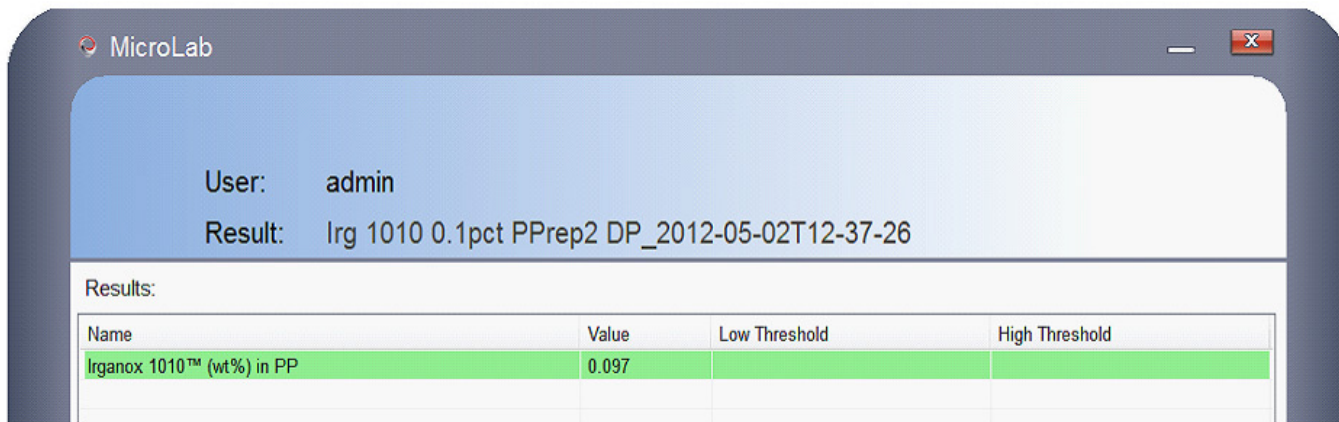
**Figure 5.** The peak ratio component addition in the MicroLab PC FTIR software. After plotting the calibration data, the resulting linear regression line's slope is entered in the 'Scale' field and the Y-axis offset in the 'Offset' field.

## Analysis

With the ratio defined, the new method is ready to be used to obtain at least triplicate measurements of each calibration standard. Unknown polymer coupons should also be run with a minimum of three measurements around the coupon. This process is made simple and convenient with the DialPath or TumbIIR transmission cells. Users can see the exact point of measurement in real time, and quickly reposition the sample for the replicate measurements.

Plot the values measured for the ratio relative to the Irganox 1010 concentration (Figure 2), and insert the slope and offset values back into the method as shown in Figure 5. Once the slope and offset values have been entered, the MicroLab PC FTIR software method will report the Irganox 1010 concentration.

The MicroLab PC software method, Polymer — Irganox 1010 in Polypropylene v1, includes the calibration data from Figure 2. This calibrated method is available with the Agilent 5500 and 4500 Series DialPath or TumbIIR FTIR spectrometers, as well as the Cary 630 FTIR spectrometers. This method and software performs all the calculations automatically and reports the final value as wt% Irganox 1010 in PP (Figure 6).

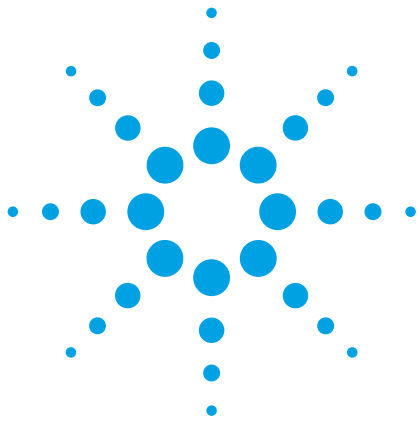


**Figure 6.** The MicroLab PC FTIR software prediction result for a 0.10 wt% Irganox 1010 in polypropylene sample

The values obtained from triplicate determinations should be averaged to give the final reported concentration.

## Conclusion

This analytical method demonstrates how the Agilent Cary 630 FTIR can be used to easily and accurately measure polymer thin films. The unique sampling capabilities of the DialPath and Tumbler provide a simple mechanism to mount your sample, while the step-by-step method-driven software with color-coded, actionable results guides you through your analysis to ensure that your samples are measured with minimum effort and highest accuracy.



# Determination of the vinyl content of polyethylene resins

## Analytical method

Polymers

### Authors

Dr. Wayne Collins\*, John Seelenbinder† and Frank Higgins†

Agilent Technologies  
\* Wilmington, DE, USA  
† Danbury, CT, USA



### Scope

This method is for the determination of the number of vinyl groups (C=C) in polyethylene resins by infrared spectroscopy. The test is used primarily for resins made with chromium catalyst technology, which gives a vinyl group at the end of each polymer chain, rather than resins made with titanium-based catalysts, which have few unsaturation sites. The method is applicable to powder, pellets or pieces cut from finished parts, but cannot be used for filled or pigmented samples.



Agilent Technologies

## Summary

This method determines the number of sites of unsaturation per 1000 carbon atoms by relating the intensity of the infrared absorption vinyl band at  $908\text{ cm}^{-1}$  to a calibration curve for standards derived from nuclear magnetic resonance (NMR) measurements, which is the primary measurement technique.

An analytically representative sample of the polyethylene resin is molded into a film with a thickness of 0.4 to 0.5 mm. Molding conditions are not important to the results obtained by this method, as long as the resin is not subjected to temperatures of more than  $250\text{ }^{\circ}\text{C}$  for more than 2 to 3 minutes, and the films have a smooth, consistent surface. The film is placed in the infrared spectrometer and the spectrum is obtained at 2 wavenumber resolution. Using the Agilent DialPath or TumbIIR accessories, the film or coupon can be inserted into the infrared beam path between the top and bottom crystals (Figure 1). Both these accessories are unique to Agilent and provide a revolutionary new way to measure thin polymer films or liquids. The horizontal mounting provides a simple, fast and reproducible mechanism to mount the sample by simply laying it down flat and rotating the crystal into position, eliminating errors and providing accurate and reliable answers — fast! The absorbance of the band at  $908\text{ cm}^{-1}$  is measured and corrected to a baseline drawn between  $950$  and  $875\text{ cm}^{-1}$ . This absorbance value is divided by the absorbance of a reference band at  $2019\text{ cm}^{-1}$  relative to a baseline drawn between  $1981$  and  $2108\text{ cm}^{-1}$ . Substitution of this ratio into the linear regression calibration equation derived from similar measurements on the standards gives the vinyl content in units of number of vinyl groups per 1000 carbon atoms. The vinyl content of a polyethylene sample is primarily determined by the catalyst used to manufacture the resin. Generally, resins made with a chromium catalyst will have significant vinyl content, greater than 0.5 vinyls/1000 carbon atoms, while resins from titanium catalysts typically have low vinyl content, less than 0.5 vinyls/1000 carbon atoms.



**Figure 1.** The Agilent DialPath transmission cell used for polymer analysis of coupons or films

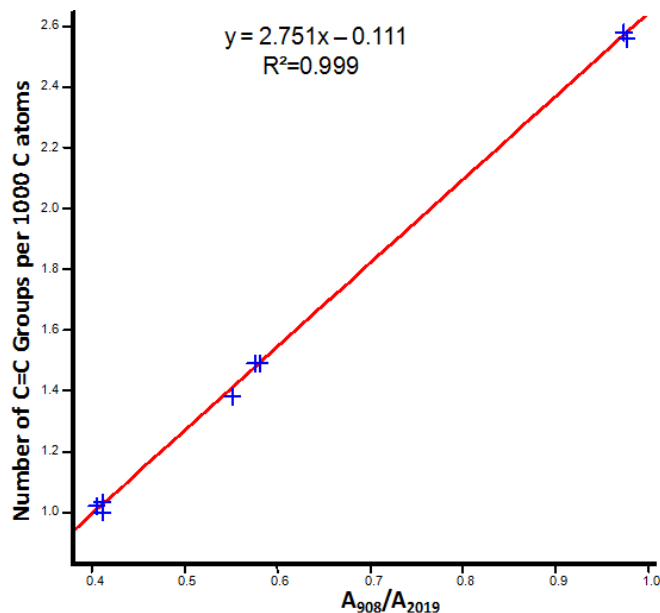
## Apparatus

- Data is obtained using an Agilent Cary 630 FTIR spectrometer equipped with a DialPath or TumbIIR sample interface with a  $1000\text{ }\mu\text{m}$  path length. Equivalent FTIR spectrometers, such as the mobile or portable Agilent 5500/4500 Series FTIR, can also be used.
- Hydraulic press — with heated platens capable of maintaining  $200\text{ }^{\circ}\text{C}$  and a ram force of 25,000 pounds.
- Chase mold — to control thickness (optional).
- Aluminum sheet —  $0.05\text{--}0.18\text{ mm}$  thick.

## Calibration

To perform the calibration, a spectrum is obtained for three films prepared from each standard resin. Determine the area of the analytical absorbance band relative to the baseline at  $908\text{ cm}^{-1}$  and the area of the reference band at  $2019\text{ cm}^{-1}$  following the same procedure as for samples described in this method. All absorbance values should be less than 1.6 units. Perform a linear least squares regression of the known vinyl content versus the ratio  $A_{908}/A_{2019}$  using all data points; do not include the origin as a data point.

The calibration curve and equation obtained for this method is shown in Figure 2.



**Figure 2.** Calibration curve for the number of vinyl C=C groups per 1000 C atoms in polyethylene. The correlation coefficient,  $R^2$ , was 0.999 and the 95% confidence interval was  $\pm 0.1$  C=C per 1000 C atoms.

$$\text{Vinyl C=C groups per 1000 C atoms} = M \times (A_{908} / A_{2019}) + N$$

Where:

Vinyl C=C groups per 1000 C atoms = Vinyl C=C groups per 1000 C atoms in the polyethylene

$A_{908}$  = Peak area absorbance of vinyl group at  $908 \text{ cm}^{-1}$

$A_{2019}$  = Absorbance of polyethylene reference band at  $2019 \text{ cm}^{-1}$

M = Calibration constant

N = Intercept

The vinyl content of each standard is typically determined by multiple analyses by  $\text{C}^{13}$  NMR spectroscopy.

## Procedure

### Sample preparation

Obtain a representative sample of the resin to be analyzed; statistical sampling techniques are recommended (cone and quarter technique, chute splitter, rotary splitter, roto-riffler, and so forth). Molding conditions are not important to the results obtained by this method, as long as the resin is not exposed to temperatures of more than  $250 \text{ }^\circ\text{C}$  for more than 2 to 3 minutes. A typical preparation technique is as follows:

Place the chase mold on a sheet of aluminum and slightly overfill each cavity in the chase with the resin. Another sheet of aluminum is placed on top and the stack is carefully placed in the hydraulic press with the platens heated to  $200 \text{ }^\circ\text{C}$ . The press is closed to apply minimal force for 1 or 2 minutes while the sample melts. The force is increased to at least 25,000 pounds, held for approximately 30 seconds and released. The stack is then removed from the press and allowed to cool on the benchtop or in a cold press. The aluminum sheet is stripped from the chase and the films are pushed from the cavities and trimmed to remove the flash.

Once the samples are prepared, each sample is examined for surface defects and checked to ensure that the thickness is between 0.4 and 0.5 mm. Samples with defects or thickness outside of the range are discarded; at least three suitable films are required for the analysis.

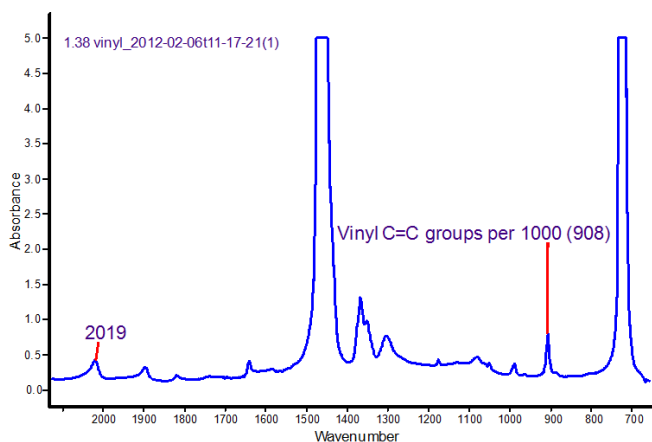
### Operating conditions

The infrared spectrometer should be turned on and allowed to stabilize for at least 15 minutes prior to analysis. The resolution should be set to 2 wavenumbers or better.

Collect for a minimum of 30 seconds (37 scans) for each of the triplicate film samples.

## Method configuration

To determine the vinyl concentration, measure the area under the absorbance band for the vinyl CH wag group at 908 cm<sup>-1</sup> relative to a baseline drawn between 926 and 898 cm<sup>-1</sup>. A typical spectrum is shown in Figure 3. The specified peak areas and baseline points can easily be set in an Agilent MicroLab PC FTIR software method. Each peak measurement is called a component and the baseline limits are easily set as shown in Figure 4. The peak type of 'Peak Area with Dual Baseline' is first set. Then parameters for measurement of the area under the reference polyethylene absorbance band at 2019 cm<sup>-1</sup> relative to a baseline drawn between 2097 and 1987 cm<sup>-1</sup> (Figure 5) are set. The component is further configured to report the absorbance value to five decimal places as shown in Figures 4 and 5.



**Figure 3.** Typical spectrum for the measurement of the vinyl group (CH wag) in polyethylene

A ratio of the analyte band absorbance to the reference band is used for this analysis.

$$\text{Number C=C per 1000 C atoms} = M \times [A_{908} / A_{2019}] + N$$

with M and N as determined in the the Calibration section.

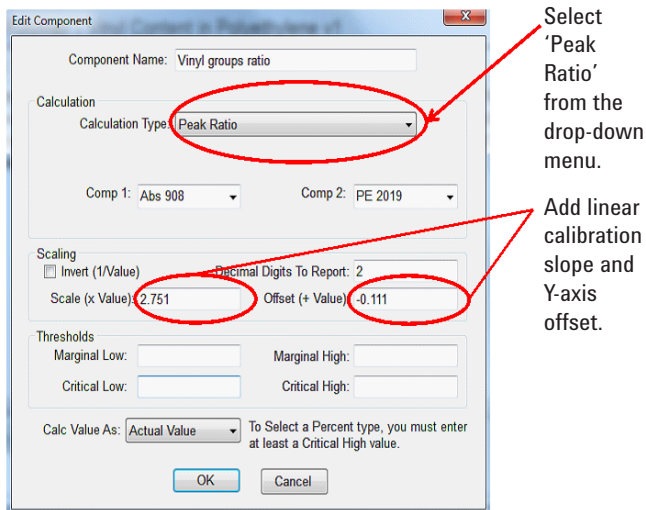
The ratio calibration equation for this analysis is:

$$\text{Number C=C per 1000 C atoms} = 2.751 \times [A_{908} / A_{2019}] - 0.111$$

**Figure 4.** The vinyl peak area absorbance (component) measurement at 908 cm<sup>-1</sup> in the MicroLab PC FTIR software. The peak start and stop refers to the area under the peak to be integrated. Single point baselines should be set up with the same baseline start and stop points

**Figure 5.** The polyethylene reference peak component addition in the MicroLab PC FTIR software

The MicroLab PC FTIR software makes the peak ratio calculation easy to set up. Simply edit the method by selecting the 'Peak Ratio' calculation type and the peak components that are to be ratioed (Figure 6).



**Figure 6.** The peak ratio component addition in the MicroLab PC FTIR software. After plotting the calibration data, the resulting linear regression line's slope is entered in the 'Scale' field and the Y-axis offset in the 'Offset' field.

### Analysis

With the ratio defined, the new method is ready to be used to obtain at least triplicate measurements of each calibration standard. Unknown polymer coupons should also be run with a minimum of three measurements around the coupon. This process is made simple and convenient with the DialPath or TumbIIR transmission cells. Users can see the exact point of measurement in real time, and quickly reposition the sample for the replicate measurements.

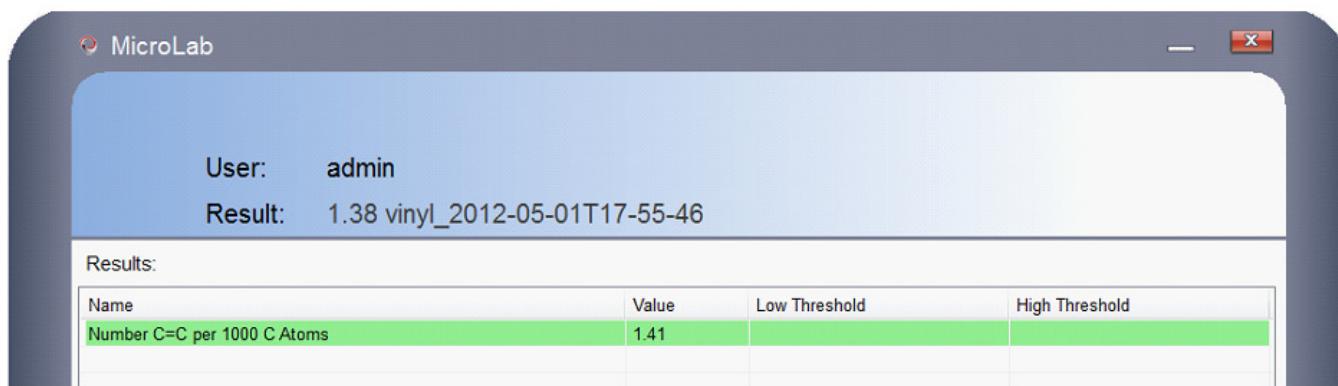
Plot the values measured for the ratio relative to the vinyl group concentration (Figure 2), and insert the slope and offset values back into the method as shown in Figure 6. Once the slope and offset values have been entered, the MicroLab FTIR software method will report the vinyl group concentration.

The MicroLab PC FTIR software method, Polymer – Vinyl Content in Polyethylene v1, includes the calibration data from Figure 2. This calibrated method is available with the Agilent 5500 and 4500 Series DialPath or TumbIIR FTIR spectrometers, as well as the Cary 630 FTIR spectrometers. This method and software performs all the calculations automatically and reports the final value as Number C=C per 1000 C Atoms (Figure 7).

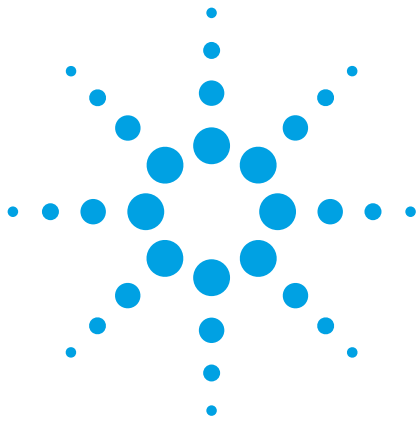
The values obtained from triplicate determinations should be averaged to give the final reported concentration.

### Conclusion

This analytical method demonstrates how the Agilent Cary 630 FTIR can be used to easily and accurately measure polymer thin films. The unique sampling capabilities of the DialPath and TumbIIR provide a simple mechanism to mount your sample, while the step-by-step method-driven software with color-coded, actionable results guides you through your analysis to ensure that your samples are measured with minimum effort and highest accuracy.



**Figure 7.** The MicroLab PC FTIR software prediction result for a 1.38 vinyl C=C groups per 1000 C atoms in polyethylene sample



# Determination of percent glycerol monostearate in polypropylene by infrared spectroscopy

Analytical method

Polymers

## Authors

Dr. Wayne Collins\*, John Seelenbinder† and Frank Higgins†

Agilent Technologies  
\* Wilmington, DE, USA  
† Danbury, CT, USA



## Scope

This method is for the determination of the glycerol monostearate (GMS) content and chemically identical antistatic additives in polypropylene where the additive package is known. The method utilizes a characteristic ester carbonyl band associated with the additive that is common in many other additives. Therefore, the total additive package must be known to confirm that other additives present do not contain bands that would interfere with the measurement. The method is typically used for process control of additive addition and is not recommended for filled or pigmented resins. The method has been validated over the range of 0.05 to 0.8% GMS content and can be used for either powder or pellet samples. Certain ester-based antioxidants, such as Irganox 1010 and Irganox 3114 have been found to interfere with the determination and therefore a correction factor is necessary for resins containing these additives. The purity of GMS additive for polymers ranges from 40 to 95% monoglyceride content. A correction to account for the purity must be made to determine the quantity of raw additive incorporated into the polymer. The sample must be pressed into a film or coupon prior to the analysis.



**Agilent Technologies**



## Summary

An analytically representative sample of the polypropylene resin is molded into a 0.4 to 0.7 mm thickness film. Molding conditions are not important to the results obtained by this method, as long as the resin is not subjected to temperatures of more than 250 °C for more than 2 to 3 minutes, and the films have a smooth, consistent surface. The film is placed in the infrared spectrometer to obtain the spectrum at 4 wavenumber resolution or better. Using the Agilent DialPath or TumbIR accessories, the film or coupon can be inserted into the infrared beam path between the top and bottom crystals (Figure 1). Both these accessories are unique to Agilent and provide a revolutionary new way to measure thin polymer films or liquids. The horizontal mounting provides a simple, fast and reproducible mechanism to mount the sample by simply laying it down flat and rotating the crystal into position, eliminating errors and providing accurate and reliable answers — fast! The ester absorbance of the GMS additive band is measured at 1739  $\text{cm}^{-1}$  and the absorbance is measured for the reference polypropylene band at 1044  $\text{cm}^{-1}$  to provide a path length or film thickness correction. To obtain the additive concentration in the sample, the ratio of the ester GMS band to the reference band is substituted into a linear regression calibration equation, constructed from measurements of prepared standards with known concentrations of additive. This Beer's Law calibration is linear through the 0.05 to 0.8% GMS range, however, non-linearities have been observed due to surface residues. Simply cleaning the film samples with a dry lint-free wipe removes the surface residues. Triplicate films are averaged to obtain a result.



**Figure 1.** The Agilent DialPath transmission cell used for polymer analysis of coupons or films

## Apparatus

- Data is obtained using an Agilent Cary 630 FTIR spectrometer equipped with a DialPath or TumbIR sample interface with a 1000  $\mu\text{m}$  path length. Equivalent FTIR spectrometers, such as the mobile or portable Agilent 5500/4500 Series, can also be used.
- Hydraulic press — with heated platens capable of maintaining 200 °C and a ram force of 25,000 pounds.
- Chase mold — to control thickness (optional).
- Aluminum sheet — 0.05–0.18 mm thick.

## Calibration

Standards are prepared by blending known amounts of GMS with polypropylene powder, and compounding under a nitrogen blanket until thoroughly mixed. To perform the calibration, prepare and analyze at least three films for each standard resin in accordance with the requirements of this method. All absorbance values in the calibration and prediction measurements should be less than 1.6 absorbance units. Perform a linear least squares regression of the concentration of the analyte versus normalized absorbance using all data points;

do not include the origin as a data point. Divide the peak height of the GMS ester absorbance band by the peak height of the reference polypropylene absorbance band to normalize the result. The calibration equation obtained for the standards used in this study is:

$$\text{Wt\% GMS} = M \times (A_{1739}/A_{1044}) + N$$

Where:

- Wt% GMS = Weight % of GMS in the polypropylene  
 $A_{1739}$  = Absorbance of GMS at  $1739\text{ cm}^{-1}$   
 $A_{1044}$  = Absorbance of polypropylene reference band at  $1044\text{ cm}^{-1}$   
M = Calibration constant  
N = Intercept

The calibration curve for the determination of GMS in polypropylene for the standards used in this study is shown in Figure 2.

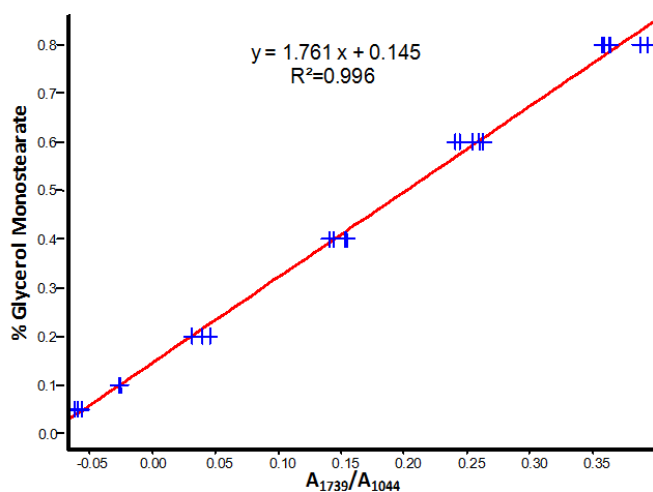


Figure 2. Calibration curve for % GMS in polypropylene.

## Procedure

### Sample preparation

Molding techniques and conditions used to prepare the sample do not significantly influence the results, as long as the resin is not subjected to temperatures of more than  $250\text{ }^{\circ}\text{C}$  for more than 2 to 3 minutes, and the prepared films have a smooth, consistent surface. A typical preparation procedure is as follows:

Obtain a representative sample of the resin to be analyzed; statistical sampling techniques are recommended (cone and quarter technique, chute splitter, rotary splitter, roto-riffler, and so forth). Place the chase mold on a sheet of aluminum and slightly overfill each cavity in the chase with the resin. Another sheet of aluminum is placed on top and the stack is carefully placed in the press with the platens heated to  $200\text{ }^{\circ}\text{C}$ . The press is closed to apply minimal force for 1 or 2 minutes while the sample melts. The force is increased to at least 25,000 pounds, held for approximately 30 seconds, and released. The stack is then removed from the press and allowed to cool on the benchtop. The aluminum sheet is stripped from the chase and the films are pushed from the cavities and trimmed to remove the flash. Examine the sample for surface defects and check to ensure that the thickness is between 0.4 and 0.7 mm. Samples with defects or thickness outside of the range are discarded; at least three suitable films are required for the analysis

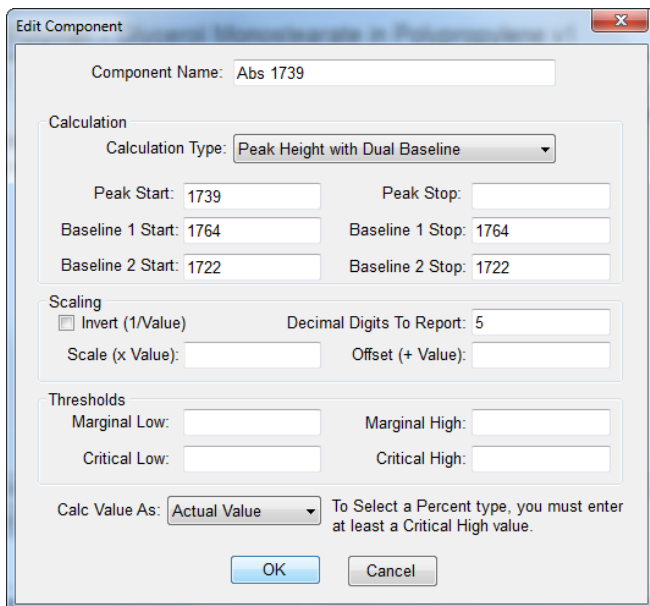
### Operating conditions

The infrared spectrometer should be turned on for at least 15 minutes prior to analysis. The resolution should be set to at least 4 wavenumbers.

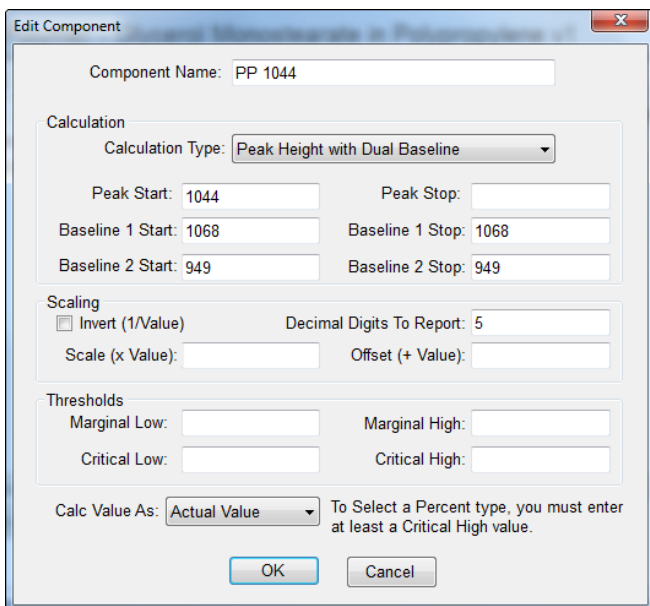
Collect for a minimum of 30 seconds (74 scans) for each of the triplicate film samples.

### Method configuration

To determine the GMS concentration, measure the peak height absorbance for GMS at  $1739\text{ cm}^{-1}$  measured by a vertical intersecting line to a baseline drawn between  $1764$  and  $1722\text{ cm}^{-1}$ . The specified peak height and baseline points can easily be set in an Agilent MicroLab PC FTIR software method. Each peak measurement is called a component and the baseline limits are easily set as shown in Figure 3. The peak type of 'Peak Height with Duel Baseline' is first set. Then parameters for measurement of the peak height polypropylene absorbance band at  $1044\text{ cm}^{-1}$  relative to a baseline drawn between  $1068$  and  $949\text{ cm}^{-1}$  (Figure 4) are set. The 'Peak Stop' field is left blank for peak height measurements. The component is further configured to report the absorbance value to five decimal places as shown in Figures 3 and 4.



**Figure 3.** The GMS peak height absorbance (component) measurement at 1739 cm<sup>-1</sup> in the MicroLab PC FTIR software. The peak start refers to the peak maxima position from which the peak height is measured. Single-point baselines should be set up with the same baseline start and stop points.



**Figure 4.** The polypropylene reference peak component addition in the MicroLab PC FTIR software.

A ratio of the analyte to reference absorbance band is used in the calibration for this analysis.

GMS equation:

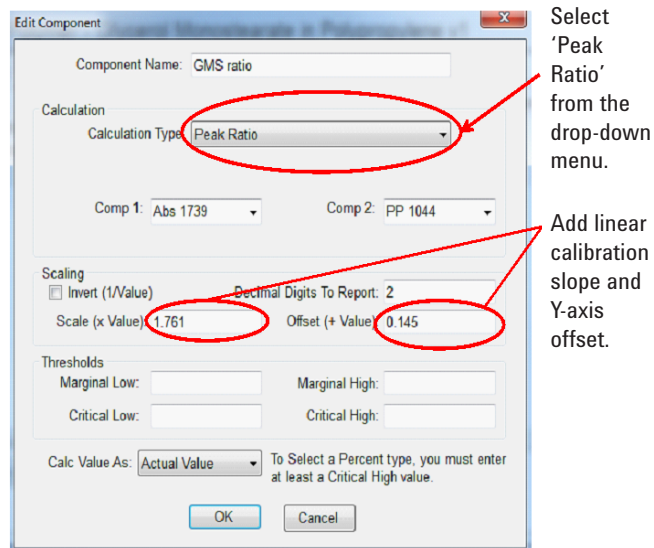
$$\text{Wt\% GMS} = M \times (A_{1739}/A_{1044}) + N$$

GMS resulting calibration values:

$$\text{Wt\% GMS} = 1.761 \times (A_{1739}/A_{1044}) + 0.145$$

with M and N as determined in the the Calibration section.

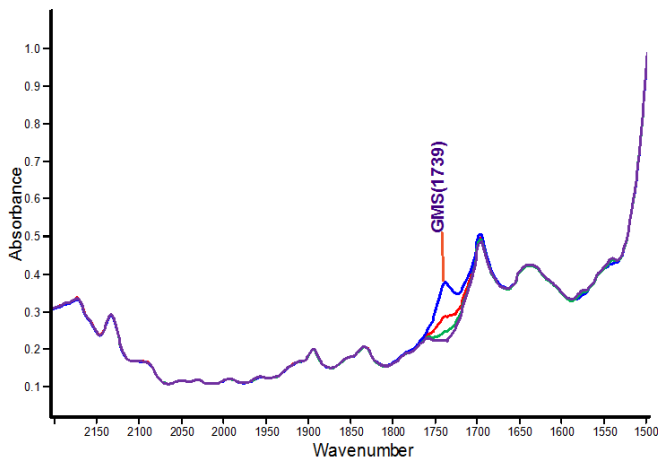
The MicroLab PC FTIR software makes the peak ratio calculations easy to set up. Simply edit the method by adding two new components and selecting the 'Peak Ratio' calculation type. Then add the peak components that are to be ratioed (Figure 5).



**Figure 5.** The peak ratio component addition for the calibration in the MicroLab PC FTIR software. After plotting the 0.05–8% GMS calibration data, the resulting linear regression line's slope is entered in the 'Scale' field and the Y-axis offset in the 'Offset' field.

## Analysis

The specimen is placed in the sample compartment and the spectrum is recorded; the typical spectra in the 2200–1500 cm<sup>-1</sup> range are overlaid in Figure 6. The presence of an absorption band at 1745 cm<sup>-1</sup> suggests that the resin contains an ester-based antioxidant such as Irganox 1010 or Irganox 3114. If the presence of these antioxidants is confirmed, the GMS measurement must be corrected to compensate for the absorbance of the antioxidants.



**Figure 6.** Typical ester carbonyl absorbance for glycerol monostearate in polypropylene

With the ratio defined from the Method Configuration section, the new method is ready to be used to obtain at least triplicate measurements of each calibration standard. Unknown polymer coupons should also be run with a minimum of three measurements around the coupon. This process is made simple and convenient with the DialPath or Tumbler transmission cells. Users can see the exact point of measurement in real time, and quickly reposition the sample for the replicate measurements.

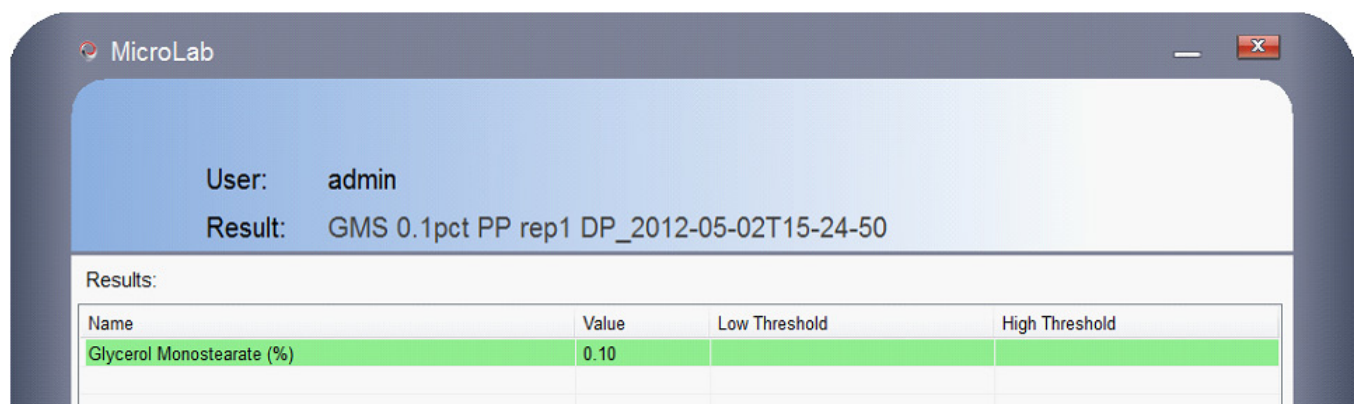
Plot the values measured for the ratio relative to the GMS concentration (Figure 2), and insert the slope and offset values back into the method as shown in Figures 5 and 6. Once the slope and offset values have been entered, the MicroLab PC FTIR software method will report the GMS concentration.

The MicroLab PC FTIR software method, Polymer — Glycerol Monostearate in Polypropylene v1, includes the calibration data from Figure 2. This calibrated method is available with the Agilent 5500 and 4500 Series DialPath or Tumbler FTIR spectrometers, as well as the Cary 630 FTIR spectrometers. This method and software performs all the calculations automatically and reports the final value as % Glycerol Monostearate (Figure 7).

The values obtained from triplicate determinations should be averaged to give the final reported concentration.

## Conclusion

This analytical method demonstrates how the Agilent Cary 630 FTIR can be used to easily and accurately measure polymer thin films. The unique sampling capabilities of the DialPath and Tumbler provide a simple mechanism to mount your sample, while the step-by-step method-driven software with color-coded, actionable results guides you through your analysis to ensure that your samples are measured with minimum effort and highest accuracy.



**Figure 7.** The MicroLab PC FTIR software prediction result for a 0.1% GMS in polypropylene sample



# Advanced Atomic Force Microscopy: Exploring Measurements of Local Electric Properties

## Application Note

*Sergei Magonov, John Alexander*  
*Agilent Technologies*

### Introduction

In the past two decades Atomic Force Microscopy (AFM)<sup>1</sup> has been recognized as a powerful characterization method of surfaces at small scales and in different environments. In addition to high-resolution visualization of surface morphology and nanoscale structures, AFM microscopes are also broadly applied for examination of mechanical, electromagnetic, optical and other properties. The core of this technology is the measurement and control of force interactions between a minute probe and a sample surface. Practically, such measurements can be performed at a single location and applied for surface imaging with contact or oscillatory techniques. The techniques complement each other yet studies of soft matter are mostly carried out with oscillatory amplitude modulation (AM) mode.<sup>2-3</sup> Despite an expanding penetration of AFM and the related scanning probe microscopy methods into academic and industrial research, a critical analysis of the existing capabilities of this method reveals a number of undeveloped areas that are essential for further progress of the field. We will mention only a few of them. The current efforts towards imaging with true molecular and atomic resolution in different environments benefit from an extension of frequency modulation (FM) mode<sup>4</sup> to measurements in air and under liquid.<sup>5</sup> The improvement of noise characteristics of AFM electronics and the minimization of thermal drift of the microscopes will undoubtedly assist researchers using extremely sharp probes in achieving superior imaging resolution. In the probing of local mechanical and electric properties increasing attention is paid to multi-frequency measurements that offer new capabilities for quantitative analysis. Studies employing multi-frequency measurements in the broad frequency range help avoid cross-talk of

topography with mechanical and electric tip-sample force effects and have other advantages. A successful realization of these possibilities simultaneously with improved resolution of imaging and mapping of materials' properties will open new horizons for AFM characterization especially if these applications can be performed in the properly-controlled environments. This goal can be achieved only in direct interplay of instrumentation developments and their practical verification on various samples. This is our vision of advanced AFM and we hope that this paper supports it.

In the commercial scanning probe microscopes made by Agilent Technologies the first steps towards advanced AFM measurements were undertaken with the introduction of the MAC III accessory especially useful for multi-frequency measurements. The MAC III has three dual phase lock-in amplifiers (LIA) converting the AC inputs to amplitude and phase. These digitally-controlled analog LIA have a broad bandwidth (up to 6 MHz) that covers the operation bandwidth of the photodetector employed in the microscope. The auxiliary inputs and drive outputs are accessible through the MAC III signal access box. The software, which is flexible in routing signals back to the microscope controller, supports two servo systems related to these LIA. One LIA is used for AM tracking of sample topography with the probe peak-to-peak amplitude or its X-, Y- vector components used for feedback. The other servo can be applied to electric or mechanical measurements. The third LIA can be used for tuning the operational parameters or for recording various signals (lateral response, torsional signal, harmonics, etc) during measurements. Voltages up to 20 V in DC or in different pulse regimes can be applied to the probe-sample junction as an external stimulus for lithography or other applications.

## Electrostatic force effects in AFM

In microscopy, the compositional mapping of heterogeneous materials is based on recognition of dissimilar sample components. In AFM this is achieved by differentiating the probe-sample interactions at the locations with different mechanical (modulus, friction, adhesion, viscoelasticity, etc), magnetic, electric or other properties. Compositional mapping is the compelling industrial application for analysis of multicomponent materials and it will be advanced further as the contrast variations observed in AFM images will be interpreted quantitatively in terms of materials properties. Although the AFM-based mechanical studies are the most explored application area, this paper is focused on studies of local electric behavior of various samples. Both contact and oscillatory techniques are used for AFM-based electric characterization yet we will consider mostly oscillatory AM mode and only in some cases will mention its companion – the FM mode. In the experiment, as the oscillating probe, which initially vibrates at or near its first flexural resonance  $\omega_{\text{mech}}$  with amplitude  $A_0$ , approaches the sample, first, it will sense van der Waals forces, which change the tip-sample force gradient and shift the probe resonance to lower-frequencies. In a non-dissipative case, this shift is the only effect changing the amplitude-versus-frequency ( $A$ - $v$ - $\omega$ ) dependence. In AM mode, the amplitude change at  $\omega_{\text{mech}}$  is employed by a feedback loop to keep the tip-sample interaction constant during surface profiling. On further approach toward the sample, the probe comes into intermittent contact and the topography and phase images are collected at set-point amplitude ( $A_{\text{sp}}$ ) chosen by the researcher. For a particular probe and chosen  $A_0$  the tip-sample force can be adjusted by varying  $A_{\text{sp}}$ . The experiments can be performed either at low tip-sample forces – the condition for a most gentle and high-resolution imaging of surfaces, or at elevated forces – the condition for compositional imaging based on differences of local mechanical properties.<sup>6</sup> In many cases, the phase images obtained at elevated tip-sample forces are most informative for such qualitative analysis of heterogeneous samples. The situation becomes more complicated when the probe behavior is also influenced by electrostatic tip-sample interactions.

In traditional AM studies the electrostatic forces between a conducting probe and a sample surface with local charges manifest themselves in many ways. The

amplitude-vs-Z (AvZ) and phase-versus-Z curves will have a signature of long-range electrostatic interactions, which also impact imaging in the non-contact regime. Figures 1A-H illustrate these effects showing the AvZ curve and images taken at different  $A_{\text{sp}}$  on the surface of a  $\text{LiNbO}_3$  crystal with Ag particles deposited along a grain boundary. The AvZ curve demonstrates a gradual drop of amplitude at large tip-sample separations. The topography and phase images recorded at  $A_{\text{sp}}$ , which is chosen along this part of the curve, show that on approach of the probe to the sample, the Ag particles are first detected in the phase image (grey circle). This is due to higher sensitivity of the

phase changes to long-range electrostatic forces between the charged Ag particles and the conducting probe. On further approach, the increasing attractive force leads to higher phase contrast, and the similar pattern appears in the topography images (red and green circles). As some probe-sample distance the oscillating tip comes into intermittent contact and the AvZ curve changes from the gradual decline to the abrupt one. At  $A_{\text{sp}}$  along the steep part of the AvZ curve (blue circle) the topography image distinctively shows a granular morphology of the  $\text{LiNbO}_3$  surface and the string of Ag particles. The related phase image enhances the edges of the grains similar to the amplitude (error

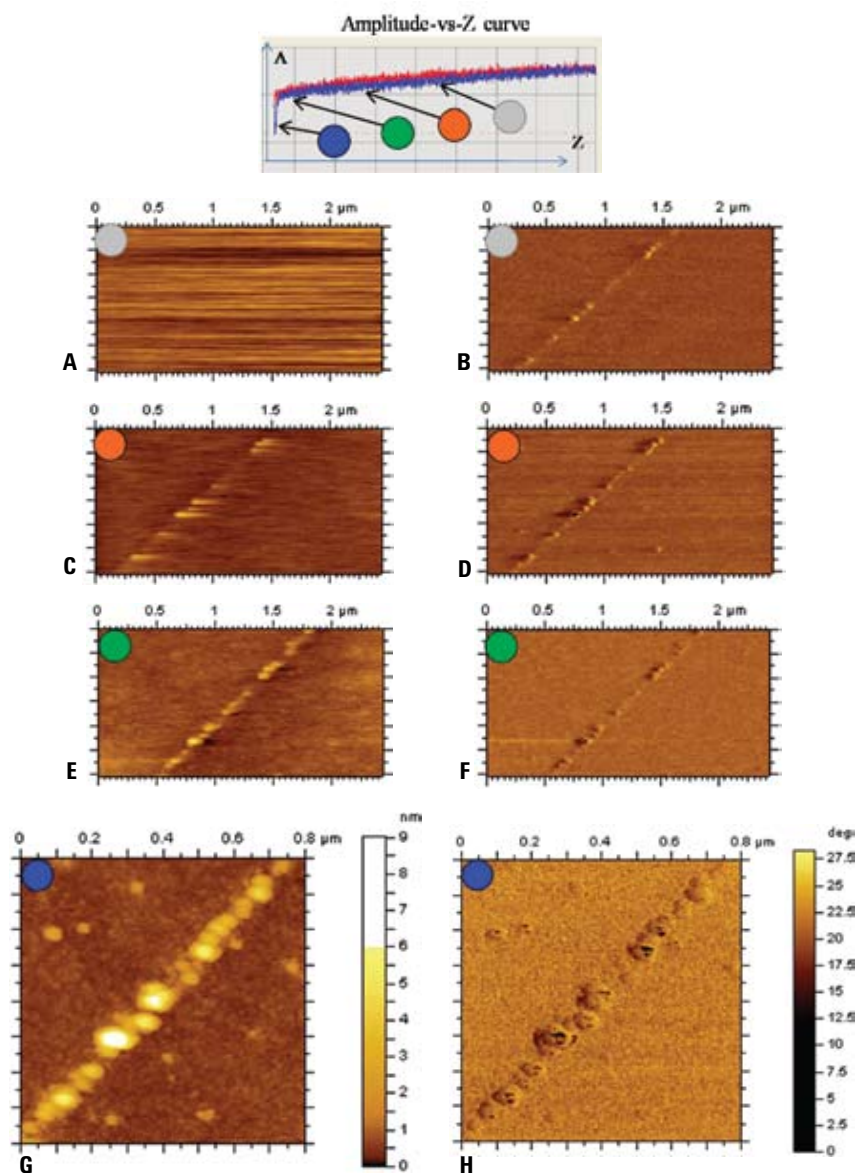


Figure 1A-H. Top – amplitude-versus-distance curve on  $\text{LiNbO}_3/\text{Ag}$  surface. The topography (A, C, E) and phase images (B, D, F) at different  $A_{\text{sp}}$  as marked by color dots.

signal) image indicating the overwhelming contribution of tip-sample mechanical interactions to the image contrast. In other words, in AM mode when the probe behavior is measured at single frequency ( $\omega_{\text{mech}}$ ), the electrostatic forces dominate the probe response in the non-contact regime but their effect becomes negligible in the intermittent contact.

The intermittent contact AM imaging of samples with charged locations can be “disturbed” by a voltage applied to a conducting probe as shown in Figures 2A-F. The images of semifluorinated alkane  $\text{F}(\text{CF}_2)_{14}(\text{CH}_2)_{20}\text{H}$  (further referred as  $\text{F}_{14}\text{H}_{20}$ ) adsorbates on graphite exhibit strong contrast variations of several domains (one is outlined with a red circle) as the probe voltage is changing. When imaging was performed with a non-biased probe, the domains in the topography image were not distinguishable from their surrounding yet they exhibited different contrast in the phase images. The same locations became pronounced in the topography images once the probe was biased (+3 V and -3 V) with respect to the sample. This observation raises a question regarding true topography measurements in AM. The false topography contrast is often observed in AM studies of smooth heterogeneous surfaces where more adhesive regions are “elevated” compared to less adhesive ones.<sup>7</sup> This effect is a consequence of a shift of the probe resonance frequency by attractive tip-sample interactions. Therefore, a negative charge of the outlined domain can explain its appearance in Figures 2C, 2E. Actually, surface charges might influence the topography measurements even when a regular Si probe is applied. Such probes have some level of conductivity and the surface charge can induce mirror charges in the probe and the related attractive interaction. A compensation of the surface charge effect by a proper voltage applied to the probe will help reveal the precise topography.

Figures 3A-B present another case when a voltage applied to the probe enhances a number of particles in the topography image of thermoplastic vulcanizate – the material, which contains carbon black buried inside a polypropylene and rubber blend. These changes are caused by electrostatic force between the probe and carbon black particles contributing to a conducting percolation network in this composite material. A subtraction of the topography images will show these particles with even higher resolution as

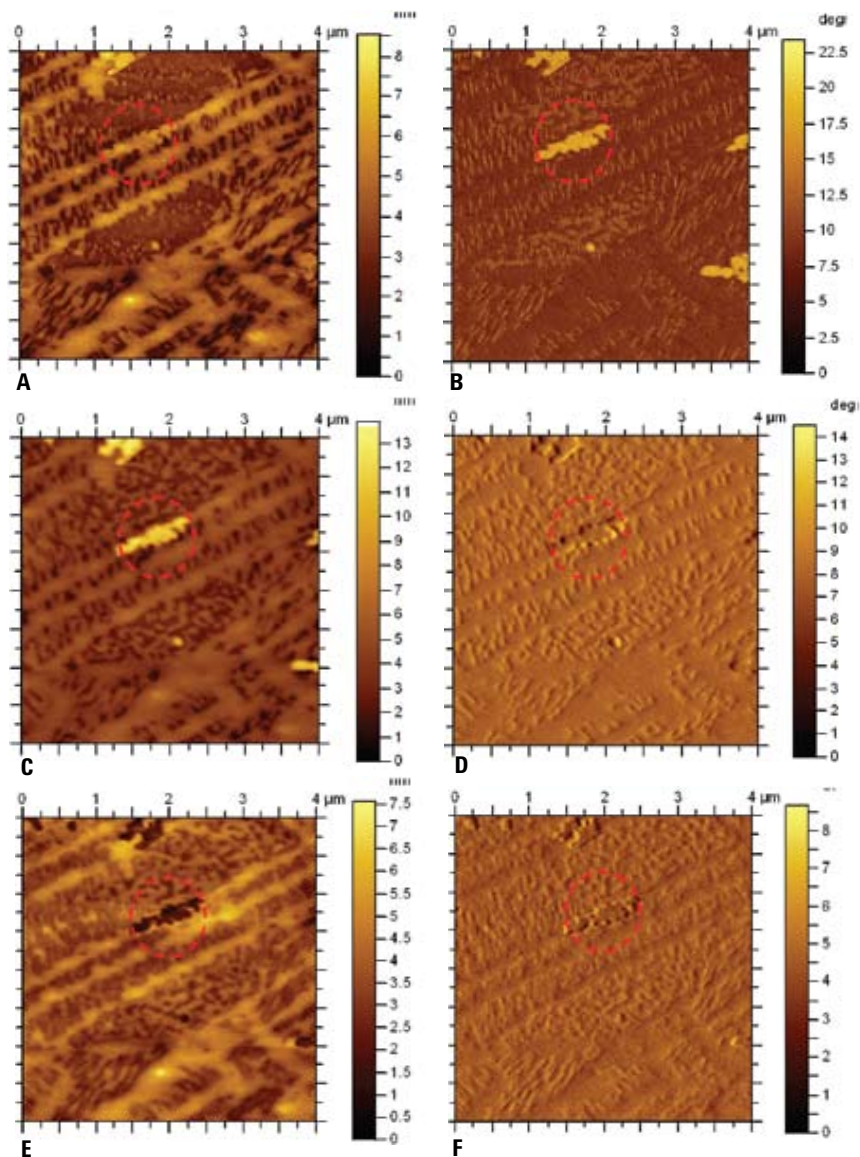


Figure 2A-F. Topography (A, C, E) and phase (B, D, F) images of an adsorbate of semifluorinated alkane  $\text{F}_{14}\text{H}_{20}$  on graphite. The images in (A)-(B) were obtained with a non-biased probe, the images in (C)-(D) were recorded with the bias voltage +3 V and the images in (E)-(F) – with the bias voltage of -3 V.

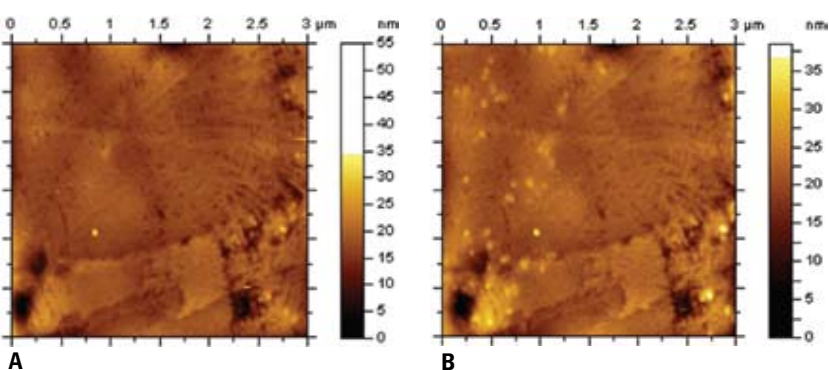


Figure 3A-B. The topography images of thermoplastic vulcanizate obtained with a non-biased probe (A) and with the bias voltage of +3 V.

compared to one of the 2-path electric force microscopy (EFM) enabled by a lift technique.<sup>8</sup> In the latter mode the probe is positioned above the surface and this lowers the EFM resolution. These examples clearly demonstrate that the probe responds simultaneously to the tip-sample mechanical and electrostatic interactions and their separation is the most essential problem of AFM-based electric measurements.

## Background on Electric Force Microscopy (EFM) and Kelvin Force microscopy (KFM)

The use of AFM for examination of local electric properties of surfaces was suggested since the advent of this technique. A typical scheme of detection of electrostatic forces includes a conducting probe which is biased with respect to a back electrode or substrate carrying a sample on top. In a simplified form the contribution of electrostatic force is proportional to  $\Psi^2$  and  $\frac{\partial C}{\partial z}$ , where  $\Psi$  – potential difference,  $C$  – capacitance and  $Z$  – the probe-sample separation.

$$(1) F_{elec}(Z) = \frac{1}{2} \frac{\partial C}{\partial z} \Psi^2$$

When DC ( $U_{DC}$ ) voltage and AC ( $U_{AC}$ ) voltage at frequency  $\omega$ , are applied to the probe then the electrostatic force can be expressed as

$$(2) F_{elec}(Z) = \frac{1}{2} \frac{\partial C}{\partial z} [(\varphi - U_{DC} - U_{AC} \sin(\omega t))^2],$$

where  $\varphi$  – surface potential or contact potential difference between the probe and the sample.

This equation can be separated into three components defining the DC and frequency responses:

$$(3) F_{DC}(Z) = \frac{1}{2} \frac{\partial C}{\partial z} (\varphi - U_{DC})^2 + \frac{1}{2} U_{AC}^2$$

$$(4) F_{\omega}(Z) = - \frac{\partial C}{\partial z} [(\varphi - U_{DC}) U_{AC} \sin(\omega t)]$$

$$(5) F_{2\omega}(Z) = - \frac{1}{4} \frac{\partial C}{\partial z} U_{AC}^2 \cos(2\omega t)$$

This set of equations describes the electrostatic force measurements in the capacitor-like set-up. The idea of using two frequencies for simultaneous and independent measurements of surface topography and electrostatic forces was implemented in one of the first AFM applications.<sup>9</sup> In these non-contact experiments, AC voltage was applied to a conducting probe at  $\omega_{elec}$  and the changes of the probe amplitude at this frequency were detected at different probe-sample separations, which were adjusted by changing  $A_{sp}$  at the frequency of mechanical resonance,  $\omega_{mech}$  ( $> \omega_{elec}$ ). These measurements

showed high sensitivity of the applied detection scheme. In the next step, maps of electric properties of a photoresist on a Si substrate and of a working  $p$ - $n$  junction in a transistor were obtained by recording the amplitude changes at  $\omega_{elec}$  and  $2\omega_{elec}$ .<sup>9</sup>

In other experiments during the same time,<sup>10</sup> surface charges, which were made by voltage pulses between a tip and PMMA layer on the Si substrate, were examined in AM mode operating in the non-contact regime ( $\omega_{mech} = 20$  kHz). The surface charges have induced the false topography profiles – similar to those demonstrated above in the non-contact and intermittent contact images in Figures 1C, 1D and 2C, 2E, respectively. The AM imaging of the surface charges was further extended by using low-frequency AC voltage ( $\omega_{elec} = 300$  Hz) and monitoring the amplitude changes at  $\omega_{elec}$  and  $2\omega_{elec}$ .<sup>11</sup> These pioneering measurements of the AFM probe response to electrostatic forces and mapping it over a scanned area defined electric force microscopy (EFM). The extraction of quantitative electric properties from surface maps of amplitude changes at  $\omega_{elec}$  is a challenging task.<sup>12</sup> The quantitative detection of surface potential was simplified with a null-force method.<sup>13</sup> In this procedure, a combination of DC and AC (at  $\omega_{elec}$ ) voltages was applied to the probe and the DC level is changed until the AC vibration of the probe (at  $\omega_{elec}$ ) is nullified, see equation (4). In first demonstration of the null-force method a voltage map of the precision operational amplifier in a functioning state was made. Later, the null-force method was applied to detection of local contact potential difference (CPD)<sup>14</sup> and this set-up was named Kelvin probe force microscopy (KFM). In addition to EFM and KFM, probing of local electrostatic properties in non-contact mode has been diversified by using the  $2\omega_{elec}$  response [see equation (5)] for the feedback mechanism.<sup>15-17</sup> In such a way one can get information regarding the local dielectric constant and its high-frequency dispersion.<sup>15</sup> Simultaneous measurements of sample topography ( $\omega_{mech} = 70$  kHz), surface potential ( $\omega_{elec}$ ) and dielectric or polarization response ( $2\omega_{elec}$ ) were performed while the probe was scanning  $\sim 30$  nm above the sample surface.<sup>17</sup> The use of EFM and KFM has increased as they become available in commercial scanning probe microscopes. This happened with the introduction of the lift mode, that makes possible 2-pass EFM and KFM measurements at the single frequency ( $\omega_{mech}$ ). The 2-pass method is a simple separation of the mechanical and

electrostatic interactions by switching between the intermittent contact and the non-contact operations. In principle, this switching can be realized by changing  $A_{sp}$ . Yet due to thermal drift and other instrumental imperfections the imaging in the non-contact regime where the probe feels only long-range forces is not stable. The problem is solved when in each scan line the probe is raised above the surface only a small height to the non-contact position where the electrostatic response is measured separately from the topography. The tradeoff is the extra time needed for such operation and the remote position of the probe sensing electrostatic forces.

## Outlook on EFM and KFM applications

The practical value of EFM and KFM has been established in applications to different materials, ranging from semiconductor structures to biological specimens. In studies of semiconductors and metals, KFM is applied for quantitative measurements of the surface potential of small structures such as thin films, layers, lines, quantum dots and the planar and cross-section dopant profiles. The correlation of the surface potential or CPD data with Fermi level and the influence of surface contamination, oxide coverage and environment on these data are of special concern. The KFM measurements were also made on various small-scale devices including organic thin-film transistors. The mapping of surface potential in the accumulation layer revealed surface potential changes at the film interfaces between the source and drain elements.<sup>18-19</sup> A correlation between surface photovoltage and polymer blend morphology has been examined in polyfluorene-based photodiodes in dark and illuminated conditions.<sup>20</sup> In the bilayer geometry, two polymers, which serve as holes-rich and electrons-rich reservoirs, adopt a complex morphology with domains of different charges. Particularly, low photodiode efficiency was explained by a presence of charged domains caused by steric hindrances to their recombination. The morphology-surface potential relationship was examined in another photovoltaic material – the 100 nm film of an organic blend consisting of soluble fullerene derivative (acceptor) and para-phenylene-vinylidene (PPV)-based polymer on ITO substrate (acceptor).<sup>21</sup> The data were applied for the explanation of different photovoltaic behavior of the films prepared from different solvents.



A dependence of surface potential on molecular order was found in studies of poly-3-methylthiophene at various doping levels.<sup>22</sup> The surface potential was different not only between amorphous and crystalline components but also between individual sectors of crystallites.<sup>23</sup> This invokes a challenging task – the interpretation of surface potential in terms of molecular arrangement, molecular chemical structures and their dimensions. Semifluorinated compounds, which exhibit a strong polar nature due to the dipole at the  $-\text{CH}_2-\text{CF}_2-$  bond, are suitable compounds for studying this problem. The KFM images, which were obtained on a mixed monolayer of perfluorodecanoic acid (FC) and arachidic (HC) polyion complexed with (poly(4-methylvinyl pyridinium) iodide, revealed the phase-separation in this material.<sup>24</sup> The surface potential contrast of the components was explained by different strength of dipoles of  $\text{C}^{\delta+}-\text{F}^{\delta-}$  and C-H bonds of the FC and HC components. In another example, a micro-contact-printed pattern with alternative domains of alkylsilane  $[\text{H}_3\text{C}(\text{CH}_2)_{17}\text{Si}(\text{OCH}_3)_3]$  - ODS and fluoroalkylsilane  $[\text{F}_3\text{C}(\text{CF}_2)_7(\text{CH}_2)_2\text{Si}(\text{OCH}_3)_3]$  - FAS on a Si substrate was prepared as a test structure for KFM.<sup>25</sup> The highest-contrast images, which differentiate the fluorinated material ( $\Delta V = 171$  mV), originate from the surface potential difference between alkylsilane and fluoroalkylsilane domains. An estimate of the surface potentials of the QDS and FAS layers based on the calculated dipoles of individual molecules (ODS – 1.18D and FAS – 1.47D) and their orientation gives a much stronger  $\Delta V$  compared to the measured one. Therefore, several other factors such as intermolecular interactions, screening and depolarization effects should be considered for the rational interplay between the experimental and theoretical results.

There is a promise that KFM applications will also become important in studies of biological samples, yet applicability of this method in water solutions is not fully clarified. A condensation of dipalmitoylphosphatidylcholine (DPPC) monolayer at the air-water interface in a Langmuir-Blodgett trough was monitored with KFM.<sup>26</sup> This process includes structural transitions from the expanded condition state to a mixture of liquid expanded (LE) and liquid condensed (LC) phases and, finally, to solid condensed (SC) state. The single layers, which were transferred to an Al-coated glass substrate, exhibit a surface potential  $\sim 270$  mV higher than that of bare Al. Surface potential of the layers increases 50-100 mV on transition from LE to LC

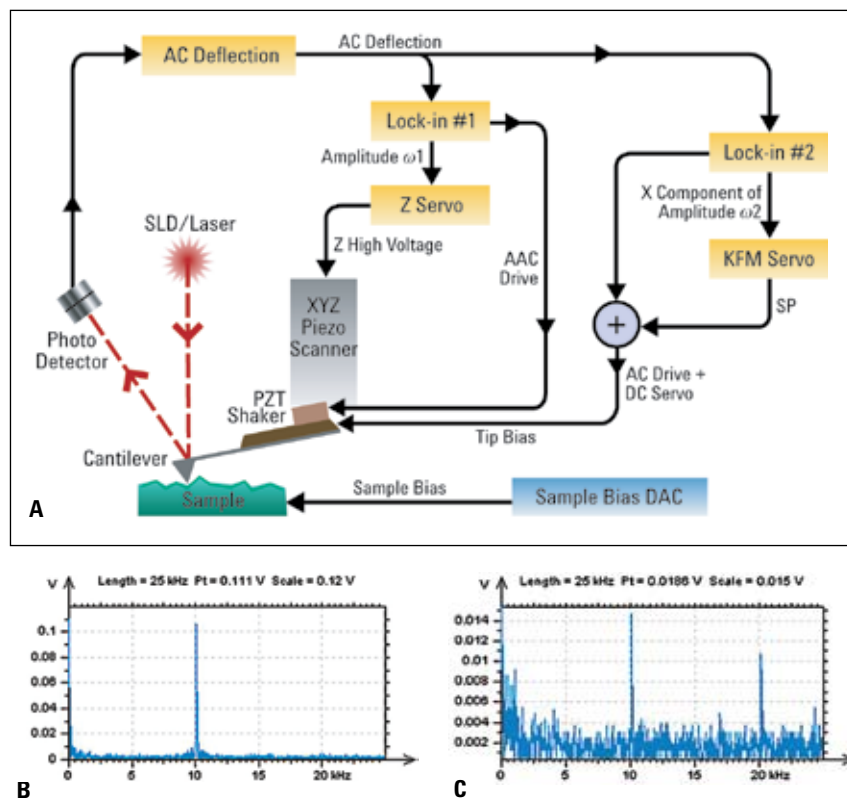


Figure 4A-C. A block-diagram of the implementation of KFM in Agilent 5500 scanning probe microscope using the MACIII accessory. (B)-(C) Amplitude-vs-frequency sweeps of LIA-2 signal (X-component of amplitude) with the electric servo loop in the "off" and "on" states, respectively.

phase and 300 mV on transition from the LC to the SC state. The increase of molecular density was an adequate explanation of the changes of LE and LC potentials, whereas the steep potential raise in the SC phase resulted from a compression-induced change of the effective dipole near the polar head group of lipid molecules.

### KFM measurements with Agilent 5500 scanning probe microscope

There is no doubt that local measurements of the electrostatic force are among the most essential capabilities of a modern scanning probe microscope. The practical implementation of EFM and KFM in Agilent 5500 scanning probe microscope is enabled with the MACIII accessory, see the general set-up in Figure 4A. A sample on a microscope stage is grounded (or biased) and an electric signal is applied to a conducting probe. The probe oscillation, which is excited at or near its resonance  $\omega_{\text{mech}}$ , changes its response to the tip-sample forces that is monitored with a photodetector. The photodetector output carrying the AC probe amplitude is sensed in parallel by LIA-1 and LIA-2. The LIA-1 is tuned to  $\omega_{\text{mech}}$ , and it delivers the

error amplitude signal ( $A_i - A_{\text{sp}}$ , where  $A_i$  – measured amplitude in a new surface location) to the servo that controls the vertical tip-sample separation. This servo loop is used for topography imaging. LIA-2 is tuned to  $\omega_{\text{elec}}$  and from the input signal the X-component of amplitude at  $\omega_{\text{elec}}$  is selected for servoing the tip voltage to nullify the incoming signal. In preparation for KFM imaging the phase of LIA-2 is tuned to maximize the X-component signal. The operation of the electric servo loop can be monitored and controlled with LIA-3, which sweeps the frequency around  $\omega_{\text{elec}}$ . Typical sweep curves in the "on" and "off" states of the electric servo loop are shown in Figures 4B-C, where the scale is  $\sim 10\times$  smaller in C. The detection of the amplitude signal at  $\omega_{\text{elec}} = 10$  kHz in the "off" state helps to optimize the experiment parameters, e.g. the level of AC voltage applied to the probe in the second loop. The MAC III accessory can provide a voltage up to  $\pm 10$  volts, however the voltage should be chosen as small as possible to minimize its influence on the sample's electronic states. We have operated with the voltages in the 1-5 V range. In the "on" state one should minimize the remainder of the amplitude signal (the error signal in the feedback operation)

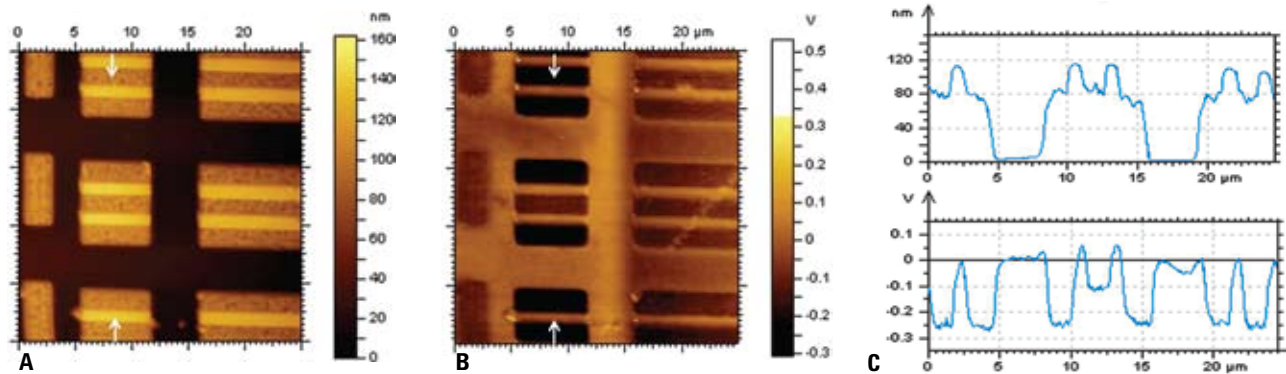


Figure 5A-C. The topography (A) and surface potential (B) images of SRAM. The cross-section profiles along the directions indicated with white arrows in (A) and (B) are shown in the top and bottom parts of (C).

at  $\omega_{\text{elec}}=10$  kHz by optimizing servo gain parameters. The experimental protocol for KFM also includes a compensation of the occasional contribution to surface potential measurements from the probe and sample surroundings; which causes a dependence of surface potential on the probe-sample separation. This dependence is eliminated by finding the proper offset voltage. The optimization procedures for KFM measurements are described in more detail in <sup>27</sup>.

In the single-pass KFM experiment one needs to select  $\omega_{\text{mech}}$  and  $\omega_{\text{elec}}$ . A mechanical drive of the probe is typically done at  $\omega_{\text{mech}}$  chosen near the first flexural resonance of the cantilever, whereas the electric servo loop is set either at much lower frequency or at the second or even third flexural mode. The following arguments are usually considered in the choice of  $\omega_{\text{elec}}$ . The electrostatic probe response is higher at the resonant frequencies, yet this also increases the possibility the cross-talk between different force interactions. The cross-talk is less probable when  $\omega_{\text{elec}} \ll \omega_{\text{mech}}$  but the probe response at non-resonant frequencies is also smaller. If the sensitivity is the real problem, then one can try to use the second flexural mode for  $\omega_{\text{mech}}$  and first flexural mode for  $\omega_{\text{elec}}$ . The particular choice of the frequencies is also related to the type of AFM probes used in KFM studies. For example, most of the measurements described in this paper were made with conducting Pt-coated Si probes (Olympus), which have a spring constant of 3-5 N/m and the resonance of the first flexural mode in the 60-80 kHz range. Low-frequency of 10 kHz and the second flexural mode of the probes (400-500 kHz) were most often chosen for  $\omega_{\text{elec}}$ . TEM micrographs of these probes showed that their apex has a diameter of 20 nm or less.

In some cases, we also used the T-shaped Si probes (MikroMasch) with the tip being offset from the main cantilever axis. These probes exhibit pronounced torsional motion when the tip comes into interaction with the sample. The torsional resonant frequency (around 700 kHz) was successfully applied as  $\omega_{\text{elec}}$  for KFM imaging of semifluorinated alkanes. It is worth noting that a doping level of these probes was sufficient enough to use them for electrostatic measurements without a conducting coating.

From the analysis of the KFM results it became clear that the operation in the non-contact regime substantially limits its spatial resolution, which is in the range of a few tens of nanometers. The remote positioning of the conducting probe while recording the electrostatic force response is also a feature of the lift mode. The only exception is the KFM measurements performed with FM mode in UHV, where the surface potential images made on atomically smooth surfaces demonstrated atomic-scale features.<sup>28</sup> However this mode is not very suitable for imaging at ambient conditions on corrugated surfaces. The examples of AM imaging in Figures 1A-H demonstrated that when the position of  $A_{\text{sp}}$  changed from the gradual sloped part of the AvZ curve to the steep one (in other words, from the non-contact operation to the intermittent contact regime) the topography image shows well-resolved surface features yet the electrostatic response was lost, most likely, due to the use of the same frequency:  $\omega_{\text{mech}}$ . Therefore, it appears quite intriguing to perform the single-pass KFM measurements at  $\omega_{\text{mech}}$  and  $\omega_{\text{elec}}$  in the intermittent contact regime. One might expect that resolution of the electrostatic force detection in this operation will be improved while cross-talk between topography and the electrostatic force

response might become evident. These features will be of concern in the analysis of KFM applications in the intermittent contact regime, which are shown below. Most of these images were obtained with  $A_0 = 10-15$  nm and  $A_{\text{sp}} = 0.6A_0$  – the parameters, which according to the AvZ curves are unambiguously related to the intermittent contact regime in a low-humidity environment (RH<20%) where the studies were performed.

### KFM in the intermittent contact regime: Practical examples

The first two examples are taken from KFM studies of semiconductor samples: SRAM and a SiGe structure. The topography and surface potential images of the same sample regions show dissimilar patterns, Figures 5 and 6. The locations of different doping types and levels as well as few local defects visualized in surface potential images are clearly different from topographic features. This is confirmed by the cross-section profiles taken in the images along the directions marked with white arrows. Therefore, we conclude that the cross-talk between the topography and the probe response to the electrostatic forces is negligible. In the control experiments we obtained surface potential images of SRAM with different combinations of  $\omega_{\text{mech}}$  and  $\omega_{\text{elec}}$  (first flexural resonance/10 KHz, first flexural resonance/second flexural resonance; second flexural resonance/first flexural resonance). The comparison of the quantitative values in the surface potential profiles showed that the variations did not exceed 10%. As regarding the sensitivity of this approach, the variations as small as 10 mV are distinguished in the surface potential profiles, Figures 5C and 6C. It is also noticeable that surface potential is substantially negative in the SRAM locations and around 0 in the SiGe

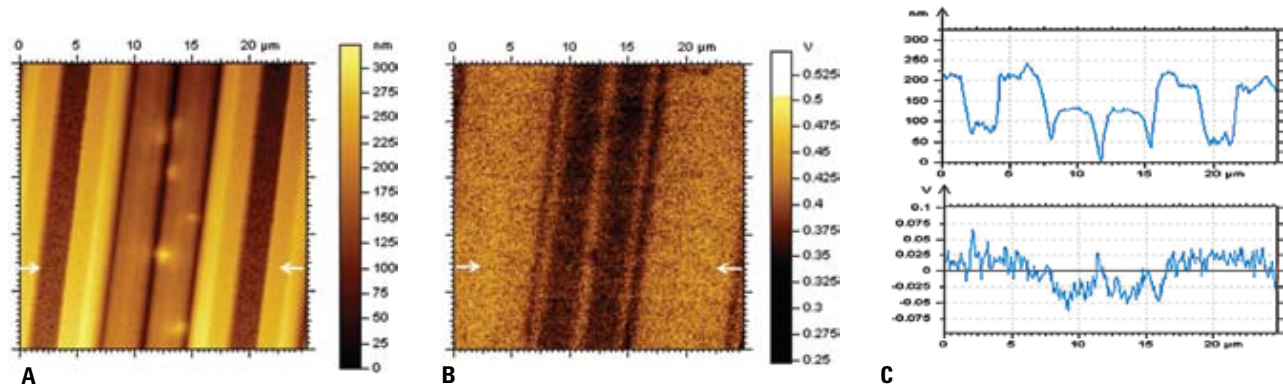


Figure 6A-C. The topography (A) and surface potential (B) images of a SiGe structure. The cross-section profiles along the directions indicated with white arrows in (A) and (B) are shown in the top and bottom parts of (C).

structure. In KFM of semiconductors a correlation between the surface potential as the probe location and surface Fermi level is established by a following equation:

$$(6) E_{Fs} - E_{vac} - V_{probe} - \phi_p,$$

where  $E_{Fs}$  - the surface Fermi level,  $E_{vac}$  - vacuum level,  $V_{probe}$  - surface potential measured by the probe, and  $\phi_p$  - work function of the probe material. Therefore, evaluation of local surface Fermi level is a feasible task in KFM of semiconductor samples,<sup>29</sup> after a proper calibration of the probe, an appropriate sample preparation and thoroughly performed the experiments. These applications are beyond the scope of this paper.

In further evaluation of KFM operation we conducted experiments similar to those described in<sup>10</sup>, which are often used for surface lithography.<sup>30-31</sup> In these experiments, surface charges were deposited by a tip-sample voltage discharge on surface of PMMA and normal alkane  $C_{60}H_{122}$  layers on Si and graphite, respectively. The charges were deposited above the voltage threshold, which is around 5-10 V (depending on a layer thickness and annealing state), and a 2 msec pulse was used. The first pair of images in Figures 7A-B shows the PMMA topography and a circular surface charge pattern with maximum around 1.5 V. In this case, there is no discernible cross-talk between the charge and topography. The situation is different when a higher voltage impulse was applied, Figures 7C-D. The topography image exhibits a pattern of complex shape with negative and positive levels, thus demonstrating a strong involvement of the electrostatic forces in the tracking feedback when the local charge is large, Figure 7D. In other words, the large spatial dimensions and high

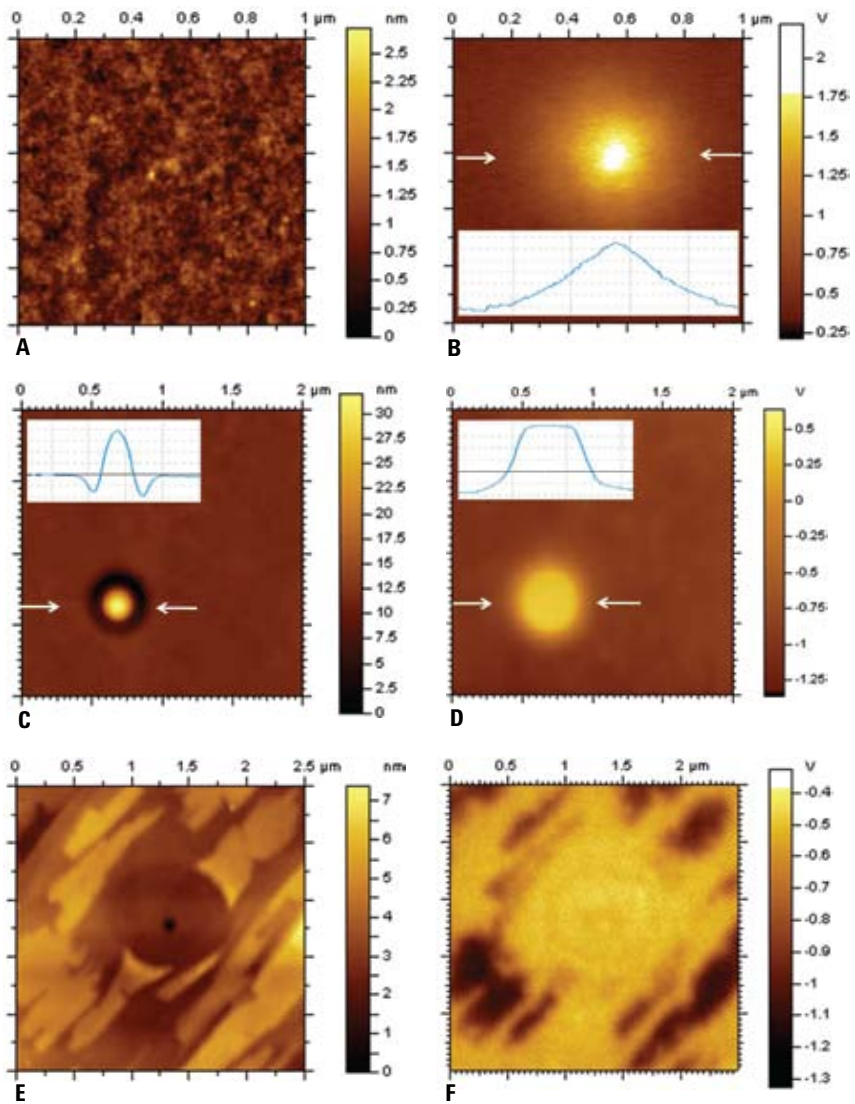


Figure 7A-F. The topography (A, C, E) and surface potential (B, D, F) images of PMMA layers on Si around the locations subjected to tip-voltage pulses. The inserts in the (B-D) show the cross-section profiles along the directions indicated with white arrows. (E) - (F) The topography and surface potential images of normal alkane  $C_{60}H_{122}$  adsorbate on graphite around the location subjected to a tip-voltage pulse.

intensity of the generated charge makes its compensation by the probe voltage inefficient. AFM studies of ultrathin adsorbates of normal alkanes on graphite revealed that the alkanes form lamellar domains in which the chains are aligned parallel to the surface.<sup>32</sup> The voltage pulse applied to the  $C_{60}H_{122}$  layer on graphite induced a circular damage pattern in the adsorbate and even in graphite substrate visible as a hole in the center. The surface potential shows a bright-contrast at the

circular pattern, which can be assigned to the surface potential of the substrate. In addition, dark patterns surrounding the disk-like region represent the generated negative charges on the elevated alkane domains. The negative charges on the alkane domains have persisted for several days. Further high-resolution AFM images (not shown here) demonstrated that the lamellar order of the domains was destroyed and the material of the domains displays a granular morphology. Most

likely, the discharge caused a variety of different chemical processes. Therefore, this approach can be applied not only for lithography but also for local initiation and monitoring of chemical reactions.

The AM imaging of an adsorbate of semifluorinated alkanes  $F_{14}H_{20}$  on graphite (Figures 2A-F) provides subtle clues of a negative charge on the self-assemblies, and these samples were examined with KFM. The topography, phase and surface potential images of this material are shown in Figures 8. The topography image reveals a brighter aggregate among patches of the featureless material lying on a thinner layer of  $F_{14}H_{20}$ , Figure 8A. A small hole with a tiny rim is seen in the bottom right part of the image. It was made by a tip voltage pulse and it was expected that the pulse will ablate the material and expose the graphite surface underneath. The phase image resolves fine structures in the aggregate, which are slightly brighter than the rest of the image, Figure 8B. Otherwise, the phase contrast is fairly homogeneous with the error-signal-like features at the edges of the patches and the hole. The surface potential image, which exhibits several levels of the contrast, is most informative, Figure 8C. First of all, the aggregate exhibits surface potential substantially more negative (up to  $-0.8$  V) than that of the substrate seen at the location in the hole. This is best seen in Figure 8D, which presents the cross-section profiles taken along the directions indicated with white arrows in images A and C. The topography profile traversing the hole shows that the thickness of the patches is only few nanometers. Also, the very dark patches seen in the surface potential image of the aggregate suggest that its constituents might form structures with larger charge. Besides the aggregate and the hole, the contrast of the remainder of the image is more homogeneous with small variations between areas with the featureless adsorbate.

Self-assembly of  $F_{14}H_{20}$  adsorbates results in nanoscale structures of different morphologies (toroids, ribbons, spirals and their intermediates) and various packing motifs<sup>33</sup> that make them attractive for a demonstration of KFM resolution. A region of  $F_{14}H_{20}$  adsorbate on graphite, which is densely populated with deformed toroids and short ribbons, is shown in the topography image in Figure 9A. The

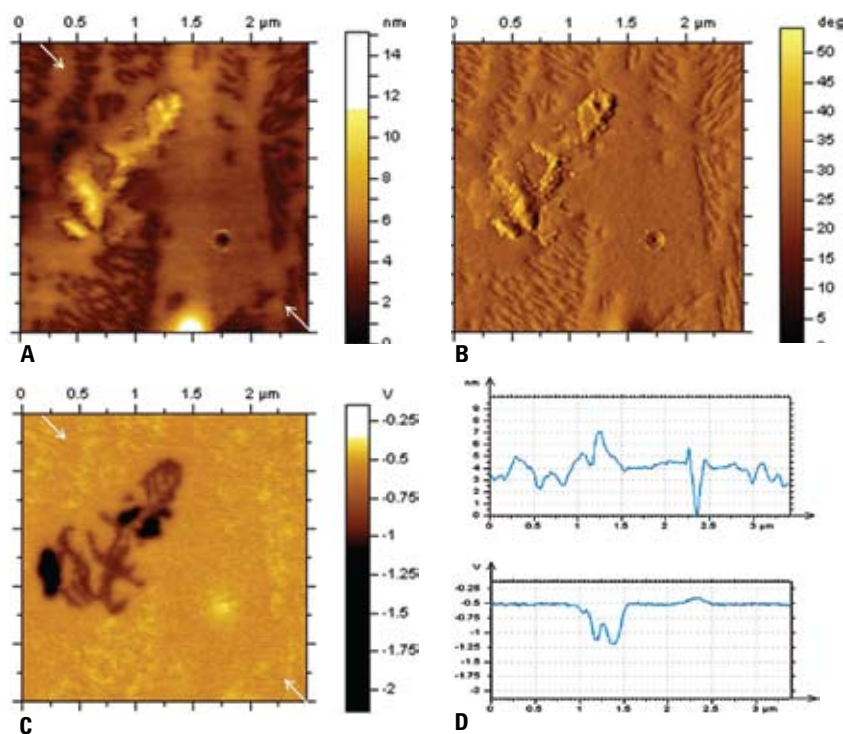


Figure 8A-D. The topography (A), phase (B) and surface potential (C) images of  $F_{14}H_{20}$  adsorbate on graphite. The cross-section profiles taken along the directions shown with white arrows in (A) and (C) are presented in the top and bottom parts of (D), respectively.

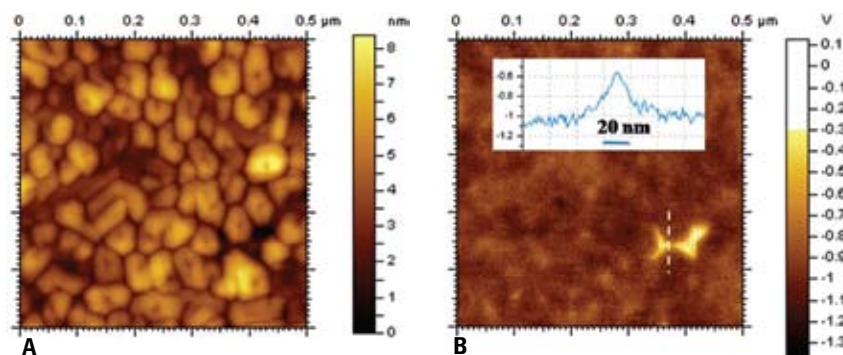


Figure 9A-B. The topography (A) and surface potential (B) images of  $F_{14}H_{20}$  adsorbate on graphite. The insert in (B) shows a cross-section profile along the direction marked with a white dashed line.

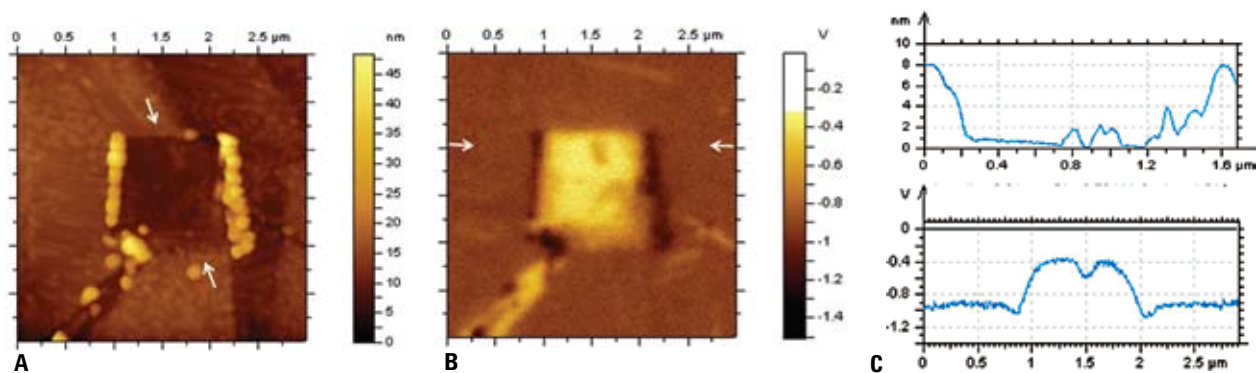


Figure 10A-C. The topography (A) and surface potential (B) images of  $F_{14}H_{20}$  adsorbate on graphite in the area around the “window” made by the AFM tip scanning in the contact mode. The top and bottom graphs in (C) – show the cross-section profiles across this area in (A) and (B), which were taken along the directions marked with white arrows.

surface potential contrast of this area is not very pronounced, except for the bright spot seen at the location, which is closer to the substrate than the rest of the surface, Figure 9B. This is apparently a void in the packing of surface structures. The cross-section profile in the insert of the image indicates that the width of the void is less than 10 nm. This allows us to claim that the spatial resolution of KFM operating in the intermittent contact mode is better than 10 nm. The variations of the contrast between the different self-assembled structures (up to 0.2 V) are much smaller as compared to the 0.8 V average contrast between the void’s location and the rest of the image. The fact that the void contrast is approximately that of the substrate is confirmed by the images and cross-section profiles shown in Figures 10A-C. The topography image in Figure 10A presents a larger area of the  $F_{14}H_{20}$  adsorbate after its central part was removed from the substrate by mechanical abrasion (scanning of this location in the contact mode). This procedure, which is often applied for the evaluation of thickness of adsorbates on different substrates, is also useful in KFM analysis because it provides access to the substrate. The surface potential image in Figure 10B clearly demonstrates that the “window” is  $\sim 0.7$  V higher in potential than the rest of the area. The images and the cross-section profiles in Figure 10C, which were taken along the directions marked with white arrows, show that the adsorbate is  $\sim 8$  nm thick and that mechanical interference of the probe induced the formation of large micelles at the “window” edges and several ribbons inside the “window”. Both the micelles and the ribbons are discernible in the

surface potential image, where they are seen respectively darker and brighter than their immediate surroundings.

Up to this point, we have shown that KFM in the intermittent contact mode is not subject to noticeable cross-talk artifacts and provides sensitive imaging of surface potential with a spatial resolution of 10 nm or better. In studies of semifluorinated alkane  $F_{14}H_{20}$ , KFM distinctively differentiates material’s features and ordered self-assemblies with the latter exhibiting negative surface potential. These applications were performed using the probe amplitude at  $\omega_{elec}$  as a measure of electrostatically-induced tip-sample force interactions. Following the classification given in <sup>34</sup> we will use AM-AM abbreviation for this mode. This abbreviation indicates that AM is used in both feedback loops employed for topography tracking and electrostatic measurements. Another approach to KFM measurements and its use in the intermittent contact regime are introduced below.

### KFM in AM-FM operation with Agilent 5500 microscope

The problem of sensitivity and spatial resolution in the AFM-based electrostatic measurements attracted increasing attention for several years. A thorough consideration of the imaging procedures, optimization of probe and data interpretation was given in <sup>35</sup>. The authors estimated the cantilever, tip cone and tip apex contributions to the electrostatic probe-sample force and force gradient and came to the

conclusion that high spatial resolution can only be achieved when the tip-apex contribution is dominant. This condition can be realized by using probes with a special geometry (the probes with long and sharp tips) or by employment of force gradient detection. The other possibility – imaging at tip-sample distances smaller than 2 nm was expected to be difficult in practice. Higher spatial resolution and higher sensitivity in the force-gradient based KFM was shown in <sup>36</sup> – the paper, in which electrostatic force measurements in AM and FM detection schemes were critically analyzed. Particularly, the surface potential data obtained on a KCI sub-monolayer on Au (111) in FM nicely agree with results of ultraviolet photoelectron spectroscopy. Also in contrast to AM-detection, the surface potential measured with FM did not vary with probe-sample separations in the 30 nm range. The state-of-the-art EFM and KFM were presented in <sup>34</sup> where the AM-AM, FM-AM and FM-FM combinations used for such measurements were mentioned and briefly described. Surprising is the absence of the AM-FM combination despite the above considerations suggesting the high value of FM detection of electrostatic forces. We have implemented this capability in the Agilent 5500 microscope and critically evaluate this mode in studies of a variety of samples in the intermittent contact regime.

The block scheme of the AM-FM mode is presented in Figure 11A. The principal difference of this set-up with the one used for the AM-AM approach (Figure 4A) is that the input of LIA-2 is connected to LIA-1 for measuring the phase data at  $\omega_{\text{mech}}$ . The phase changes are directly related to changes in the force gradient that defines AM-FM type studies. Practically, the AC voltage is applied to the probe at  $\omega_{\text{elec}}$ , which should be within the bandwidth of the LIA-1. The probe response, at the mixed frequency,  $\omega_{\text{mech}}$  and  $\omega_{\text{elec}}$  is detected by LIA-2 and used for KFM feedback. The amplitude sweeps in the “off” and “on” states of the electric servo loop are presented in Figures 11B-C. The electrostatic forces between the cantilever and sample cause the cantilever to deflect at  $\omega_{\text{elec}}$ , and at twice that frequency. The voltage

modulation also causes a modulation of the force gradient which is greatest between the tip and the sample. These changing force gradient causes the resonant frequency of the cantilever to shift giving rise to side bands on the mechanical resonance of the cantilever. After demodulation by LIA-1, the output shows modulation at  $\omega_{\text{elec}}$  and at twice that frequency. The two forms of KFM are similar in that the DC bias has a servo to minimize the  $\omega_{\text{elec}}$  component from the input of LIA-2. The main differences between operation of AM-AM and AM-FM modes are related with choice of  $\omega_{\text{elec}}$ , which in case of AM-FM is limited to low frequency (say 5kHz), low feedback gains of the electric servo loop and to lower AC voltages (usually much less than 1 V). The use of lower voltages is very positive remembering the possible

voltage influence on sample surface electric properties.

There is another implementation of AM-FM combination in which the Y-vector of amplitude is used, instead of the phase signal of LIA-1. When the phase of LIA-1 is adjusted so the amplitude of the cantilever is aligned with the X-component then the tip-sample force interactions can be observed as the Y-component variations. The latter naturally reflect the phase signal, which is calculated using the X- and Y-component data. Therefore, for improved signal-to-noise ratio it might be worth using just the Y-component. Practically, with LIA-1 set to  $\omega_{\text{mech}}$  one needs to maximize the X-component and make the Y-component close to zero. Then, the Y component should be directed to LIA-2 and the electric servo loop.

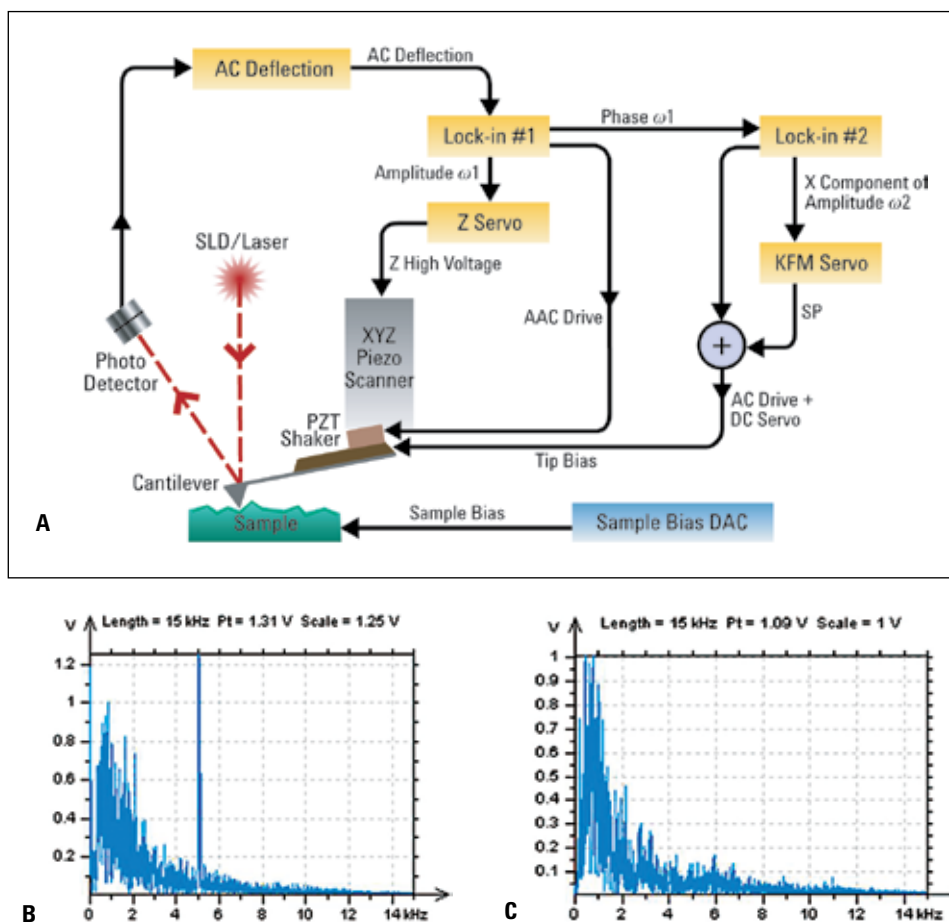


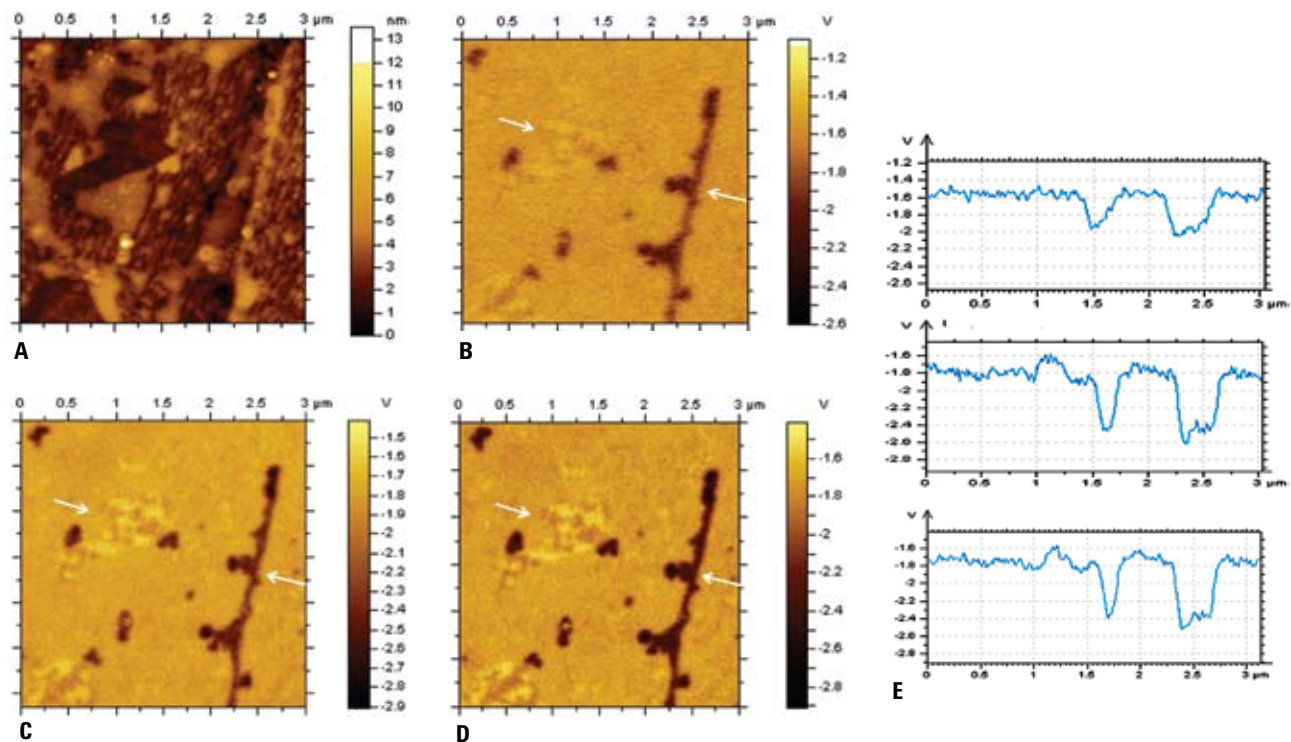
Figure 11A-C. A block-diagram of the implementation of KFM in Agilent 5500 scanning probe microscope using the MACIII accessory. (B)-(C) Amplitude-vs-frequency sweeps of LIA-2 signal (X-component of amplitude) with the electric servo loop in the “off” and “on” states, respectively.

### KFM with AM-FM operation in the intermittent contact: Practical results

After implementation of AM-FM approach in KFM we have checked the value of the phase- and Y-component-based operations by comparing these modes and AM-AM approach in the intermittent contact imaging of  $F_{14}H_{20}$  adsorbate, Figures 12A-E. The chosen sample of  $F_{14}H_{20}$  adsorbate has many of heterogeneities due to partial self-assembly of the material into individual micelles and their aggregates. As expected from our AM-AM studies the

self-assemblies exhibits strong surface potential contrast what indeed is noticed in the images obtained with all three modes, Figures 12B-D. The comparison of the images and also the surface potential profiles shown in Figure 12E demonstrates the favorability of AM-FM approaches in studies of semifluorinated alkanes. The images in Figures 12C-D exhibit higher contrast, and therefore resolution than the image in Figure 12B. Particularly, a visualization of the patches in the top right parts of the images is the best illustration. The cross-section profiles also show that the values of the surface potential are

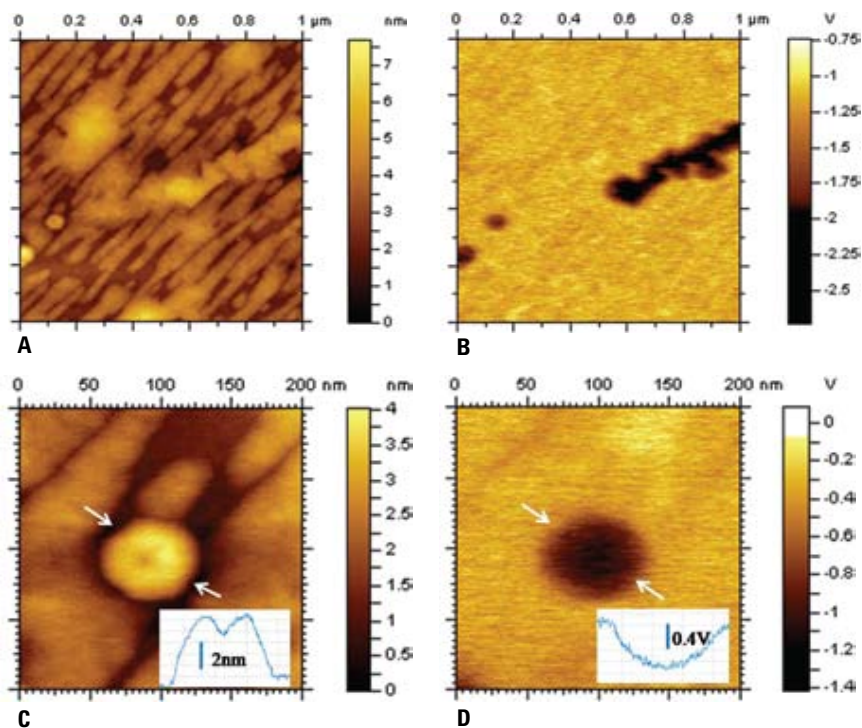
higher in AM-FM modes compared to the AM-AM. As expected the surface potential signal obtained with the phase-based and Y-component-based operations are quantitatively the same but the signal-to-noise ratio is definitely improved in the Y-component-based operation. Most likely the values of the surface potential in the 0-1.0 V range obtained in the AM-FM studies are defining surface charges more precisely than the potential data obtained in the AM-AM operation similar to the findings in<sup>36</sup>.



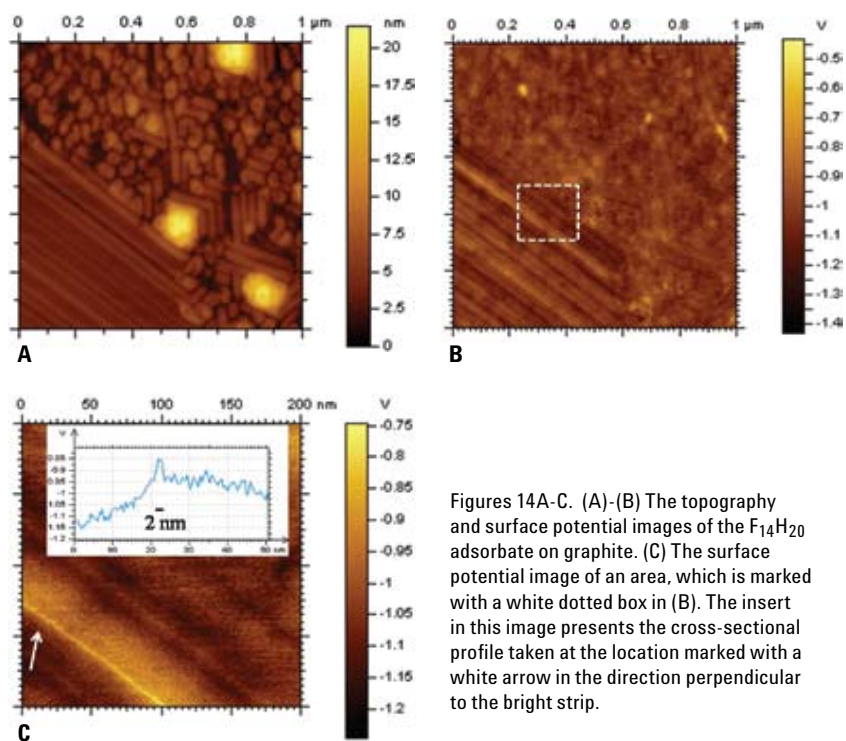
Figures 12A-E. The topography (A) and surface potential (B) images of  $F_{14}H_{20}$  adsorbate on graphite obtained in the AM-AM operation. (C)-(D) Surface potential images of the same location as in (A) and (B) obtained in AM-FM operation with the phase and the Y-component signals for the electric servo loop. (E) The cross-section profiles taken along the direction indicated with white arrows in (B) – top, (C) – middle, (D) – bottom.

In an attempt to determine the spatial resolution of KFM in the AM-FM operation we further examined  $F_{14}H_{20}$  adsorbates at scales of 1 micron and smaller, and the results, which were obtained in the phase-based AM-FM operation, are collected in Figures 13 and 14. The images in Figures 13A-D show an aggregate of self-assembled structures and a single toroid less than 50 nm in diameter. As expected the aggregate, which consists of a number of toroids and other elementary self-assemblies exhibits strong negative contrast ( $\sim -1.0V$ ) even larger than that of the toroid ( $\sim -0.8V$ ). Remarkably, the other adsorbate patches being of comparable size and height to the self-assembled aggregate do not exhibit any noticeable variations of surface potential. The toroid, which is presented in the images in Figures 13C-D, has a height of  $\sim 3.2$  nm and surface potential of  $\sim 0.8V$ . The latter is consistent with surface potential of a Langmuir-Blodgett layer of similar compound determined with a macroscopic Kelvin probe.<sup>37</sup> The toroid is most likely formed of extended molecules (contour length 4.6 nm) with fluorinated groups pointed away from the surface. At the toroid edges, the hydrocarbon segments are bending towards the surface to compensate the mismatch of electron density in the hydrocarbon and fluorinated structures. Therefore, the  $-CF_2-CH_2-$  dipole orientation towards the substrate is primarily responsible for the surface charges observed in KFM. Self-assemblies of  $F_{14}H_{20}$  and other semifluorinated alkanes  $F_nH_m$  have been under examination for some time. Despite the fact that a number of techniques (X-ray reflectivity, AFM, surface IR techniques and a macroscopic Kelvin probe) were applied to examination of molecular arrangements in these nanostructures their molecular architecture is still not clarified.<sup>38-40</sup> In the ongoing KFM studies of  $F_{14}H_{20}$  and related compounds we examined their self-assemblies on different substrates and in different environments in pursuit of a better understanding of their structures and behavior.<sup>41</sup>

As regarding the KFM resolution we point out fine features in the sub-10 nm range, which were observed in the topography and surface potential images of the  $F_{14}H_{20}$  adsorbate, Figures 14A-C. This area is filled by the toroids and self-assembled ribbons. The surface potential of the



Figures 13A-D. The topography (A, C) and surface potential (B, D) images of  $F_{14}H_{20}$  adsorbate on graphite obtained in the AM-FM operation. The inserts in (C-D) show the cross-section profiles taken along the directions indicated with white arrows.



Figures 14A-C. (A)-(B) The topography and surface potential images of the  $F_{14}H_{20}$  adsorbate on graphite. (C) The surface potential image of an area, which is marked with a white dotted box in (B). The insert in this image presents the cross-sectional profile taken at the location marked with a white arrow in the direction perpendicular to the bright strip.

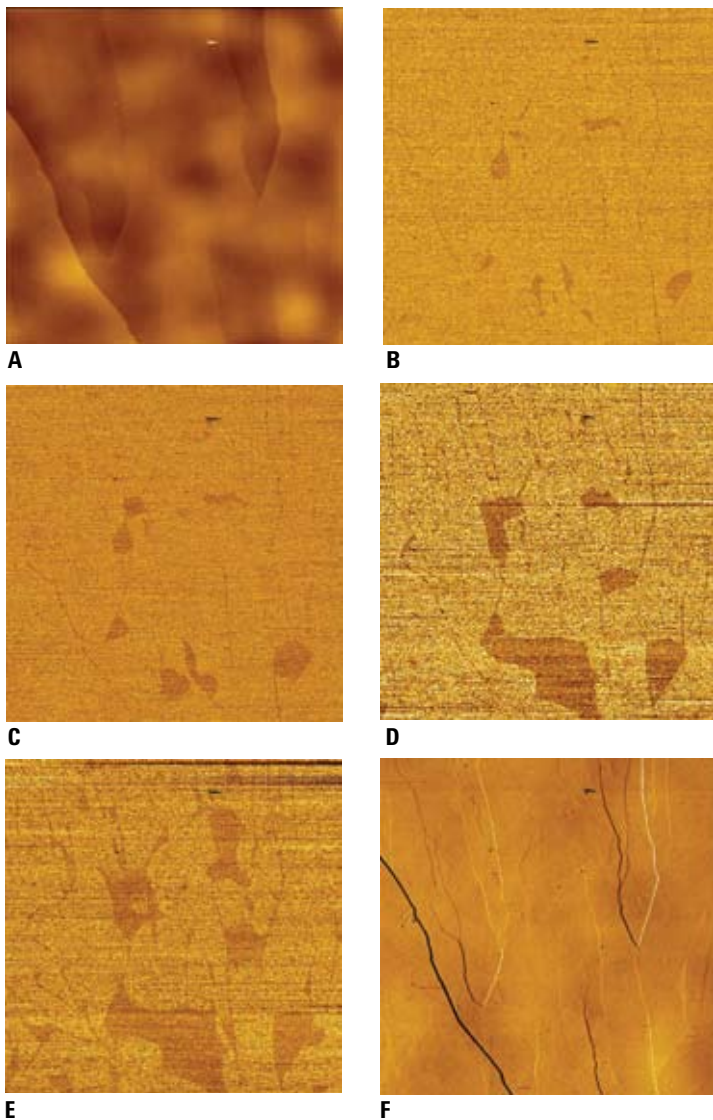


ribbons is only slightly different from that of the toroids, similar to the observations in Figure 8B. Nevertheless, there are few locations with very pronounced contrast: the voids between the toroids and the slits between the ribbons. At these locations the probe “feels” the substrate better than elsewhere. The high-resolution surface potential images of the area outlined with a red dotted square is given in Figure 14C. The insert shows the profile across one of the slits in the location pointed with

a white arrow. The width of the 0.1 V peak seen in this profile is around 2 nm that can be used as a measure of spatial resolution of KFM AM-FM operation in the intermittent contact mode. This result suggests that the sensing apex area of the AFM probe, which is much smaller than the tip diameter (~20 nm), dominates in the electrostatic measurements. The achieved high-resolution is in line with the expectation of<sup>35</sup> where the force-gradient detection combined with a small

tip-sample distance was advocated as a way to enhance resolution. The use of sharper conducting probes might help to increase the resolution further.<sup>42</sup>

In exploring the use of KFM for the mapping of surface heterogeneities we conducted long-term imaging of a freshly-cleaved sample of graphite. Several images of the series are documented in Figures 15A-F. The topography and surface potential images taken 2 hours after the cleavage show a surface region with several steps of graphite planes (Figure 15A) and few dark patches with different potential. Such patches were not seen at shorter times after the cleavage and, therefore, they are assigned to air-borne contamination deposited on the surface. As time progresses, these patches increased in size, and new patches originated as well. This process is visible in the images in Figures 15C, D, E, which were recorded in 15 minutes intervals after the ones in Figures 15A-B. The difference of the potentials of the fresh and contaminated surfaces was ~60 mV and did not change as the contamination grows. At longer times the contamination has covered the entire area and the surface potential image becomes homogeneous again. Remarkably, phase images were not as sensitive to the growing contamination as the surface potential images. The phase image in Figure 15F is the first in which the patches became distinguishable. The simultaneously recorded surface potential image revealed the contamination areas in more pronounced way, Figure 15E. KFM images of freshly prepared Au (111) also showed a contamination traces at the edges of gold terraces.<sup>43</sup> Our data demonstrate the high-sensitivity of KFM to the air-borne contamination of the substrates often used in AFM. These results should be considered by researchers using these substrates.

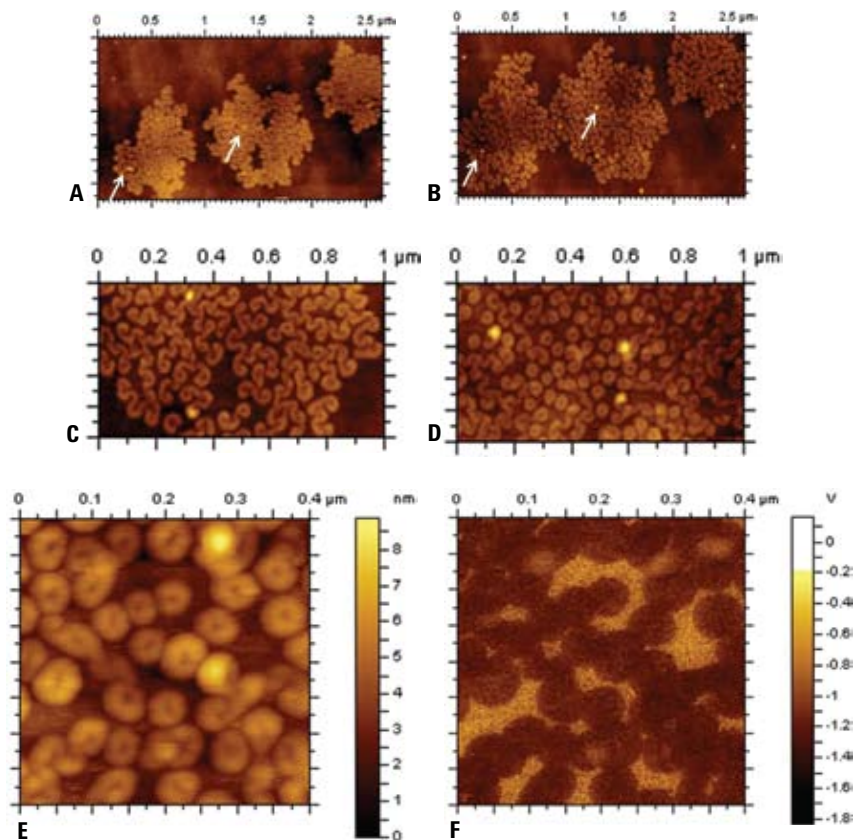


Figures 15A-F. (A)-(B) The topography and surface potential images of graphite 2 hr after cleavage. (C)-(D) The surface potential images of graphite 2.25 and 2.5 hr after the cleavage. (E)-(F) The surface potential images of graphite 2.75 hr after cleavage. Scan size: 20  $\mu\text{m}$ .

As the final example of KFM capabilities we chose the images of  $F_{14}H_{20}$  adsorbate on Si substrate (Figures 16A-F), which were collected when the sample was held in humid atmosphere in the environmental chamber of an Agilent 5500 microscope. The experiments lasted over two days, and the changes in surface topography that happened after the first 24 hours are shown in Figures 16A-B. Three domains consisting of spiral self-assemblies have substantially expanded in the lateral dimensions as evidenced by the reference positions of two contamination features indicated with white arrows. The spiral self-assemblies loosen their initial tight packing inside the domains and the individual spirals became well-separated from their neighbors as clearly seen in Figure 16C. Three factors should be considered in the tentative explanation of this observation. They include the negative charge of individual spirals, an influence of humidity on their adhesion to the substrate and the possible tip-force involvement in the spirals' motion. More changes occurred after the 48 hours exposure of the sample to humid environment as many spirals have converted into individual toroids, Figures 16C-D. Surprisingly, this process, which was noticed in vapors of organic solvents,<sup>32</sup> can also take place in a humid atmosphere. The topography and surface potential images of an array of  $F_{14}H_{20}$  toroids are shown in Figures 16E-F. The surface potential of the toroids in humid air (-0.4 V) is much smaller than in dry air. One might suspect a partial shielding of surface charges similar to the non-contact KFM observations of semiconductor samples.<sup>44</sup> However, this effect is expected to be less when KFM studies are performed in the intermittent contact regime. This problem will be further explored.

## Conclusions

This paper describes KFM operations using an Agilent 5500 scanning probe microscope enhanced with a MACIII accessory that allows multi-frequency AFM measurements with 3 dual phase lock-in amplifiers. Instrumental set-ups allowing force- and force-gradient-based KFM studies (AM-AM and AM-FM) are described and the value of these approaches is verified in studies of the doped areas of semiconductor samples, surface charges created on organic layers by voltage discharge, the contamination traces on graphite and self-assemblies of semifluorinated alkanes  $F_{14}H_{20}$  on graphite and Si substrates in dry and humid air. The



Figures 16A-F. (A)-(B) The topography images of  $F_{14}H_{20}$  adsorbates on Si substrate after the sample was placed in humid air and after 24 hr exposure to humid air, respectively. (C)-(D) The topography images of  $F_{14}H_{20}$  adsorbates on Si substrate after 24 hr and 48 hr exposure to humid air, respectively. (E)-(F) The topography and surface potential images of the sample shown in (D). All images were collected in humid air.

novelty of these applications is that they were performed in the intermittent contact regime and the AM-FM combination was introduced. The simultaneous and independent measurements of sample topography and surface potential (as small as 10 mV) were successfully demonstrated in these single-pass KFM studies. The comparative studies of  $F_{14}H_{20}$  self-assemblies with AM-AM and AM-FM demonstrated that the AM-FM operation provide higher and, likely more accurate values of surface potential of these nanostructures. Remarkably, the AM-FM approach in the intermittent contact mode led to high-resolution surface potential measurements where the 2-nm wide features were clearly resolved. We undertook only the first steps in the practical evaluation of new capabilities offered by KFM studies and there are several opened questions to clarify. They include finding of ways of reproducible and precise measurements of surface local work functions, development of better probes that are fully conducting

with 1 nm apex size, expanding KFM measurements to different environments and various temperatures and others. Furthermore, the discussed results were obtained in the intermittent contact mode at relatively small tip-sample interactions when phase images do not exhibit the pronounced contrast related to variations of local mechanical properties. It might be quite informative to perform KFM imaging at elevated tip-sample force, i.e. in the repulsive force regime to get simultaneously topography and maps of local electric and mechanical properties as was recently suggested.<sup>45</sup>

## Acknowledgements

We are thankful to Prof. M. Moeller (RWTH, Aachen, Germany) for providing us with a sample of semifluorinated alkane,  $F_{14}H_{20}$ . The sample of  $LiNbO_3$  with Ag particles is a kind gift from the laboratory of R. Nemanich (ASU, Tempe, AZ, USA).

## References

1. G. Binnig, C.F. Quate, and Ch. Gerber "Atomic force microscope" *Phys. Rev. Lett.* **1986**, *56*, 930-933.
2. Y. Martin, C.C. Williams, and H.K. Wickramasinghe "Atomic force microscope-force mapping and profiling on a sub 100-Å scale" *J. Appl. Phys.* **1987**, *61*, 4723-4729.
3. Q. Zhong, D. Innis, K. Kjoller, V. Elings "Fractured Polymer/Silica Fiber Surface Studied by Tapping Mode Atomic Force Microscopy" *Surf. Sci. Lett.* **1993**, *290*, L688-L692.
4. T. Albrecht, P. Grutter, D. Horne, and D. Rugar "Frequency modulation detection using high-Q cantilevers for enhanced force microscopy sensitivity" *J. Appl. Phys.* **1991**, *61*, 668-673.
5. T. Fukuma, T. Ichii, K. Kobayashi, H. Yamada, and K. Matsushige "True-molecular resolution imaging by frequency modulation atomic force microscopy in various environments" *Appl. Phys. Lett.* **1995**, *86*, 034103-034105.
6. S. Magonov "AFM in Analysis of Polymers" in *Encyclopedia of Analytical Chemistry*, (R. A. Meyers, Ed.), pp. 7432-7491, John Wiley & Sons Ltd., Chichester, **2000**.
7. M. Bai, S. Trogisch, S. Magonov, and H. Taub "Explanation and correction of false step heights in amplitude modulation atomic force microscopy measurements on alkane films" *Ultramicroscopy*, **2008**, *108*, 946-952.
8. V.B. Elings, and J.A. Gurley "Scanning probe microscope using stored data for vertical probe positioning" US Patent 5,308,974, **1994**.
9. Y. Martin, D.A. Abraham, and H. K. Wickramasinghe "High-resolution capacitance measurement and potentiometry by force microscopy" *Appl. Phys. Lett.* **1988**, *52*, 1103-10005.
10. J.E. Stern, B.D. Terris, H.J. Mamin, and D. Rugar "Deposition and imaging of localized charge on insulator surfaces using a force microscope" *Appl. Phys. Lett.*, **1988**, *53*, 2717-2719.
11. B.D. Terris, J.E. Stern, D. Rugar, and H.J. Mamin "Localized charge force microscopy" *J. Vac. Sci. Technol.* **1990**, *A8*, 374-377.
12. T. Ohta, Y. Sugawara, and S. Morita "Feasibility study on a Novel Type of Computerized Tomography Based on Scanning Probe Microscope" *Jpn. J. Appl. Phys.* **1996**, *35*, L1222-L1224.
13. J.M.R. Weaver and D.W. Abraham, "High-resolution atomic force microscopy potentiometry" *J. Vac. Sci. Techn.* **1991**, *B9*, 1559-1561.
14. M. Nonnenmacher, M.P. O'Boyle, and H.K. Wickramasinghe "Kelvin probe force microscopy" *Appl. Phys. Lett.* **1991**, *58*, 2921-2923.
15. H. Yokoyama and M.J. Jeffery "Imaging high-frequency dielectric dispersion of surfaces and thin films by heterodyne force-detected scanning Maxwell stress microscopy" *Colloids Surf. A* **1994**, *93*, 359-373.
16. M. Fujihira "Kelvin probe force microscopy of molecular surfaces" *Annu. Rev. Mater. Sci.* **1999**, *29*, 353-380.
17. M. Luna, D.F. Ogletree, and M. Salmeron "A study of the topographic and electric properties of self-assembled islands of alkylsilanes on mica using a combination of non-contact force microscopy techniques" *Nanotechnology* **2006**, *17*, S178-S184.
18. L. Buergi, H. Sirringhaus, and R.H. Friend "Noncontact potentiometry of polymer field-effect transistors" *Appl. Phys. Lett.* **2002**, *80*, 2913-2916.
19. K.P. Puntambekar, P.V. Pesavento, and C.D. Friesbie "Surface potential profiling and contact resistance measurements on operating pentacene thin-film transistors by Kelvin probe microscopy" *Appl. Phys. Lett.* **2003**, *83*, 5539-5541.
20. M. Chiesa, L. Buergi, J.-S. Kim, R. Shikler, R.H. Friend and H. Sirringhaus "Correlation between surface photovoltage and blend morphology in polyfluorene-based photodiodes" *Nano Letters* **2005**, *5*, 559-563.
21. T. Glatzel, H. Hoppe, N.S. Sariciftci, M.Ch. Lux-Steiner, and M. Komiyama "Kelvin probe force microscopy study of conjugated polymer/fullerene organic solar cells" *Jpn. J. Appl. Phys.* **2005**, *44*, 5370-5373.
22. O.A. Semenikhin, L. Jiang, K. Hashimoto, and A. Fujishima "Kelvin probe force microscopic study of anodically and cathodically doped poly-3-methylthiophene" *Synthetic Metals* **2000**, *110*, 115-222.
23. E. Perez-Garcia, J. Abad, A. Urbina, J. Colchero, and E. Palacios-Lidon "Surface potential domains on lamellar P3OT structures" *Nanotechnology* **2008**, *19*, 065709 (6).
24. M. Fujihira, and H. Kawate "Scanning surface potential microscope for characterization of Langmuir-Blodgett films" *Thin Solid Films* **1994**, *242*, 163-169.
25. H. Sugimura, K. Hayashi, N. Saito, O. Takai, and N. Nakagiri "Kelvin probe force microscopy images of microstructured organosilane self-assembled layers" *Jpn. J. Appl. Phys.* **2001**, *40*, 4373-4377.
26. T. Inoue, and H. Yokoyama "Imaging of surface electrostatic features in phase-separated phospholipid monolayers by scanning Maxwell stress microscopy" *J. Vac. Sci. Technol. B* **1994**, *12*, 1569-1571.
27. J. Alexander, S. Magonov, Technical Support Note, Agilent, Chandler AZ, **2008**.
28. S. Kitamura, K. Suzuki, M. Iwatsuki, and C.B. Mooney "Atomic-scale variations in contact potential difference on Au/Si(111) 7×7 surface in ultrahigh vacuum" *Appl. Surf. Sci.* **2000**, *157*, 222-227.
29. T. Matsukawa, S. Kanemaru, M. Masahara, M. Nagao, H. Tanoue, and J. Itoh "Doping diagnosis by evaluation of the surface Fermi level using scanning Maxwell-stress microscopy" *Appl. Phys. Lett.* **2003**, *82*, 2166-2168.
30. P. Mesquida, and A. Stemmer "Attaching Silica Nanoparticles from Suspension onto Surface Charge Patterns Generated by a Conductive Atomic Force Microscope Tip" *Adv. Mater.* **2001**, *13*, 1395-1398

31. R.V. Martinez, N.S. Losilla, J. Martinez, Y. Huttel, and R. Garcia "Patterning Polymeric Structures with 2 nm Resolution at 3 nm Half Pitch in Ambient Conditions" *Nano Letters* **2007**, *7*, 1846-1850.
32. S.N. Magonov, and N. Yerina "High Temperature Atomic Force Microscopy of Normal Alkane C<sub>60</sub>H<sub>122</sub> Films on Graphite" *Langmuir* **2003**, *19*, 500-504.
33. A. Mourran, B. Tartsch, M. Gallyamov, S. Magonov, D. Lambrea, B.I. Ostrovskii, I.P. Dolbnya, W.H. de Jeu, and M. Moeller "Self-assembly of the perfluoroalkyl-alkane F<sub>14</sub>H<sub>20</sub> in ultrathin films" *Langmuir* **2005**, *21*, 2308-2316.
34. M. Nakamura, and T. Yamada in "Roadmap 2005 of Scanning Probe Microscopy" ed. S. Morita, Ch.6 "Electrostatic Force Microscopy" pp. 43-51, Springer, (Springer, Berlin, **2006**).
35. J. Colchero, A. Gil, A.M. Baro "Resolution enhancement and improved data interpretation in electrostatic force microscopy" *Phys. Rev. B* **2001**, *64*, 245403 (11).
36. U. Zerweck, CH. Loppacher, T. Otto, S. Grafstroem, and L.M. Eng "Accuracy and resolution limits of Kelvin probe force microscopy" *Phys. Rev. B* **2005**, *71*, 125424 (10).
37. A. El Abed, M-C. Faure, E. Pouzet, and O. Abilon "Experimental evidence for an original two-dimensional phase structure: An antiparallel semifluorinated monolayer at the air-water interface" *Phys. Rev. E* **2002**, *5*, 051603 (4).
38. T. Kato, M. Kameyama, M. Eahara, and K. Iimura "Monodisperse Two-Dimensional Nanometer Size Clusters of Partially Fluorinated Long-Chain Acids" *Langmuir* **1998**, *14*, 1786-1798.
39. Y. Ren, K. Iimura, A. Ogawa, and T. Kato "Surface micelles of CF<sub>3</sub>(CF<sub>2</sub>)<sub>7</sub>(CH<sub>2</sub>)<sub>10</sub>COOH on aqueous La<sup>3+</sup> subphase investigated by atomic force microscopy and infrared spectroscopy" *J. Phys. Chem. B* **2001**, *105*, 4305-4312.
40. M. Maaloum, P. Muller, and M.P. Krafft "Monodisperse surface micelles of nonpolar amphiphiles in Langmuir monolayers" *Angew. Chem.* **2002**, *114*, 4507-4510.
41. J. Alexander, S. Magonov, M. Moeller "Topography and Surface Potential in Kelvin Force Microscopy of Perfluoroalkyl Alkanes Self-Assemblies" *JVST*, **2008**, submitted.
42. M. Zhao, V. Sharma, H. Wei, R.R. Birge, J.A. Stuart, F. Papadimitrakopoulos and B.D. Huey "Ultrasharp and high aspect ratio carbon nanotube atomic force microscopy probes for enhanced surface potential imaging" *Nanotechnology* **2008**, *19*, 235707 (7)
43. J. Alexander, and S. Magonov "Exploring organization of amphiphilic compounds with atomic force microscopy" Proceedings of X. Annual AFM Winter Workshop, Linz, **2008**, in press.
44. H. Sugimura, Y. Ishida, K. Hayashi, O. Takai, and N. Nakagiri "Potential shielding by the surface water layer in Kelvin probe force microscopy" *Appl. Phys. Lett.* **2002**, *80*, 1459-1461.
45. R.W. Stark, N. Naujoks, and A. Stemmer "Multifrequency electrostatic force microscopy in the repulsive regime" *Nanotechnology* **2007**, *18*, 0655023 (7).

# Agilent 5600LS AFM High-resolution Imaging Molecular-level Understanding of n-Alkanes Self-Assembly onto Graphite

## Application Note

Jing-jiang Yu, Ph.D.  
Agilent Technologies

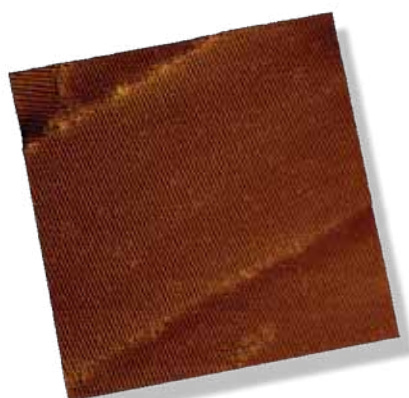


Figure 1. AFM topographic image of n-C<sub>36</sub>H<sub>74</sub> on graphite. Scan size: 350 nm × 350 nm.

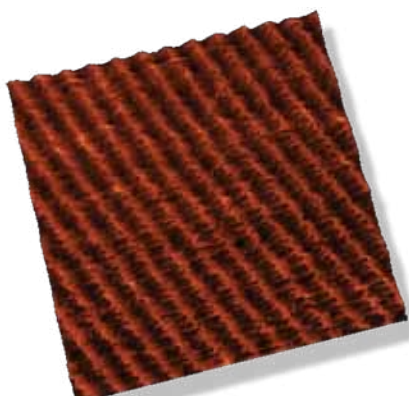


Figure 2. AFM topographic image of n-C<sub>36</sub>H<sub>74</sub> on graphite. Scan size: 55 nm × 55 nm.

The adsorption of organic molecules from solution onto a solid surface has attracted tremendous attention as it is fundamentally associated to many phenomena of both industrial and academic relevance. Governed by an intricate balance between adsorbate-substrate and adsorbate-adsorbate interactions, spontaneous self-organization of molecules at the interface may lead to the formation of delicate ultrathin films with nanometer-scale ordered surface structures due to the molecular-level packing in a particular way. Various techniques have been reported to investigate those organic layers. For instance, differential scanning calorimetry (DSC) provides an effective means to probe the surface phase behavior. The structural information normal to the interface, to some extent, can be extracted from neutron reflectivity measurements. So far, the real time 3D structural characterization with atomic or molecular scale details of the assemblies especially the top layer comes mainly from scanning probe microscopy techniques.

In this application brief, the capability of atomic force microscopy (AFM) to directly visualize soft thin film materials with true molecular resolution is demonstrated using self-assembly of n-C<sub>36</sub>H<sub>74</sub> molecules on graphite as an example. All the data displayed here are acquired from an Agilent 5600LS system with a 90 μm large scanner. A typical AFM topographic image of n-C<sub>36</sub>H<sub>74</sub> upon adsorption on HOPG is shown in Figure 1, from which rich information about this sample is revealed. First, molecules are aligned on the substrate with long-range

order and exhibit a striped morphology. Second, existence of local defect areas is captured. As can be seen, the whole image is divided into four segments by two long and one short domain boundaries and a protrusion island is observed near the bottom location. Those surface features correspond to adsorbed molecules in an amorphous state. Third, two different orientations of the molecular packing are identified. The stripes in the left-upper corner are exactly 60° rotated with respect to those in the remaining three domains, reflecting the impact of underneath substrate (i.e., the 6-fold symmetry graphite) on n-C<sub>36</sub>H<sub>74</sub> alignment on the surface. Figure 2 is another n-C<sub>36</sub>H<sub>74</sub> / graphite topography image with a larger magnification to deliver important information at single molecular level. It shows that the stripe width is about 4.5 nm, which is matching well with the molecular length of n-C<sub>36</sub>H<sub>74</sub> with a fully extended configuration. Furthermore, the linear backbones (i.e., hydrocarbon chains with an all-tans configuration) of individual n-C<sub>36</sub>H<sub>74</sub> molecules are resolved at lower part of the image. These results unambiguously illustrate that n-C<sub>36</sub>H<sub>74</sub> molecules are lying down and orderly aligned on graphite to form a lamellar packing structure.

In conclusion, AFM is a powerful surface characterization tool with an unprecedented high-resolution. Materials surface structures with sub-5 nm size in lateral dimensions can be resolved clearly, thus making it possible to achieve molecular-level understanding of the adsorption behavior of long-chain molecules at the solid-solution interface.

# Several Aspects of High Resolution Imaging in Atomic Force Microscopy

## Application Note

Sergei Magonov  
Agilent Technologies

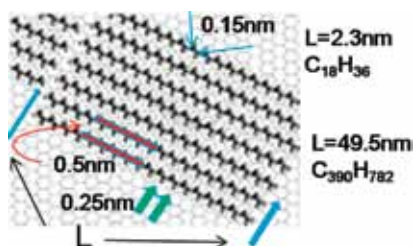


Figure 1. Sketch showing lamellar and molecular order of normal alkane on graphite.

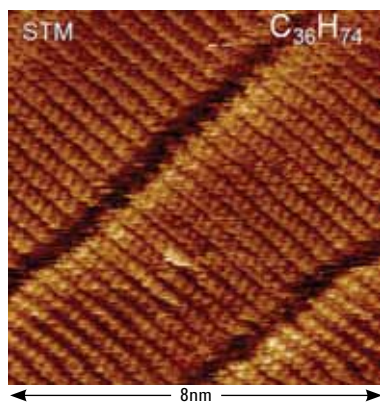


Figure 2. STM image of C<sub>36</sub>H<sub>74</sub> alkanes on graphite.

High-resolution imaging has been the primary feature that attracted the researchers' attention to scanning probe microscopy yet there are still a number of outstanding questions regarding this function of scanning tunneling microscopes and atomic force microscopes. Here I would like to address a few related issues starting with AFM imaging of alkane layers on graphite. Normal alkanes (chemical formula C<sub>n</sub>H<sub>2n+2</sub>) are linear molecules with a preferential zigzag conformation of the -CH<sub>2</sub>- groups. The terminal -CH<sub>3</sub> groups are slightly larger than -CH<sub>2</sub>- groups but more mobile. At ambient conditions the alkanes with  $n=18$  and higher are solid crystals (melting temperature of C<sub>18</sub>H<sub>38</sub> – 28°C) with the chains oriented practically vertical to the larger faces of the crystals. Such surface of the C<sub>36</sub>H<sub>74</sub> crystal, which is formed of -CH<sub>3</sub> groups, was examined in contact mode, and the AFM images revealed the periodical arrangement of these groups [1]. It has been known for a long time that on the surface of graphite the alkane molecules are assembled in flat-laying lamellar structures, in which the fully extended molecules are oriented along three main graphite directions, Fig. 1. This molecular order is characterized by a number of periodicities: the 0.13 nm spacing between the neighboring carbon atoms, the 0.25 nm spacing between the -CH<sub>2</sub>- groups along the chain in the zigzag conformation, the 0.5 nm interchain distance inside the lamellae and the lamellae width—the length of the extended C<sub>n</sub>H<sub>2n+2</sub> molecule. The latter varies from 2.3 nm for C<sub>18</sub>H<sub>38</sub> to 49.5 nm for C<sub>390</sub>H<sub>782</sub> (the longest alkane synthesized).

The alkane adsorbates on graphite were first examined with STM [2]. In such experiments a droplet of saturated alkane solution is deposited on graphite surface and the metallic tip penetrates this droplet and a molecular adsorbate at the liquid-solid interface until it detects a tunneling current. At these conditions the tip is scanning over the ordered molecular layer in immediate vicinity of the substrate. Such STM images of normal alkanes on graphite (as one reproduced from the paper [3] and presented in Fig. 2) clearly demonstrate the fine details of the molecular arrangement such as the lamellar edges, individual chains inside lamellae and the zigzag conformation of the alkane chains. A specific feature of the STM imaging at the liquid-solid interface is that the probe is surrounded by the alkane saturated solution. Any instability of the imaging and the use of low tunneling gap resistance cause a mechanical damage of the alkane order, and the probe might record the image of the underlying graphite. If the gap is increased again the alkane order is restored due to a pool of the alkane molecules. It is practically impossible to get STM images of "dry" alkane layers on graphite because an occasional damage of the layer will be non-repairable.

Studies of dry alkane layers on graphite can be performed with AFM but the "STM" resolution of the lamellae arrangement has not been achieved so far. Initially, the lamellar adsorbates of C<sub>60</sub>H<sub>122</sub> on graphite were examined in amplitude modulation mode and the spacing of 7.6 nm on different lamellar planes and multilayered structures is

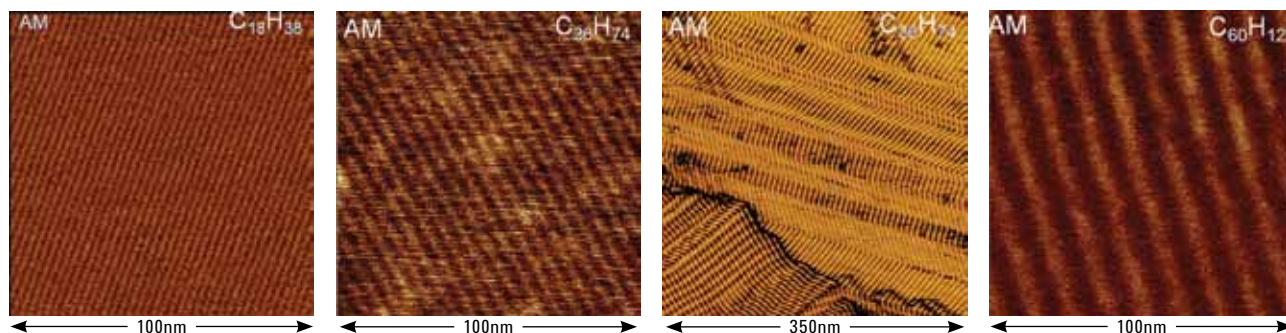


Figure 3. AFM images of normal alkanes on graphite obtained in amplitude modulation mode.

clearly seen in the images [4]. These periodical structures can be employed for the X- and Y- axis calibration of the scanners in lack of the standards for the few nanometers range. For a while the detection of such images was considered as the demonstration of the high resolution imaging by a particular scanning probe microscope. The visualization of the 7.6-nm strips is not challenging anymore and getting images of smaller lamellar structures of  $C_{36}H_{74}$  (4.5 nm spacing) and  $C_{18}H_{38}$  (2.3 nm spacing) can be considered as proof of the microscope performance and the operator experience. Typical AFM images of  $C_{18}H_{38}$ ,  $C_{36}H_{74}$  and  $C_{60}H_{122}$  lamellae on graphite obtained with the 5500 microscope are shown in Fig. 3. The lamellar edges are clearly resolved in these images. The origin of the contrast is the difference of the effective stiffness of the lamellar core ( $-CH_2-$  sequences) and its edges ( $-CH_3$  and nearby  $-CH_2-$  groups). A complex pattern of  $C_{36}H_{78}$  lamellae seen in the 350-nm image is caused by the grains of the substrate and peculiarities of the chain order inside lamellae. In some sample preparations the neighboring chains are shifted to better accommodate the bulky  $-CH_3$  end groups and this leads to the chains' tilt in respect to the lamellar edges. Therefore the individual lamellae width might be smaller than the length of alkane chains.

Having in mind the STM images of the normal alkanes on graphite, it is rather curious if such resolution can be achieved in AFM: either in the contact or in the oscillatory (amplitude modulation - AM and frequency modulation - FM) modes. There is definite progress in this respect as it is demonstrated with AFM images of three different alkanes

( $C_{18}H_{38}$ ,  $C_{242}H_{486}$  and  $C_{390}H_{782}$ ) on graphite obtained in the contact mode, Figs. 4-5. The spacings, which are related to the lamellae and individual chains, are distinguished in the image of  $C_{18}H_{38}$  lamellae, Fig. 4 (left). The zigzag pattern along the closely packed alkane chains is seen in the image of the ultra long alkane -  $C_{390}H_{782}$ , Fig. 4 (right). Several slightly twisted lamellae were detected in the images of  $C_{242}H_{486}$ , Figs. 5. A number of linear defects caused by the missing chains or their parts are also distinguished in the 100-nm image. The individual alkane chains, which are extended between the edges of the lamellae, are also noticed in the 55-nm image.

The collection of high-density images with a number of pixels from 1K to 4K is needed for observations of the lamellar edges and individual chains of

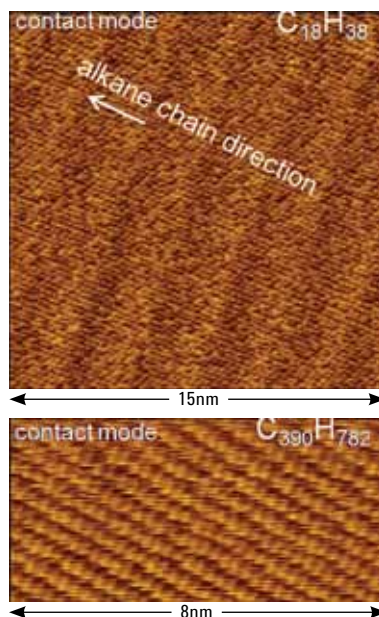


Figure 4. AFM images of  $C_{18}H_{38}$  and  $C_{390}H_{782}$  lamellae on graphite obtained in the contact mode.

long alkanes within the same image. Such imaging takes time and requires the low-thermal drift of the instrument. The demonstrated visualization of the molecular spacing down to 0.25 nm in the contact mode gives us a hope that similar observations can be achieved in the oscillatory AM and FM modes when they are applied in ambient conditions or under the liquid. The 0.25 nm resolution in visualization of the molecular structure of pentacene was been already achieved in the FM experiments in UHV and at low temperatures [5]

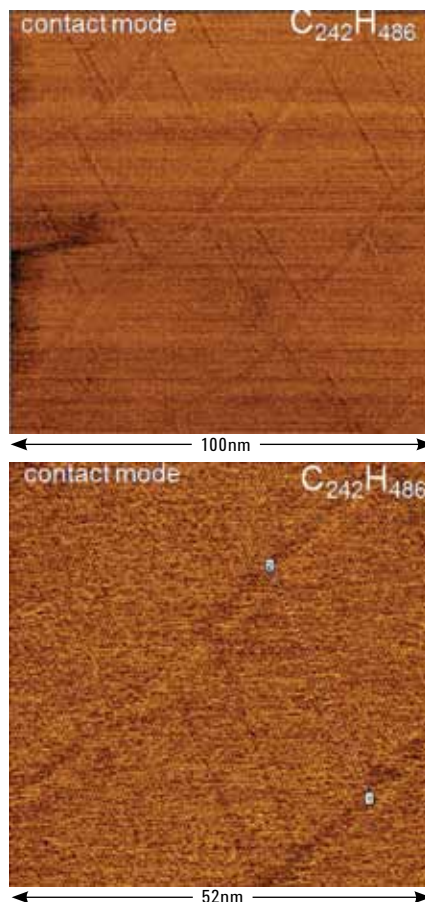


Figure 5. AFM images of  $C_{242}H_{486}$  lamellae on graphite obtained in the contact mode.

For a number of years, the progress in AFM is in part related to the developments and applications of FM mode. Nowadays this technique, which was originally employed in UHV as the alternative (to AM) way of detection tip-sample force interactions and scanning, is also used for high-resolution imaging in air and under liquid. The high-resolution images of mica, self-assemblies of alkanethiols, and polydiacetylene (PDA) crystals were recorded with FM using the home-made set-ups [6–7]. These periodical structures are characterized by spacings above 0.5 nm and in some cases the molecular-scale individual defects were observed. The similar findings were reported with AM mode [8]. Several high-resolution images, which were obtained in AM with the 5500 microscope, are shown at the right.

A number of molecular-resolution images in AM mode were obtained in air on surface of PDA crystal. This crystal can be cleaved and the largest atomically-smooth face of the PDA crystal with few linear defects (Fig. 6, top right) is most suitable for molecular-scale imaging. At higher magnification, the periodical pattern mimicking the crystalline structure of the *bc*-plane can be obtained, Figs. 6 (top right and bottom). This lattice with the orthogonal spacings of 0.5 nm (the repeat distance along the *c*-axis) and 0.7 nm (a half of the repeat distance along the *b*-axis) is detected in the experiments with different probes, Figs. 7. Despite the similarity of the image patterns obtained with different probes the image variations are noticeable and there is definitely a lack of high-resolution of fine atomic-scale features. The latter is the common feature of the images obtained in AM and FM modes in air and under liquid is that the spacings smaller than 0.5 nm are poorly resolved. The situation is only slightly better for the images in the contact mode, where in addition to visualization of mica surface the lattices of MoS<sub>2</sub> or graphite can be also observed. The contact mode images of these layered materials are shown in Figs. 8. The original images are quite noisy and the periodical lattices can be enhanced with FFT procedure that leads

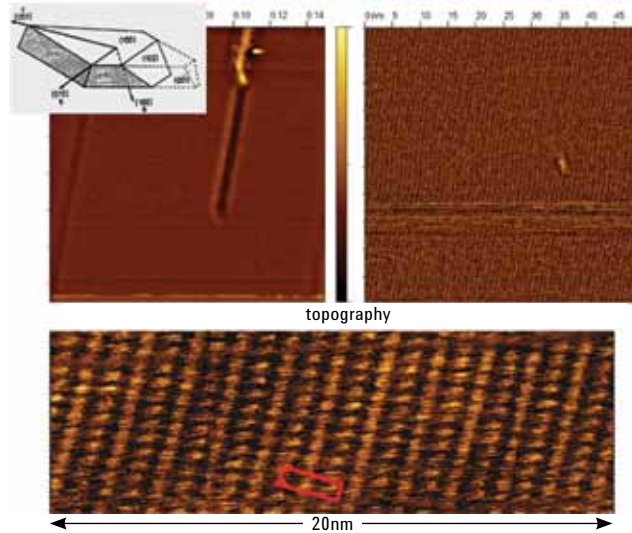


Figure 6. AFM images of polydiacetylene crystal obtained in amplitude modulation mode in air. A red rectangle indicates the crystallographic lattice on the *bc*-plane of this crystal.

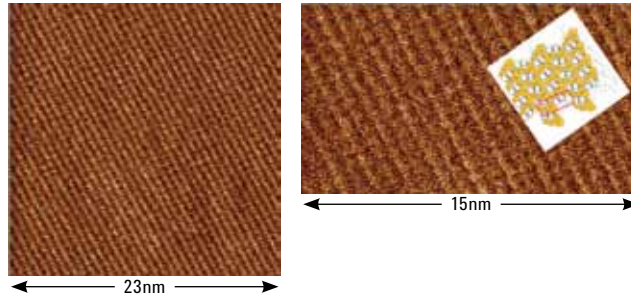


Figure 7. AFM images of polydiacetylene crystal obtained in amplitude modulation mode in air. The probe was different from that in the experiment in Figure 6.

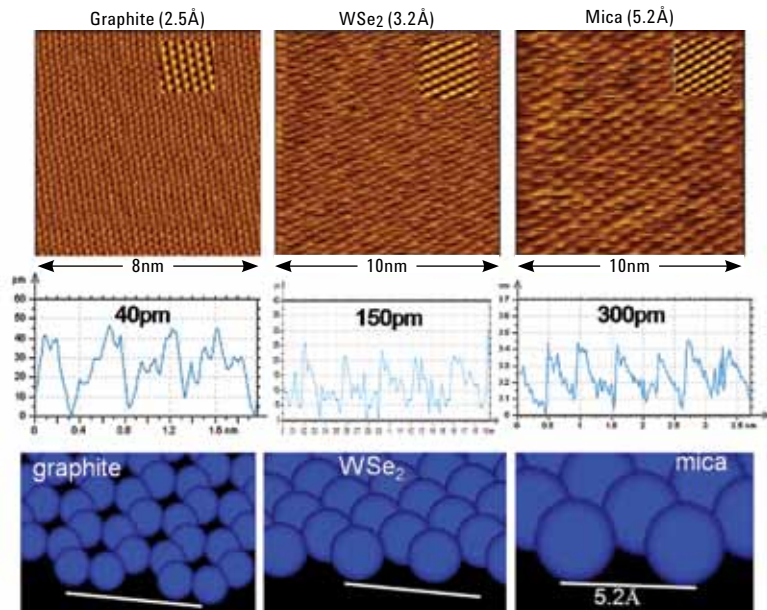


Figure 8. Top row – topography images of three layered crystals obtained in the contact AFM mode. The topography contours along these images are presented underneath them in the middle row. Bottom row – 3D representations of the crystallographic surface structure of carbon, Se and potassium atoms.



to perfect hexagonal patterns, which are imbedded in the top part of the images. The topography traces along the images are presented underneath, and they show that the surface corrugations increase from 40 pm (graphite) to 300 pm (mica). Therefore, the molecular-scale imaging of mica is less demanding due to the larger corrugations and interatomic separations as seen from the 3D sketches of the atomic surface structure of the crystals (see the bottom of Figs. 8).

In summary, the current status of the atomic-scale imaging in AFM is not satisfactory and there is a room for further improvements. The progress of the high-resolution imaging in the oscillatory AM and FM modes is most desirable because these modes can be applied to much broader range of materials including soft objects as compared with the contact mode AFM. This progress relies on instrumental improvements (better signal-to-noise characteristics, low thermal drift, improved detection and control of the tip-sample forces, etc.) and the use of sharp probes. The other issue is related to the better understanding of the nature of atomic-scale resolution in AFM, which is discussed since first successful visualization of atomic- and molecular-scale lattices in the contact mode. In this mode the single atomic-scale defects have never been practically recorded. Therefore, such imaging provides only the lattice resolution in the contrast to true atomic resolution where a detection of such defects is expected. The imaging of the periodical lattices with the defects was later demonstrated in FM and AM images (first in UHV and later in ambient conditions) yet the results of the computer simulation revealed that visualization of the defects does not necessarily mean that the surrounding molecular order is correctly reproduced in the images [9–10]. These findings emphasize a need of a thorough interplay between the experiment and theory in the analysis of the atomic-scale data.

## References

1. W. Stocker et al *Polym. Bull.* **1991**, *26*, 215–222
2. G. C. McGonigal, R. H. Bernhardt, and D. J. Thomson, *Appl. Phys. Lett.* **1990**, *57*, 28.
3. W. Liang et al *Adv. Mater.* **1993**, *5*, 817–821.
4. S. N. Magonov, and N. A. Yerina *Langmuir* **2003**, *19*, 500–504.
5. L. Gross et al, *Science* **2009**, *324*, 142.
6. T. Fukuma et. al. *Appl. Phys. Lett.* **2005**, *86*, 193108.
7. T. Fukuma et. al. *Appl. Phys. Lett.* **2005**, *86*, 034103.
8. D. Klinov, and S. Magonov *Appl. Phys. Lett.* **2004**, *84*, 2697.
9. S. Belikov, and S. Magonov *Jap. Jour. Appl. Phys.* **2006**, *45*, 2158.
10. S. Belikov, and S. Magonov *Proc. Amer. Control Soc.*, St. Louis, **2009**, 979.

# Compositional Mapping of Materials with Single-Pass Kelvin Force Microscopy

## Application Note

Sergei Magonov and John Alexander  
Agilent Technologies

### Abstract

This note describes the applications of single-pass Kelvin force microscopy (KFM) to a broad range of samples. Particularly, it will be shown that KFM substantially complements phase imaging in compositional mapping of complex multicomponent materials.

### Description of Single-Pass Kelvin Force Microscopy Measurements

Currently, the expansion of AFM applications is governed by a multifrequency detection of mechanical and electric tip-sample force interactions. In studies of local electric properties, these advances are related to single-pass Kelvin force microscopy (KFM) that can be implemented in different frequencies set-ups. For the past couple of years we have explored various single-pass KFM implementations, which are schematically shown in Fig. 1. This diagram illustrates that a combined detection of the mechanical and electric tip-sample interactions can be realized with amplitude modulation (AM) and frequency modulation modes (FM). Most of the experiments so far were conducted with the AM detection of the tip-sample forces that are used for topography profiling at the resonant frequency of the probe. Simultaneously with the topography measurements the electrostatic force interactions between the conducting probe and the sample are stimulated with AC voltage applied to the probe at much lower frequency. These electrostatic forces are measured with the AM or FM detection and their nullification with DC voltage in the KFM servo operation provide the quantitative surface potential data. Recently we have started using AFM measurements with FM servo for topography profiling and two related KFM modes: FM-AM and FM-FM are currently under scrutiny.

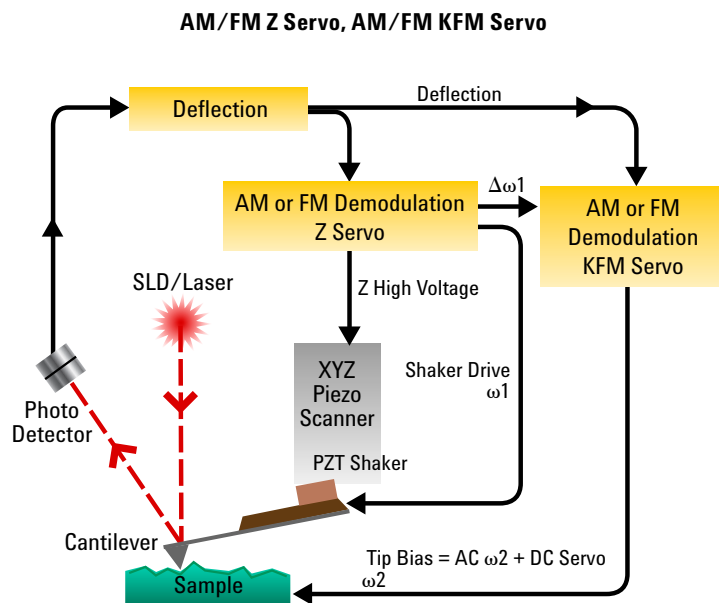


Figure 1. Sketch of different implementations of Kelvin force microscopy. Two servo-loops, which are based on the lock-in amplifiers (LIA), are employed for simultaneous detection of the mechanical and electrostatic tip-sample interactions. Topography profiling is arranged at the probe resonant frequency,  $\omega_1$ , with the Z-servo using amplitude modulation (AM) or frequency modulation (FM). The KFM servo operates at  $\omega_2$  ( $\ll \omega_1$ ) and it is based on the deflection or phase signals, respectively in AM and FM approaches. Different KFM set-ups: AM-FM, AM-AM, FM-AM, FM-FM can be chosen for studies of local electric properties. The 3<sup>rd</sup> LIA can be used for collection of dC/dZ response at  $2\omega_2$ .

Single-pass KFM studies have been known for a while [1–2] and these measurements are usually performed with the probe scanning a sample in the non-contact mode. We have applied the single-pass KFM mode in the intermittent contact mode at set-point amplitudes in the  $0.9\text{--}0.5A_0$  range ( $A_0$  — the oscillating amplitude of the non-interacting probe). On one hand, at these conditions a short contact of the conducting probe with a sample (even when it is a semiconductor or metal) does not perturb these specimens. On another hand, having the probe in the immediate vicinity of the sample is favorable for the sensitive KFM measurements with high spatial resolution. This is the definite advantage of the single-pass KFM compared to the Lift mode detection [3], in which the probe is removed away from the sample.

The main features and peculiarities of the AM-AM and AM-FM modes were explored on the samples of fluoroalkanes  $F_nH_m$  [ $F_nH_m = CF_3(CF_2)_n(CH_2)_mCH_3$ ] whose self-assemblies exhibit strong surface potential due to the vertical orientation of the chains carrying the molecular dipole at the  $-CH_2-CF_2-$  bond [4]. A set of  $F_{12}H_{20}$  self-assembled structures (most are toroids) on Si substrate was examined in KFM multi-frequency experiments in which, in addition to the surface potential images at 5 kHz, the  $dC/dZ$  were recorded at 10 kHz Fig. 2. These measurements were performed at averaged probe-sample distances of 1 nm, 7 nm, 15 nm and 30 nm (top to bottom columns in Fig. 2). The images indicate that surface potential of these structures does not depend on the separation and its value (around  $-0.7\text{ V}$ ) is consistent with predominantly vertical alignment of the molecular chains. The same self-assemblies in the  $dC/dZ$  maps exhibit the most pronounced contrast at 7 nm separation. Actually, the  $dC/dZ$  contrast, which generally is associated with dielectric constant, uniquely reveals a partitioning of the toroids into seven sectors. The surface potential images in Fig. 2 were obtained in AM-FM mode. In comparing the AM-FM and AM-AM modes applied for detection of the

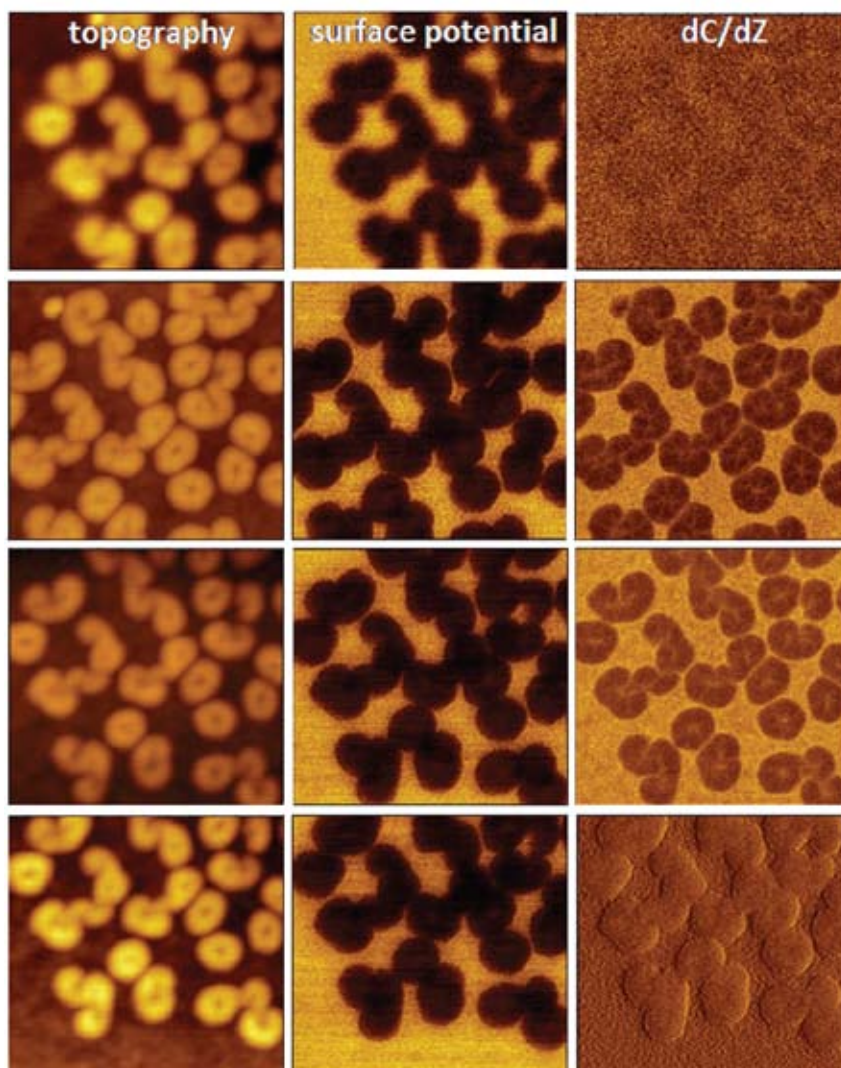


Figure 2. Topography, surface potential and  $dC/dZ$  and  $dC/dV$  images of  $F_{12}H_{20}$  adsorbates on Si. The images were obtained in the AM-FM mode. Scan area 300 nanometers. The contrast covers the height and potential changes in the  $0\text{--}200\text{ nm}$  and  $0\text{--}1\text{ V}$  ranges. The contrast of  $dC/dZ$  maps is in relative units. The images in the columns from top to bottom were obtained respectively at the probe-sample distances of 1 nm, 7 nm, 15 nm, and 30 nm.

electrostatic forces we found out that the FM detection of the electrostatic forces has definite advantages in agreement with the results obtained earlier in UHV [5]. It requires lower AC voltages (usually less than 1 V) and in most cases provides higher and more correct surface potential data. Actually, our first measurements in the FM-AM and FM-FM modes are showing the similar trend. This example also shows that in the multifrequency AFM measurements there is the increasing number of variables for the experiment optimization. Therefore a researcher should be aware about making the correct choice of imaging mode,

finding the optimal imaging parameters, choosing the most appropriated probe and a sample preparation.

The sensitivity and resolution of KFM are rather complicated issues. The sensitivity is essential in mapping the small potential variations in the  $1\text{--}10\text{ mV}$  range. Besides electronics the probe dimensions are one of the important factors influencing the signal-to-noise ratio in KFM experiments. The images obtained with the larger probe (tip apex around 60 nm) show substantially lower noise level in the sub-10 mV range compared to the sharp probe with the 20-nm apex. Therefore when nanometer

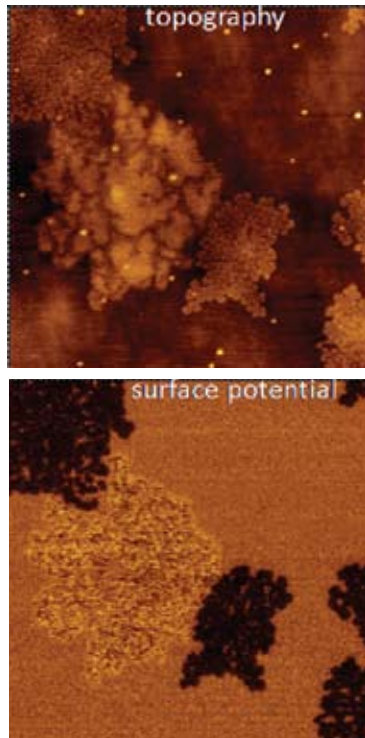


Figure 3. Topography and surface potential images of  $F_{14}H_{20}$  adsorbate on Si surface. The images were recorded at relative humidity over 95%. Scan size  $3\mu m$ . The contrast covers the topography and surface potential variations in the 0–14 nm and 0–1.6 V ranges.

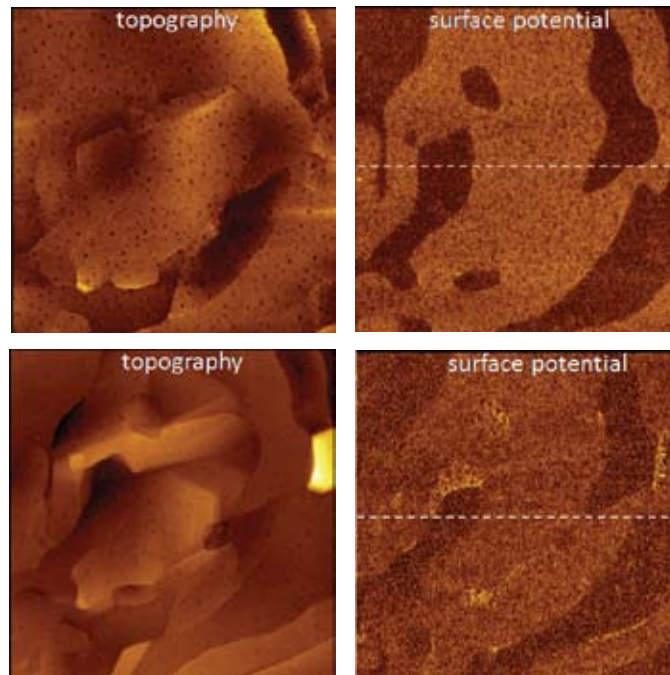
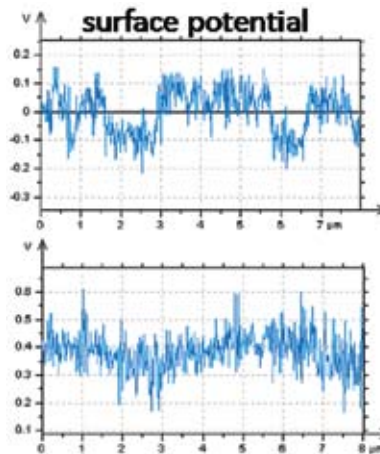


Figure 4. Two pairs of topography and surface potential images obtained at the same location of the Bi/Sn soldering material. Scans are  $8\mu m$ . The first pair of images was obtained immediately after the sample preparation and the second – 24 hr later. In the first pair of images, the contrast covers the height and potential changes in the 0–50 nm and 0–0.8 V ranges. In the second pair of images, the contrast covers the height and potential changes in the 0–100 nm and 0–1.2 V ranges. The surface potential profiles taken along the directions indicated with the white dashed lines are presented separately.



spatial resolution is not essential the larger probes can be chosen for sensitive potential measurements. The latter can also benefit from slow scanning rates. As regarding the spatial resolution a strict criterion is the width of the surface potential transient region at the step between the substrate and adsorbate having different potential values. The analysis of the surface potential profiles at the steps of the fluoroalkane self-assembles shows that true spatial resolution is around 20 nm comparable with the size of the commercial conducting probes. For KFM compositional imaging of heterogeneous materials the spatial resolution of visualization of the heterogeneities is also important and we resolved the 2 nm features in such surface potential images [2].

As KFM applications broaden, this technique was applied to a wide range of the samples in different environments. The KFM studies in the intermittent contact mode, which were carried out in high humidity [4] revealed that screening of the sample surface potential was less substantial compared to the results of KFM experiments conducted in the non-contact mode. The imaging of the fluoroalkanes in high humidity demonstrates this capability, Fig. 3. In these images a water adsorbate is seen between two domains of the fluoroalkanes, which exhibit strongly negative patterns in the surface potential images. At  $RH > 95\%$  the value of the surface potential of  $F_{14}H_{20}$  is around -0.6 V that is only slightly smaller than at ambient conditions (-0.75 V).

*Below we will overview the applications of single-pass KFM to different materials: metals and semiconductors, organics and polymers.*

### Metals and Semiconductors

Surface potential of metals is directly related to their work function that varies in the 4 V–5.5 V range for most common metals [6]. KFM can be employed for compositional images of metal alloys and even polycrystalline metal samples because the surface potential is different on various crystalline facets. The examples of KFM images of incomplete alloys of Bi with Sn are shown in Fig. 4. In these soldering materials KFM reveals domain morphology of this compound. The domains of Bi and Sn are distinguished in surface potential

images due to the difference of their work functions. Actually, the surface potential change of 0.2 V, which was found in freshly prepared samples, corresponds well to the difference of these metals' work functions [6]. The surface potential images and the cross-sections in Figs. 4 demonstrate that the contrast disappears with time due to the oxidation of metals (particularly Sn) in air. The flat surface of the Bi/Sn sample was prepared by hot pressing between two smooth Si plates, which were removed after the sample was chilled to room temperature. Most likely, this procedure induced some internal stresses that have been released at room temperature. The related change of the sample surface is seen from the topography images in Figs. 4.

The use of KFM for compositional imaging of metals and semiconductors is further demonstrated by imaging of the test structures made by FIB deposition of Pt and SiO<sub>2</sub> lines on surfaces of Si wafer and graphite [7]. The images of these cross structures are shown in Figs. 5–6. The contrast of the lines differentiates them in the surface potential images. The quantitative data are seen from the cross-section profiles placed under the images. The potential of the Pt strips on both substrates are close to that of the conducting probe. The potential of SiO<sub>2</sub> strips, which are 20 nm in height, differs from that of Si substrate that has only 2–3 nm of naturally grown oxide film. Although the Pt and SiO<sub>2</sub> lines on graphite are partially “lost” amidst the numerous surface steps, the surface potential pattern shows only the material-related contrast, Figs. 6. The comparison of the lines' dimensions in the topography images with their surface potential blueprints indicates that the effective probe is substantially larger in the electric measurements. This means that a larger part of the probe is involved in the electrostatic tip-sample interactions compared to the tip-sample intermittent mechanical contact. At the current stage of KFM developments and applications the use of these and similar standards is useful for understanding the basics of this method. Such fundamental studies can be further assisted by computer

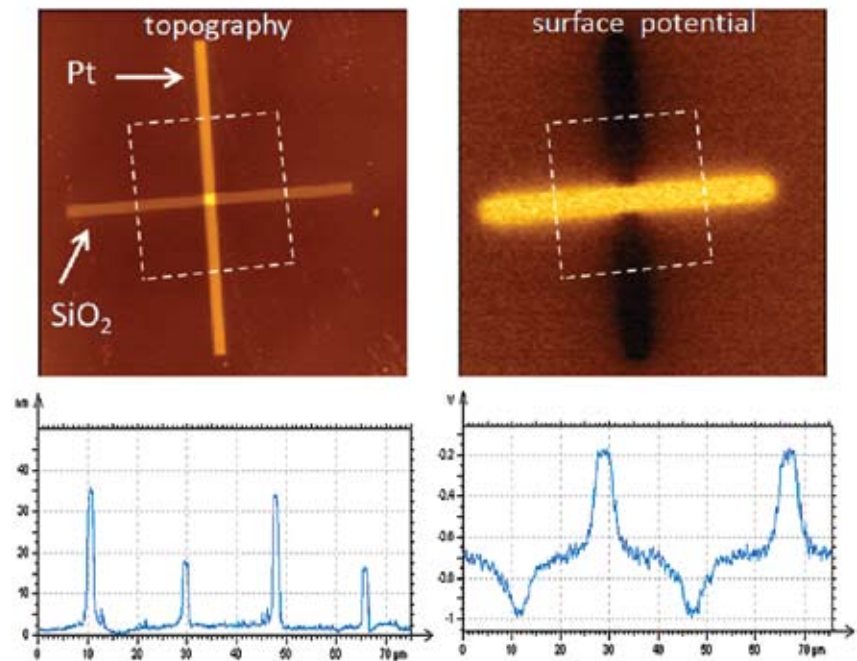


Figure 5. Topography and surface potential images of FIB-deposited lines of Pt and SiO<sub>2</sub> on Si substrate. Scan size 40 μm. The contrast covers the height and potential changes in the 0–60 nm and 0–1 V ranges. The cross-section profiles taken along the directions pointed with the white dotted lines are placed underneath the images.

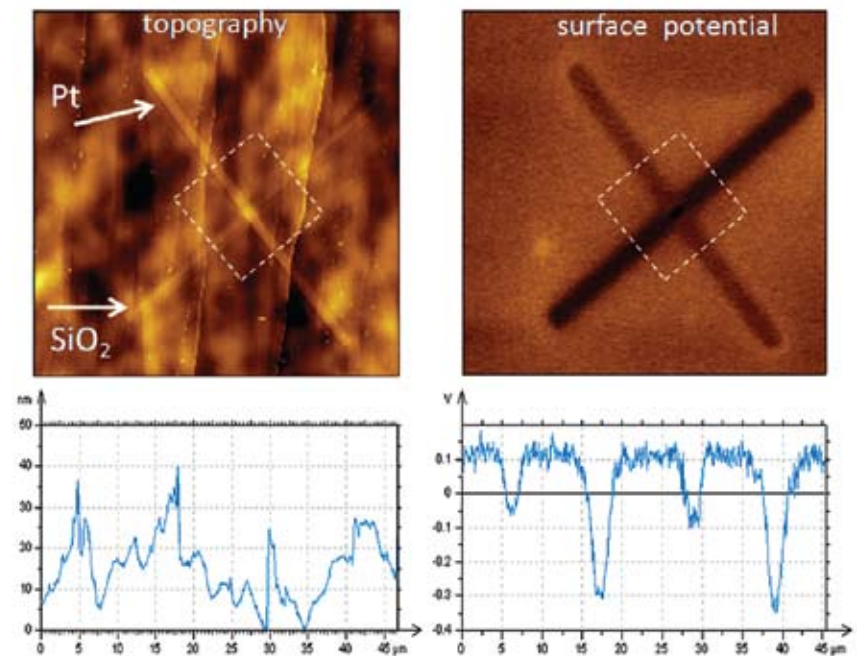


Figure 6. Topography and surface potential images of FIB-deposited lines of Pt and SiO<sub>2</sub> on graphite. Scan size 40 μm. The contrast covers the height and potential changes in the 0–100 nm and 0–3 V ranges. The cross-section profiles taken along the directions pointed with the white dotted lines are placed underneath the images.

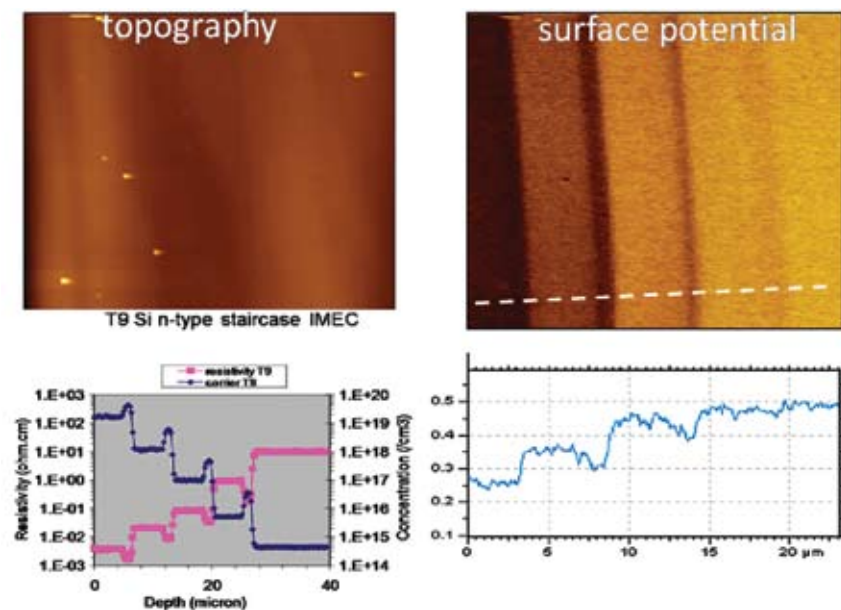


Figure 7. Topography and surface potential images of T9 standard sample with layers having different doping level. Scan size  $25\ \mu\text{m} \times 30\ \mu\text{m}$ . The contrast in the topography image covers the height corrugations in the 0–20 nm range. The resistivity (dark blue) and doping (magenta) profiles are placed underneath the topography image. The cross-section profile along the direction marked with a white dashed line in the surface potential image is shown below it.

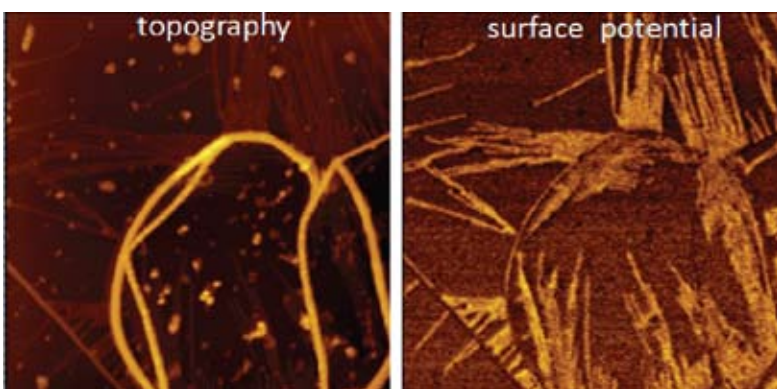


Figure 8. Topography and surface potential of CdTe nanowires formed from a suspension of CdTe nanoparticles. Scan size  $2\ \mu\text{m}$ . The contrast covers the height and potential variations in the 0–22 nm and 0–1 V ranges.

simulation of the electrostatic force interactions, the surface potential and  $dC/dZ$  of metals and semiconductors.

The more sophisticated standards, which have surface layers with different doping type and level, are employed for verification of different AFM-based electric techniques capability of quantitative tracking these industrially important properties. KFM images of the IMEC standard (n-type Si staircase T9 [8]) on the surface with the doped

layers running perpendicular are shown in Fig. 7 together with the resistivity and doping profiles determined by different methods.

The face with the layers having doping levels increasing from  $1 \times 10^{14}$  to  $1 \times 10^{18}\ \text{cm}^{-3}$  does not show noticeable surface corrugations. The layers do manifest themselves in the surface potential image as the bands whose contrast increases with the increase of the doping level. The potential varies

250 mV on the locations covering 4 orders of magnitude of dopant density. This data set is in good agreement with the earlier experimental results obtained on Si wafers with different doping density [9]. The difference of 0.240 eV between Fermi levels of the n-Si samples with  $1.1 \times 10^{14}$  and  $7 \times 10^{19}\ \text{cm}^{-3}$  doping densities was estimated from the surface potential data. The well-pronounced steps of the potential profile (Fig. 7) correlates well to the width of the differently doped layers. However, it is rather premature to claim that surface potential provides the direct quantitative measure of the doping density. In many cases the potential differences detected within the single image are relatively reliable. Less reproducible are absolute potential values recorded in different images. Surface contamination, varying oxide coverage and environmental effects are among the possible reasons of the poor reproducibility.

### Low-Dimensional Semiconductor Structures

Low-dimensional semiconductor and metal systems offer variety of unique structural, optical and electric properties. Some of these highly ordered materials can be prepared in mild conditions by self-assembly. The formation of CdTe nanowires is one of the related examples. It has been shown that crystalline nanowires are built up of CdTe nanoparticles in water solution upon controlled removal of organic stabilizers [10]. The strong dipole-dipole interactions were suggested as the driving force of self-organization of the nanoparticles into the pearl necklace aggregates that re-crystallized into the nanowires. The formation of the CdTe nanowires from suspension of the nanoparticles during its drying on mica substrate was monitored with KFM [11]. The topography and surface potential images, which were recorded at the end of this process, are shown in Figs. 8. These images show individual CdTe nanowires, which are 20–30 nm in width and few nm in height, as well as their arrays whose growth was likely nucleated from thicker linear structures. The surface potential image is dominated by bright contrast (approx.

0.5V) of the nanowires. Additionally to nanowires, there are also the small nanoparticles (20–30 nm in diameter), which are brighter than the nanowires in the topography images but darker in the surface potential image. These features can be assigned to the traces of the organic stabilizers of the CdTe nanoparticles.

The KFM results suggest that self-assembly of CdTe nanoparticles into crystalline nanowires is accompanied by structural transitions leading to the formation or realignment of molecular dipoles. Dipole moments in CdTe nanoparticles with cubic lattice are not expected unless they appear at structural defects that induce asymmetry of molecular structure. Therefore, the formation of the nanowires entails the radical changes of local symmetry of molecular groups.

### Organic Electronic Materials

Current developments of organic materials for electronics strongly depend on understanding structure-property relationships in molecular films applied in field effect transistors, light emitting diodes, and organic solar cells. Getting such knowledge becomes non-trivial for objects consisting of a single sheet of molecules where electron transport has a two-dimensional character and the molecular scale imperfections need to be examined. AFM and, particularly, electric modes can be very helpful in the characterization of such structures and related devices. This has been proved in numerous studies of semiconducting molecular layers of oligo-thiophene [9] and pentacene [10]. Single-pass KFM can further improve the characterization of these materials.

KFM images of a pentacene adsorbate, which was evaporated on Si substrate in vacuum, are shown in Figs. 9. This is the single layer film with several 2<sup>nd</sup> layer dendritic structures. The 1<sup>st</sup> layer is composed of tightly packed vertically standing molecules and it has the domain substructure. The domain boundaries are best seen as bright

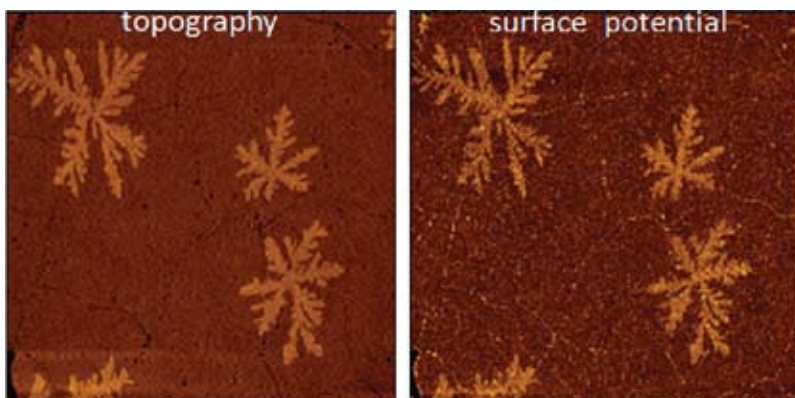


Figure 9. Topography and surface potential images of a pentacene adsorbate on Si. Scan size 8  $\mu\text{m}$ . The contrast covers the height and surface potential variations in the 0–10 nm and 0–1 V ranges. AC stimulated voltage was 4 V.

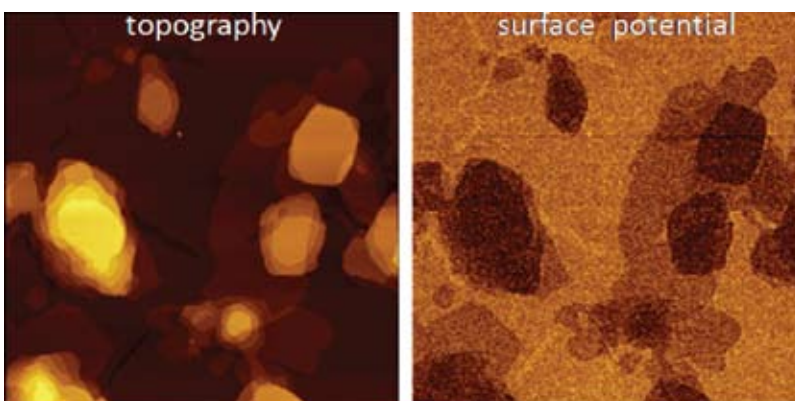


Figure 10. Topography and surface potential images of a 7-thiophene adsorbate on Si. Scan size 7  $\mu\text{m}$ . The contrast covers the height and surface potential variations in the 0–50 nm and 0–1 V ranges.

features in the surface potential image. This contrast is observed only when the stimulating AC voltage is above 3 V that indicates on the voltage-induced dipoles at the domains' edges. The surface potential of the dendritic structures, whose height also indicated on the vertical orientation of the molecules, is more positive ( $\sim 80$  mV) than that of the 1<sup>st</sup> layer, and it does not depend on a magnitude of the stimulated voltage. Actually, the smaller potential change of 50 mV was observed between the 1<sup>st</sup> and 2<sup>nd</sup> pentacene layers on Si using the Lift mode [11]. The nature of the surface potential contrast of pentacene layers is not yet established. The possible contribution of the interfacial dipoles is considered as a factor leading to the observed surface potential [12].

Self-assembled monolayer transistors in which oligo-thiophene molecules form a single layer on dielectric Si gate have been recently tested [13]. In this case the devices can be obtained by spin-casting of the thiophene solution of appropriate concentration or by immersing the substrate in it. KFM studies of these devices reveal the grain boundaries in the single layer and also a presence of extra material in form of multilayers. Both structural features can be considered as imperfections which influence semiconductor behavior of the molecular film. The multilayer morphology of one of the adsorbates of the 7-thiophene with a hydrocarbon tail is evident from KFM images in Figs. 10. The topography image demonstrated the multilayer domains formed on the

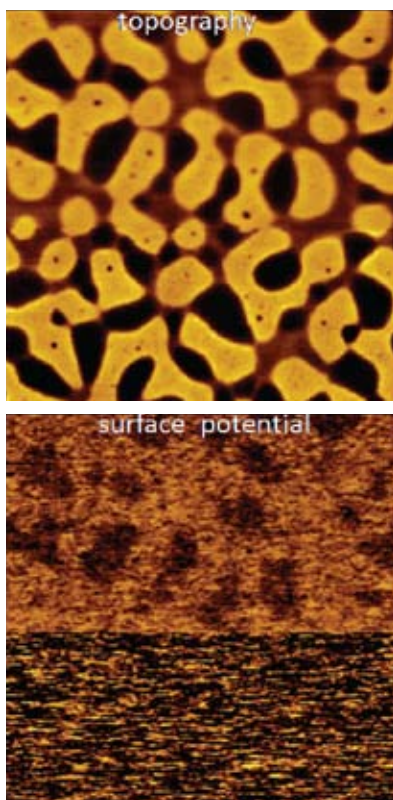


Figure 11. Topography and surface potential images of a film of 3PS/7PMMA blend on Si substrate. Scan size 6  $\mu\text{m}$ . The images were recorded at RH=20%. The contrast covers the height and potential variations in the 0–12 nm and 0–0.8 V ranges. AC stimulated voltage was 0.5 V and 6 V in the bottom and top parts of the image, respectively.

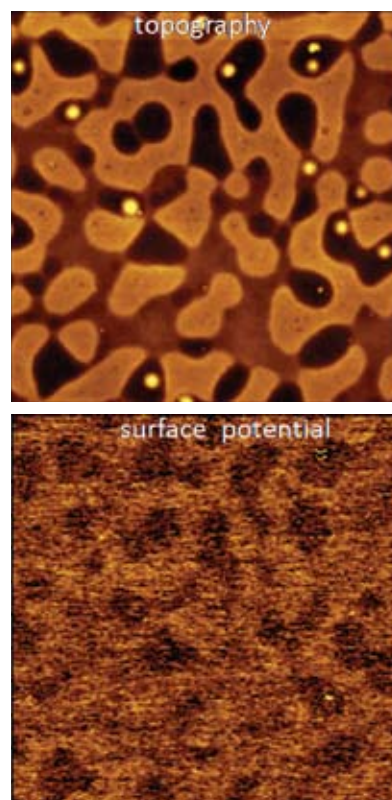


Figure 12. Topography and surface potential images of a film of 3PS/7PMMA blend on Si substrate. Scan size 6  $\mu\text{m}$ . The images were recorded at RH>95%. The contrast covers the height and potential variations in the 0–40 nm and 0–2.7 V ranges. AC stimulated voltage was 1 V.

single molecular layer that completely covers the Si substrate. The surface potential of these top layers decreases with height and the difference is reaching 0.5 V.

### Heterogeneous Polymers

Compositional mapping of heterogeneous polymers is usually achieved in phase imaging performed at elevated tip-sample forces [14]. The phase contrast is assigned to differences of local mechanical properties and variations of energy dissipated in the tip-sample interactions. Surface potential images can play a similar role in identifying the surface locations with different electric properties. Fluorinated polymers are good candidates for compositional analysis because they usually possess molecular dipoles moments that

lead to surface potential contrast [15]. A range of polymer materials that might be sensed by KFM can be expanded by including acrylic polymers. Macroscopic Kelvin probe studies of thin films of poly(methyl methacrylate) [PMMA] indicated that their surface potential depend on stereoregularity and molecular conformations of this polymer [16]. Therefore KFM might distinguish PMMA domains in blends and block copolymers with other polymers. This is indeed the case as seen from the images of PS/PMMA blends (PS-polystyrene) with different composition and symmetric block copolymers. The KFM images of a 20-nm thick film of 3PS/7PMMA film (weight ratio of the components is 3:7), which was deposited on Si substrate by spin-casting, are shown in Figs. 11. The scanning was performed in the upwards direction and the stimulated AC voltage

changed from 0.5 V to 6 V in the middle of the scan. This change caused a drop of the potential noise and the related drastic improvement of the surface potential image. The binary contrast pattern with the averaged difference of  $\sim 60$  mV was detected in the top part of this image where the dark patches are a minor component. These patches correspond to the surface dimples seen in the topography image. The increase of the electrostatic force interactions was favorable for the potential's noise reduction in air. When the KFM study of this sample was performed in humid atmosphere (RH>95%) the surface potential noise was smaller even at low stimulating AC voltages, Figs. 12. The surface potential exhibits the binary patterns similar to one observed at high AC voltages in air. Additionally, the multiple bright droplets, which are located inside the dimples, have



appeared in the topography image. They might present the condensed water droplets which form a relatively large contact angle that indicates on hydrophobicity of the underlying locations. Therefore the dimples with the droplets can be tentatively assigned to polystyrene domains, which are expected to be hydrophobic.

As we mentioned before, the spatial resolution of compositional imaging with single-pass KFM is in the nanometer range. The additional evidence comes with KFM imaging of PS-b-PMMA block copolymer. The images of the 50-nm film of this block copolymer on Si are presented in Figs. 13. These images show the phase separation pattern with 30-nm wide blocks. The phase image recorded simultaneously with the images did not show the contrast variations. The phase contrast becomes noticeable when the imaging is performed at larger tip-samples forces and with stiffer probes than the ones (Olympus and Mikromasch Pt-coated probes with 4–5 N/m stiffness) we are regularly using for KFM studies.

Studies in humid environment can be helpful for compositional imaging of the materials with hydrophilic components. This result was obtained in imaging of two industrial polymer materials: perfluorinated membrane (Nafion™) and conducting blend of poly(3,4-ethylenedioxythiophene) and poly(styrenesulfonate) [PEDOT:PSS]. In Nafion polymer, a hydrophobic polytetrafluoroethylene backbone

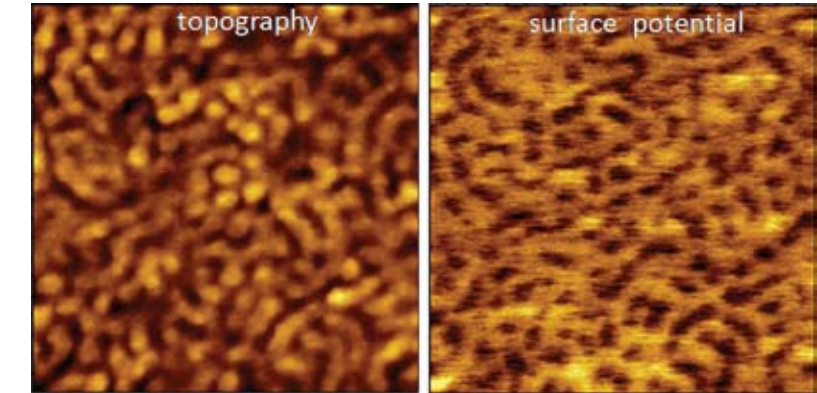


Figure 13. Topography and surface potential of PS-b-PMMA block copolymer on Si substrate. Scan size 1  $\mu\text{m}$ . The contrast covers the height and potential changes in the 0–10 nm and 0–0.8 V ranges.

coexists with hydrophilic -  $\text{SO}_3\text{H}^+$  acid groups connected to the backbone via -O-CF-CF<sub>3</sub>-CF<sub>2</sub>-O-CF<sub>2</sub>-CF<sub>2</sub>- side chains. Due to its outstanding chemical stability and proton conductivity this polymer is used as the proton exchange membrane in electrolyte fuel cells. The cell functioning substantially depends on ion conductivity in the polymer membrane that is defined by its microphase separation morphology. In other words, a nanoscale distribution of hydrophilic and hydrophobic regions is the most essential for optimal membrane performance.

The Nafion membranes are intensively examined using microscopic (TEM, AFM) and diffraction (small angle X-ray scattering, SAXS, and neutron scattering) methods in attempts to

clarify the film nanostructure. The recent model based on the SAXS data suggests that cylindrical hydrophilic domains arranged in parallel water channels with a mean size of about 2.4 nm [17]. High-resolution visualization of Nafion film morphology with AFM revealed the ionic domains of ~4 nm in size [19] is consistent with TEM data. Most of AFM experiments on Nafion samples were conducted in air and the measurements under water did not show a well resolved nanostructure.

As it was shown above in the studies of PS/PMMA blends, the 5500 scanning probe microscope (Agilent Technologies) is the most suitable for AFM and KFM measurements at high humidity. The images obtained during studies of Nafion films at different

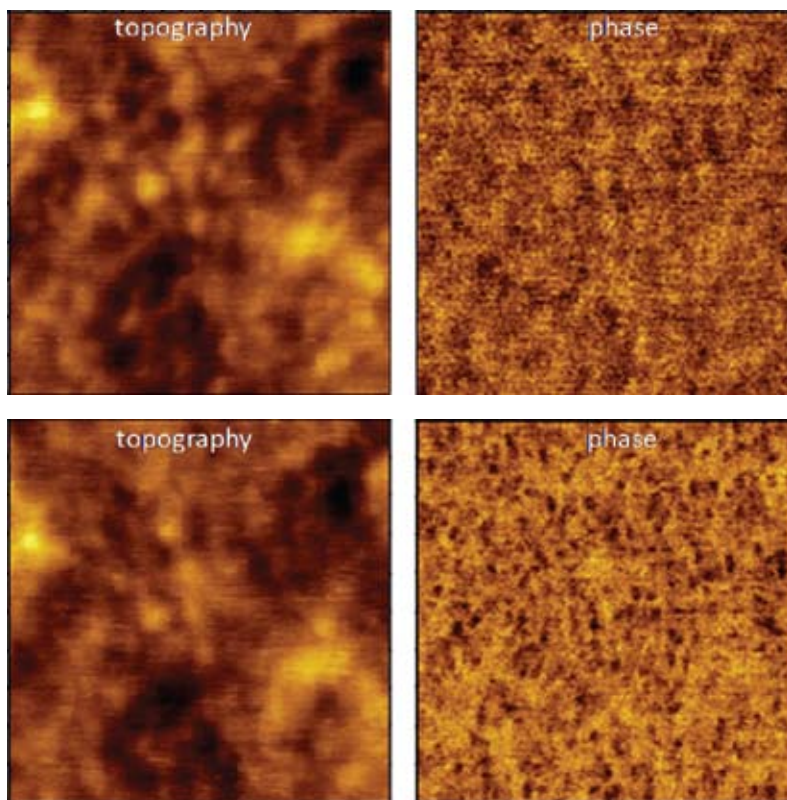


Figure 14. Top: topography and phase images of Nafion™ film on Si substrate at RH=60%. Bottom: topography and phase images of Nafion™ film on Si substrate at RH>95%. Scan size 100 nm. The contrast covers the height and phase variations in the 0–3 nm and 0–35 degrees ranges.

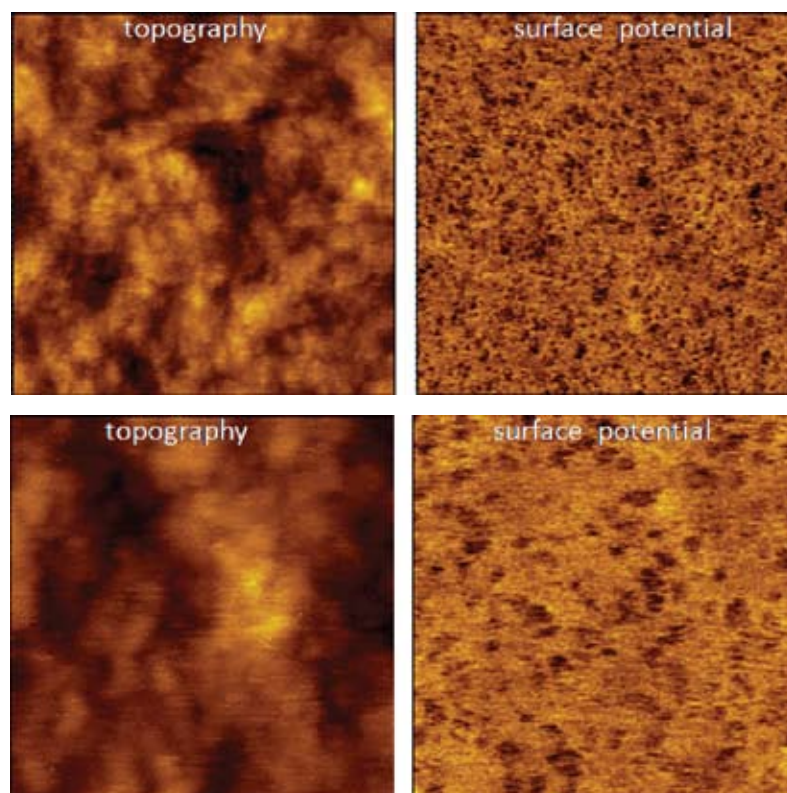


Figure 15. Topography and surface potential images of Nafion™ film on Si substrate at RH>95%. Top scans: 300 nm; bottom scans: 100 nm. The contrast covers the height and potential variations in the 0–5 nm and 0–0.4 V ranges.

humidity are presented in Figs. 14–15. In the imaging of Nafion films at elevated humidity one should take into account that the membrane is swelled with water and becomes much softer than at normal and low humidity. The gentle imaging of swelled films at RH=60% and at RH>95% was achieved with the regular Si probe which were driven in oscillatory amplitude modulation mode at small amplitude around 1 nm. The topography images recorded at these operational conditions exhibit the same pattern independent on humidity. The phase images are quite different and numerous dark spots of 2–3 nm in size appeared in the image recorded at higher humidity. These regions can be assigned to softer locations such as water channels described in the model introduced in [17]. This nanoscale phase separated morphology is similar to that recorded in the ambient-conditions AFM images [19]. Remarkably, KFM images with different magnification, which were recorded at RH>95%, show that the surface potential pattern is characterized by numerous 3–4 nm spots with lower potential, Figs. 14. Most likely, these spots are observed on the water-enriched locations and their slightly larger dimensions can be related to the larger size of the conducting probes that are employed for KFM. The assignment of lower potential regions to the swelled locations is supported by the data presented below.

Intrinsically conducting PEDOT:PSS blends are often used as a component in organic solar cells and light emitting diodes. Therefore morphology and electric properties of PEDOT:PSS films are among the factors influencing the cell and diode performance. PEDOT is a hydrophobic and conducting component, where as hydrophilic PSS is an insulator. The correlation between the blend composition, film morphology and conductivity is examined by variety of the techniques with emphasis on local current studies with conducting AFM methods [20]. Particularly, it was shown that topography depressions correlate with low conductivity locations and the number of such locations correlates with amount

of PSS component. TEM studies of morphology PEDOT:PSS films reveal the phase separation in this material [21]. According to the suggested model PEDOT:PSS films are composed of spherical grains with diameter in the 50–80 nm range. Based on EDX analysis it has been assumed that these grains consist of a 5–10-nm-thick PSS-rich shell and a PEDOT-rich core.

PEDOT:PSS blends are made commercially and they are distributed as water suspensions. Conductivity of these blends depends on their composition and highly conducting PEDOT:PSS (1:2.6) material was used for the preparation of films on Si substrate by spin-casting. These films were examined with KFM in the broad range of humidity. The images of the same location of the 50-nm PEDOT:PSS film, which were obtained at extremely dry and wet conditions, are shown in Figs. 16. A comparison of the topography images the change of humidity led to smoothing of surface morphology and the numerous deep dimples became less pronounced. The change of the surface potential images is much more drastic and a homogeneous pattern seen at dry conditions converted into a binary map with the 200 mV potential difference between the components. These images were obtained at low forces therefore the phase images don't exhibit any noticeable contrast. The darker spots in the surface potential map are located at the dimples. These regions can be assigned to PSS-rich material because the conductive AFM measurements (not shown here) revealed lower conductivity compared to their surroundings that are most likely enriched in PEDOT. The lower surface potential of hydrophilic inclusions can be tentatively attributed to apparent dipole moment developed in the locations swelled (or filled) with water. In any case, KFM imaging of PEDOT:PSS film at high humidity provides a compositional map of this material and thus improves the understanding of the structure-property relationship.

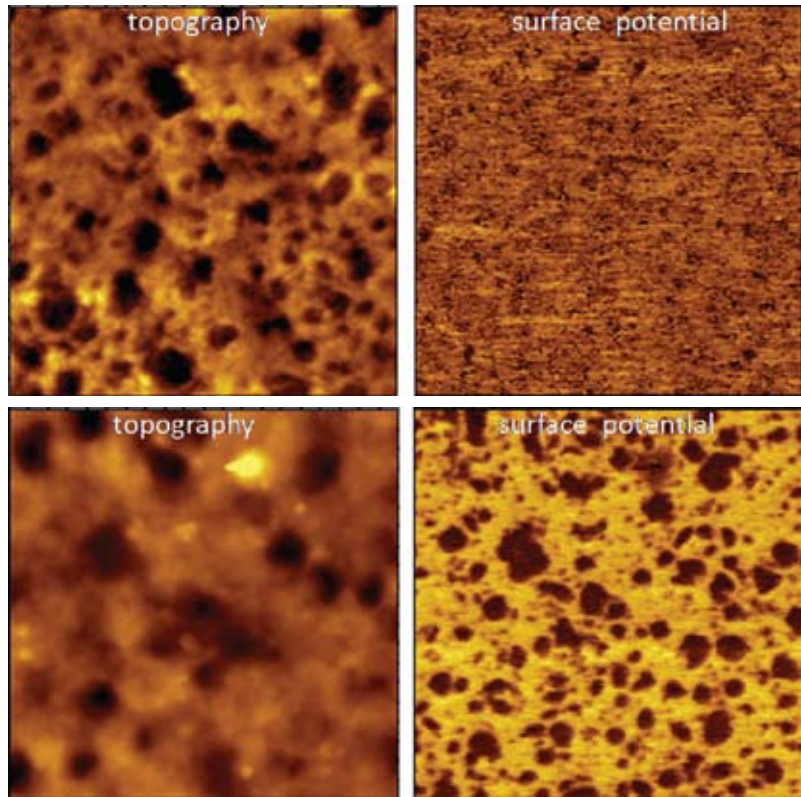


Figure 16. Top: topography and surface images of PEDOT:PSS film on Si substrate at RH=2%. Scan size 300 nm. The contrast covers the height and potential variations are in the 0–55 nm and 0–0.6 V ranges. Bottom: topography and phase images of PEDOT:PSS film on Si substrate at RH>95%. Scan 2 μm. The contrast covers the height and potential variations are in the 0–100 nm and 0–0.5 V ranges.

### Conclusions

Single-pass KFM mode with FM detection of the electrostatic forces improves sensitivity and spatial resolution of surface potential imaging when applied in the intermittent contact mode. The extension of KFM applications to a wide range of materials shows its exceptional value for compositional imaging. In this function KFM complements phase imaging by advancing to earlier not accessible areas such as metal alloys. Due to the stiffness range of commercial probes phase imaging is typically useful for studies of heterogeneous soft materials with high image contrast being achieved in operation at elevated forces. The use of phase imaging to hard materials is quite limited. The KFM studies in different environments are also bringing new and valuable information about

morphology of heterogeneous polymers. The area of environmental AFM will further benefit from local electric and mechanical measurements with multiple frequency detection.

### Acknowledgments

The materials that were used in studies described in this note were kindly provided by Prof. M. Moeller (DWI, Aachen, Germany), Prof. N. Kotov (University of Michigan), Dr. R. Berger (MPIP, Mainz, Germany) and Dr. V. Kalihari (University of Minnesota). The part of the experiments described above was conducted during S. Magonov's research visits to MPIP in Mainz and DWI in Aachen.

## References

1. Y. Martin, D. A. Abraham, and H. K. Wickramasinghe "High-resolution capacitance measurement and potentiometry by force microscopy" *Appl. Phys. Lett.* **1988**, *52*, 1103–10005.
2. M. Nonnenmacher, M. P. O'Boyle, and H. K. Wickramasinghe "Kelvin probe force microscopy" *Appl. Phys. Lett.* **1991**, *58*, 2921–23.
3. V. B. Elings, and J. A. Gurley "Scanning probe microscope using stored data for vertical probe positioning" US Patent 5,308,974, **1994**.
4. J. Alexander, S. Magonov and M. Moeller "Topography and surface potential in Kelvin force microscopy of perfluoroalkyl alkanes self-assemblies" *J. Vac. Sci. Techn. B*, **2009**, *27*, 903–911.
5. U. Zerweck, CH. Loppacher, T. Otto, S. Grafstroem, and L. M. Eng "Accuracy and resolution limits of Kelvin probe force microscopy" *Phys. Rev. B*, **2005**, *71*, 125424.
6. H. B. Michaelson "The work function of the elements and its periodicity" *J. Appl. Phys.* **1977**, *48*, 4729–4733.
7. R. Berger, H.-J. Butt, M. Retschke, S. Weber "Electrical Modes in Scanning Probe Microscopy" *Macromolecular Rapid Communications* **2009**, *30*, 1167.
8. T. Matsukawa, S. Kanemaru, M. Masahara, M. Nagao, H. Tanoue, and J. Itoh "Doping diagnosis by evaluation of the surface Fermi level using scanning Maxwell-stress microscopy" *Appl. Phys. Lett.* **2003**, *82*, 2166–2169.
9. T. W. Kelley and C. D. Frisbie, "Gate Voltage Dependent Resistance of a Single Organic Semiconductor Grain Boundary" *J. Phys. Chem. B* **105**, 4538, 2001.
10. D. Knipp, R. A. Street, and A. R. Voelkel "Morphology and electronic transport of polycrystalline pentacene thin-film transistors" *Appl. Phys. Lett.* **2003**, *82*, 3907–3909.
11. V. Kalihari, David J. Ellison, G. Haugstad, and C. D. Frisbie "Observation of unusual homoepitaxy in ultrathin pentacene films and correlation with surface electrostatic potential" *Adv. Mater.* **2009**, *21*, 1–7.
12. L. Chen, R. Ludeke, X. Cui, A. G. Schrott, C. R. Kagan, and L. E. Brus "Electrostatic field and partial level pinning at the pentacene-SiO<sub>2</sub> interface" *J. Phys. Chem. B* **2005**, *109*, 1834–1838.
13. S. G. J. Mathijssen, E. C. P. Smits, P. A. van Hal, H. J. Wondergem, S. A. Ponomarenko, A. Moser, R. Resel, P. A. Bobbert, M. Kemerink, R. A. J. Janssen, and D. M. de Leeuw "Monolayer coverage and channel length set the mobility in self-assembled monolayer field-effect transistors" *Nature Nanotechnology* **2009**, *4*, 674–680.
14. S. N. Magonov "AFM in Analysis of Polymers" in *Encyclopedia of Analytical Chemistry*, (R. A. Meyers, Ed.), pp. 7432–7491, John Wiley & Sons Ltd, Chichester, **2000**.
15. M. Chiesa, L. Buergi, J.-S. Kim, R. Shikler, R. H. Friend and H. Sirringhaus "Correlation between surface photovoltage and blend morphology in polyfluorene-based photodiodes" *Nano Letters* **2005**, *5*, 559–563.
16. J.-J. Kim, S.-D. Jung, and W.-Y. Hwang "Molecular Conformation and Application of Stereoregular PMMA Langmuir-Blodgett Films" *ETRI Journal* **1996**, *18*, 195–206.
17. M. Retschke, R. Berger, H.-J. Butt, and S. Magonov, the manuscript in preparation.
18. K. Schmidt-Rohr, Q. Chen "Parallel cylindrical water nanochannels in Nafion fuel cell membranes" *Nature Mater.* **2008**, *7*, 75-83.
19. R. S. McLean, M. Doyle, and B. B. Sauer "High-resolution imaging of ionic domains and crystal morphology in ionomers using AFM techniques" *Macromolecules* **2000**, *33*, 6541–6550
20. L. S. C. Pingree, B. A. MacLeod, and D. S. Ginger "The changing face of PEDOT:PSS Films: substrate, bias, and processing effects on vertical charge transport" *J. Phys. Chem.* **2008**, *112*, 7922–7929.
21. U. Lang, E. Mueller, N. Naujoks, and J. Dual "Microscopical Investigations of PEDOT:PSS Thin Films" *Adv. Funct. Mater.* **2009**, *19*, 1215–1220.



# Atomic Force Microscopy Studies in Various Environments

## Application Note

Sergei Magonov  
Agilent Technologies

### Abstract

Atomic force microscopy imaging of organic and polymer samples with Agilent 5500 microscope in humid air and vapors of solvents (methanol, toluene, benzene, tetrahydrofuran) is presented. The observed vapor-induced structural transformations and swelling of the samples improves characterization of these objects at the small scales.

### Introduction

Comprehensive characterization of surface structures with atomic force microscopy (AFM) is one of the important areas of modern science and technology. The essence of this technique is the use of a miniature probe, which consists of a cantilever with a tip at its free end, for a detection of different tip-sample forces. The optical level method, in which the cantilever deflection or oscillation in a response to the tip apex interacting with a sample is magnified on a photodetector, provides unique sensitivity. This sensitivity combined with the high-precision 3D translation of the probe over the sample surface makes the atomic force microscope the unique tool for visualization of atomic and molecular-scale structures. The applications of AFM are not limited to high-resolution and low-force profilometry. The probe sensitivity to mechanical and electromagnetic tip-sample interactions allows using

it for local examination of various materials properties and related compositional mapping. In addition, AFM can be applied in a broad range of environments (UHV, air, liquid, gases, etc). This is the unique feature of the microscopic method that makes it a necessary tool in research laboratories. Naturally, imaging under liquid has attracted a major interest because of biological studies and, despite some difficulties related to the control of oscillatory AFM techniques in viscous media, these applications are well recognized. On other side, the use of AFM in ultra high vacuum (UHV) is also well-established with its own specifics. In UHV the quality factor of the probe is extremely high and this makes frequency modulation mode practically exclusive for the applications. Such studies are addressing fundamental issues of surface science and catalysis with the experiments performed on clean crystalline samples at the atomic-scale. A high-cost of UHV equipment and labor-intensive measurements does not allow this field to become expansive. There is another area of AFM applications i.e. the studies in different gas environments that is not yet in the focus of many researchers. A potential of observing new phenomena in the environmental experiments is very high because AFM is practically the only microscopic technique that provides an access to materials and their changes caused by the environment.

A short review of AFM measurements in various gas environments is the subject of this Application Note. The studies were performed on different organic and polymer samples in an environmental chamber of the Agilent 5500 scanning probe microscope, Figure 1. A sample plate is at the top of the chamber, which is made of glass and has several fittings limiting an exchange with the laboratory air. Injection of a small volume (1-3ml) of water or organic solvents to the bottom of the chamber followed by its evaporation will change the sample environment making it humid or filled with organic vapors. The humidity level is judged by a humidity meter inserted into the chamber and drying can be assisted by purging inert gases (such as nitrogen or argon) through four ports. Methanol, toluene, benzene and tetrahydrofuran were applied in our studies, some of them continued for many hours, and these solvents did not cause any deterioration of the microscope.

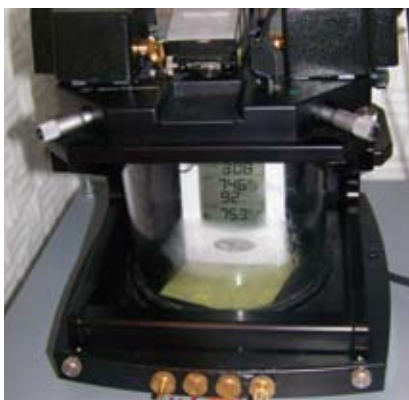


Figure 1. An environmental chamber of Agilent 5500 scanning probe microscope. The humidity meter shows 92%RH environment.

spirals were preserved on the surface basically for unlimited time. These observations can be rationally explained by a sublimation of self-assemblies formed of shorter  $F_{12}H_8$  molecules. The self-assemblies are constructed of fluoroalkane molecules with chains oriented in the vertical direction with the fluorinated parts facing air [2]. This

will explain the height difference of the  $F_{12}H_{20}$  and  $F_{12}H_8$  self-assemblies. Their identical surface potential is related to strength and orientation of molecular dipole at the  $-CH_2-CF_2-$  central junction [3]. Weak intermolecular interactions between the fluoroalkanes molecules lead to the sublimation of their shorter homologs at ambient conditions.

Specific features of using different substrates such as gold and graphite in ambient conditions studies should be considered by AFM practitioners. Our earlier surface potential studies revealed that Au(111) and graphite substrates are contaminated in air: the first one – fast, the second slowly, within the hours. In air, graphite and similar substrates, e.g.  $MoS_2$ , can be covered by molecular layers of volatile compounds. For example, a presence of dodecanol vapor near these substrates might induce a formation of stripped molecular patterns on their surface. The phase images of such patterns

### AFM Studies in Ambient Conditions

AFM measurements are routinely performed at ambient conditions and we might undermine the fact that some dynamic processes proceed in this environment. The illustrative example is taken from studies of fluoroalkanes –  $F(CF_2)_n(CH_2)_mH - F_nH_m^-$ , which are molecules that form different self-assemblies due to dissimilar nature of their hydrogenated and fluorinated parts [1]. When a solution containing  $F_{12}H_{20}$  and  $F_{12}H_8$  molecules was spread on mica substrate, self-assemblies of two types were formed on the substrate. The topography and surface potential images, which were recorded in single-pass Kelvin force microscopy (KFM), in Figure 2A revealed the compact domains and arrays of spirals. The spirals arrays are slightly higher than the compact domains but their surface potential are practically identical. The images were recorded within the 1<sup>st</sup> hour after the preparation and 3 hours later the compact domains vanished from the surface as seen from the images in Figure 2B. The arrays of

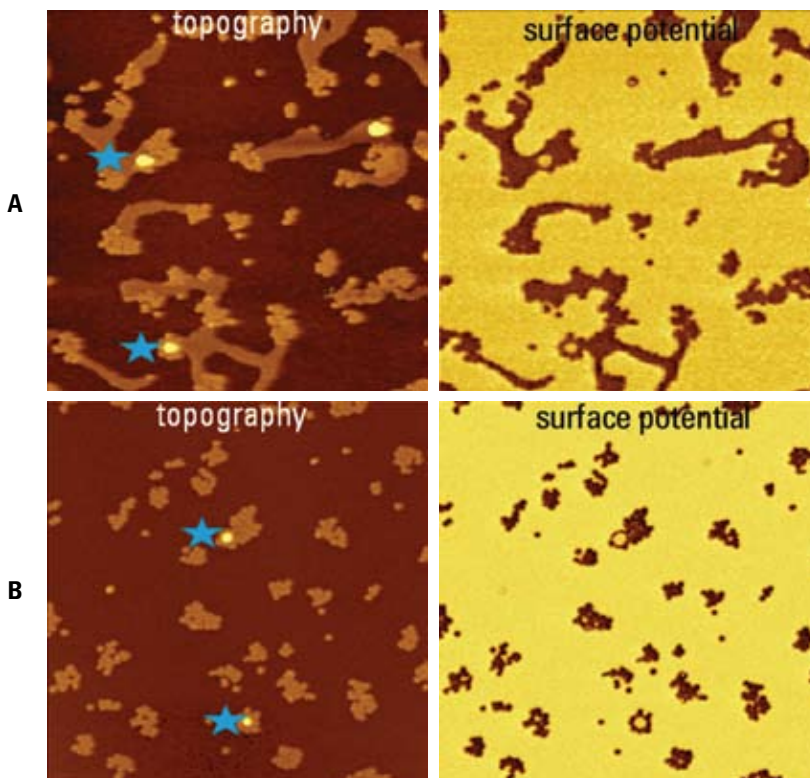


Figure 2. (A) AFM images of  $F_{12}H_{20}$  and  $F_{12}H_8$  self-assemblies on Si substrate. The sample was examined within 1 hour after its preparation. (B) AFM images of the same sample location 3 hours later. The images were recorded at ambient conditions. The contrast covers height corrugations in the 0-9 nm range, surface potential variations in 0-1.64 V range. Scan size: 3  $\mu m$ .

on graphite and MoS<sub>2</sub> are shown in Figure 3. These structures are characterized by the spacings of 1.6 nm and 3.2 nm that are consistent with the extended single and double length of these molecules. Therefore the observed patterns are most likely associated with chains structure of dodecanol lamellae similar to those visualized in STM images of dodecanol on graphite [4]. Traces of molecular structures with similar and larger spacings, which can be found in AFM images on graphite, might be caused by volatile molecules of fragrance components and short chained alkanes.

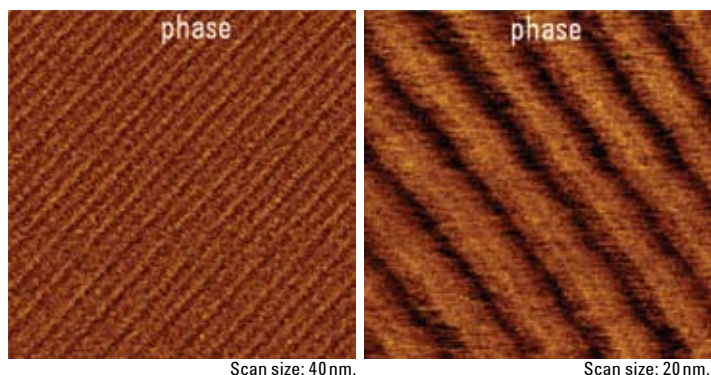


Figure 3. AFM images of dodecanol layer on graphite and MoS<sub>2</sub> substrates. The contrast covers the phase variations in the 0-10 degrees range.

### Examples of AFM Applications in Different Environments

Observations of single macromolecules are one of the attractive AFM applications that start with visualization of DNA molecules. First synthetic macromolecules, which were portrayed with AFM, were single strands of block copolymer of polymethylmethacrylate (PMMA) and polystyrene (PS) [5]. The single macromolecules of the block copolymer were transferred from a water sub-phase of a Langmuir trough onto a mica substrate. The AFM images showed that hydrophilic PMMA segments were unfolded and the hydrophobic PS segments were coiled. On a change of humidity from moderate to 95% RH (RH-relative humidity) a reversible coiling of PMMA segments were monitored with the AFM. Similar structural reorganization was monitored for individual macromolecules of star-polymer, which was prepared from poly(n-butyl methacrylate) (PBMA) and poly(ethylene glycol) methyl ether methacrylate (PEGMA) using multifunctional macroinitiator. PBMA is forming the core of the polymer and PEGMA hydrophilic arms are extended away on mica substrate [6]. This conformation is clearly seen in AFM images recorded at low and moderate humidity, Figure 4A. At conditions of high humidity the molecules are changing their conformation to globular that is reflected in their height increase,

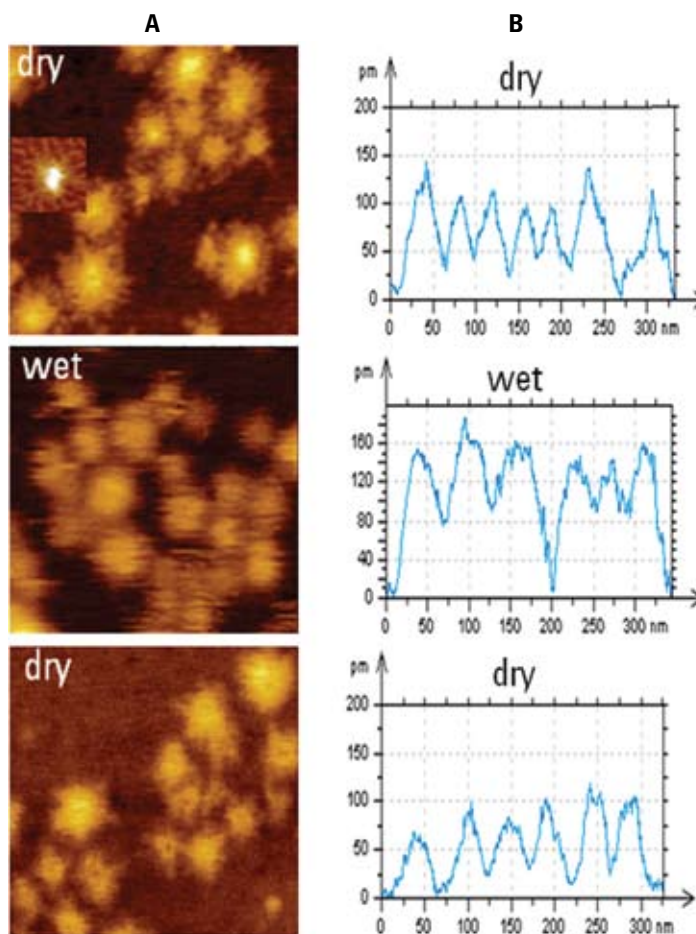


Figure 4. (Left) Topography images of star-shaped block copolymer on mica substrate in dry and wet (95%RH) environment. A high-resolution pattern of the macromolecule is inserted in top image. (Right) Topography cross-section profiles taken across of several macromolecules. Scan size: 250 nm.

Figure 4B. This can be tentatively explained by an aggregation of molecular arms with water molecules. This process is reversible and the initial conformation was restored when the sample was dried.

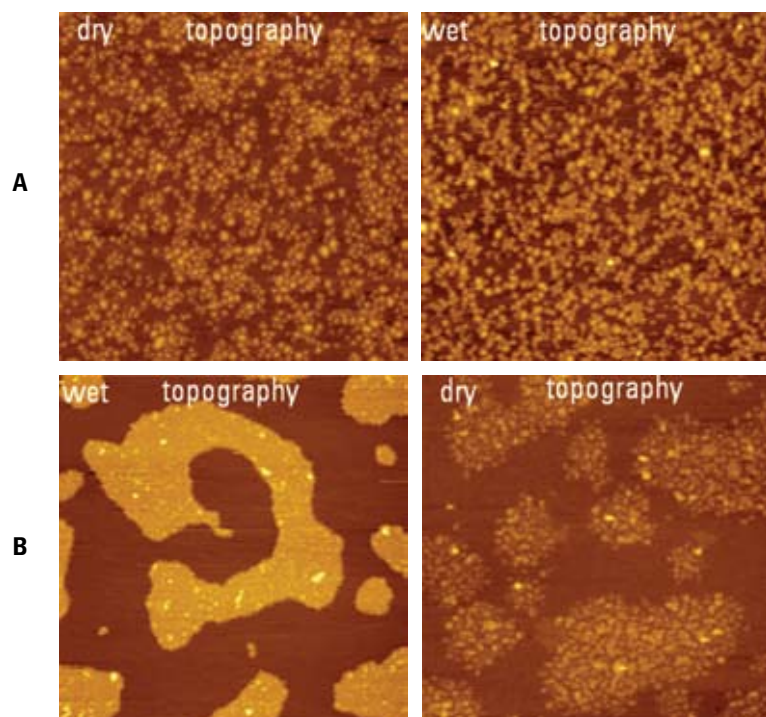


Figure 5. AFM images of star-shaped block copolymer on mica substrate in dry and wet (95%RH) environment. The contrast covers height corrugations in the 0-0.8nm range. Scan size: 2  $\mu$ m.

On the larger scale the humidity-induced transformations were first less noticeable with only through height changes of individual molecules, Figure 5A. However after several hours in wet environment the individual molecules formed the compact domains most likely through intermolecular interactions of peripheral hydrophilic segments, Figure 5B. The results of drying the conformational changes led to a "decomposition" of the domains into individual molecules which adopt the conformation with the stretched hydrophilic arms. The demonstrated

monitoring of structural molecular changes caused by humidity changes can be substantially broaden to other molecular systems. A presence of ultrathin water layer on mica surface in humid atmosphere can promote different self-assembled processes such as described in [7], where the *ex-situ* AFM monitoring has been applied for visualization of the water-induced peptide self-organization.

Fluoroalkanes,  $F_nH_m$ , form different self-assembled structures such as spirals, toroids, ribbons and their

intermediates. An energy balance in these self-assemblies is quite delicate and transformations of one type of self-assembly to another can be promoted by various stimuli including organic vapors [2]. It was shown that an exposure of  $F_{14}H_{20}$  adsorbate, which was prepared by spin-casting from decalin solution on mica, to hexafluoroxylyene (HFX) vapor initiated a conversion of the straight ribbons to bent ribbons and spirals. In the experiments with a HFX born sample, a decalin vapor triggered a transformation of the spirals to straight ribbons. The conversion of the spirals to toroids was also observed when the  $F_{14}H_{20}$  sample on Si wafer spent 2 days in humid atmosphere [3]. Recently we have extended the experiments in humidity to methanol and dodecanol environments. In these studies we used single-pass KFM in the intermittent contact that avoids screening of local electric properties common for non-contact KFM applications [8].

$F_{14}H_{20}$  spirals are commonly seen in the fluoroalkanes adsorbate on Si substrate, which are prepared by spin-casting of their solutions in perfluorodecalin. Topography images in Figures 6A-B reveal the arrays of spirals, which are between 3 and 4 nm in height. In between the arrays a thin layer of fluoroalkane molecules covers the substrate. According to KFM data [3] these molecules are lying flat so that their dipole moment doesn't contribute to surface potential the way the vertically oriented molecules of the self-assemblies do. When the sample environment was changed to

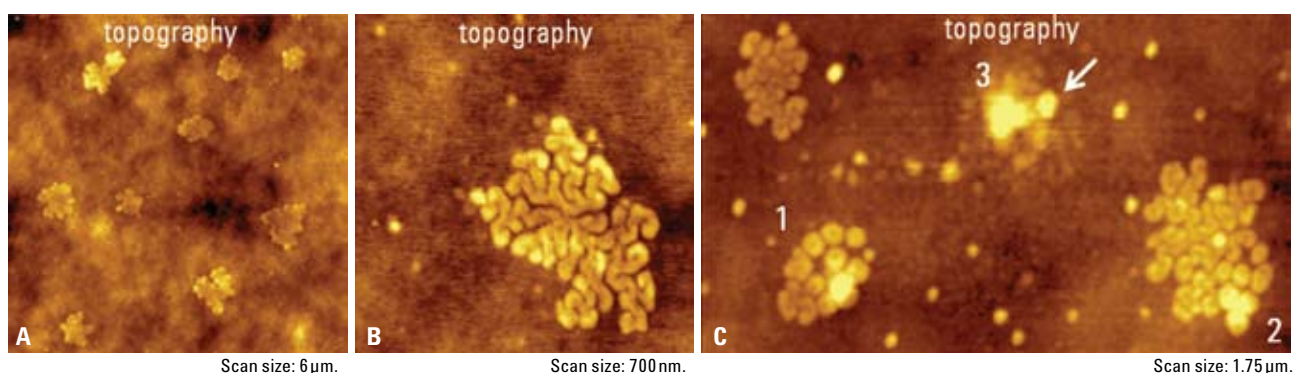


Figure 6. AFM images of  $F_{14}H_{20}$  self-assemblies on Si substrate in dry (A, B) and in 95%RH (C) environments. In C a white arrow indicates a single toroid self-assembly and numbers 1-3 designated the arrays and location that underwent structural changes. The contrast covers height corrugations in the 0-8nm range in A, in the 0-6nm range in B and in the 0-12nm range in C.



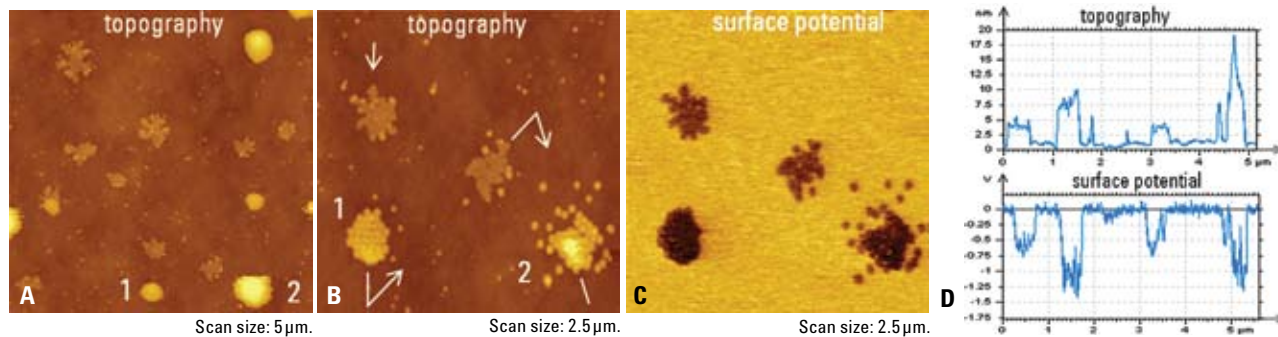


Figure 7. (A-C) AFM images of  $F_{14}H_{20}$  self-assemblies on Si substrate in environment of dodecanol vapor. (D) Cross-section profiles taken in topography (B) and surface potential (C) images across the direction indicated in B with white lines and arrows. The contrast covers the height corrugations in the 0-60 nm range in A, in the 0-20 nm range in B and the potential variations in the 0-2.2V range in C.

humid with 92-95%RH and it stayed there for many hours, several effects were noticed. First of all, one can see a formation of nanodroplets of condensed water in different sample locations some of them are the arrays of  $F_{14}H_{20}$  spirals. If additional amount of water was not injected into the chamber the droplets slowly evaporated leaving toroids structures at their formed locations in the spirals arrays. Two such locations (#1 and #2) are marked in the topography image in Figure 6C. Newly formed toroids are more bulky than nearby spirals whereas the latter are also slightly increased in height compared to their dimensions in air. This observation hints on a formation of water-fluoroalkane aggregate that facilitate the spirals-toroid conversion. Additionally one can also see the surface locations free of the  $F_{14}H_{20}$  spirals where water droplets have been present. One of such locations is marked as #3 in Figure 6C. It is likely that a water nanodroplet has perturbed this area making it elevated and structured into small grains with one bulky toroid emerged.

Similar changes of spirals' dimensions and their slow transformation into toroids was observed in methanol vapor [9]. The images in Figure 7A-C demonstrate the effect of dodecanol vapor. Several bright patterns in topography image (Figure 7A) represent dodecanol droplets condensed on the arrays of  $F_{14}H_{20}$  spirals. This process was promoted by a slight cooling of the sample environment, 5-8 degrees below room temperature. On return to room temperature, these droplets evaporated

and left a set of toroids instead of spirals as seen from a comparison of locations #1 and #2 in Figures 7A-B. At the location #2 a number of toroids were spread away most likely in presence of the dodecanol droplet that covered them. The comparison of the arrays of spirals and sets of newly formed toroids in topography and surfaces potential images (Figures 7B-C) showed that these structures are quite different. These differences are best seen in the cross-section profiles (Figure 7D), which were taken along the "zigzag" direction marked with white arrows and lines in the topography image. The cross-section profiles have revealed that the toroids are much higher and exhibit stronger negative potential. The effects are most likely related to a presence of dodecanol molecules in the toroids or closely attached to them. This suggestion was supported by the fact that after opening the chamber to air these differences were practically eliminated. In case of the toroids formed in presence of water (Figure 6C), the height increase was similar but the changes of surface potential much smaller. They also disappeared after the sample was brought to ambient conditions (humidity ~40%RH). These observations indicate that electrostatic interactions between the fluoroalkane and polar water and alcohol molecules are involved in the self-assembly process of  $F_{14}H_{20}$ . High surface potential (~-1.25V) in the suggested complexes of dodecanol molecules and the fluoroalkane self-assembly requires a better understanding.

Compositional AFM imaging of block copolymers is one of the common applications of this technique in studies of polymer materials. A dissimilar nature of the polymer blocks in these materials leads to microphase separation with typical spacings in the 5-100 nm range. When block copolymer films are prepared on flat substrates by spin-casting of their solution the equilibrium morphology might not be formed during fast evaporation of the solvent. In such cases thermal annealing of the block copolymer films well above their glass transition temperatures ( $T_g$ ) is applied to achieve the regular microphase separated patterns. The latter depends on the nature and volume of the components and can be properly chosen to address the needs of nanoscale lithography and design of nanoporous structures. AFM has been applied for *ex situ* and *in situ* monitoring of thermal annealing of block copolymers and visualization of dynamics of structural defects [10]. Swelling of block copolymer films in vapor of common solvent, which initiate molecular motions of the components, is alternative procedure for achieving equilibrium microphase morphology of block copolymers [11]. In this way there is no danger of heating-related problems of unwanted polymer oxidation. An example of AFM *in situ* observations of a solvent-vapor assisted annealing of triblock copolymer poly(styrene)-*b*-poly(butadiene)-*b*-poly(styrene) (PS-*b*-PB-*b*-PS) film on Si substrate is shown in Figures 8A-D. As PS is the major component in the examined polymer its morphology is characterized by PB cylinders imbedded into PS matrix. In

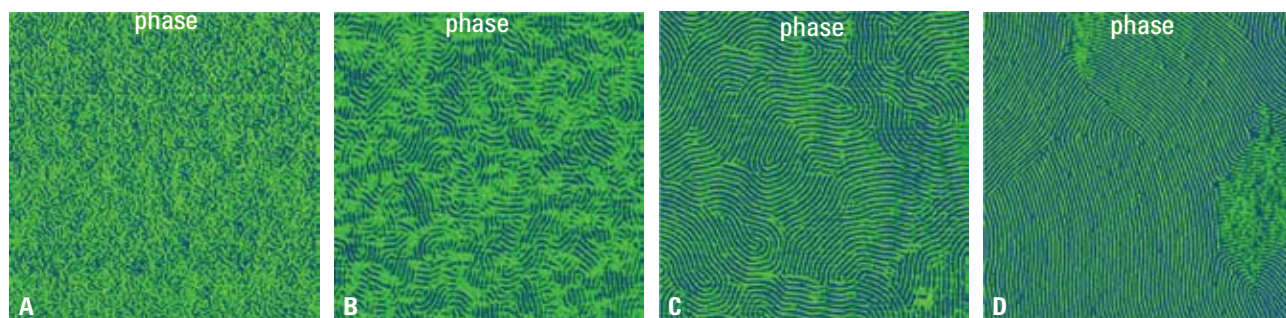


Figure 8. AFM images of thin film of triblock copolymer PS-*b*-PB-*b*-PS on Si substrate. The image in A was obtained immediately after toluene was injected into the environmental chamber. The images in B-D were recorded after 3 hours intervals. The contrast covers the phase changes in the 0-20 degrees range. Scan size: 2.5  $\mu$ m.

the spin-cast film the PB cylinders are short and curved (Figure 8A) and the microstructure exhibits no long-range order. The situation gradually changed with the film exposure to toluene vapor. The in-plane cylinders become extended and formed the ordered domains of hundreds of nanometers in size at 3 hours exposure. On further vapor-induced annealing the extended cylinders and their domains reached several microns in size, Figures 8C-D.

In the attempt to use the poly(ethylene oxide-*b*-methyl methacrylate-*b*-styrene) (PEO-*b*-PMMA-*b*-PS) morphology as a nanoporous media thin films of this block copolymer were annealed in benzene vapor at different humidity [12]. This motivation was based on the high lateral order and facile degradability of the constituents of this block copolymer. In ideal nanoporous morphology the vertically oriented PMMA cylinders should be perfectly ordered (and finally etched away) within the PS matrix with PEO blocks interfacing these components. The initial 20-nm thin film was prepared on a Si substrate by spin-casting its benzene solution. The morphology changes that accompanied the annealing of ultrathin film of this block copolymer in benzene vapor at moderate humidity of 40% RH are illustrated in Figures 9A-B. The images in Figure 9A show the gradual surface changes after the injection of benzene. The left image was recorded in the scanning up direction and the initial benzene effect caused the disappearance of small bright domains inside the surface depressions. The effect can be explained by dissolving of minor blocks. In the continuing images (middle and right) the surface order was gradually changing and

nanoscale features become smeared. This observation is consistent with the fact that benzene is a good solvent for this block copolymer. The morphology changes were stopped by opening the chamber to air and the sample morphology was slightly changed as compared with the initial one (left image in Figure 9B). Further morphology changes, which finally led to the microphase separation pattern with in-plane cylinders [13], are presented in the middle and right images of Figure 9B. In another experiment the PEO-*b*-PMMA-*b*-PS film was deposited from its benzene solution on oriented polytetrafluoroethylene (PTFE) layer, which was prepared by a unidirectional rubbing of this polymer on glass at 300°C. In this case the vapor-induced annealing lead to the well-oriented structure with two preferential orientations of cylinders: along the rubbing direction and perpendicular to

it, Figure 10. This example emphasizes the role of the substrate in defining the morphology of block copolymers in thin layers.

A combined use of environmental studies with compositional imaging of heterogeneous polymers can make easy recognition of the individual components. Selective swelling induces a lowering of  $T_g$  of a particular constituent that provokes a change of its local mechanical and electric properties and the related image contrast. For example an increase of humidity induces a swelling of water channels in Nafion membranes and the latter became pronounced in phase images and in surface potential images. Similar, the high-humidity swelling of hydrophilic poly(styrene sulfonate)(PSS) domains lowered their surface potential, and this component became clearly distinguished in surface potential

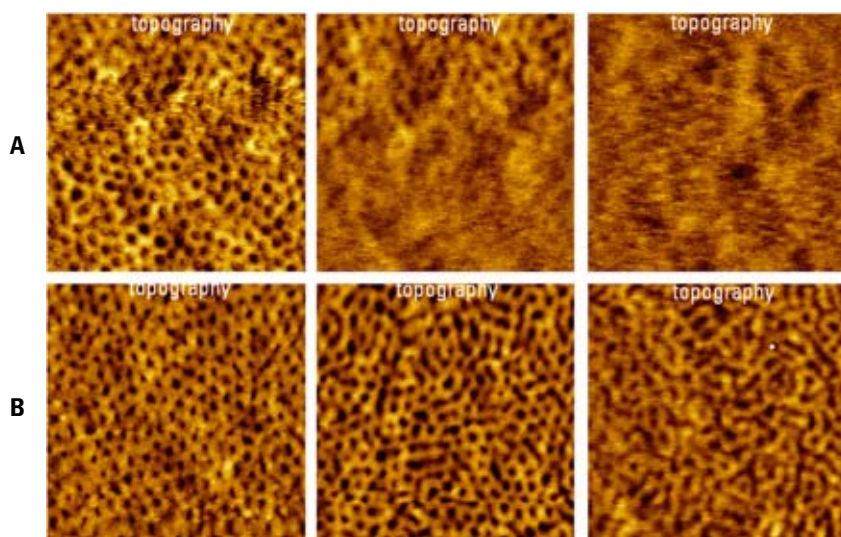


Figure 9. AFM images of ultrathin film of PEO-*b*-PMMA-*b*-PS triblock copolymer on Si substrate. The images in A were recorded in benzene vapor. The images in B were recorded in air. The contrast covers the height corrugations in the 0-4 nm range. Scan size: 700 nm.

images of PEDOT:PSS blend, (PEDOT - poly(3,4-ethylenedioxythiophene), which is the important component of organic solar cells and transistors. These examples were described in the previous Application Note [13]. Here we present the combined use of environmental imaging and detection of electrostatic force gradient ( $dC/dZ$ ), which provides the information about local dielectric properties of materials [14, 15]. In single-pass measurements of topography, surface potential and  $dC/dZ$  the electrostatic force interactions are measured at low frequency ( $\omega_{elec} = 3-5\text{ kHz}$ ) whereas tracking of topography is arranged at the resonant frequency of AFM probes (typically in the 50-350 kHz range). The electrostatic force is stimulated by applying AC voltage at  $\omega_{elec}$  and its response at and  $2\omega_{elec}$  is employed, respectively, for surface potential and  $dC/dZ$  studies. The polymer blend consisting of equal amounts of PS and poly(vinyl acetate) was examined with  $dC/dZ$  measurements at various humidity and in methanol and toluene vapors.

Topography and  $dC/dZ$  images (amplitude and phase), which are presented in Figures 11A-C, were collected in the scan direction from bottom to top. At the beginning of the scan 2 ml of methanol were injected into the chamber and the methanol vapor effect becomes noticeable at the middle of the scan. Initial morphology of PS-PVAC blend is characterized by the micron-size spherical domains embedded into a matrix, Figure 11A. In recent study of PS-PVAC in UHV [16] the dielectric contrast of the domains has changed at temperatures near  $T_g$  of PVAC and, therefore, the domains were

assigned to this component. A bright appearance of the spheres in the  $dC/dZ$  amplitude image in Figure 11B is consistent with the assignment. There was practically no contrast in the  $dC/dZ$  phase image when imaging was performed in air, Figure 11C. The image changes induced by methanol vapor become noticeable in all three images. In the topography image narrow rims, which surround the spheres and reflect an immiscibility of the blend components, disappeared due to swelling and expansion of the PVAC domains. On methanol exposure the  $dC/dZ$  amplitude signal has substantially increased. The  $dC/dZ$  phase contrast most likely reflects complex permittivity of PVAC in swollen state at a particular frequency. These changes were reversible and immediately disappeared as the chamber was opened to air.

### Concluding Remarks

This application note is written to bring the attention of AFM practitioners to capabilities of environmental studies, which are not fully developed and appreciated but which offer unique possibilities for characterization of

different materials. A collection of practical examples discussed above demonstrates the strength of AFM studies in different gas environments for organic and polymer samples. The solvent and water molecules initiate swelling and structural transformations in a number of samples that helps identification of the components of multi-component materials and explore novel phenomena at the nanoscale level. A combined use of environmental imaging and AFM-based methods of high-resolution visualization of surface structures and local mechanical and electric studies is the solid basis for comprehensive nanoscale characterization of materials.

### Acknowledgments

The author is thankful to Prof. M. Moeller (DWI, Aachen, Germany), Prof. E. Kramer (UCSB, Santa Barbara, USA) and Prof. H.-A. Klok (EPFL, Lausanne, Switzerland) for samples of fluoroalkanes, PEO-*b*-PMMA-*b*-PS and multiarm star block copolymer, respectively.

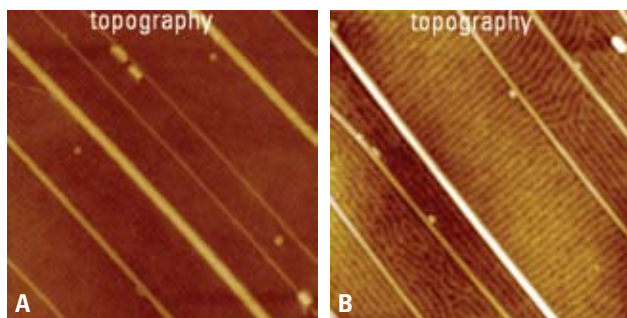


Figure 10. AFM images of thin film of PEO-*b*-PMMA-*b*-PS triblock copolymer on rubbed PTFE layer. The contrast covers the height corrugations in the 0-10 nm scale. Scan size: 3  $\mu\text{m}$ .

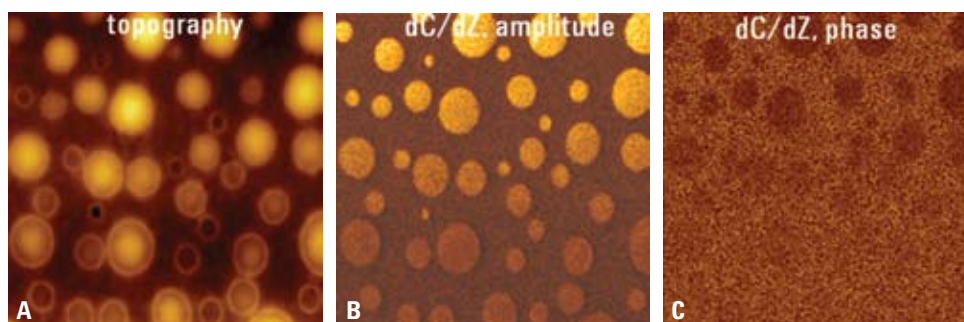


Figure 11. AFM images of 80-nm thick film of PVAC/PS blend on ITO glass. The images were obtained by scanning from bottom to top. The methanol was injected at the beginning of the scan (scan rate 0.8 Hz). The contrast covers height corrugations in the 0-35 nm range,  $dC/dZ$  amplitude alternations in the 0-180 mV range and  $dC/dZ$  phase changes in the 0-20 degrees range. Scan size: 3  $\mu\text{m}$ .

## References

1. J.F. Rabolt, T.P. Russell, and R.J. Twieg "Structural studies of semifluorinated n-alkanes. 1. Synthesis and characterization of  $F(CF_2)_n(CH_2)_mH$  in the solid state" *Macromolecules* **1984**, *17*, 2786–2794.
2. A. Mourran, B. Tartsch, M. Gallyamov, S. Magonov, D. Lambrea, B.I. Ostrovskii, I.P. Dolbnya, W.H. de Jeu, and M. Moeller "Self-assembly of the perfluoroalkyl-alkane F14H20 in ultrathin films" *Langmuir* **2005**, *21*, 2308–2316.
3. J. Alexander, S. Magonov and M. Moeller "Topography and surface potential in Kelvin force microscopy of perfluoroalkyl alkanes self-assemblies" *J. Vac. Sci. Techn. B*, **2009**, *27*, 903–911.
4. C.L. Claypool, F. Faglioni, W.A. Goddard III, H.B. Gray, N.S. Lewis, and R.A. Marcus "Source of image contrast in STM images of functionalized alkanes on graphite: a systematic functional group approach" *J. Phys. Chem. B* **1997**, *101*, 5978–5995.
5. J. Kumaki, Y. Nichikawa, and T. Hashimoto "Visualization of Single-Chain Conformations of a Synthetic Polymer with Atomic Force Microscopy" *JACS* **1996**, *118*, 3321–3322.
6. G. Kreutzer, C. Ternat, T.Q. Nguyen, C.J.G. Plummer, J.-A. E. Månson, V. Castelletto, I.W. Hamley, F. Sun, S.S. Sheiko, and H.-A. Klok "Water-soluble, unimolecular containers based on amphiphilic multiarm star block copolymers" *Macromolecules* **2006**, *39*, 4507–4516.
7. H. Li, F. Zhang, Y. Zhang, M. Ye, B. Zhou, Y.-Z. Tang, H.-J. Yang, M.-Y. Xie, S.-F. Chen, J.-H. He, H.-P. Fang and J. Hu "Peptide Diffusion and Self-Assembly in Ambient Water Nanofilm on Mica Surface" *J. Phys. Chem. B*, **2009**, *113*, 8795–8799.
8. H. Sugimura, Y. Ishida, K. Hayashi, O. Takai, N. Nakagiri "Potential shielding by the surface water layer in Kelvin probe force microscopy" *Appl. Phys. Lett.* **2002**, *80*, 1459–1461.
9. S. Magonov and J. Alexander "Single-Pass Kelvin Force Microscopy and dC/dZ Measurements in the Intermittent Contact: Applications to Polymer Materials" *Beilstein Journ. Nanotech.* **2010**, submitted.
10. C. Harrison, D.H. Adamson, Z. Cheng, J.M. Sebastian, S. Sethuraman, D.A. Huse, R.A. Register, P.M. Chaikin, "Mechanisms of ordering in striped patterns" *Science* **2000**, *290*, 1558–1560.
11. G. Kim and M. Libera "Morphological Development in Solvent-Cast Polystyrene–Polybutadiene–Polystyrene (SBS) Triblock Copolymer Thin Films" *Macromolecules*, **1998**, *31*, 2569–2577.
12. J. Bang, S.H. Kim, E. Drockenmuller, M.J. Misner, T.P. Russell and C.J. Hawker "Defect-free nanoporous thin films from ABM triblock copolymers" *JACS* **2006**, *128*, 7622–7629
13. J. Bang, B.J. Kim, G.E. Stein, T.P. Russell, X. Li, J. Wang, E.J. Kramer and C.J. Hawker "Effect of Humidity on the Ordering of PEO-based Copolymer Thin Films", *Macromolecules* **2007**, *40*, 7019–7025.
14. S. Magonov, and J. Alexander "Compositional mapping of materials with single-pass Kelvin force microscopy" Application note EN 5900-0000; Agilent Technologies, Inc. March 4, **2010**.
15. L. Fumagalli, G. Gramse, D. Esteban-Ferrer, M.A. Edwards, and G. Gomilla, "Quantifying the dielectric constant of thick insulators using electrostatic force microscopy" *Appl. Phys. Lett.* **2010**, *96*, 183107–183109.
16. C. Riedel, R. Sweeney, N.E. Israeloff, R. Arinero, G.A. Schwartz, A. Alegria, Ph. Tordjeman and J. Colmenero, "Imaging dielectric relaxation in nanostructured polymers by frequency modulation electrostatic force microscopy" *Appl. Phys. Lett.* **2010**, *96*, 213110–213112.

# Young's Modulus of Dielectric 'Low-k' Materials

## Application Note

Jennifer Hay

### Introduction

In digital circuits, insulating dielectrics separate the conducting parts (wire interconnects and transistors) from one another. As components have scaled and transistors have gotten closer and closer together, the insulating dielectrics have thinned to the point where charge build up and crosstalk adversely affect the performance of the device. It is this reduction in scale which drives the need for insulating materials with lower dielectric constant. A 'low-k' material is one with a small value for dielectric constant relative to silicon dioxide (SiO<sub>2</sub>)—a former dielectric of choice. The dielectric constant of SiO<sub>2</sub> is 3.9. This number is the ratio of the permittivity of SiO<sub>2</sub> divided by permittivity of vacuum,

$\epsilon_{\text{SiO}_2}/\epsilon_0$ , where  $\epsilon_0 = 8.854 \times 10^{-6} \text{ pF}\mu\text{m}$ . There are many materials with lower dielectric constants, but few of them can be suitably integrated into a semiconductor manufacturing process [1].

At the extreme, dry air (20C, 1 atm) has a dielectric constant of 1.00059 [2], but dry air cannot keep conducting materials mechanically separated, so it cannot be used as an insulator. But as one incorporates material for structure, the dielectric constant also increases. So the optimization problem in materials development for semiconductors is to lower the permittivity of the dielectric material as far as possible without compromising mechanical integrity, as quantified by the Young's modulus. Generally, processes purposed for reducing permittivity (such as pore introduction) also have the effect of reducing Young's modulus.

For over ten years now, we have provided value to the semiconductor industry by giving them a way to measure Young's modulus of low-k materials as deposited on silicon wafers as shown in Figure 1. This is the single largest industrial application for our technology. This note reports the results for two dielectric materials supplied by a loyal customer.

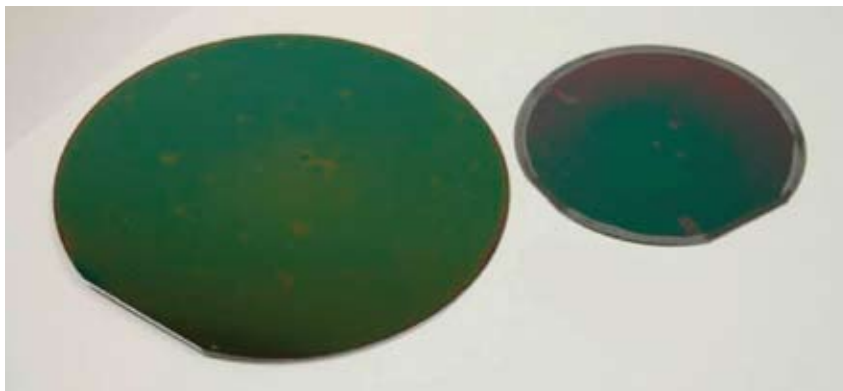


Figure 1. Whole silicon wafers, coated with low-k materials.

## Theory

Instrumented indentation testing (IIT) is a technique for measuring the mechanical properties of materials. It is a development of traditional hardness tests such as Brinell, Rockwell, Vickers, and Knoop. Instrumented indentation testing is similar to traditional hardness testing in that a hard indenter, usually diamond, is pressed into contact with the test material. However, traditional hardness testing yields only one measure of deformation at one applied force, whereas during an IIT test, force and penetration are measured for the entire time that the indenter is in contact with the material. Nearly all of the advantages of IIT derive from this continuous measurement of force and displacement. Instrumented indentation testing is particularly well suited for testing small volumes of material such as thin films, particles, or other small features. It is most commonly used to measure Young's modulus ( $E$ ) and hardness ( $H$ ) [3, 4]. The Young's modulus for a material is the relationship between stress and strain when deformation is elastic.

Using data from a single instrumented indentation test, the reduced modulus ( $E_r$ ) is calculated as

$$E_r = \frac{\sqrt{\pi}}{2} \frac{S}{\sqrt{A}} \quad (\text{Eq. 1})$$

where  $A$  is the contact area and  $S$  is the elastic stiffness of the contact. The elastic stiffness of the contact may be determined in two different ways. It may be determined semi-statically as the change in force with respect to displacement when the indenter is first withdrawn from the sample, because this part of the test manifests purely elastic recovery. It may also be determined dynamically by oscillating the indenter [4, 5]. If  $S$  is determined by the first (semi-static) method, then modulus can only be

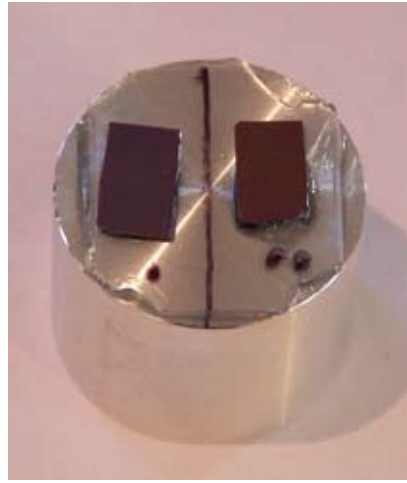


Figure 2. Two low-k samples, as mounted for testing in the G200.

realized at the maximum penetration. But if  $S$  is determined by the second (dynamic) method, then modulus can be determined as a continuous function of penetration depth. This ability to determine properties as a continuous function of penetration depth is particularly useful when testing dielectric films on silicon [6]. Once the elastic stiffness  $S$  has been determined by either method, Young's modulus is calculated from the reduced modulus as

$$E = (1 - \nu^2) \left[ \frac{1}{E_r} - \frac{1 - \nu_i^2}{E_i} \right]^{-1}, \quad (\text{Eq. 2})$$

Where  $\nu_i$  and  $E_i$  are the Poisson's ratio and Young's modulus of diamond, respectively, and  $\nu$  is the Poisson's ratio for the test material. Although calculation of Young's modulus (Eq. 2) requires knowing the Poisson's ratio of the sample ( $\nu$ ), the sensitivity is weak. Sensitivity analysis reveals that a generous uncertainty of 40% in the Poisson's ratio manifests as only a 5% uncertainty in the Young's modulus. Typically, a value of 0.18 is used for dielectrics.

## Experimental Method

The Agilent G200 Nanoindenter was used to test two low-k films on silicon; the thickness of the first film was 1007nm and the thickness of the second film was 445nm. Figure 2 shows the two samples mounted for testing. The G300 Nanoindenter could be used to perform the same measurements with the added benefit of using vacuum to anchor the whole wafer for testing. Both platforms (the G200 and the G300) may be used with either of two actuating/sensing mechanisms or "heads": the XP head or the DCM II head. The DCM II head offers the best precision in fundamental measurements of force, displacement, and phase shift. Thus, it is the best choice for testing low-k films. A DCM II head fitted with a Berkovich diamond indenter was used for all tests reported in this note.

Agilent Nanoindenters have been the industry choice for low-k testing precisely because of the *continuous stiffness measurement* (CSM) option, which measures elastic contact stiffness ( $S$ ) dynamically. With the CSM option, every indentation test returns a complete depth profile of Young's modulus. Using this option, eight tests were performed on each sample. Loading was controlled such that the loading rate divided by the load ( $P'/P$ ) remained constant at 0.05/sec; loading was terminated when the indenter reached a penetration depth of 200nm. The excitation frequency was 75 Hz, and the excitation amplitude was controlled such that the displacement amplitude remained constant at 1 nm.

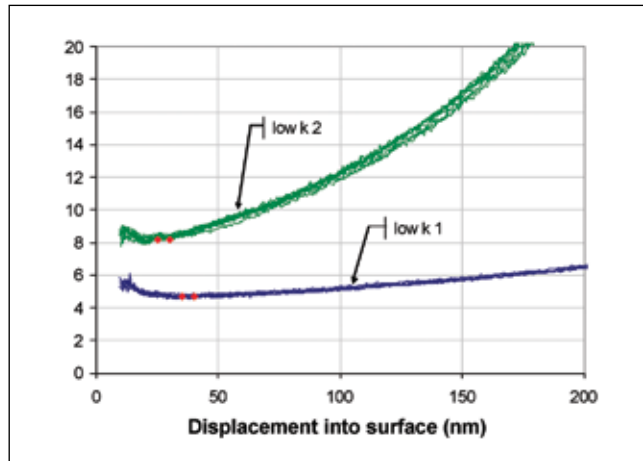


Figure 3. Young's modulus as a function of surface penetration for both samples; all eight tests on each sample are shown. Modulus increases with depth due to increasing substrate influence. Displacement range for citing modulus is bounded by red diamonds.

Sample	Film thickness, nm	Displacement range for cited properties, nm	E, GPa	$\sigma(E)$ , GPa
Low-k 1	1007	35-40	4.69	0.07
Low-k 2	445	25-30	8.23	0.13

Table 1. Summary of results.

## Results and Discussion

Figure 3 shows the depth profiles of Young's modulus; the results of all 16 tests (eight on each sample) are shown. The repeatability is remarkable: it is due to the ultra-high precision of the DCM II and the smoothness and uniformity of the samples. Young's modulus increases as a function of displacement, because the silicon substrate increasingly affects the measurement. Because "low-k 2" is a thinner film, the Young's modulus increases more quickly with depth, relative to "low-k 1". Having such profiles, one can easily discern the critical depth at which the substrate begins to affect the measurement, and thus report film properties over a depth range which is shallower than this critical depth.

The following analysis procedure was applied to each sample to report Young's modulus *for the film alone*. First, a representative displacement range was identified. The minimum value of this range should be large enough to be unaffected by surface anomalies. The

maximum value of this range should be small enough to be unaffected by substrate. These identified ranges are shown on the graph of Figure 3. For the first test, all readings within this displacement range were averaged to get  $E_1$ . Values for subsequent tests were calculated in the same way to get  $E_2, E_3, \dots, E_8$ .

Finally, the average and standard deviation were calculated for all  $n = 8$  tests as

$$\bar{E} = \frac{1}{n} \sum_{j=1}^n E_j, \text{ and} \quad (\text{Eq. 3})$$

$$\sigma(\bar{E}) = \sqrt{\frac{1}{n} \sum_{j=1}^n (E_j - \bar{E})^2}. \quad (\text{Eq. 4})$$

These calculations are fully automated within the regular CSM test method of the controlling software, NanoSuite. The Young's moduli calculated in this way for the two materials are reported in Table 1.

## Conclusions

The Young's moduli of "low-k 1" and "low-k 2" were  $4.67 \pm 0.07$  GPa and  $8.23 \pm 0.13$  GPa, respectively. Because it has a higher modulus, "low-k 2" should withstand the rigors of semiconductor manufacturing better.

The Agilent G200 Nanoindenter with a DCM II head is the industry choice for these measurements because of its high-precision, speed, ease of use, and the CSM option, which delivers properties as a continuous function of penetration depth. With the CSM option, the influence of the substrate is easily discerned, thus allowing properties to be cited at depths that are shallow enough to be free of substrate influence. Without the CSM option, Young's modulus can only be realized at the maximum penetration depth. Therefore, the user must know the zone of substrate independence *a priori* in order to wisely specify the maximum indentation depth. Often, such information is not available prior to testing—CSM is valuable precisely because it eliminates the need for such information. The zone of substrate independence can be identified *after testing* is complete.

## References

1. [http://en.wikipedia.org/wiki/Low-K#Spin-on\\_organic\\_polymeric\\_dielectrics](http://en.wikipedia.org/wiki/Low-K#Spin-on_organic_polymeric_dielectrics)
2. <http://hyperphysics.phy-astr.gsu.edu/Hbase/tables/diel.html>
3. I.N. Sneddon, "The Relation Between Load and Penetration in the Axisymmetric Boussinesq Problem for a Punch of Arbitrary Profile," *Int. J. Eng. Sci.*, Vol. 3, pp. 47-56, 1965.
4. W.C. Oliver and G.M. Pharr, "An Improved Technique for Determining Hardness and Elastic Modulus Using Load and Displacement Sensing Indentation Experiments," *J. Mater. Res.*, Vol. 7 (No. 6), pp. 1564–1583, 1992.
5. W.C. Oliver and J.B. Pethica, "Method for continuous determination of the elastic stiffness of contact between two bodies," U.S. Patent 4848141, 1989.
6. J.L. Hay, "Measuring substrate-independent modulus of dielectric films by instrumented indentation," *J. Mater. Res.*, Vol. 24 (No. 3), pp. 667-677, 2009.





# Nanoindentation, Scratch, and Elevated Temperature Testing of Cellulose and PMMA Films

## Application Note

### Introduction

As plastics and plastic composites are placed into service in more demanding applications, surface modifications are performed to enhance the durability and increase service life. Commonly, hard coatings are used on display screens to prevent damage; for example, coatings are applied to cellular telephone display screens to prevent scratching while the phone is placed in a pocket with keys and other sharp objects. Other surface modifications are made to increase adhesion of multilayered systems, create fade resistant properties, or to increase flexibility. In this article, polymer films with different surface treatments are characterized through nanoindentation, scratch testing,

and elevated temperature testing. Major differences in the indentation and scratch results are shown for the coated samples. In addition, the results for elastic modulus and hardness at elevated temperatures are supplied on four different cellulose films.

### Samples

Seven polymer samples were supplied by a display screen manufacture. The samples were triacetyl cellulose film (coated and uncoated), coated poly(methylmethacrylate) (PMMA), acetate propionate cellulose films, and alcohol saponification cellulose. Table 1 lists each sample and supplies a description.


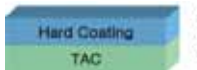

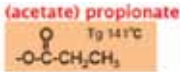
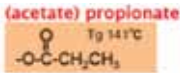
Sample	Description	Sample Geometry
A	triacetyl cellulose film (TAC)	 80µm Triacetyl Cellulose Film
B	Coated TAC	 13µm UV Cured Hard Coating Film 80µm Triacetyl Cellulose Film
C	Coated PMMA	 10µm UV Cured Hard Coating 800µm Polymethylmethacrylate Sheet 10µm UV Cured Hard Coating
D – 1 – 1 (before)	acetate propionate cellulose	
D – 1 – 2 (after)	Alcohol saponification cellulose	
D – 2 – 1 (before)	acetate propionate cellulose	
D – 2 – 2 (after)	Alcohol saponification cellulose	

Table 1. Sample descriptions.

## Test Equipment

All of the tests conducted in this article were performed using an Agilent Nano Indenter G200 equipped with the XP transducer that combines superb load and displacement resolutions with unmatched flexibility in force and displacement ranges. The XP transducer is a Nanomechanical Actuating Transducer (NMAT) that is used to apply loads and measure displacements during indentation tests. Its novel design includes decoupled force application and displacement measurement for unparalleled control and flexibility during testing. A cross-section of the XP-NMAT is shown in Figure 1.

Each of the design elements shown in Figure 1 contribute to the repeatable and reliable measurements performed by the Nano Indenter systems. Control of force is performed using electromagnetic actuation providing three primary advantages:

- 1) High accuracy in force control due to the simple linear relationship between current passed through the coil and the force that is produced.
- 2) Force application over a large displacement range due to the stability of the permanent magnetic field over large distances.
- 3) Flexible force application in both actuating directions because electromagnetic actuation works equally well in both the push and pull directions.

Two leaf springs are used to secure the indentation column for stability and maximum lateral stiffness. The ISO 14577 standard specifies that the samples surface should be within one degree of orthogonal alignment with the indenter; in actuality, this is not just a recommendation, it is a must for repeatable and reliable data. As shown in "Indentation Rules of Thumb" errors in orthogonal alignment can lead to larger errors than expected due to finite lateral stiffness in transducer design [1]. High lateral stiffness is a critical design element of the NMAT and is accomplished by the doubly secured indentation shaft that prevents lateral deflection when indenting and scratching samples with surface roughness or misalignment.

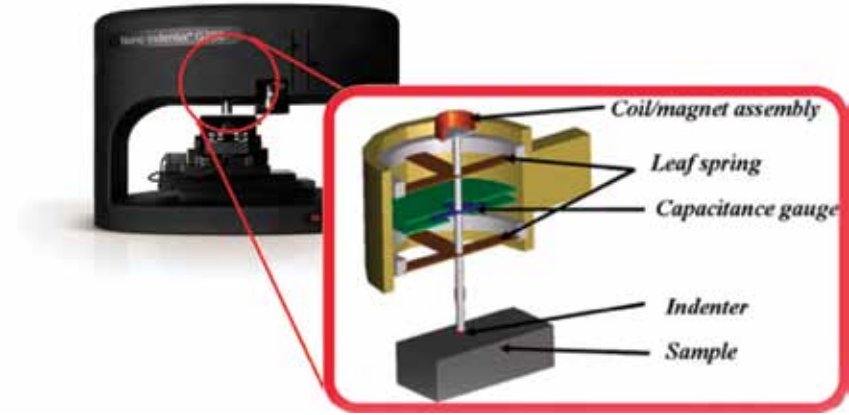


Figure 1. The Agilent Nano Indenter G200 and a cross-sectional diagram of the XP-NMAT.

Range of indenter travel	>1.5 mm
Displacement resolution	0.01 nm
Typical leaf spring stiffness	100 N/m
Maximum Load	500 mN
Load resolution	50 nN
Thermal drift rate*	0.05 nm/s

\*Thermal drift rates are dependent on lab environments.

Table 2. XP-NMAT Specifications.

The final critical design component of the NMAT is the capacitance gauge which is used for sensing displacement. All commercially available nanoindenter platforms use capacitance gauges for measuring displacement. However, the capacitance gauge used in the Agilent transducers are specifically designed to allow ultra-high resolution with unparalleled displacement ranges providing users with maximum testing flexibility. Table 2 lists the specifications of the XP Nano Mechanical Actuating Transducer.

## Test Procedure

### Indentation Tests

To ensure measurements of mechanical properties with the highest integrity, indirect verification of the performance of the Nano Indenter G200 was completed just prior to testing the polymer samples using methods prescribed by ISO 14577, the international standard that governs hardness and mechanical properties measurements by instrumented indentation [2]. In completing this verification, two reference materials,

Corning 7980 (SiO<sub>2</sub>) and Corning 7740 (Pyrex®) were tested at a range of forces from 10 mN to 500 mN. The results from the test method provide a Pass or Fail indication of performance for the instrument. The Pass or Fail criteria are determined by comparing the nominal values of elastic modulus supplied with the reference materials to the measured results and ensuring that the uncertainties in the measured hardness and elastic modulus are less than five percent.

To examine the full load range and the large displacement capabilities of the Nano Indenter G200, nanoindentation tests were performed on samples A, B, and C using a standard tip that allows up to 30 μm of penetration depth. The combination of the large force range and the large displacement range, without compromising instrument resolutions, allowed the complete film response to be measured. While these tests could also be performed using the ISO test method, a cyclic test method was used to highlight the repeatability of the measurements. In this test method the indenter is successively loaded multiple times up to the maximum load, in the same test location, without coming out of contact with the sample. A loading time of 3 seconds was used, with a holding time of 5 seconds and an unloading time of 3 seconds. After the final loading, the load was reduced by 90% and the force was held constant for 75 seconds to determine the drift in the sample. Following the hold for thermal drift evaluation, the indenter was withdrawn completely.

The samples listed as “D” samples were tested at elevated temperature over the range from room temperature to 100 degrees Celsius using the Hot Stage option that is available with the Nano Indenter G200. These tests used a loading time of 1.5 seconds, a hold time of 1.5 seconds, and an unloading time of 1.5 seconds. The tests performed on the hot stage were conducted quickly to avoid problems associated with thermal drift of the sample. Surface temperature of the sample was maintained at the set temperature within  $\pm 0.1$  degrees Celsius. The Hot Stage option allows elevated temperature testing to be completed using nanoindentation over the temperature range from room temperature to 350°C. While the sample is maintained at the set point temperature, an active cooling system is used to remove waste heat from the enclosure and an argon gas supply is used to encapsulate the sample and reduce corrosion on the surface; the argon gas supply is primarily used for testing at temperatures over 200°C.

### Scratch Tests

A ramp-load scratch test was used to conduct five tests on each sample. In a ramp-load scratch test, a tip is brought into contact with the sample; then, the tip is loaded at a constant loading rate while simultaneously translating the sample. Prior to and following the scratch test, a single-line-scan of the surface topography is completed for comparing the original surface to the deformation caused by the scratch test. Therefore, each scratch test consists of three steps: a single-line pre-scan of the area to be scratched, the ramp load scratch test, and a final scan to evaluate the residual deformation. Before and after each step, a pre-profile and a post-profile, usually equal to 20% of the scratch length, is performed so that the software can automatically align the data in the three steps. The original and residual single-line scans allow for the evaluation of deformation mechanisms and the quantification of deformation. The scratch process is diagrammed in Figure 2.

The data from the scratch test provides a plot of the aligned displacement curves on one graph so that the deformation during and after the scratch

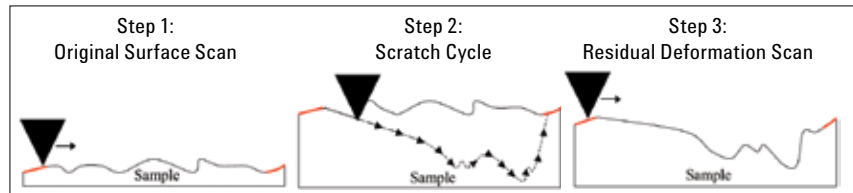


Figure 2. The three step scratch process. The red segments show the pre- and post-profiles performed during each step for aligning the data on a single graph.

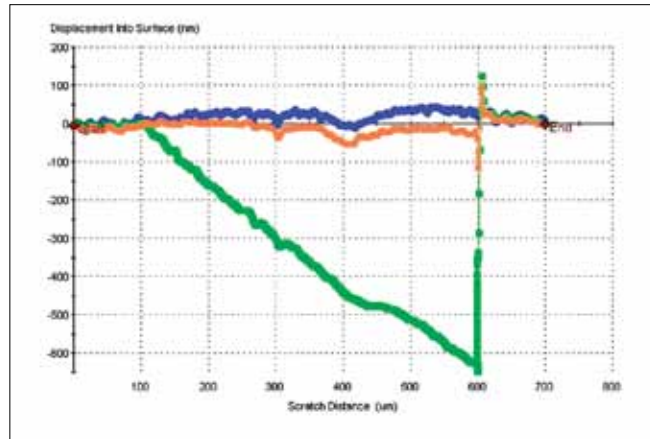


Figure 3. An example of the results from a ramp-load scratch test like the one shown in Figure 2. The original surface morphology is shown in blue, the scratch cycle is shown in green, and the residual deformation scan is shown in orange.

<b>Samples A and B</b>	Scratch Velocity	30 $\mu\text{m/s}$
	Ramp Load Loading Rate	1.1 mN/s
	Maximum Load	A (3mN); B (20 mN)
<b>Sample C</b>	Scratch Velocity	30 $\mu\text{m/s}$
	Ramp Load Loading Rate	0.3 mN/s
	Maximum Load	C (5mN)

Table 3. Scratch parameters for the ramp-load scratch tests. A conical tip with a 10  $\mu\text{m}$  tip radius was used for testing all samples.

can easily be evaluated. Figure 3 shows an example of the aligned displacement curves from an actual scratch test. The original surface morphology is shown in blue, actual scratch cycle is shown in green, and residual deformation scan is shown in orange. In addition to the graph of the displacement curves the lateral force and critical loads are also reported as results.

When performing scratch testing on any sample set, it is critical that the test parameters of scratch velocity, loading rate, and tip geometries remain consistent throughout the samples being compared. This ensures that qualitative comparisons can be made using the resulting data. The test parameters used in testing the polymer materials are listed in Table 3. The

maximum loads vary based on the load required to induce continued failure in the samples.

The tip chosen for conducting the scratch tests was a conical tip with a radius that was approximately 10  $\mu\text{m}$ . A conical tip was chosen because the films and layers were thick. Conical tips are commonly used for scratch testing when localized stress concentrations are undesirable. Another tip that is often used in scratch testing is the cube-corner tip which is a three-sided pyramid and creates a triangular projected contact with the sample; this tip geometry creates high levels of stress in the material during the scratch. Cube-corner tips are commonly used when film thicknesses are less than 2  $\mu\text{m}$ .

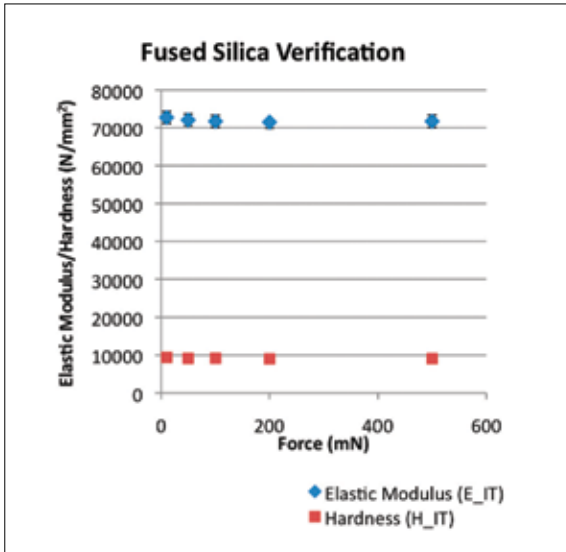


Figure 4. Results for the indirect verification of performance on the fused silica reference material.

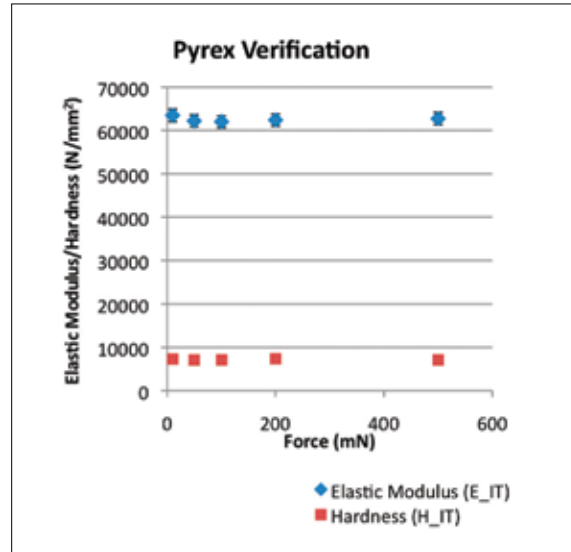


Figure 5. Results for the indirect verification of performance on the Pyrex reference material.

## Results and Discussion

### Indentation Test Results

#### Instrument Indirect Verification per ISO 14577

Fused silica and Pyrex reference materials were tested for instrument verification at loads of 500 mN, 200 mN, 100 mN, 50 mN, and 10 mN. The nominal values of the elastic modulus for the fused silica and Pyrex are 74008 N/mm<sup>2</sup> and 63256 N/mm<sup>2</sup>, respectively. The results of elastic modulus and hardness on the reference materials are shown in Figure 4 and Figure 5, respectively. Each force passed verification for performance on both reference materials. In order to obtain a “Pass” for indirect verification, the instrument must measure the elastic

modulus of two materials and obtain results that are sufficiently close to the values measured by ultrasound; the algorithm for defining “sufficiently close” is prescribed in ISO 14577, Part 2, sections 5.2.5 and 5.2.6. In addition, the repeatability for hardness must be within the limit specified by the standard.

The ease of having a “Pass” or “Fail” result for the indirect verification of the instrument makes the evaluation of the instrument’s performance quick and ensures that measurements with integrity are made. As an example of the information provided for the indirect verification of the instrument, the results for the five tests completed on

the Pyrex reference material at a load of 10 mN are provided in Table 4. Notice that the second column provides a clear indication of acceptable performance.

#### Indentation Results for Samples A, B, and C

Samples A, B, and C were tested using standard nanoindentation with a tip that allows up to 30 μm of penetration depth. Each sample was tested over a range from 1 mN to 500 mN providing near surface results along with the bulk sample results. These samples experienced up to 11 μm of penetration depth when exposed to the maximum load of 500 mN during the tests.

Test	Verification	Maximum Force	Elastic Modulus (E_IT)	Uncertainty in E_IT (Unc. E_IT)	Hardness (H_IT)	Uncertainty in H_IT (Unc. H_IT)	Drift Correction	Test Temperature
		mN	N/mm <sup>2</sup>	N/mm <sup>2</sup>	N/mm <sup>2</sup>	N/mm <sup>2</sup>	nm/s	C
1	PASS	10	62663	1384.1	7224	158.7	-0.045	24.762
2	PASS	10	63447	1409.7	7369	163.2	-0.052	24.746
3	PASS	10	63796	1397.4	7322	161.5	-0.066	24.734
4	PASS	10	63877	1432	7281	161.5	-0.06	24.722
5	PASS	10	63629	1435.6	7282	161.3	-0.062	24.719
Mean		10	63483	1411.8	7296	161.3	-0.057	24.737
Std. Dev.		0	487	22.1	54	1.6	0.008	0.018
% COV		0.05	0.77	1.57	0.74	1	-14.81	0.07

Table 4. Results for the indirect verification at 10 mN of force on the Pyrex reference material. Notice the second column that notifies the user of a “Pass” or “Fail” for the instrument verification.

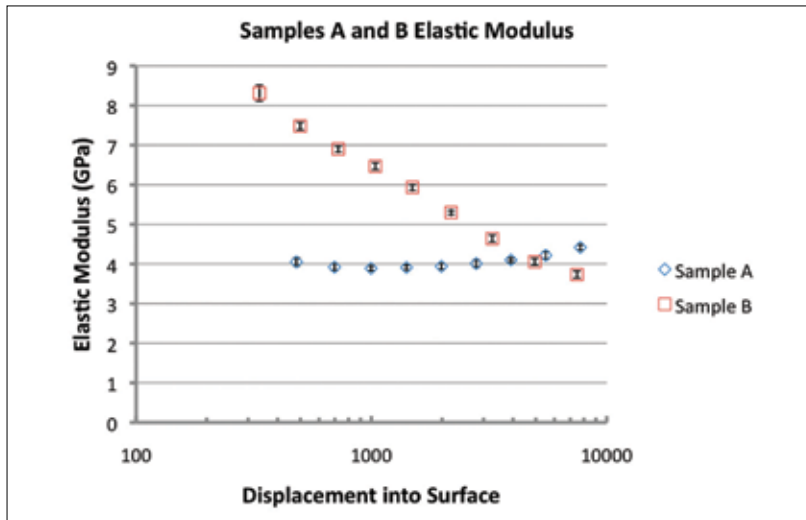


Figure 6. Elastic modulus results for samples A and B. The support of the aluminum sample puck are seen in the results for Sample A past 3000 nm of penetration.

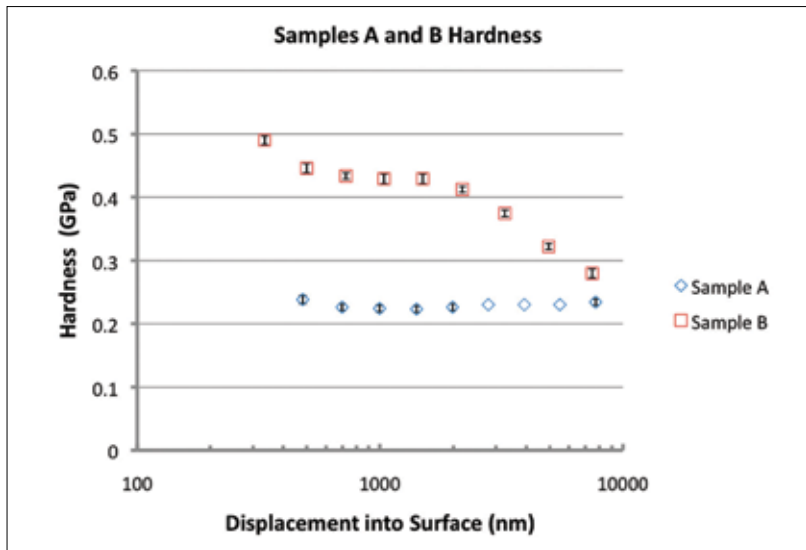


Figure 7. Hardness results for samples A and B. The coating has provided elevated hardness results to 10 μm of penetration.

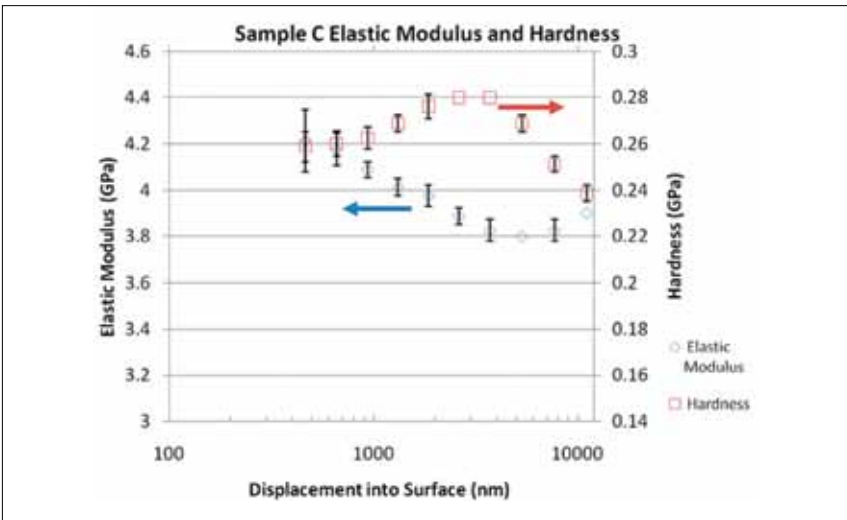


Figure 8. Elastic modulus (left axis) and hardness (right axis) results for Sample C.

The results of the elastic modulus and hardness for samples A and B are shown in Figures 6 and 7. Both of the figures show that the 13 μm hard coating on Sample B provides substantial enhancement of the mechanical properties at the surface of the sample. In Figure 6, the elastic modulus of Sample A shows a significant increase after 3 μm of penetration; however, this rise is not due to an actual change in mechanical properties, it is an artifact of having the thin sample mounted to an aluminum sample puck. Typically, hardness measurements may be made up to 10% of the films thickness, but the elastic modulus is rarely unaffected by the substrate (or in this case the mounting puck) at 10% of the film thickness. Further examination of the 10% rule-of-thumb for obtaining mechanical properties up to 10% of the film thickness is completed elsewhere [1]. Sample B does not show the effects of the sample puck because the sample is much thicker than Sample A.

Hardness results shown in Figure 7 also do not show any influence of the sample mounting puck. Hardness measurements are commonly unaffected by the underlying materials until the penetration depth becomes greater than 10% of the film thickness. The results on Sample B illustrate this response; in Figure 7 the hardness of the 13 μm coating shows properties that are unaffected by the TAC layer up to approximately 12% of the coating thickness. This coating experienced a plateau in hardness of 0.43 GPa between penetration depths of 700 nm and 1500 nm; this is a good representation of the hardness of this coating. Only a small amount of influence from the sample puck is seen in the results of hardness for Sample A and this slight influence starts appearing at 6000 nm.

Sample C also showed enhanced mechanical properties at the surface due to the 10 μm hard coating. Figure 8 displays the results for measurements of elastic modulus and hardness on Sample C. Similar to Sample B, a plateau in the hardness results are seen; however, the plateau in Sample C occurs at penetration depths that are greater than 10% of the thickness of the

coating. The results on this film show that the mechanical properties change as the film is penetrated. As opposed to a plateau in the results of elastic modulus, a minimum exists at 4000 nm of penetration. After the minimum was reached, the tests gradually reached the interface with the PMMA sheet and the elastic modulus started to increase. Undoubtedly, the hardness and elastic modulus measurements were greatly affected by the PMMA sheet at the minimums and maximums obtained from the graph in Figure 8. The reported values are probably lower than the actual values—hardness to a lesser extent—because the nominal elastic modulus for PMMA is approximately 3 GPa [3]. Since this is significantly lower than the measured values for the hard coating, the measured mechanical properties will be deflated at penetration depths that are greater than 10% of the coating thickness. The results for the elastic modulus from this sample could be more accurately determined by using a model that compensates and removes substrate influences from the results; one such model, which was developed by Rar et al., has been seamlessly integrated into the Agilent NanoSuite software to provide researchers with the ability to make substrate independent measurements of elastic modulus on films and coatings [4].

#### *Elevated Temperature Testing of "D" Samples*

The samples that were listed as "D" samples were tested at temperatures ranging from room temperature up to 100°C. Prior to elevating the temperature, each sample was tested 10 times using dynamic indentation, with the Continuous Stiffness Measurement (CSM) option, to a penetration depth of 2000 nm, to determine if the surface properties of the samples changed as a function of penetration into the sample. Figures 9 and 10 show the results for elastic modulus and hardness, respectively, for all four D samples. The benefits of the CSM option are apparent in Figures 9 and 10; this option allows the evolution of mechanical properties to be observed continuously

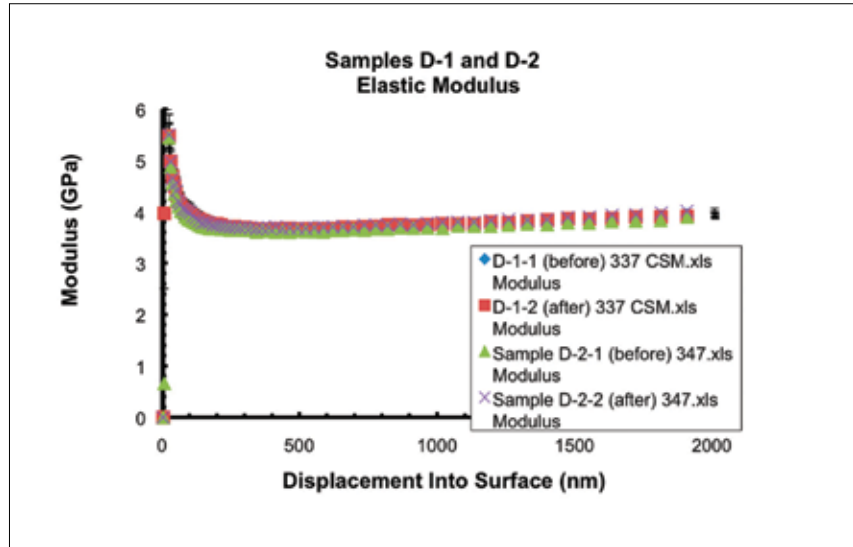


Figure 9. Elastic modulus results for the D Samples using dynamic indentation at room temperature. No separation in the mechanical response of the samples was seen as a function of penetration.

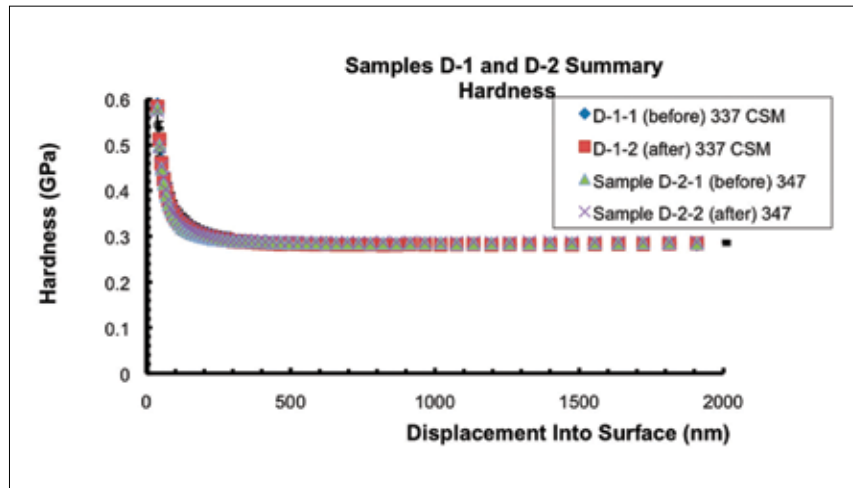


Figure 10. Hardness results for the D Samples using dynamic indentation at room temperature. No separation in the mechanical response of the samples was seen as a function of penetration.

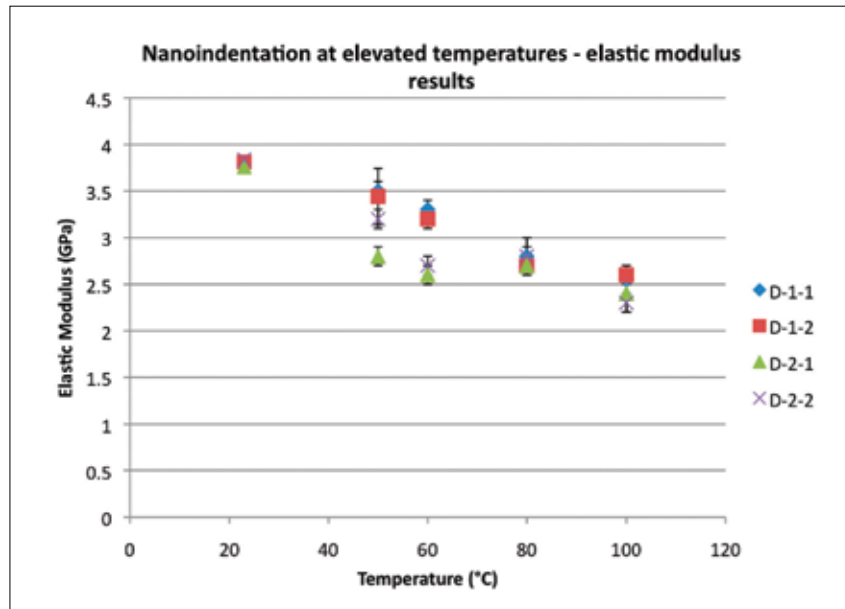


Figure 11. Elastic modulus results for the “D” samples tested at elevated temperatures.

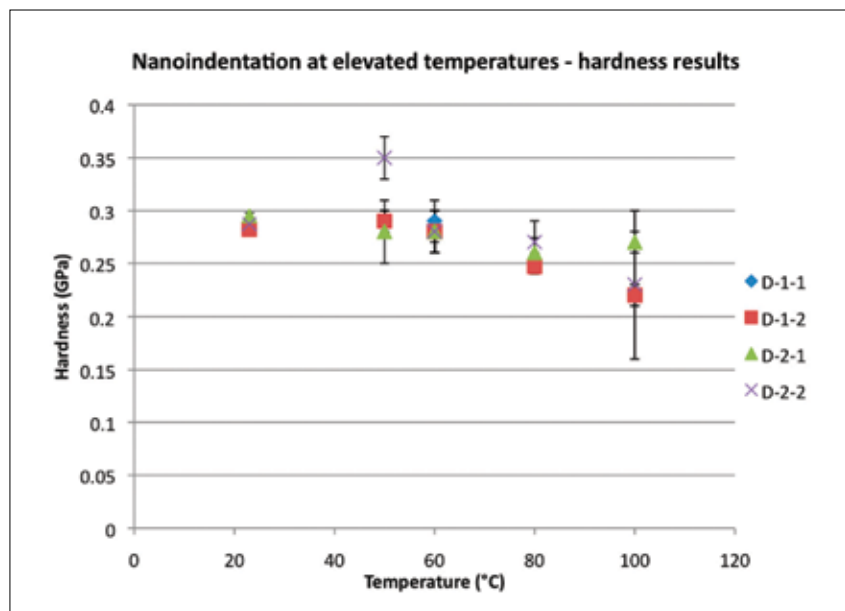


Figure 12. Hardness results for the “D” samples tested at elevated temperatures.

as a function of penetration into the surface of the sample. Surface properties just after contact along with bulk material properties can be measured with only a single indentation. Multiple indentation tests provide a measurement of repeatability for the mechanical properties of the sample; the data displayed in Figures 9 and 10 have one standard deviation errors bars displayed. This data represents the excellent repeatability of the Nano Indenter G200. It is clear from the data that, at room temperature, surface affects are not differentiators between the raw acetate propionate cellulose samples and the alcohol saponification cellulose samples.

Dynamic indentation was used at room temperature to determine if differences in surface properties were present. However, dynamic indentation is only available for room temperature testing; therefore, a set load was selected for performing quasi-static indentation tests at elevated temperatures—in application, the force limit is a user defined input and can be set to any appropriate limit. A maximum indentation load of 8 mN was selected to provide mechanical properties at approximately 1200 nm of penetration.

Ten quasi-static indentation tests to a maximum load of 8 mN were performed on each of the D samples at set temperatures of 50°C, 60°C, 80°C, and 100°C. The results, with one standard deviation error bars, of elastic modulus and hardness for the D samples are shown in Figures 11 and 12, respectively. Close examination of the results reveals that there are no major statistical differences in the mechanical properties of the raw acetate propionate cellulose samples and the alcohol saponification cellulose samples up to a temperature of 100°C. Only minor differences were observed in the measurements of elastic modulus at temperatures of 50°C and 60°C. At these temperatures the two samples listed as D-2 experienced a significant drop in elastic modulus as compared to the D-1 samples.

In Figure 12, Sample D-2-2 had an unusually high hardness at 50°C; more tests should be completed to ensure that this observed difference was not a test or positional artifact. It would be unusual for the hardness of this polymer film to increase as the temperatures increased. In addition, the results on this sample experienced a higher standard deviation as compared to the other samples tested at the same temperatures; this was especially the case for the hardness results at 100°C. The reported hardness values for Sample D-2-2 at temperatures other than 50°C were in line with the results from the other samples.

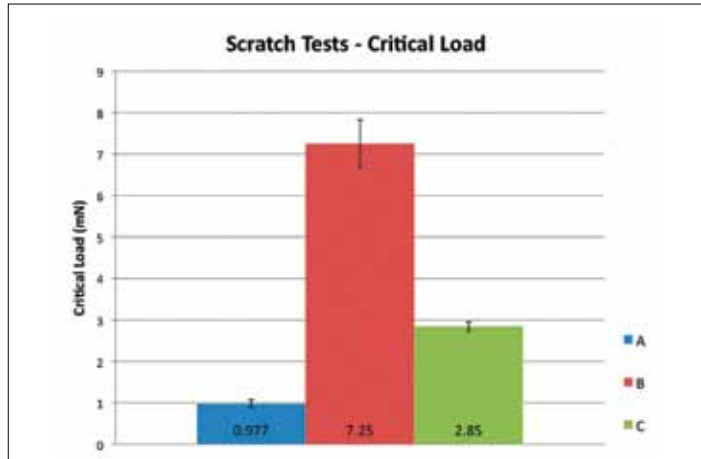


Figure 13. Results for the critical load of each sample.

### Scratch Test Results

The coated samples and the bulk TAC sample were subjected to scratch testing to observe the difference in the deformation mechanisms and to evaluate failure. Each sample was scratched 8 times to ensure repeatability and establish the scatter in the results. A bar graph of the critical loads for each sample is shown in Figure 13. It is clear from the bar graph that the scratch resistance of Sample B has been greatly enhanced by its hard coating when compared to the scratch resistance of Sample A; Sample A failed at a critical load of 0.977 mN while the hard coating on Sample B failed at an average load of 7.25 mN.

Not only did the critical loads differ, differences in the scratch curves and the residual deformations were also apparent for each of the samples. Typical scratch curves for each of the samples tested are displayed in Figures 14 through 19; these figures show the real-time deformation of the samples as the scratch tests progressed. Along with the scratch curves for each sample, a graph of the coefficient of friction during the scratch cycle is also supplied.

### Sample A

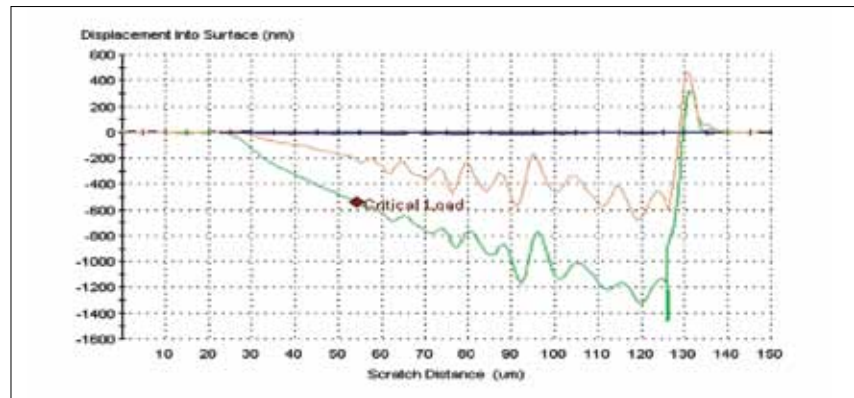


Figure 14. Scratch curves for Sample A. The blue along the x-axis is the original morphology scan, the green trace is the scratch cycle, and the orange trace is the residual deformation scan. All of the curves are aligned and shown on a common graph for the evaluation of failure and examination of deformation mechanisms.

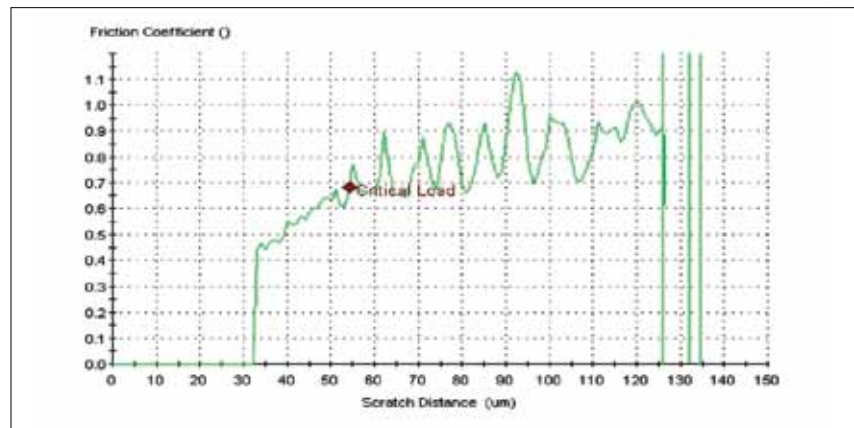


Figure 15. Coefficient of friction during the scratch cycle for Sample A. This is the coefficient of friction for the green penetration curve shown in Figure 19.



## Sample B

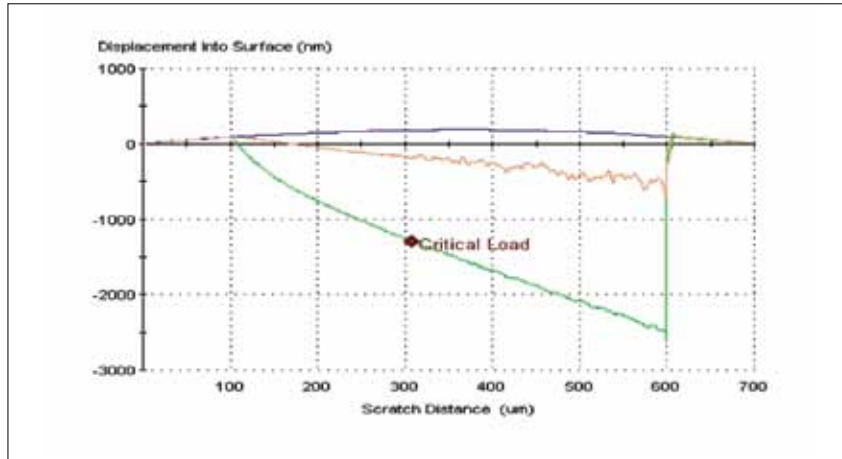


Figure 16. Scratch curves for Sample B. Notice that the scratch cycle (green curve) is smooth while the residual deformation scan (orange curve) shows fluctuation in the penetration depth. This signifies that minor fracturing is occurring instead of the ripping shown in Figure 19.

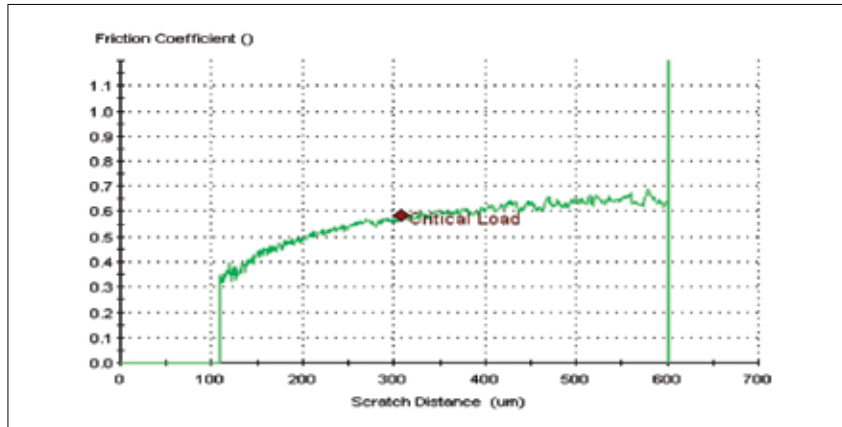


Figure 17. Coefficient of friction during the scratch cycle for Sample B. Minor fluctuations in the coefficient of friction here support the conclusion that minor fracturing is occurring during the scratch.

When comparing the scratch curves of Sample A (Figure 14) to Sample B (Figure 16), two primary differences are noticed. First, the displacement curves display dramatically different failure mechanisms. The green curve in Figure 14 (the green curve shows the path of the scratch tip during the actual scratch cycle) shows that the penetration of the scratch tip wildly fluctuates after the critical load is reached. This suggests that Sample A has experienced massive failure and the material piled up in front of the indenter and ripped off as the test progressed. Notice that the green scratch curve for Sample B does not show the wild fluctuations. During the scratch tests on Sample B, the scratch cycle progressed smoothly and the fluctuations in penetration are only seen in the orange residual deformation scan. Fluctuations in the residual deformation scan along with the absence of fluctuations in the scratch curve, as seen in the results for Sample B, are typically representative of small scale fracturing behind the scratch tip during the test—material behind the scratch tip experiences high tensile stress during the scratch cycle.

To further support the failure modes expressed in the scratch tests of Samples A and B are the differences in the graphs of the coefficient of friction during the scratch cycles. Figures 15 and 17 show the coefficient of friction for samples A and B, respectively, during the scratch cycle. The wild fluctuation in the coefficient of friction for Sample A, shown in Figure 15, make it apparent that material is being ripped off during the scratch cycle. In contrast, Sample B, shown in Figure 17, experienced a smooth slide through the sample during the scratch; very small fluctuations in the coefficient of friction are seen due to the formation of small fractures occurring behind the scratch tip.

Similar to the scratch response of the hard coating on Sample B, Sample C smoothly deformed during the scratch cycle; the displacement curves for Sample C are shown in Figure 18 and the coefficient of friction during the scratch cycle is shown in Figure 19. Both of these figures show that small fractures occurred in the hard coating as the scratch test progressed. One of the most interesting occurrences in the failure of Sample C is shown at a scratch distance of 400  $\mu\text{m}$  in Figure 19. In this figure, the coefficient of friction experienced a step increase at the point of critical load; this step was present in all 8 tests of this sample. In addition to smooth failure, Sample C also showed a large amount of elastic recovery—the amount of elastic recovery is shown by the area bounded by the scratch cycle and the residual deformation scan (green and orange curves, respectively); permanent deformation is shown by the area bounded by the original surface scan and the residual deformation scan (blue and orange curves, respectively).

### Sample C

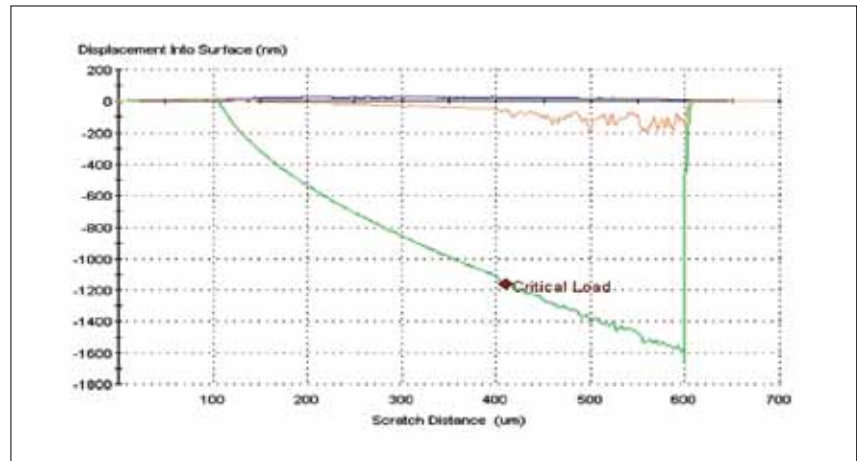


Figure 18. Scratch curves for Sample C. Just as in Sample B, smooth deformation is seen in the scratch curve (green curve) while fluctuations in the residual deformation scan (orange curve) signify minor fracturing.

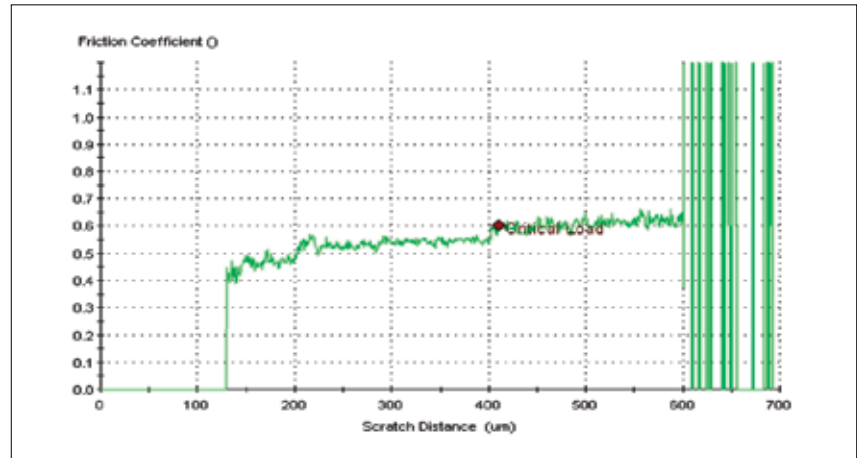


Figure 19. Coefficient of friction during the scratch cycle for Sample C. All of the tests performed on Sample C experienced a step increase in the coefficient of friction at the critical load that is located at a scratch distance of 400  $\mu\text{m}$ .

## Conclusions

Nanoindentation and scratch testing was completed on seven polymer samples and the results showed enhanced surface properties for the hard coated samples and excellent repeatability for all of the samples. The four "D" samples were tested using nanoindentation at elevated temperatures ranging from room temperature to 100°C. Even though two of the samples had been processed differently, the measured results of elastic modulus and hardness showed no statistical differences between the samples; this was with the exception of a minor difference seen in the results of elastic modulus at 50°C and 60°C. At these temperatures samples D-2-1 and D-2-2 experienced a statistical drop in elastic modulus as compared to samples D-1-1 and D-1-2.

The results from scratch testing showed significant differences in samples A, B, and C. the two hard coated samples experienced smooth scratching and their residual deformation scans showed minor fracturing was occurring behind the scratch tip. Sample A showed unique failure mechanisms in that during the scratch tests material was ripped off. This was clearly identifiable in the scratch curves and the residual deformation scans for this sample. Data for the coefficient of friction during the scratch cycles provided additional support for the failure mechanisms that occurred during the scratch tests.

## References

1. B. Crawford. "Indentation Rules of Thumb." Agilent Technologies Application Note, 2010.
2. "Metallic Materials – Instrumented indentation test for hardness and materials parameters." ISO 14577, 2002.
3. [www.efunda.com/materials/polymers/properties/polymer\\_ddatasheet.cfm?MajorID=acrylic&MinorID=4](http://www.efunda.com/materials/polymers/properties/polymer_ddatasheet.cfm?MajorID=acrylic&MinorID=4)
4. A. Rar, H. Song, and G.M. Pharr. "Assessment of new relation for the elastic compliance of a film-substrate system." *Mater. Res. Soc. Symp. Proc.* 695, pp. 431–438 (2002).



# Measuring the Complex Modulus of Polyethylene Using Instrumented Indentation

## Application Note

Jennifer Hay

### Introduction

The mechanical properties of a material determine manufacturability, performance, and longevity; thus, knowing mechanical properties is essential for making good design decisions. Polymers are exceptionally complex materials—mechanical properties depend on chemistry, processing, and thermo-mechanical history. Specifically, mechanical properties depend on the type and length of the parent chain, branching, cross-linking, strain, temperature, and frequency, and these dependencies are generally interrelated. Further, it is likely that mechanical properties also depend on volume constraints. That is, we should not be surprised if a certain polymer manifests different mechanical properties depending on whether it is in the form of a thin film or a large block, because volume constraints can affect molecular mobility. Thus, in order to gain useful information for making sound decisions when designing with polymers, mechanical property measurements should be made on a relevant sample in a relevant context. Instrumented indentation testing makes such context-specific

measurements more accessible, because samples can be small and minimally prepared.

Polymers are often employed in products because of their ability to both store and damp energy. The *complex modulus* is a phase vector which incorporates both capacities:

$$E^* = E' + iE'' \quad \text{Eq. 1}$$

The real part ( $E'$ ) of the complex modulus is called the storage modulus because it quantifies the material's ability to store energy elastically. In materials with insignificant damping, the storage modulus is equivalent to Young's modulus. The imaginary part of the complex modulus ( $E''$ ) is called the loss modulus, because it quantifies the material's ability to damp out energy.

Instrumented indentation can be used to measure complex modulus by oscillating the indenter while in contact with the material. The amplitude of the force oscillation ( $F_0$ ) is set, and the amplitude ( $z_0$ ) and phase shift ( $\phi$ ) of the resulting displacement oscillation are measured. The theory behind this

measurement technique has been explained in another application note [1]. Here, we provide only the end of the analysis, which is that storage modulus depends substantially on the real part of the amplitude ratio:

$$E' \approx \frac{(1-\nu^2)}{d} \frac{F_o}{z_o} \cos \phi, \quad \text{Eq. 2}$$

and the loss modulus depends substantially on the imaginary part of the amplitude ratio:

$$E'' \approx \frac{(1-\nu^2)}{d} \frac{F_o}{z_o} \sin \phi. \quad \text{Eq. 3}$$

(Here,  $\nu$  and  $d$  are the Poisson's ratio of the test material and the diameter of the contact, respectively. These are constants for a particular sample.) The dimensionless loss factor is independent of contact geometry, because it is the ratio of the loss to the storage modulus:

$$LF \equiv \frac{E''}{E'} = \tan \phi, \quad \text{Eq. 4}$$

In this work, we demonstrate the application of the technique to the characterization of four samples of polyethylene (or more properly, "polyethene"), which is the most widely used plastic in the world. In this work, we tested high-density polyethylene (HDPE), linear low-density polyethylene (LLDPE), low-density polyethylene (LDPE) and very-low-density polyethylene (VLDPE,  $\rho = 0.87 \text{ g/cm}^3$ ).

### Experimental Method

The four polyethylene samples (HDPE, LLDPE, LDPE, and VLDPE) were acquired from a petrochemical company. Each polyethylene sample was a small disk, having a diameter of about 8mm and a thickness of about 1mm. The four polyethylene samples were adhered to a glass-topped aluminum puck as shown in Figure 1. (The glass top provided a smooth and disposable surface.)



Figure 1. Four polyethylene samples, mounted for testing.

An Agilent G200 NanoIndenter, with XP-style actuator and CSM option, was used for all testing. The XP-style actuator applies force electromagnetically and measures displacement using a three-plate capacitive gage. The CSM option allows the superposition of an oscillating force.

When testing polymers, flat-ended cylindrical tips are advantageous for two reasons. First, they tend to cause deformation that is consistent with the assumption of linear viscoelasticity. Second, the contact area is known and independent of penetration depth. Two different indenter tips were used for this work. Both were flat-ended cylindrical punches made of diamond, but one had a diameter of about 100  $\mu\text{m}$  and the other had a diameter of about 20mm. The 20mm punch was used to test the stiffer materials (HDPE, LLDPE, LDPE) and the 100  $\mu\text{m}$  punch was used to test the VLDPE, which was very compliant. Indenters were chosen

with the goal of generating a contact stiffness that was large relative to the instrument stiffness.

The NanoSuite test method "G-Series XP CSM Flat Punch Complex Modulus" was used for this work. Table 1 summarizes the details of testing. All tests were conducted at room temperature. At least ten different sites were tested for each material. A single "test" consisted of bringing the indenter into full contact with the surface, and then oscillating the indenter at a number of specific frequencies between 1Hz and 45Hz. Thus, each test yielded complex modulus as a function of frequency for a specific test site. The amplitude of the force oscillation ( $F_o$ ) was automatically determined at the beginning of each test as that value which would cause a displacement oscillation ( $z_o$ ) of about 50nm. The stiffer materials required a greater value for  $F_o$  in order to achieve this given value of  $z_o$ . Once determined, the forcing amplitude  $F_o$  was fixed for the remainder of the test.

Material	Temp, C	Freq range, Hz	Punch diam, $\mu\text{m}$	Force amp ( $F_o$ ), $\mu\text{N}$
VLDPE	27.3	1-45	107.1	70
LDPE	26.8	1-45	21.15	445
LLDPE	27.3	1-45	21.15	750
HDPE	27.1	1-45	21.15	2200

Table 1. Summary of Experiments

## Results and Discussion

Table 2 summarizes the results for all materials at 1 Hz. Results as a function of frequency are plotted in Figures 2 and 3. In these plots, each data point represents the average result for all tests (locations) on the material at a particular frequency; error bars on the data point span one standard deviation.

With respect to the storage modulus (Figure 2), there are two important observations. First, over the frequency domain examined, the storage moduli are a weak function of frequency. Second, the storage moduli are ordered as we would expect based on chemistry. Different methods of polymerization result in dramatically different properties in part by causing more or less “branching” from the parent chain. “Branching” occurs when a polymer chain substitutes for an atom in the parent chain [2]. HDPE has relatively little branching and so polymer chains are closely packed. Thus, HDPE has a higher density, higher intermolecular forces, and on the macroscopic scale, a higher storage modulus. LLDPE, LDPE, and VLDPE have progressively more branching, respectively, and thus weaker intermolecular forces. On the macroscopic scale, these materials have progressively lower storage modulus and greater ductility for forming.

With respect to loss factor (Figure 3), the *dependence on frequency* increases with density; that is, the VLDPE shows no significant change with frequency and the HDPE shows the strongest decrease with frequency. What can we learn from this behavior? Peaks in the loss factor ( $\tan \delta$ ) as a function of frequency or temperature are associated with phase transitions in the material. If the domain is large enough, multiple peaks in loss factor may be observed that correspond with different phase transitions. For the HDPE, LLDPE, and LDPE, the loss factor decreases with frequency. This means that for these three materials, there exists a transition at lower frequencies than those investigated in this study. The slopes observed over the present domain indicate that this transition occurs at the lowest frequency for the

Material	E' @ 1Hz MPa	LF @ 1Hz Hz
VLDPE	16.2 ± 0.052	0.043 ± 0.0010
LDPE	260 ± 17.4	0.197 ± 0.0010
LLDPE	481 ± 15.1	0.150 ± 0.0020
HDPE	1554 ± 7.4	0.108 ± 0.0012

Table 2. Summary of Results

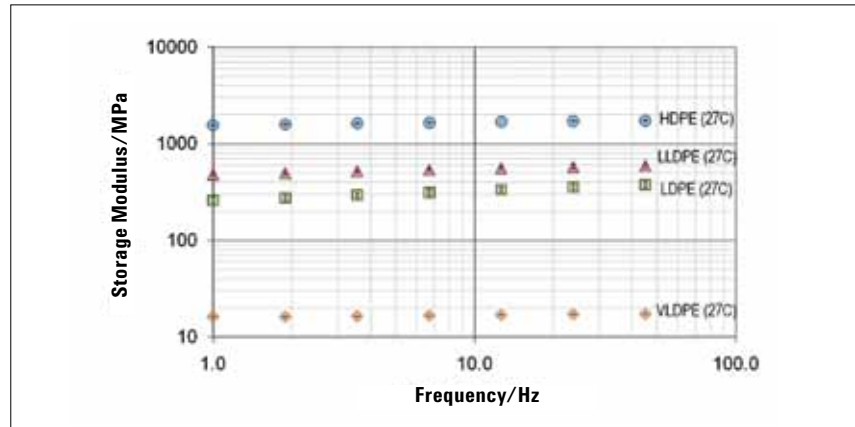


Figure 2. Storage modulus vs. frequency for the four polyethylene samples shown in Figure 1. Storage moduli are ordered as expected based on density.

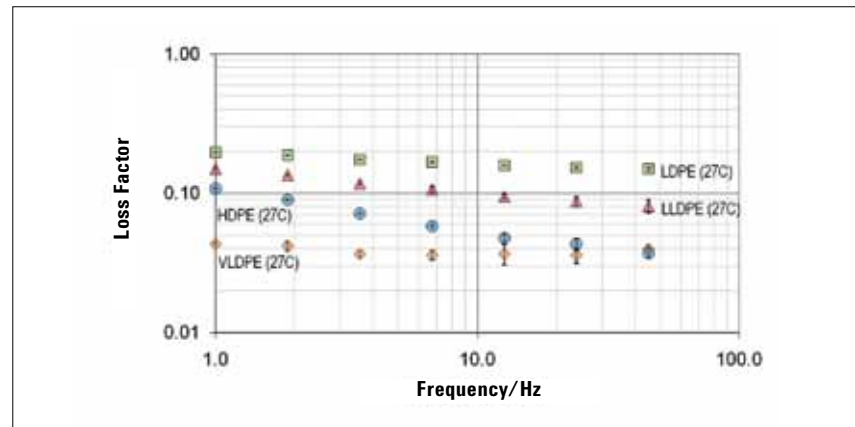


Figure 3. Loss factor ( $\tan \phi$ ) vs. frequency for the four polyethylene samples shown in Figure 1. Decrease with frequency points to a phase transition at a lower frequency.

LDPE (because it has only a weak slope) and at progressively higher frequencies for the LLDPE and HDPE (because they have progressively stronger slopes). Testing over a broader frequency range would certainly clarify these results.

A more detailed discussion of these materials, including a comparison with results obtained by others, has been published elsewhere [3].

## Conclusions

The Agilent G200 NanoIndenter was successfully used to measure the complex modulus of four types of polyethylene. Storage moduli were ordered as expected based on density. From the measurement of loss factor of HDPE, LLDPE, and LDPE, we deduced the existence of phase transitions at frequencies lower than the present domain.

## References

1. J.L. Hay, "Using Instrumented indentation to measure the Complex Modulus of Highly Plasticized Polyvinyl Chloride," Agilent application note, available online: <http://cp.literature.agilent.com/litweb/pdf/5990-6330EN.pdf>.
2. P.C. Hiemenz and T. P. Lodge, *Polymer Chemistry*, 2<sup>nd</sup> ed. Boca Raton: CRC Press, 3-9 (2007).
3. J.L. Hay and E.G. Herbert, "Measuring the complex modulus of polymers by instrumented indentation testing," Accepted for publication in *Experimental Techniques* (2011).



# Complex Shear Modulus of Commercial Gelatin by Instrumented Indentation

## Application Note

Jennifer Hay

### Introduction

All gels are comprised of a three-dimensional cross-linked polymer network and a liquid filler. Because of the structure provided by the polymer network, gels can behave like solids even though they are substantially liquid by composition. Gels are classified according to their liquid fillers: hydrogels incorporate water, organogels incorporate oil, and aerogels incorporate air.

Many practical applications derive from the mechanical similarity between gel and biological tissue. For example, gels are commonly used as tissue substitutes for evaluating both ballistics and armor [1–4]. When gel is employed as a tissue substitute, mechanical characterization of both tissue and gel is essential. Ideally, one would measure the mechanical properties of the tissue that is to be mimicked and then develop a gel which behaves similarly. It is reasonable to expect that developing a tissue substitute might require testing many different gels.

Small-scale mechanical testing by dynamic instrumented indentation presents a number of practical advantages for characterizing both biological tissue and gel. First, the necessary volume of material is small. This is especially important if the application of interest constrains the material to a small volume, such as a thin film. Also, minimal sample preparation is required; only a flat surface must be presented to the indenter. Finally, instrumented

indentation holds the possibility of mapping out the spatial variation of properties in the test material; this ability is especially relevant for characterizing biological tissue.

This note presents the theory behind measuring complex shear modulus by dynamic instrumented indentation and applies that theory to the characterization of commercial gelatin using a punch which is only 100  $\mu\text{m}$  in diameter. What makes these measurements so challenging is the combination of the compliance of the test material and the small contact size. Big contacts on compliant materials are not very difficult; neither are small contacts on stiff materials. Small contacts on compliant materials are extremely challenging, because the contact stiffness is small relative to the stiffness of the instrument. Thus, great care must be taken in characterizing the instrument. One gains a definite advantage by operating the instrument where it is most compliant, i.e. at its resonant frequency. But even with the instrument stiffness minimized, the instrument still dominates the measurement, so the instrument must be accurately characterized, and this characterization must be immediately relevant. That is, it should be at the same position, frequency, and temperature as the actual test. Thus, a new test method, “G-Series DCM CSM Flat Punch Complex Modulus, Gel”, is used in this work to seamlessly integrate instrument characterization and testing.



## Theory

The complex shear modulus ( $G^*$ ) has real and imaginary components which manifest the intrinsic elastic and viscous natures of the material:

$$G^* = G' + iG'' \quad \text{Eq. 1}$$

When a material is indented by a flat-ended cylindrical punch, the relationship between the shear modulus ( $G'$ ), Poisson's ratio ( $\nu$ ), elastic contact stiffness ( $S$ ), and punch diameter ( $D$ ) is [5]

$$G' = S(1-\nu)/(2D) \quad \text{Eq. 2}$$

Many have demonstrated the validity of an analogous definition for  $G''$  that depends on contact damping ( $C\omega$ ) [6–8]:

$$G'' = C\omega(1-\nu)/(2D) \quad \text{Eq. 3}$$

Proper dynamic analysis of the Agilent G200 NanoIndenter reveals that the contact stiffness ( $S$ ) must be obtained by subtracting the instrument stiffness ( $K_i$ ) from the total measured stiffness ( $K_S$ ):

$$S = K_S - K_i \quad \text{Eq. 4}$$

Similarly, the contact damping ( $C\omega$ ) must be obtained by subtracting the instrument damping ( $C_i\omega$ ) from the total measured damping ( $C_S\omega$ ):

$$C\omega = C_S\omega - C_i\omega \quad \text{Eq. 5}$$

Logistically, stiffness and damping are obtained by oscillating the indenter. This is accomplished electromagnetically. The amplitude of the force oscillation ( $F_0$ ) is set, and the amplitude ( $z_0$ ) and phase shift ( $\phi$ ) of the resulting displacement oscillation are measured. The values for instrument stiffness and damping are obtained by oscillating the indenter alone—that is, not in contact with any test material. Thus the instrument stiffness and damping are given by:

$$K_i = [(F_0/z_0) \cdot \cos \phi]_{\text{free-hanging}}, \quad \text{Eq. 6}$$

$$\text{and} \quad C_i\omega = [(F_0/z_0) \cdot \sin \phi]_{\text{free-hanging}} \quad \text{Eq. 7}$$

The test method “G-Series DCM CSM Flat Punch Complex Modulus, Gel” includes a “self-calibration” phase in which  $K_i$  and  $C_i\omega$  are automatically evaluated according to Eqs. 6 and 7.

The system stiffness and damping are obtained by oscillating the indenter while in full contact with the test material:

$$K_S = [(F_0/z_0) \cdot \cos \phi]_{\text{in-contact}}, \quad \text{Eq. 8}$$

and

$$C_S\omega = [(F_0/z_0) \cdot \sin \phi]_{\text{in-contact}} \quad \text{Eq. 9}$$

$K_S$  and  $C_S\omega$  are evaluated according to Eqs. 8 and 9 during the “testing” phase of the method “G-Series DCM CSM Flat Punch Complex Modulus, Gel”.

Substituting the expressions for  $K_i$  (Eq. 6) and  $K_S$  (Eq. 8) into Eq. 4, and using the resulting expression for  $S$  in Eq. 2 gives a practical expression for measuring the elastic shear modulus by instrumented indentation:

$$G' = \left( \frac{[(F_0/z_0) \cdot \cos \phi]_{\text{in-contact}} - [(F_0/z_0) \cdot \cos \phi]_{\text{free-hanging}}}{(1-\nu)/(2D)} \right) \quad \text{Eq. 10}$$

Likewise, the expression for the shear loss modulus is given by:

$$G'' = \left( \frac{[(F_0/z_0) \cdot \sin \phi]_{\text{in-contact}} - [(F_0/z_0) \cdot \sin \phi]_{\text{free-hanging}}}{(1-\nu)/(2D)} \right) \quad \text{Eq. 11}$$

Finally, the loss factor,  $\tan \delta$ , expresses the ratio of the loss modulus to the storage modulus:

$$\tan \delta = G''/G'$$

For a perfectly elastic material, the loss factor would be zero. The loss factor increases with the damping capacity of the material; a loss factor greater than 1 means that the material damps more energy than it stores. In an instrumented indentation test, the loss factor is particularly useful in that it is independent of contact area and its determination.

## Experimental Method

In order to contain the gels for testing, pucks that are normally used with the NanoVision (scanning) option were modified for this application. First, they were used as “cups” rather than “pucks”. Second, the rim of the cup was extended using 5-minute epoxy in order to provide an adequate surface for the cleaning material (i.e. tape). To make the epoxy rim, the cup was placed bottom-side up on a piece of Saran Wrap. Then 5-minute epoxy was mixed

and a toothpick was used to dab the epoxy around the rim. When the epoxy was fully cured, the Saran Wrap was removed.

Two versions of Knox® gelatin (Figure 1) were tested in this work. The first gel (“1X Gel”) was made following package directions: one package of Knox gelatin was dissolved in 8 fluid ounces (240 ml) of near-boiling water. Once dissolved, the gel was poured into a modified NanoVision cup, filling it to the rim. A second gel (“2X Gel”) was made by dissolving one package of Knox gelatin in only four fluid ounces (120 ml) of near-boiling water to create a “double concentration” version of the same gel. The second gel was poured to the rim of a second modified NanoVision cup, and then both cups were set on a plate. A little gel was poured on the plate around the two cups; then they were covered with a plastic container. The extra gel and covering provided a sealed, humid environment in which the gels could set without drying. The gels were poured about six hours prior to testing. Just before testing, a piece of double-sided tape was adhered to the epoxy lip. Figure 2 shows a gel sample ready for testing.



Figure 1. Standard and double-concentration versions of this gel were tested.

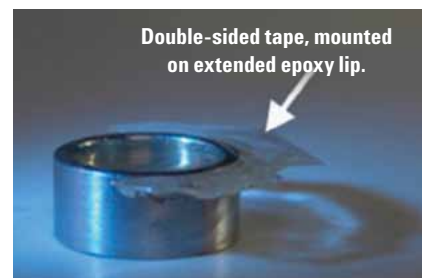


Figure 2. Gel sample, ready for testing in inverted NanoVision puck with extended epoxy lip.

Input	Value	Units
Clean Tip Between Tests? (yes=1; no=0)	1	
Oscillation Amplitude (in material)	500	nm
Phase Change For Contact	2	degrees
Poisson's Ratio	0.5	
Pre-test Compression	5	$\mu\text{m}$
Pre-test Compression Retracted? (yes=1; no=0)	0	
Punch Diameter	101.1	$\mu\text{m}$
Surface Approach Excitation	20	$\mu\text{N}$
Surface Approach Frequency	110	Hz
Testing Frequency	110	Hz
X Move to Cleaning Material	1.5	cm
Y Move to Cleaning Material	0	cm

Table 1. Summary of required inputs.

Sample	Temp. C	G' kPa	G'' kPa	tan $\delta$
1X Gel	23.9	1.822 $\pm$ 0.023	0.446 $\pm$ 0.055	0.245 $\pm$ 0.030
2X Gel	24.0	3.811 $\pm$ 0.058	0.504 $\pm$ 0.055	0.132 $\pm$ 0.016

Table 2. Summary of results. Uncertainty range represents  $\pm 1\sigma$ .

An Agilent G200 NanoIndenter was used for all testing. The system was configured with a DCM II actuator, flat-ended cylindrical punch ( $D = 101.1\mu\text{m}$ ), and CSM option. The CSM option allowed the superposition of an oscillating force. A flat-ended cylindrical punch was employed in order to generate a contact area which was known and independent of penetration depth.

The NanoSuite test method "G-Series DCM CSM Flat Punch Complex Modulus, Gel" was used for all testing, because it seamlessly integrates dynamic self-calibration, testing, and tip cleaning. Fifteen different sites were tested on each gel. Test sites were separated by  $500\mu\text{m}$ . The testing frequency was 110 Hz, because that is the resonant frequency of the DCM II actuator. (Equipment is most compliant at its resonant frequency.) Table 1 summarizes the details of testing.

## Results and Discussion

Table 2 summarizes the results for this testing. Not surprisingly, the standard-concentration gel (1X) had a modulus that was about half that of the double-concentration gel (2X). Interestingly, increasing the gel concentration had

the effect of reducing the loss factor by about half. The loss factor for the 1X gel was  $0.245\pm 0.030$ ; the loss factor for the 2X gel was only  $0.132\pm 0.016$ . These results are consistent with sensory perception; that is, the 2X gel felt stiffer and more "bouncy" than the 1X gel.

Figure 3 shows the results of preliminary testing on the gel. These tests are obviously spaced too closely together ( $200\mu\text{m}$ ). Although these tests did not provide useful quantitative results, they did provide qualitative feedback which was valuable for performing and interpreting later tests. Fortunately, the scale bar in Figure 3 is about the same length as the diameter of the indenter face. The visible deformation occurred when the indenter was *withdrawn* from the gel. Because the gel adhered to the tip as it was withdrawn from the sample, each test left behind a protrusion of gel having about the same diameter as the tip. (The fact that it was a protrusion, not an impression, was discerned by moving the optical microscope up and down to change the focal plane.) The tensile stress induced at the surface left behind circumferential "wrinkles" when the gel finally broke away from the indenter. For these tests, the indenter was cleaned between each test. The apparent

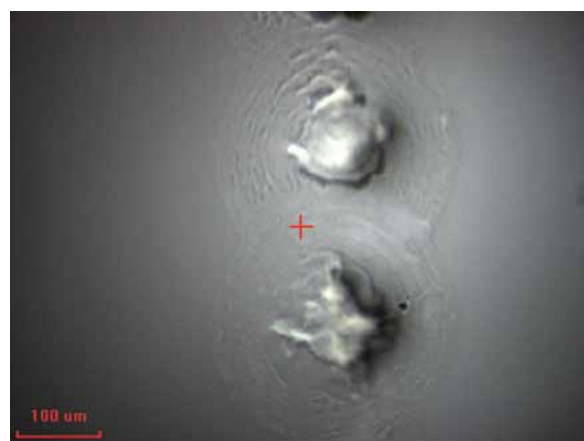


Figure 3. Residual traces from preliminary testing; scale bar is the same length as the diameter of the indenter. Tensile stresses induced by pull-off leave circumferential "wrinkles".

adhesion verified the necessity of such cleaning. The fact that subsequent tests all left similar traces confirmed that in fact, the tip was being successfully cleaned. (If bits of gel remained on the tip from one test to another, later tests would show less adhesion than earlier tests.) As a result of these preliminary tests, the test-to-test spacing was increased to  $500\mu\text{m}$  so that there would be no interference between tests.

## Conclusions

The Agilent G200 NanoIndenter was used to measure the complex shear modulus of edible gelatin. The combination of the compliance of the test material (on the order of 1 kPa) and the scale of the test ( $100\mu\text{m}$ ) makes these results novel in the field of mechanical testing. These extraordinary measurements required (1) a dynamically compliant actuator/transducer (the DCM II head, operating at its resonant frequency) and (2) a test method which integrated self-calibration, testing, and tip cleaning. The same equipment and test method may be used to characterize other kinds of gels and, most interestingly, biological tissue.

## References

1. Jain, S.K., Bhattacharayya, C.N., Badonia, B., and Singh, R.P., "Study of unusual phenomenon of contact firing on gelatine block using .38 Special revolver - forensic importance," *Forensic Science International* 133(3), 183–189, 2003.
2. Zhang, J.Y., Yoganandan, N., Pintar, F.A., and Gennarelli, T.A., "Temporal cavity and pressure distribution in a brain simulant following ballistic penetration," *Journal of Neurotrauma* 22(11), 1335–1347, 2005.
3. Zhang, J., Yoganandan, N., Pintar, F.A., Guan, Y., and Gennarelli, T.A., "Experimental model for civilian ballistic brain injury biomechanics quantification," *Journal of Biomechanics* 40(10), 2341–2346, 2007.
4. Guha, R.A., Shear, N.H., and Papini, M., "Ballistic Impact of Single Particles Into Gelatin: Experiments and Modeling With Application to Transdermal Pharmaceutical Delivery," *Journal of Biomechanical Engineering-Transactions of the Asme* 132(10), 2010.
5. Sneddon, I.N., "The relation between load and penetration in the axisymmetric Boussinesq problem for a punch of arbitrary profile," *Int. J. Eng. Sci.* 3(1), 47–57, 1965.
6. Loubet, J.L., Oliver, W.C., and Lucas, B.N., "Measurement of the Loss Tangent of Low-Density Polyethylene with a Nanoindentation Technique," *Journal of Materials Research* 15(5), 1195–1198, 2000.
7. Herbert, E.G., Oliver, W.C., Lumsdaine, A., and Pharr, G.M., "Measuring the constitutive behavior of viscoelastic solids in the time and frequency domain using flat punch nanoindentation," *Journal of Materials Research* 24(3), 626–637, 2009.
8. Herbert, E.G., Oliver, W.C., and Pharr, G.M., "Nanoindentation and the dynamic characterization of viscoelastic solids," *Journal of Physics D-Applied Physics* 41(7), 2008.



# Sensitive Polymer Analysis using Critical Point Chromatography and ELSD

## Application Note

### Author

Stephen Ball  
Agilent Technologies, Inc.

### Introduction

Liquid chromatography under critical conditions (LCCC), or critical point chromatography, is a technique used to investigate very small differences between the chemical structures of polymers. These differences could arise through the use of co-monomers or through the introduction of end-group functionality. Traditional interactive chromatographic techniques are often insensitive to small changes in structure and critical point chromatography has become the method of choice for these analyses.



**Agilent Technologies**

LCCC relies on carrying out isocratic chromatography at the so-called critical point for the polymer under investigation. In liquid chromatography of polymers, the samples are introduced into an eluent flowing through a column packed with porous media. Any retention of the polymer on the column media results from a reduction in the free energy of the polymer in solution, which can be described by:

$$\Delta G = \Delta H - T \Delta S$$

where  $\Delta G$  is the change in Gibbs' free energy,  $\Delta H$  is the change in enthalpy and  $\Delta S$  is the change in entropy. Adsorption of the polymer by a reversed/normal-phase mechanism will result in a negative  $\Delta H$  and, therefore, a negative  $\Delta G$ , whereas if a size exclusion mechanism occurs then  $\Delta S$  will be positive and again  $\Delta G$  will be negative. Separation of any components of the polymer occurs if the reduction in  $\Delta G$  differs between the individual components. For many polymers, controlling the choice of chromatographic eluent and column determines whether or not the retention mechanism is primarily or exclusively adsorption or size exclusion. Critical point conditions are reached for a given polymer/solvent combination when  $\Delta H$  and  $\Delta S$  are balanced and there is no change in  $\Delta G$  during the analysis. Under these conditions, all components of a polymer with the same chemical composition will elute at the total permeation limit of the column, regardless of the molecular weight. At the critical point, the polymer is said to be 'chromatographically invisible', as no separation is obtained. For the majority of polymers, the critical point can be determined by making the appropriate selection of column, temperature and eluent. Critical point chromatography is very useful for obtaining compositional information for polymers with differing end groups or those containing co-monomers. If critical conditions are applied for one component of a sample, that component becomes chromatographically invisible and any separation observed is controlled by other components.

Critical point chromatography is carried out under isocratic conditions and, therefore, can be performed on a standard LC system composed of a pump, injection valve, a reversed/normal-phase HPLC column and concentration detector, without the need for complex equipment. LCCC is well illustrated using a PLRP-S column and the Agilent ELSD for the analysis of modified polyethylene glycol (PEG) and poly(styrene-*b*-methyl methacrylate) (PMMA).

## Instrumentation

Column: PLRP-S 100Å 5  $\mu$ m, 150 x 4.6 mm  
(p/n PL1111-3500)

Detection: Agilent ELSD

## Materials and Reagents

Analysis of PEG

Eluent: 49% Acetonitrile in Water

Analysis of PMMA

Eluent: Polystyrene - 47% ACN in THF;

Polymethylmethacrylate - 17% ACN, 17% Water, 66% THF

## Conditions

Flow Rate: 1.0 mL/min

Injection Volume: 20  $\mu$ L

## Results and Discussion

### LCCC analysis of end-group modified polyethylene glycol

Critical point chromatography was used to analyze a PEG that had been modified with amine end groups (Figure 1). Critical point conditions for PEG were established by analyzing a series of PEG narrow standards of different molecular weights using different isocratic combinations of acetonitrile and water.

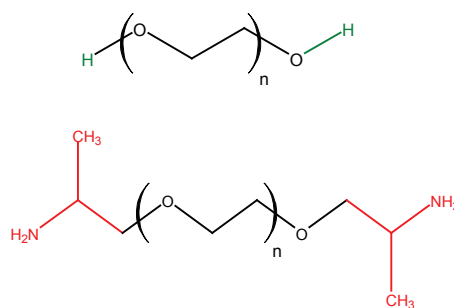


Figure 1. The structure of the original and the modified PEG materials.

Figure 2 shows chromatograms of the standards in SEC and reversed-phase mode, and at the critical point where elution is independent of molecular weight.

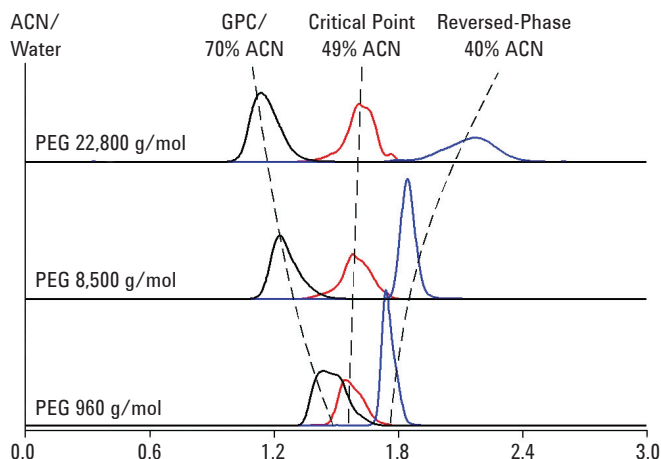


Figure 2. Analysis of PEG in SEC and reversed-phase to reveal the critical point.

Figure 3 shows a chromatogram of the amine-modified PEG material, before and after neutralization of the amine functionality with hydrochloric acid.

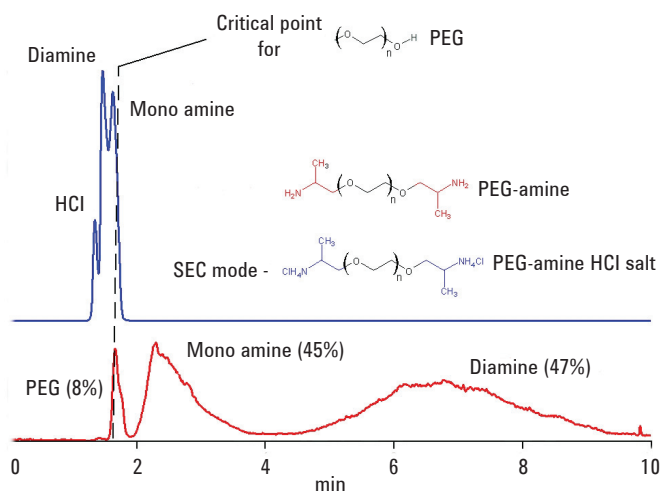


Figure 3. Amine modified PEG before and after neutralization with HCL.

Before the addition of the acid, one peak was observed at total permeation (corresponding to unmodified PEG) and two peaks were observed eluting in interactive mode (after total permeation of the column). The two peaks eluting in interactive mode were assigned as the mono and di-amine end-group modified PEGs. Based on the peak areas, the ratio of components assigned as 8% PEG, 45% mono-amine and 47% di-amine. Addition of the hydrochloric acid changed the elution to SEC mode (elution before the PEG peak), indicating the sensitivity of the chromatography at critical conditions to sample chemistry.

### LCCC Analysis of Poly(styrene-b-methyl methacrylate)

Critical point chromatography was used to analyze a sample of poly(styrene-b-methyl methacrylate) block copolymer, whose structure is shown in Figure 4.

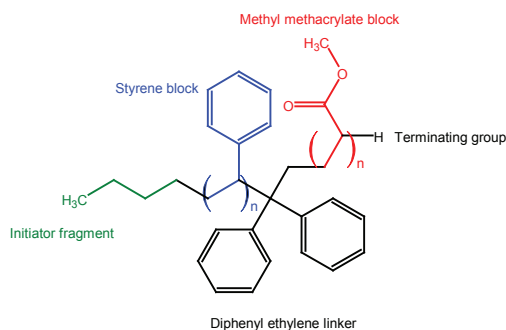


Figure 4. Structure of poly(styrene-b-methyl methacrylate).

Critical conditions were established for both polystyrene and polymethyl methacrylate by running narrow standards of varying molecular weight using different isocratic mixtures of solvents.

Figure 5 shows critical point diagrams for the polystyrene and polymethyl methacrylate standards.

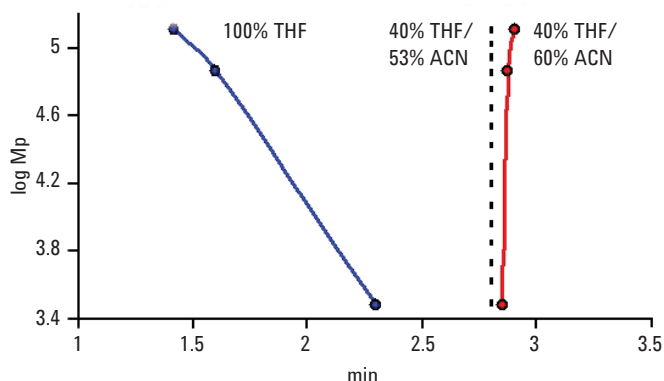
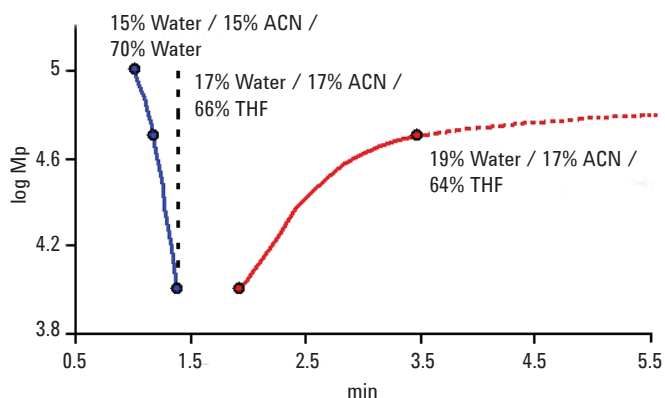


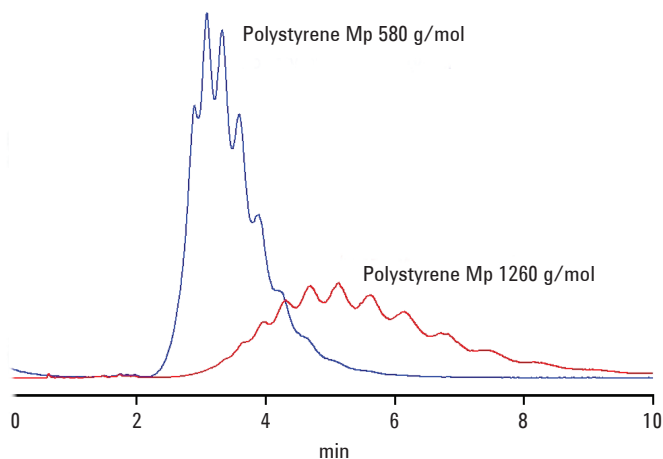
Figure 5a. Critical point diagrams for PS.



**Figure 5b. Critical point diagrams for PMMA.**

Under the critical conditions for PMMA, chromatography of PS resulted in elution based on adsorption mode.

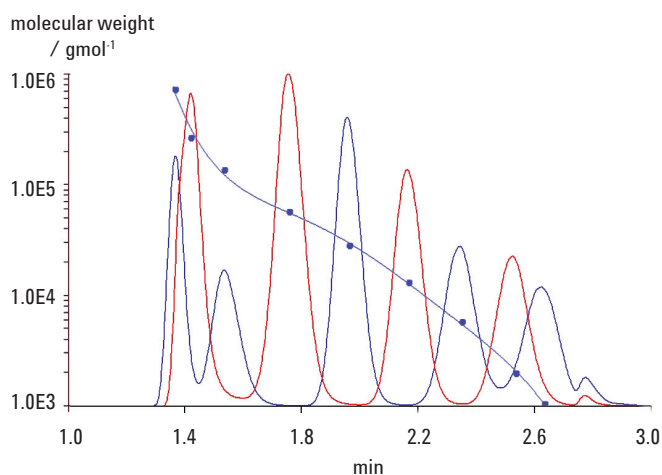
Chromatograms of two polystyrene narrow standards eluting under polymethyl methacrylate critical conditions are shown in Figure 6.



**Figure 6. Chromatograms of polystyrene standards under polymethyl methacrylate critical conditions.**

Under the critical conditions for PS, PMMA resulted in elution based on SEC.

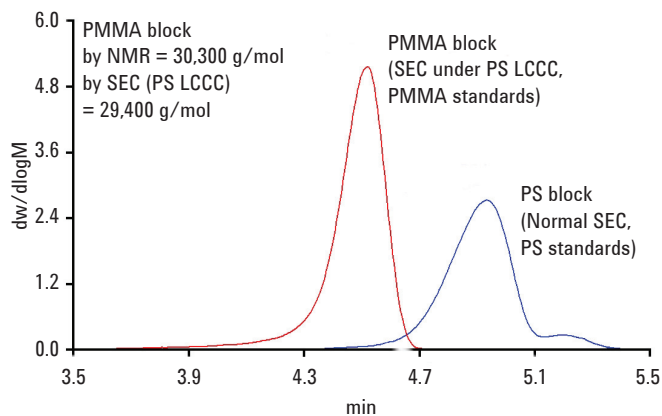
Figure 7 shows chromatograms of a series of polymethyl methacrylate narrow standards and a SEC calibration curve obtained under the polystyrene critical conditions.



**Figure 7. PMMA standards and SEC calibration curve run under PS critical conditions.**

The poly(styrene-*b*-methyl methacrylate) sample was analyzed under the critical conditions for polystyrene. Using these conditions, the elution is controlled purely by the molecular weight of the methyl methacrylate block of copolymer, the polystyrene block is 'chromatographically invisible'.

Figure 8 shows the molecular weight distributions of the polystyrene block by conventional GPC using polystyrene standards before introduction of the methyl methacrylate and growth of the PMMA block, and the PMMA block under critical conditions for polystyrene using PMMA standards.



**Figure 8. Molecular weight distributions of the styrene block before reaction with PMMA, and the PMMA block under critical conditions for polystyrene.**

Using these results, the molecular weight of the total polymer and the comparative block lengths could be determined as approximately 71% polystyrene, 29% polymethyl methacrylate. The results showed good agreement with the results from NMR experiments.

## Conclusion

Critical point chromatography is a powerful tool for analyzing small chemical changes in the structure of polymers, such as the inclusion of co-monomers to a polymer backbone or a change in end-groups.

In many cases, traditional chromatography techniques are not sufficiently sensitive to show these changes, and critical point chromatography offers a cheaper and easier route to structural analysis compared to other techniques that have been used in the past, such as NMR.

However, critical point chromatography is extremely sensitive to the chemistry of the sample and column and so a specific methodology must be developed for each application.

PLRP-S columns and the Agilent ELSD is an ideal combination for these challenging applications.

[www.agilent.com/chem](http://www.agilent.com/chem)

This information is subject to change without notice.

© Agilent Technologies, Inc. 2011

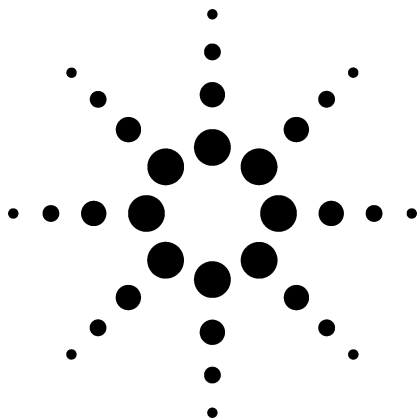
Published in UK, May 24, 2011

5990-8319EN



**Agilent Technologies**





# Fast Analysis of Phenolic Antioxidants and Erucamide Slip Additives in Polypropylene Homopolymer Formulations Using 1200 Rapid Resolution Liquid Chromatography (RRLC) with Rapid Resolution High Throughput (RRHT) Columns and Method Translator

Application

Hydrocarbon Processing

## Authors

Wei Luan and Chunxiao Wang  
Agilent Technologies (Shanghai) Co., Ltd.  
412 Ying Lun Road  
Waigaoqiao Free Trade Zone  
Shanghai 200131  
P. R. China

Michael Woodman  
Agilent Technologies, Inc.  
2850 Centerville Road  
Wilmington DE 19808  
USA

## Abstract

**Vitamin E (tocopherol), phenolic antioxidants and erucamide slip additives in polypropylene homopolymer formulations were resolved and detected using liquid chromatography with ultraviolet/visible detection, under guidelines suggested by ASTM Method D6042. Using the Agilent 1200 Rapid Resolution LC system with Agilent ZORBAX RRHT columns, the antioxidants could be rapidly separated with the same or improved resolution. The Agilent method translator was used to transfer the ASTM method into new methods based on the instrument parameters, column dimensions, and particle size in three modes: simple conversion and speed optimized and resolution optimized methods.**

## Introduction

Polymers are very popular all over the world owing to their unprecedented physical properties. Various additives are blended into polymeric materials to modify certain properties of the polymer formulation. Erucamide, Irganox 3114, Irganox 1010, Vitamin E (tocopherol), Irganox 1076, and Irgafos168 are often used as antioxidants to prevent the degradation of polypropylene homopolymer formulations by light, heat, and oxygen. In this work, with the goal to shorten the analysis time and reduce solvent consumption without losing separation quality, the existing ASTM method was recalculated for new operating conditions based on columns packed with smaller particle sizes. The chemical information of the antioxidants and Tinuvin P as internal standard is displayed in detail in Table 1.

Specific additives and their concentrations in polymer formulations are critical to the properties of polymer, and careful analysis is required to ensure that the additives and levels are appropriate for the intended use. This application will compare two different stationary phases according to analyte retention characteristics and peak shape, show the influence of different injection volume of real sample on the peak shape, and then will focus on showing how to use the method translator. The latter is used to transfer the conventional method to new methods using smaller size columns to perform simple conversion and to extend the method to greater speed and higher resolution.

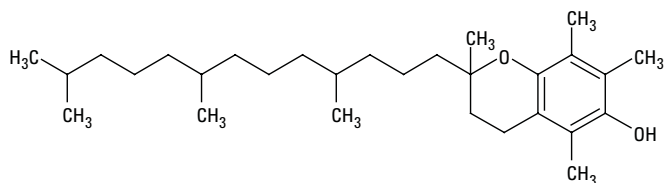


Agilent Technologies

**Table 1. Chemical Information of Antioxidants and Tinuvin P**

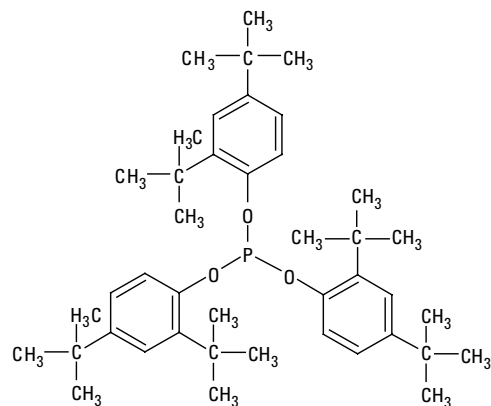
Name: Vitamin E  
 Formula:  $C_{29}H_{50}O_2$   
 Molecular Weight: 430.71  
 CAS No.: 10191-41-0

DL-all-rac- $\alpha$ -Tocopherol



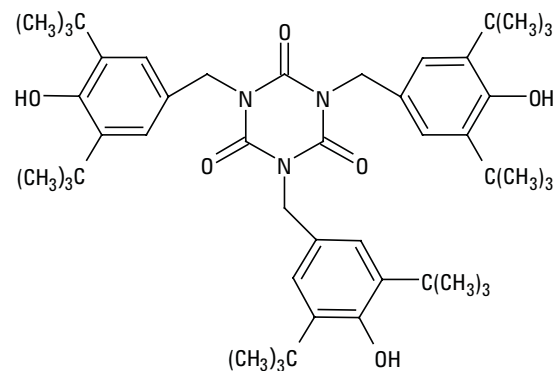
Name: Irgafos 168  
 Formula:  $[(CH_3)_3C]_2C_6H_3O]_3P$   
 Molecular Weight: 646.92  
 CAS No.: 31570-04-4

Tris(2,4 di-tert-butylphenyl) phosphite



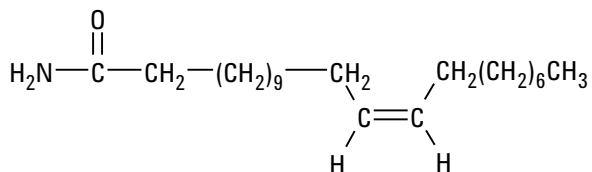
Name: Irganox 3114  
 Formula:  $C_{48}H_{69}N_3O_6$   
 Molecular Weight: 784.08  
 CAS No.: 27676-62-6

Tris(3,5-di-tert-butyl-4-hydroxybenzyl) isocyanurate



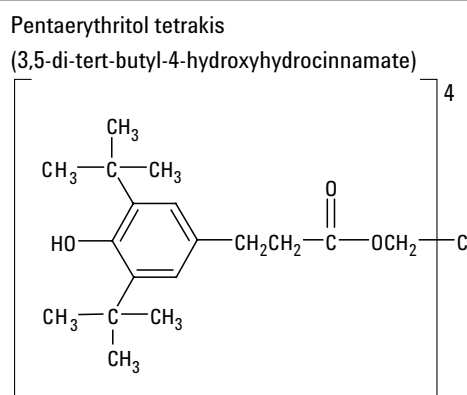
Name: Erucamide  
 Formula:  $CH_3(CH_2)_7CH=CH(CH_2)_{11}CONH_2$   
 Molecular Weight: 337.58  
 CAS No.: 112-84-5

cis-13-docosenamide

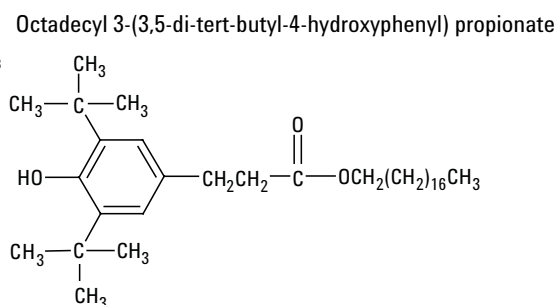


**Table 1. Chemical Information of Antioxidants and Tinuvin P (Continued)**

Name: Irganox 1010  
Formula:  $[\text{HOC}_6\text{H}_2[\text{C}(\text{CH}_3)_3]_2\text{CH}_2\text{CH}_2\text{CO}_2\text{CH}_2]_4\text{C}$   
Molecular Weight: 1177.63  
CAS No.: 6683-19-8

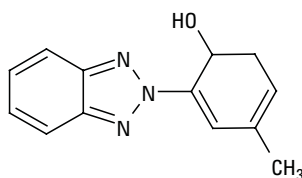


Name: Irganox 1076  
Formula:  $[(\text{CH}_3)_3\text{C}]_2\text{C}_6\text{H}_2(\text{OH})\text{CH}_2\text{CH}_2\text{CO}_2(\text{CH}_2)_{17}\text{CH}_3$   
Molecular Weight: 530.86  
CAS No.: 2082-79-3



Name: Tinuvin P  
Formula:  $\text{C}_{13}\text{H}_{11}\text{N}_3\text{O}$   
Molecular Weight: 225.25  
CAS No.: 2440-22-4

2-(2-hydroxy-5-methylphenyl)benzotriazole



## Experimental

### System

Agilent 1200 Series Rapid Resolution LC (RRLC), consisting of:  
G1379B micro vacuum degasser  
G1312B binary pump SL  
G1367C high-performance autosampler SL  
G1316B thermostatted column compartment SL  
G1315C UV/VIS diode array detector SL with 3 mm, 2  $\mu\text{L}$  flow cell  
ChemStation 32-bit version B.02.01-SR1

### Columns

Agilent ZORBAX Eclipse XDB-C18, 4.6 mm  $\times$  150 mm, 5  $\mu\text{m}$   
Agilent ZORBAX Eclipse XDB-C8, 4.6 mm  $\times$  150 mm, 5  $\mu\text{m}$   
Agilent ZORBAX Eclipse XDB-C8, 4.6 mm  $\times$  100 mm, 3.5  $\mu\text{m}$   
Agilent ZORBAX Eclipse XDB-C8, 4.6 mm  $\times$  50 mm, 1.8  $\mu\text{m}$   
Agilent ZORBAX Eclipse XDB-C8, 3.0 mm  $\times$  100 mm, 3.5  $\mu\text{m}$   
Agilent ZORBAX Eclipse XDB-C8, 3.0 mm  $\times$  50 mm, 1.8  $\mu\text{m}$

### Mobile Phase

Gradients: A: water  
B: acetonitrile (ACN)  
Gradient conditions: See individual chromatograms  
Column temperature: See individual chromatograms

### Samples

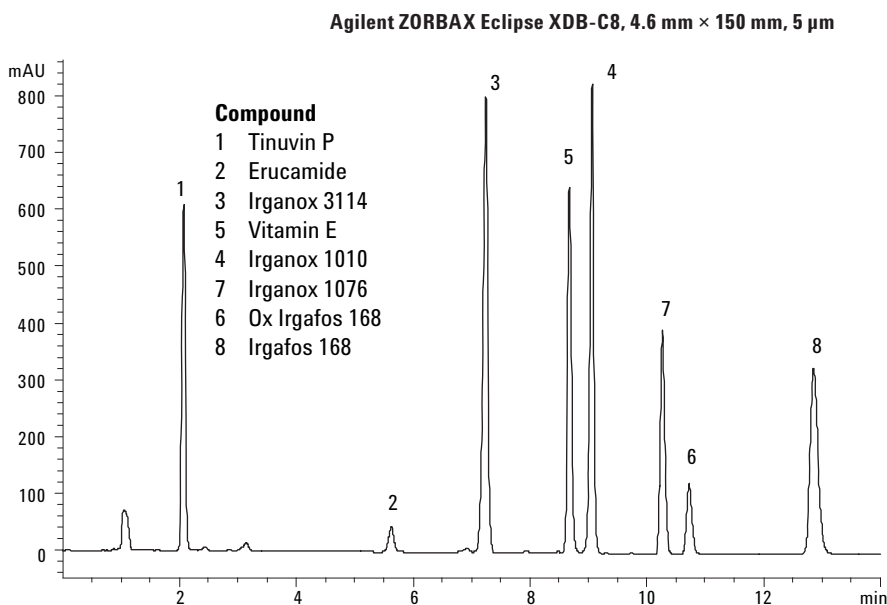
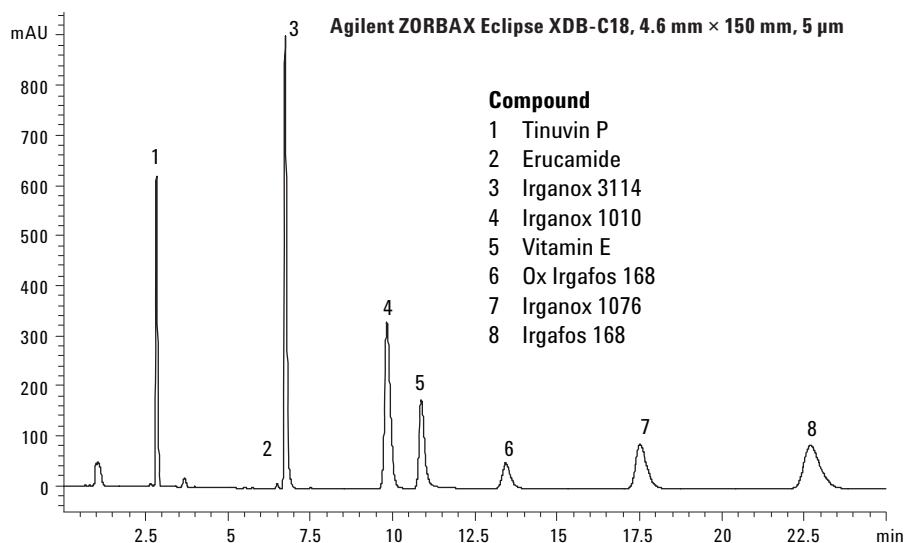
1. Standard mixture of Tinuvin P, Erucamide, Irganox 3114, Irganox 1010, Vitamin E, Irganox 1076, and Irgafos168, all 200  $\mu\text{g}/\text{mL}$  in isopropanol
2. Polypropylene Homopolymer Formulation, from customer, extracted by ultrasonic according to the method ASTM D6042-04
3. Polypropylene extract spiked with 20  $\mu\text{g}/\text{mL}$  standard mixture

## Results and Discussion

### Selection of Stationary Phase for the Separation of Antioxidants

It is desirable during method development to select a column that will provide the optimal analyte separation and shortest analysis time. Reversed phase C18 columns are recommended by ASTM D6042-04; however, in our application we deter-

mined that the retention characteristics of ZORBAX XDB-C18 columns were too strong for the specified solvents, resulting in broad peak shape and quantitation difficulties for late-eluting peaks. Compared with ZORBAX XDB-C18 columns, ZORBAX XDB-C8 columns showed better retention capability and peak shape. Therefore, we chose the ZORBAX XDB-C8 column for further method development. The different separations with ZORBAX XDB-C18 and ZORBAX XDB-C8 columns are shown in the Figure 1.



#### Conditions

Mobile phase:	A: water; B: ACN	ZORBAX chemistry:	Eclipse XDB-C18	Eclipse XDB-C8
Flow rate:	1.5 mL/min	Gradient:	Min %B	Min %B
Wavelength:	200 nm		0.00 75	0.00 75
Injection volume:	10 μL		5.00 100	8.00 100
Column temperature:	50 °C		25.00 100	15.00 100
Column size:	4.6 mm × 150 mm, 5 μm		25.10 75	15.10 75
Sample:	Standard mixture, 200 μg/mL in isopropanol		30.00 75	20.00 75

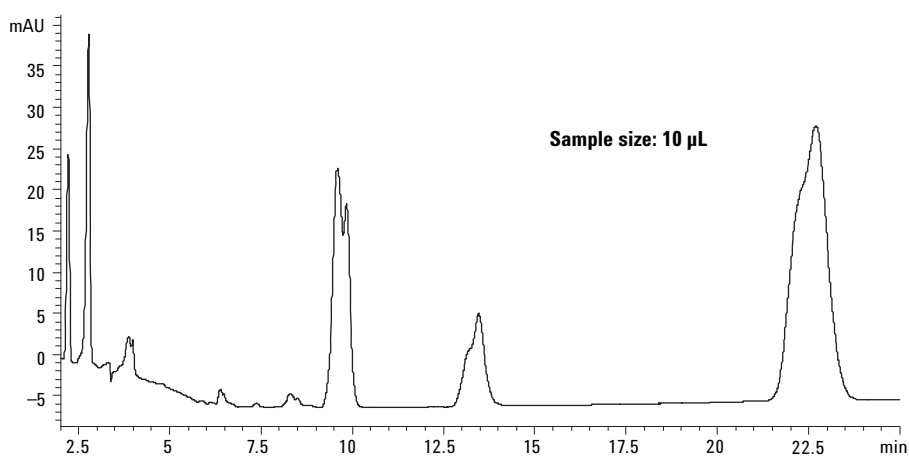
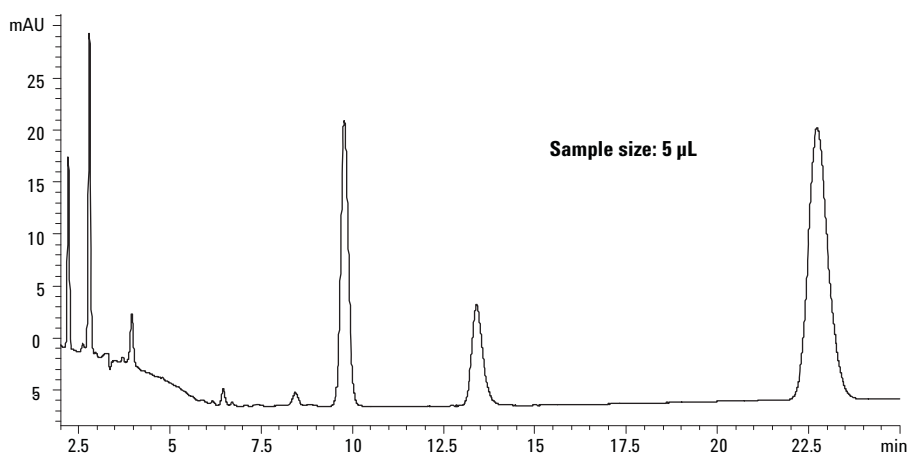
**Figure 1. ZORBAX stationary phase comparison for antioxidants.**

## Injection Volume Influence of Real Sample Extraction Solution on the Peak Shape

According to ASTM D6042-04 [1], a solvent mixture of methylene chloride and cyclohexane (1/1 v/v) is used as the extraction solvent and, after filtration, the extracted solution is directly injected into the LC. Neither methylene chloride nor cyclohexane is miscible in the acetonitrile and water mobile phase. Peak splitting was observed when the injection volume was 10  $\mu\text{L}$ . We decreased the sample size of real sample and found that the volume of 5  $\mu\text{L}$  was suitable and free of solvent influence. The split and nonsplit peaks are shown in Figure 2. At the same time, the influence of injection volume was not found in the standard solution, which was dissolved in isopropanol per ASTM method guidance.

## Fast Method Developed Based on New 1200 RRLC with Method Translator

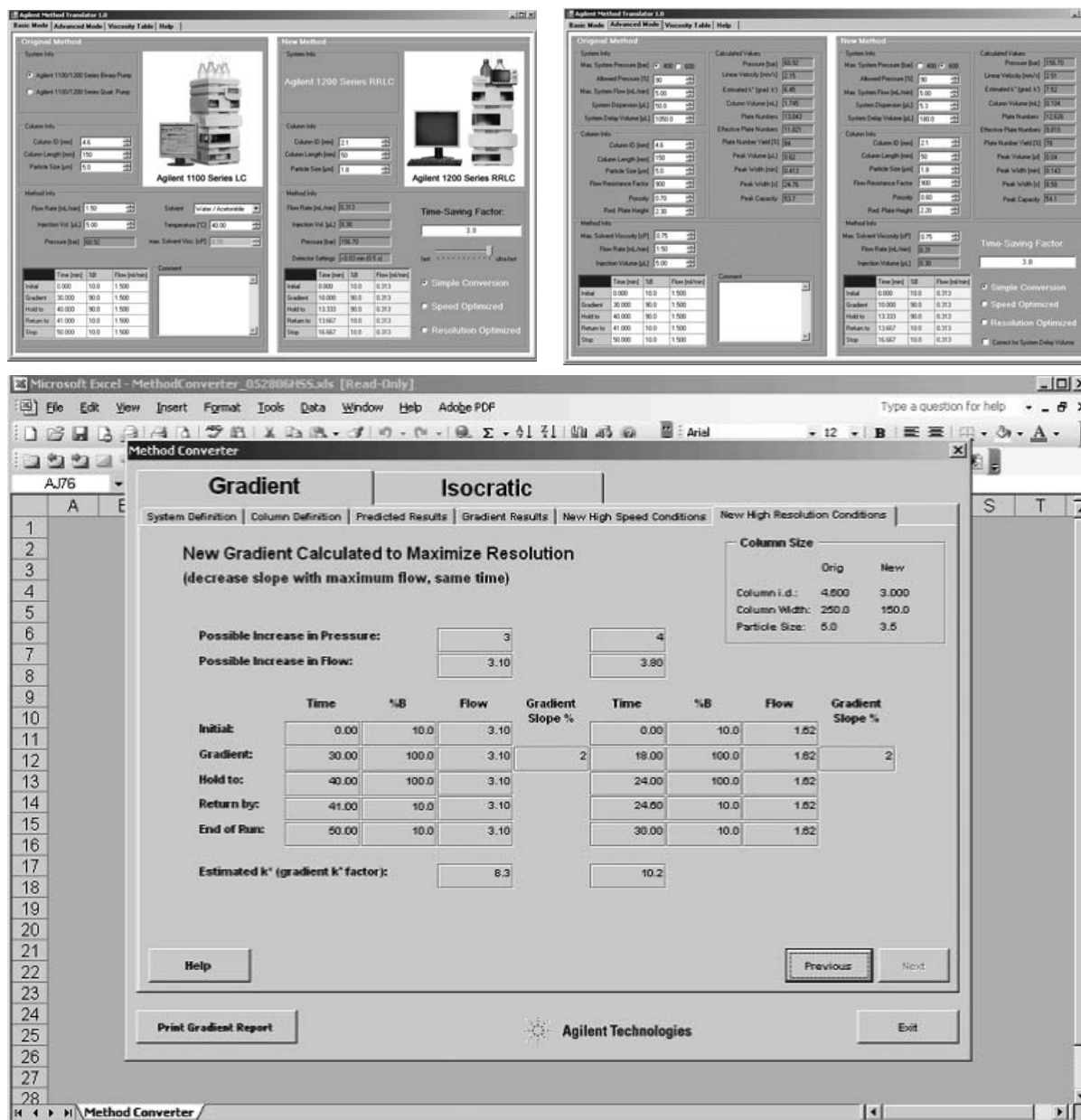
Due to the appearance of sub-two-micron columns and LC systems with higher pressure capabilities, the research of ultra-fast separation is more and more popular. Therefore, it is important to quickly and easily transfer conventional methods to fast or high-resolution methods. Agilent provides the users of RRLC systems with two versions of method translators; one is a Microsoft.net version, which requires that Net-Framework 2.0 be resident on the computer, the other is a Microsoft Excel version, which requires that Excel be resident on the PC. The interface of the two translators is displayed in Figure 3.



### Conditions

Mobile phase:	A: water; B: ACN	<b>Gradient:</b>	
Flow rate:	1.5 mL/min	Min	%B
Wavelength:	200 nm	0.00	75
Injection volume:	5 or 10 $\mu\text{L}$	5.00	100
Column temperature:	50 $^{\circ}\text{C}$	25.00	100
Column:	ZORBAX Eclipse XDB-C18	25.10	75
	4.6 mm $\times$ 150 mm, 5 $\mu\text{m}$		
Sample:	Polypropylene extraction solution	30.00	75

**Figure 2.** Injection volume influence of real sample extraction solution on the peak shape.



The upper one is the Microsoft.net version, the lower one is the Microsoft Excel version.

**Figure 3. Two different method translators.**

### Sample Preparation

The two versions of method translators provide three modes of method conversion; the first is the simple conversion, which has the same gradient slope as the conventional method, and changes the flow rate according to equation 1:

$$Flow_{Col.2} = \left[ \frac{Diam_{Col.2}}{Diam_{Col.1}} \right]^2 \times Flow_{Col.1} \quad (\text{eq. 1})$$

The second is the speed optimized conversion, which has the same gradient slope as the conventional method and maximizes the flow rate according to the LC system pressure capability. The last is

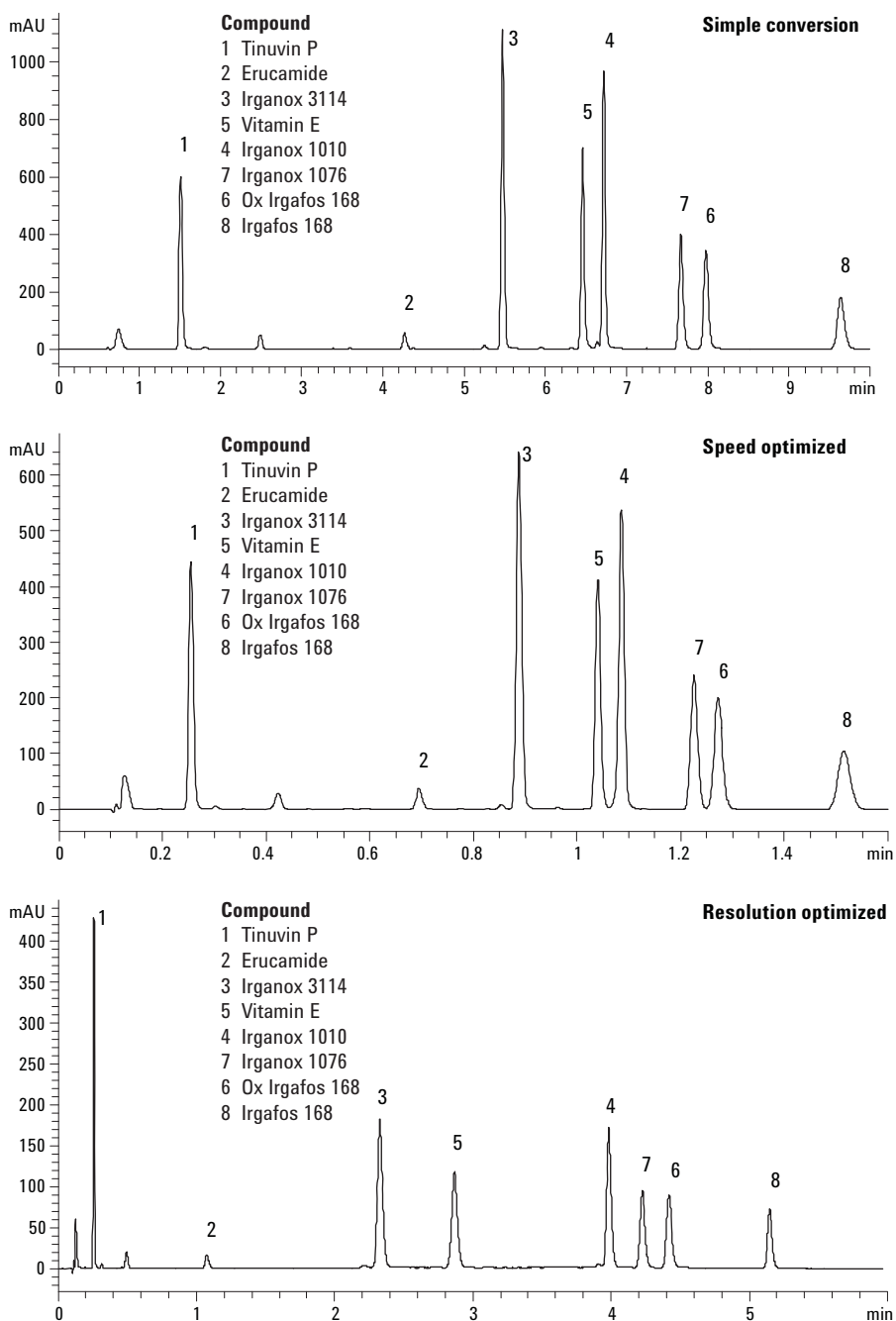
the resolution optimized conversion, which maximizes the flow rate according to the LC system pressure capability and has the same gradient time as the simple converted mode, resulting in a reduced gradient slope that normally yields higher peak resolution. For the different columns, the injection volumes should be changed according to the relationship displayed in equation 2.

$$Inj. vol_{Col.2} = \left[ \frac{Volume_{Col.2}}{Volume_{Col.1}} \right] \times Inj. vol_{Col.1} \quad (\text{eq. 2})$$

As mentioned above, the method based on the ZORBAX Eclipse XDB-C8 4.6 mm x 150 mm, 5 μm, was selected as the initial method. Afterwards, the initial method was transferred with the method

translator into three modes on different column lengths (100, 50 mm) and particle sizes (3.5, 1.8 μm), respectively. Figures 4 and 5 show

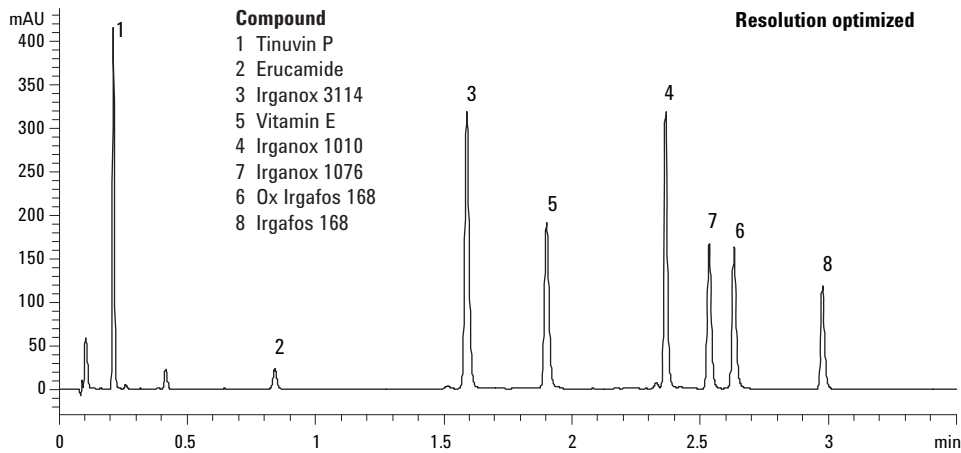
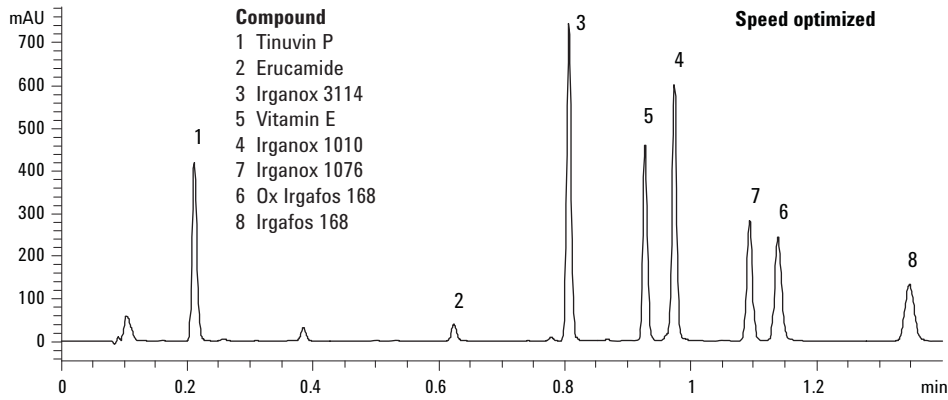
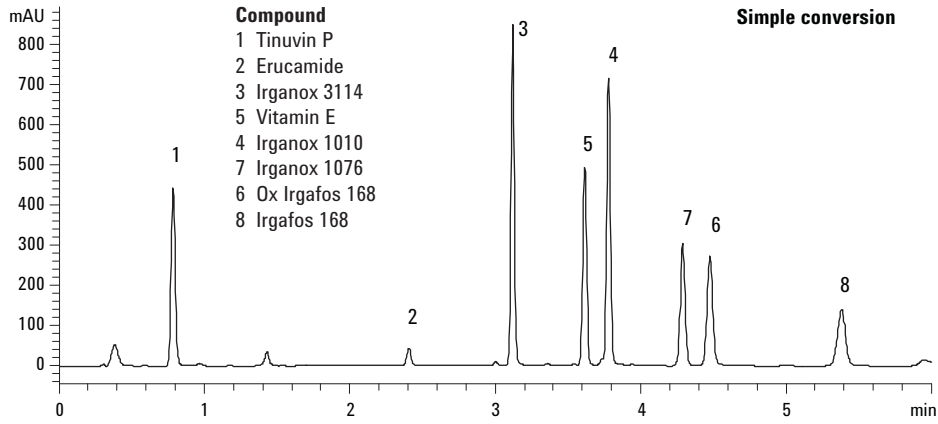
the separation of antioxidants in smaller particle size columns with the recalculated methods.



**Conditions**

Sample:	Standard mixture, 200 μg/mL in isopropanol		
Mobile phase:	A: water; B: ACN		
Temperature:	50 °C		
Wavelength:	200 nm		
Injection volume:	6.7 μL		
Column:	ZORBAX Eclipse XDB-C8 3.0 mm × 100 mm, 3.5 μm		
Mode:	Simple converted	Speed optimized	Resolution optimized
Flow rate:	0.64 mL/min	4.00 mL/min	4.00 mL/min
Pressure:	110 bar	460 bar	460 bar
Gradient slope:	3.1%	3.1%	0.5%
Analysis time:	10 min	1.6 min	5.5 min

**Figure 4. Separation of antioxidants on ZORBAX Eclipse XDB-C8 3.0 mm × 100 mm, 3.5 μm.**



**Conditions**

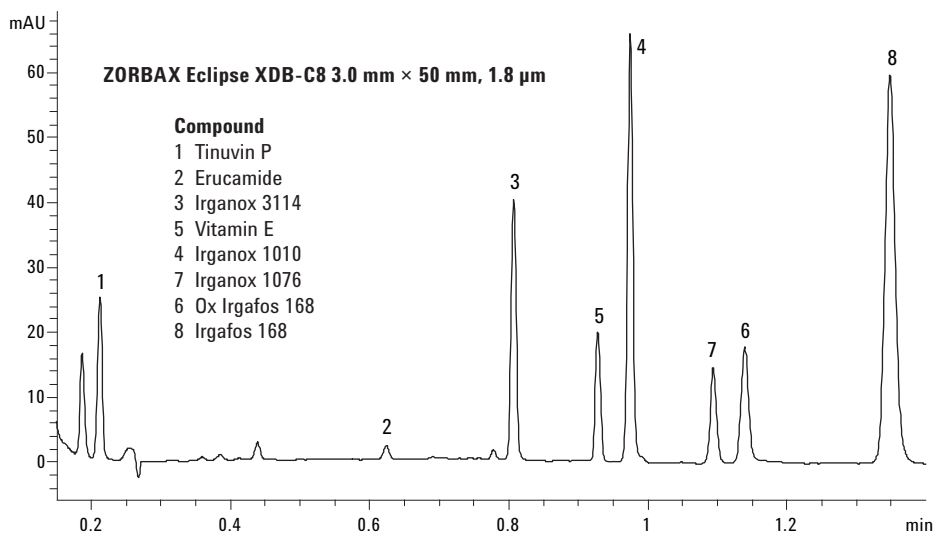
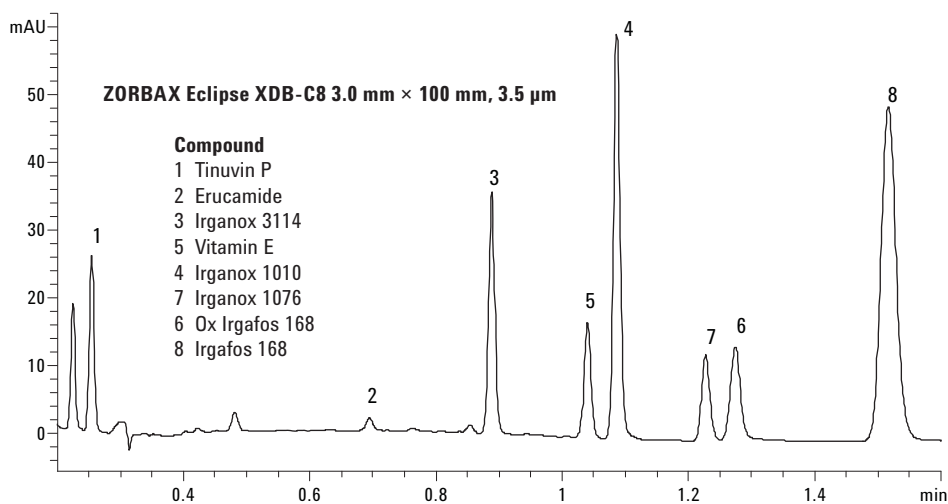
Sample:	Standard mixture, 200 µg/mL in isopropanol		
Mobile phase:	A: water; B: ACN		
Temperature:	50 °C		
Wavelength:	200 nm		
Injection volume:	3.3 µL		
Column:	ZORBAX Eclipse XDB-C8 3.0 mm × 50 mm, 1.8 µm		
Mode:	Simple converted	Speed optimized	Resolution optimized
Flow rate:	0.64 mL/min	2.50 mL/min	2.50 mL/min
Pressure:	160 bar	460 bar	460 bar
Gradient slope:	3.1%	3.1%	0.8%
Analysis time:	6 min	1.4 min	3 min

**Figure 5. Separation of antioxidants on ZORBAX Eclipse XDB-C8 3.0 mm × 50 mm, 1.8 µm.**



To identify the matrix influence on the separation, the polypropylene extract was spiked with 20 µg/mL standard mixture and injected into the LC system. Figure 6 depicts the separation of

spiked sample with the speed optimized method, which shows a sufficient separation of antioxidant in polymer matrix with about 10 times faster speed than the conventional method mentioned above.



#### Conditions

Sample:	Polypropylene extract spiked with 20 µg/mL standard mixture	
Mobile phase:	A: water; B: ACN	
Temperature:	50 °C	
Wavelength:	200 nm	
Stationary phase:	ZORBAX Eclipse XDB-C8	
Column size:	3.0 mm × 100 mm, 3.5 µm	3.0 mm × 50 mm, 1.8 µm
Injection volume:	3 µL	1 µL
Mode:	Speed optimized	Speed optimized
Flow rate:	4.00 mL/min	2.50 mL/min
Pressure:	460 bar	460 bar
Gradient slope:	3.1%	3.1%
Analysis time:	1.6 min	1.4 min

**Figure 6. Separation of spiked polypropylene extract by the speed optimized method.**

## Conclusions

As an important innovation in the advancement of liquid chromatography, the Agilent 1200 Rapid Resolution LC system provides the customer not only a rapid separation with the same or similar resolution, but also includes a method translator to convert any initial conventional method to a fast or high-resolution method according to the requirements of the user. This note applies the method translation tool in the separation of polymer additives and demonstrates the ease-of-use and power of the method translator using separations of a standard mixture and spiked real sample.

## References

1. ASTM D6042-04, "Standard Test Method for Determination of Phenolic Antioxidants and Erucamide Slip Additives in Polypropylene Homopolymer Formulations Using Liquid Chromatography (LC)"
2. Michael Woodman, "Improving the Effectiveness of Method Translation for Fast and High Resolution Separations"
3. Michael Woodman, "Screening and Qualitative Identification of Antioxidant Polymer Additives by HPLC with UV/VIS and APCI-MS Detection"

## For More Information

For more information on our products and services, visit our Web site at [www.agilent.com/chem](http://www.agilent.com/chem).

The information contained in this publication is intended for research use only and is not to be followed as a diagnostic procedure.

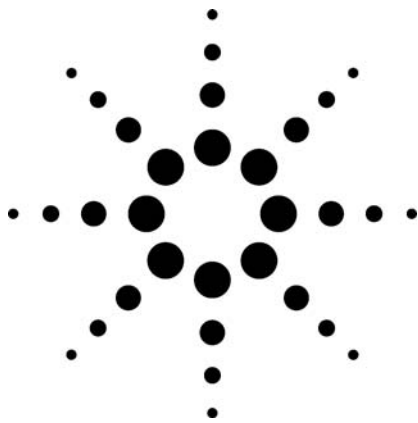
Agilent shall not be liable for errors contained herein or for incidental or consequential damages in connection with the furnishing, performance, or use of this material.

Information, descriptions, and specifications in this publication are subject to change without notice.

© Agilent Technologies, Inc. 2007

Printed in the USA  
January 5, 2007  
5989-5849EN





# Analysis of Phenolic Antioxidant and Erucamide Slip Additives in Polymer by Rapid-Resolution LC

## Application

### Hydrocarbon Processing

## Authors

Chun-Xiao Wang and Wei Luan  
Agilent Technologies (Shanghai) Co. Ltd.  
412 Ying Lun Road  
Waigaoqiao Free Trade Zone  
Shanghai 200131  
P.R. China

Michael Woodman  
Agilent Technologies, Inc.  
2850 Centerville Road  
Wilmington DE 19808  
USA

## Abstract

**Liquid chromatography with ultraviolet/visible (UV/VIS) detection is a powerful approach for analyzing additives in polymer formulations. This application illustrates the use of the Agilent 1200 Series Rapid Resolution LC (RRLC) system for the separation of antioxidants and erucamide. The system can operate significantly faster than conventional HPLC without sacrificing resolution, precision, or sensitivity. The column chemistry and temperature influence on the separation and the sample preparation method are also discussed.**

## Introduction

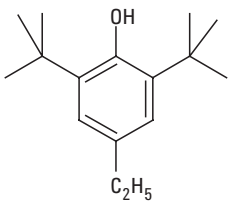
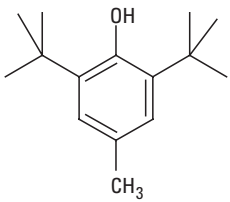
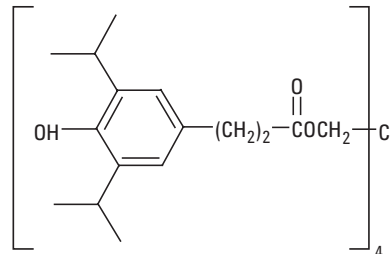
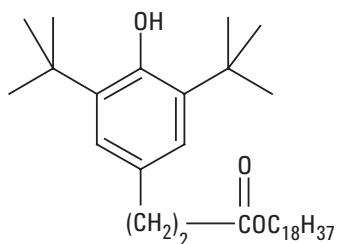
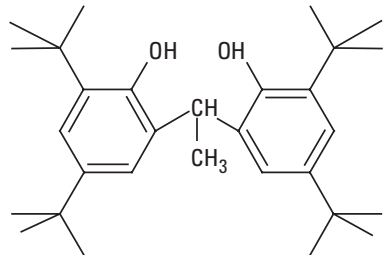
Additives are incorporated into various polymeric materials to retard the degradation caused by ultraviolet light, heat, and oxygen or to modify processing characteristics. A rapid and accurate analytical method is required to ensure that the specified amount of an additive or combination of additives is incorporated into a polymer after the extrusion process. Conventional HPLC methods for additives [1,2] often require more than 30 minutes per analysis, while the application described here can achieve comparable results in as few as 3 minutes.

Agilent has developed an easy-to-use method conversion tool for transferring existing methods for higher speed and/or higher resolution. The tool was used for the method optimization in this application. [3]

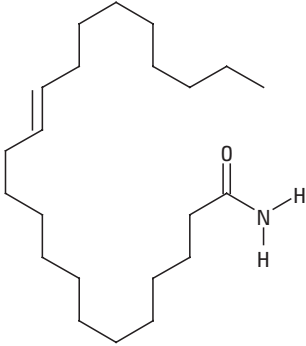
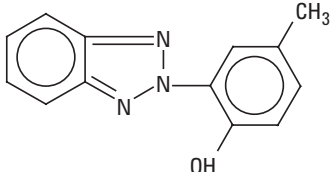
This application examines additives mentioned in ASTM Methods D5815 and D1996. The chemical structures are shown in Table 1.



**Table 1. Polymer Additives in ASTM Methods D5815 and D1996**

Registered trade name	CAS no.	Chemical name	Chemical structure
BHEB	4310-42-1	2,6-di-tert-butyl-4-ethyl-phenol or butylated hydroxyethyl benzene	
BHT	128-37-0	2,6-di-t-butyl-cresol or butylated hydroxy toluene	
Irganox 1010	6683-19-8	Tetrakis[methylene(3,5-di-t-butyl-4-hydroxy hydrocinnamate)] methane	
Irganox 1076	2082-79-3	Octadecyl-3,5-di-t-butyl-4-hydroxy hydrocinnamate	
Isonox 129	35958-30-6	2,2-ethylidene bis (4,6-di-t-butyl phenol)	

**Table 1. Polymer Additives in ASTM Methods D5815 and D1996 (Continued)**

Registered trade name	CAS no.	Chemical name	Chemical structure
Kemamide-E	112-84-5	Cis-13-docosenamide or Erucamide or Fatty acid amide (C <sub>22</sub> H <sub>43</sub> NO)	
Tinuvin P	2440-22-4	2(2'-hydroxy-5'-methyl phenyl) benzotriazole	

## Experimental

### System

Agilent 1200 Series rapid-resolution LC configured with  
G1379B microvacuum degasser  
G1312B binary pump SL  
G1367B high-performance autosampler SL  
G1316B thermostatted column compartment SL  
G1315C UV/VIS diode array detector SL  
ChemStation 32-bit version B.02.01

### Column

ZORBAX Eclipse XDB-C18, 4.6 mm × 150 mm, 5 μm  
ZORBAX Eclipse XDB-C18, 2.1 mm × 50 mm, 1.8 μm  
ZORBAX SB-C18, 4.6 mm × 150 mm, 5 μm  
ZORBAX SB-C18, 4.6 mm × 50 mm, 1.8 μm

### Mobile phase

Gradients: A: water  
B: acetonitrile (ACN)

Gradient slope: See individual chromatograms for flow rate and gradient time

Column temperature: See individual chromatograms

### Samples

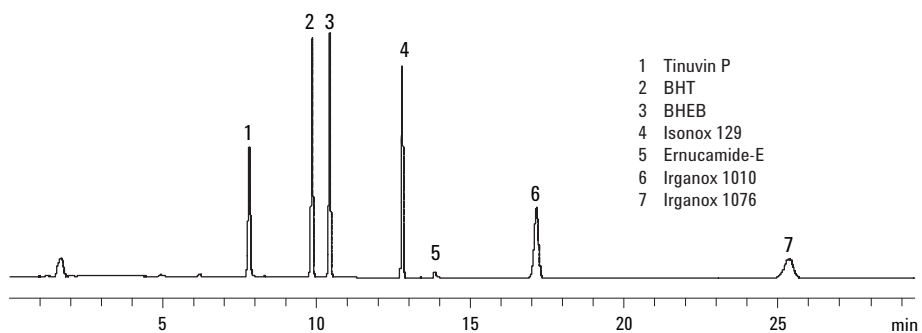
- Standard mixture described in ASTM D5815 and D1996, 50 μg/mL, 200 μg/mL in isopropanol
- Linear low-density polyethylene from customer, ground to 20 mesh, extracted by ultrasonic or reflux method

## Results and Discussion

### Fast Method Conversion

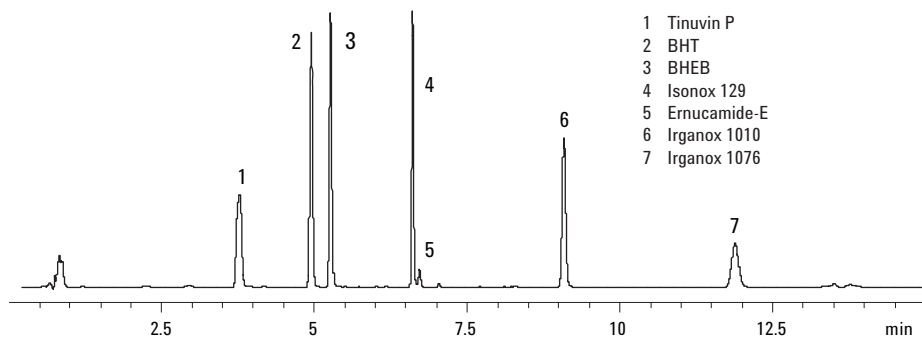
The separation was initially performed on a standard 4.6 mm × 150 mm, 5-μm ZORBAX Eclipse XDB-C18 column thermostatted to 60 °C (Figure 1) following the conditions in ASTM D5815 (or D1996). The method was then scaled in flow and time for exact translation to a 2.1 mm × 50 mm, 1.8-μm column (Figure 2). The analysis time was reduced from 25.5 to 12.5 minutes, and the solvent consumption was reduced from 25 to 2.5 mL.

The separation was then re-optimized for faster separation with the same gradient slope by increasing the flow rate from 0.21 to 0.9 mL/min and proportionately reducing the gradient time (Figure 3), achieving up to 10 times faster than conventional HPLC without sacrificing resolution, precision (shown in Table 2), or sensitivity. Figure 4 demonstrates that 1 ppm of additives can be determined with very good signal-to-noise response using the same condition in Figure 3, which exceeds the specification of 2 ppm of ASTM D5815 (or D1996). Peak 6, Irganox 1010, for example has a signal-to-noise response of 88 at 1 ppm.



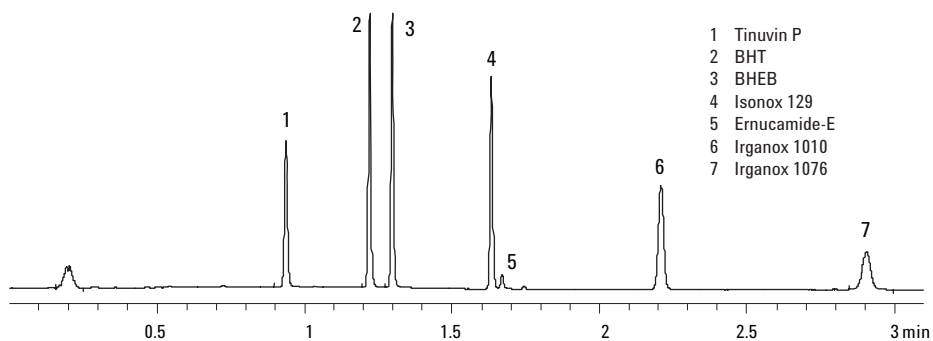
Conventional method:	Follow ASTM D5815 (or D1996) method with	<b>Gradient</b>
	ZORBAX Eclipse XDB-C18,	%B
	4.6 mm × 150 mm, 5 μm	0      50
Sample:	Standard 50 μg/mL	11     100
Sample size:	10 μL	28     100
Detector:	UV 200 nm	28.1   50
Column temperature:	60 °C	
Mobile phase:	A: water	
	B: acetonitrile	
Flow rate:	1 mL/min	

**Figure 1. Separation of additives standards on Eclipse XDB-C18, 4.6 mm × 150 mm, 5 μm.**



Simple-converted:	Translate the conventional method to a	<b>Gradient</b>
	ZORBAX Eclipse XDB-C18, 2.1 mm × 50 mm, 1.8 μm	%B
Sample:	Standard 50 μg/mL	0      50
Sample size:	2 μL	5.2    100
Detector:	UV 200 nm	12     100
Column temperature:	60 °C	12.1   50
Mobile phase:	A: water	15     50
	B: acetonitrile	
Flow rate:	0.21 mL/min (73 bar)	

**Figure 2. Separation of additives standards on Eclipse XDB-C18, 2.1 mm × 50 mm, 1.8 μm.**

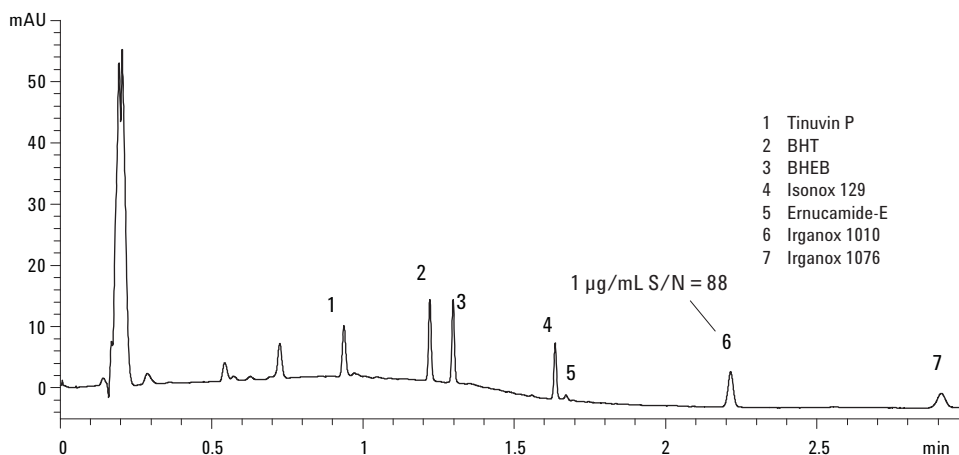


Speed-optimized:	Optimize the conventional method for speed with	<b>Gradient</b>
	ZORBAX Eclipse XDB-C18,	%B
	2.1 mm × 50 mm, 1.8 μm	0      50
Sample:	Standard 50 μg/mL	1.3    100
Sample size:	2 μL	3      100
Detector:	UV 200 nm	3.1    50
Column temperature:	60 °C	3.5    50
Mobile phase:	A: water	
	B: acetonitrile	
Flow rate:	0.9 mL/min (357 bar)	

**Figure 3. Fast separation of additives standards on Eclipse XDB-C18, 2.1 mm × 50 mm, 1.8 μm.**

**Table 2. Repeatability for the Methods of Conventional, Simple-Converted, and Speed-Optimized Methods (n = 5)**

Compounds (50 ppm)	Area, RSD%		
	Conventional	Simple-converted	Speed-optimized
Tinuvin P	0.37	0.39	0.09
Erucamide	0.40	0.57	0.13
Irganox 3114	0.44	0.49	0.22
Irganox 1010	0.38	0.39	0.26
Vitamin E	0.58	0.80	0.68
Irganox 1076	0.58	1.49	0.17
Irgafos 168	0.53	0.77	0.32



Speed-optimized method for analysis of additives standards with concentration of 1 μg/mL LC conditions is identical to that in Figure 3

**Figure 4. Fast separation of 1 μg/mL additives standards on Eclipse XDB-C18, 2.1 mm × 50 mm, 1.8 μm.**

### Optimized Column Temperature

Increasing column temperature can lower both solvent viscosity and nonspecific column/analyte interactions. The new ZORBAX StableBond RRHT columns can operate at temperatures up to 90 °C. We tested operating temperatures at 60, 75, 85, and 90 °C with a ZORBAX SB-C8 4.6 mm × 150 mm, 5- $\mu$ m column. The results (Figure 5) show that the analysis time obtained from 60 °C to 85 °C is reduced from 23.5 minutes to 17 minutes; at 90 °C, only an additional 0.5 minute is saved. Based on the combined speed reduction and optimized resolution of peaks 4 and 5, 85 °C is chosen as a suitable column temperature.

The method was then scaled in flow and time for exact translation to a 4.6 mm × 50 mm, 1.8- $\mu$ m column (Figure 6). Finally, the separation was optimized for faster separation by increasing the flow rate from 1 mL/min to 3.5 mL/min, with only a 1.7-minute analysis time (Figure 7). This is really an excellent procedure for high-throughput screening and quantitation of a large number of samples. Figure 8, the separation of an extract of linear low-density polyethylene (LLDPE) spiked with 20  $\mu$ g/mL of standard solution, shows excellent separation with real sample matrix.

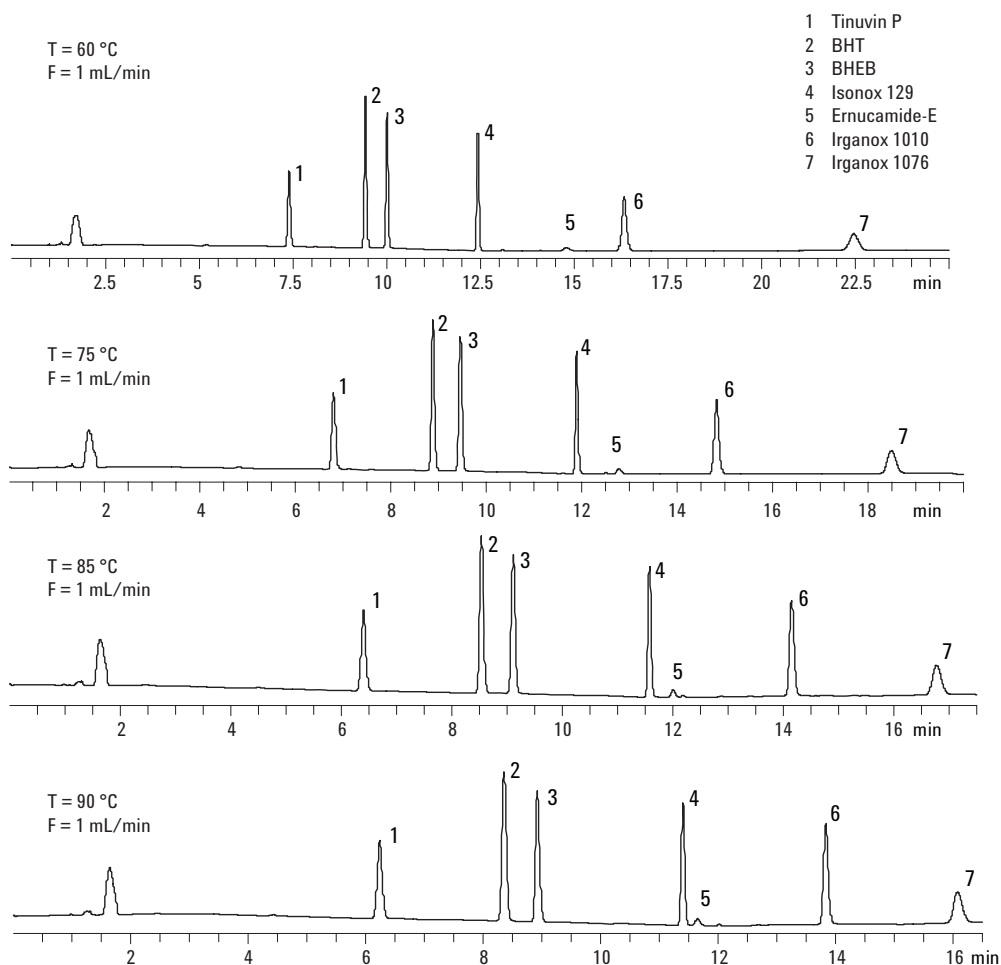
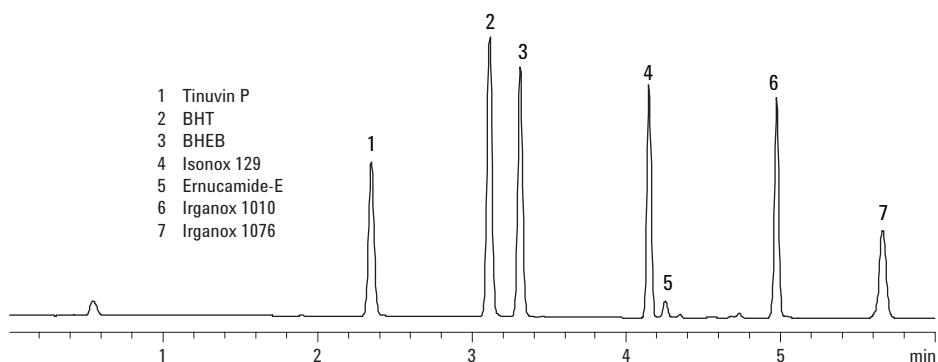


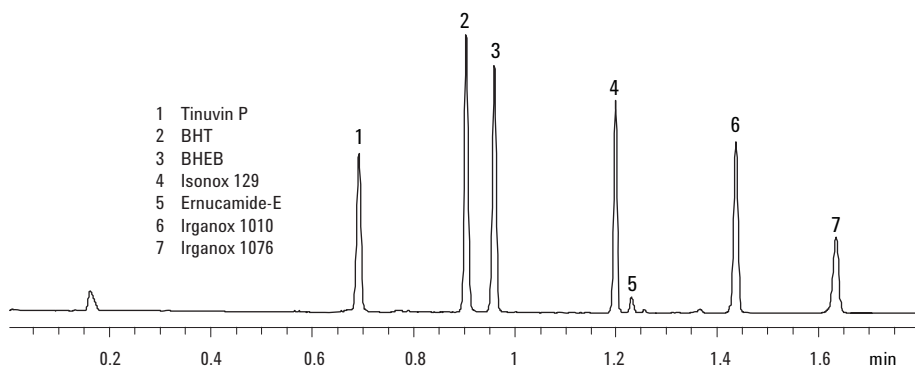
Figure 5. Separation of additives standards on ZORBAX StableBond RRHT SB-C18, 4.6 mm × 150 mm, 1.8  $\mu$ m.





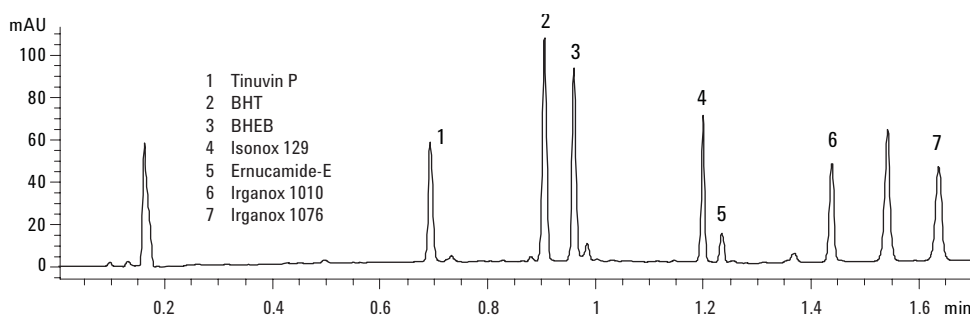
Sample: Standard 200 mg/mL  
 Sample size: 2  $\mu$ L  
 Detector: UV 200 nm  
 Mobile phase: A: water  
                   B: acetonitrile  
 Gradient slope: 6.8%  
 Flow rate: 1 mL/min

**Figure 6. Separation of additives standards on ZORBAX SB-C18, 4.6 mm  $\times$  50 mm, 1.8  $\mu$ m, at 85  $^{\circ}$ C.**



Sample: Standard\_200 mg/mL  
 Sample size: 2  $\mu$ L  
 Detector: UV 200 nm  
 Mobile phase: A: water  
                   B: acetonitrile  
 Gradient slope: 6.8%  
 Flow rate: 3.5 mL/min

**Figure 7. Fast separation of additives standards on ZORBAX SB-C18, 4.6 mm  $\times$  50 mm, 1.8  $\mu$ m, at 85  $^{\circ}$ C.**



LC conditions are identical with those in Figure 7.

**Figure 8. Fast separation of spiked real sample-LLDPE (20  $\mu$ g/mL) on ZORBAX SB-C18, 4.6 mm  $\times$  50 mm, 1.8  $\mu$ m, at 85  $^{\circ}$ C.**

## Sample Preparation

ASTM D5815 (or D1996) method recommends using a reflux apparatus for extracting additives in polymer. This requires periodic operator intervention over the 1.5-hour-long extraction period. To find a time-saving sample-preparation method, ultrasonic extraction was also tested, producing comparable results in 30 minutes. In terms of extraction efficiency, there is not much difference between these two methods. Figure 9 shows very good overlays of extractions by reflux and ultrasonic extraction methods for a LLDPE. Conditions are identical to those in Figure 1.

## Conclusions

Liquid chromatography with ultraviolet/visible detection is an effective tool for analyzing additives in polymer formulations. The Agilent 1200 Series RRLC system equipped with RRHT 1.8- $\mu\text{m}$  columns was used to achieve up to 10 times faster than the conventional HPLC method. The ultrasonic extraction method allowed fast extraction without user intervention for a significant reduction in overall analysis time. Total time saved was more than 80 minutes per sample when compared

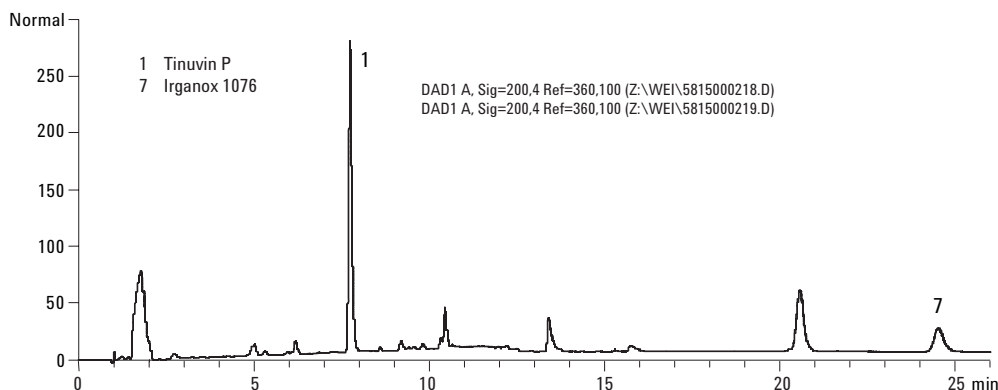
to the conventional analysis and extraction methods.

## References

1. ASTM D5815-95, "Standard Test Method for Determination of Phenolic Antioxidants and Erucamide Slip Additives in Linear Low-Density Polyethylene Using Liquid Chromatography (LC)."
2. ASTM D1996-97, "Standard Test Method for Determination of Phenolic Antioxidants and Erucamide Slip Additives in Low-Density Polyethylene Using Liquid Chromatography (LC)."
3. Agilent Application Compendium CD, 5989-5130EN, June 2006.
4. Michael Woodman, "Improving the Effectiveness of Method Translation for Fast and High Resolution Separations," Agilent Technologies, publication 5989-5177EN.

## For More Information

For more information on our products and services, visit our Web site at [www.agilent.com/chem](http://www.agilent.com/chem).



**Figure 9. Chromatogram Overlays of extractions by reflux and ultrasonic extraction methods for LLDPE.**

The information contained in this publication is intended for research use only and is not to be followed as a diagnostic procedure.

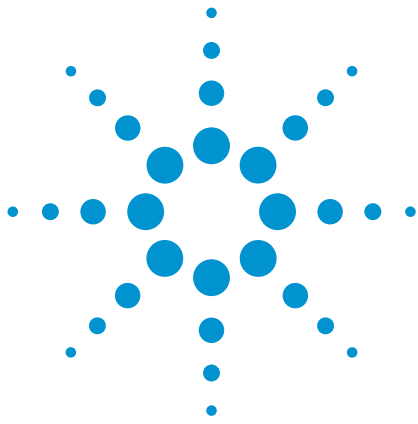
Agilent shall not be liable for errors contained herein or for incidental or consequential damages in connection with the furnishing, performance, or use of this material.

Information, descriptions, and specifications in this publication are subject to change without notice.

© Agilent Technologies, Inc. 2007

Printed in the USA  
January 17, 2007  
5989-5850EN





# Developing a UHPLC method for UV-based detection and quantification of primary aromatic amines in low concentrations

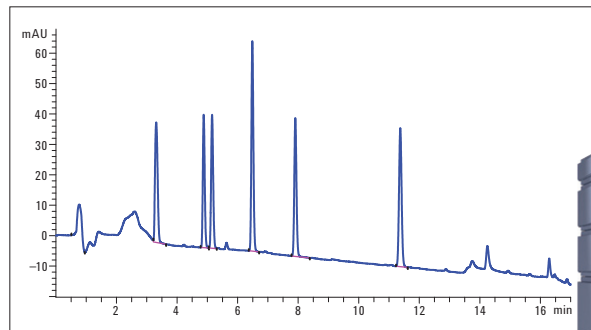
## Application Note

Consumer Products

### Authors

Edgar Naegele  
Agilent Technologies, Inc.  
Waldbronn, Germany

Ruediger Helling  
Landesuntersuchungsanstalt für das  
Gesundheits- und Veterinärwesen,  
Saxony, Dresden, Germany



### Abstract

This Application Note demonstrates that stringent sensitivity requirements for the detection of potentially harmful primary aromatic amines can be fulfilled when using an Agilent 1290 Infinity LC System equipped with the 1290 large volume injection kit. This enables the Agilent 1290 Infinity Autosampler for injection volumes up to 120  $\mu\text{L}$  for sample enrichment on the column. A high sensitivity 60-mm Max-Light flow cell in the Agilent 1290 Infinity Diode Array Detector gives additional detection sensitivity.



**Agilent Technologies**

## Introduction

Primary aromatic amines (PAAs), for example, aniline and its derivatives can originate from printing azo-dyes and azo-pigments, isocyanate based adhesives and monomers used for plastics. Since these compounds are potentially harmful and suspected to cause cancer and have other adverse effects, they have to be detected and determined, for example, in printed products, recycled paper and board material, plastic goods, and food products.

A legal requirement already exists for plastic food contact materials (FCM) within regulation 10/2011. Plastic FCM may not release PAAs in a detectable quantity. The detection limit is defined as 10 ppb (sum of all PAAs, including analytical tolerance). Similar requirements exist on the national level for paper and board materials (see BfR recommendation XXXVI on paper and board). The upcoming German regulation for printing inks used for FCM (Druckfarben V) also mentions a limit of 10 ppb for the sum of the released PAAs. Recently, problems have been reported within industry and enforcement authorities regarding the release of carcinogenic PAAs from heavily printed paper bags and napkins.

Since the legal limits apply to the sum of all PAAs, these compounds have to be detected down to a level of at least 1 ppb (1 ng/mL) for an individual PAA. One of the recommended methods for determination is HPLC with UV-based detection using a diode array detector (DAD).

This Application Note demonstrates that, in principle, this requirement can be fulfilled. Six representative primary aromatic amine compounds were tested using an Agilent 1290 Infinity LC System equipped with the 1290 large volume injection kit in the Agilent 1290 Infinity Autosampler module. This enables the Agilent 1290 Infinity

Autosampler for injection volumes up to 120  $\mu$ L for sample enrichment on the column. A high sensitivity 60-mm Max-Light flow cell in the Agilent 1290 Infinity Diode Array Detector gives additional detection sensitivity.

## Experimental

### Equipment

The Agilent 1290 Infinity LC System consisted of the following modules:

- Agilent 1290 Infinity Pump (G4220A)
- Agilent 1290 Infinity Autosampler (G4226A) equipped with 40- $\mu$ L flex loop kit (p/n 5067-4703), 1290 large volume injection kit (G4216A) and sample cooling (G1330B)
- Agilent 1290 Infinity Thermostatted Column Compartment (G1316C)
- Agilent 1290 Infinity Diode Array Detector (G4221A)

### Software

- CDS Open Lab ChemStation Edition C01.03

### Column

- Agilent ZORBAX Eclipse Plus C18, RRHT, 3.0  $\times$  100 mm, 1.8  $\mu$ m

### Method

- Agilent 1290 Infinity Pump

Solvents: A: Water and 10 mM Sodium acetate, pH 5.1  
B: Methanol

Gradient: 0 minutes–5% B,  
1 minute–5% B,  
2 minutes–20% B,  
15 minutes–70% B,  
17 minutes–90% B

Stop time: 17 minutes

Post time: 3 minutes

Flow rate: 0.75 mL/min

- Agilent 1290 Infinity Autosampler

Injection  
volume: 120  $\mu$ L

Needle wash: 6 seconds in MeOH

Sample  
temperature: 10  $^{\circ}$ C

- Agilent 1290 Infinity Thermostatted Column Compartment

Column  
temperature: 40  $^{\circ}$ C

- Agilent 1290 Infinity Diode Array Detector

Wavelength: 240/8 nm

Ref.  
wavelength: 360/100 nm

Slit: 8 nm

Data rate: 20 Hz

Cell: 60-mm Max-Light high sensitivity cell

### Samples

Stock solutions of: aniline, o-anisidine, o-toluidine, 2-methyl-5-nitroaniline, 2,4-dimethylaniline, 2,4-dichloraniline at 10 mg/100 mL in acetonitrile each. Diluted to a mixed stock solution at 1,000 ng/mL each in water/methanol 95/5 (v/v). Dilution series: 100, 50, 20, 10, 5, 2, 1, 0.5 ng/mL in water/methanol 95/5 (v/v).

Preparation of blank matrix from colorized napkins for spiking experiments:

A cold water extract of pretested napkins was prepared according to CEN standard 645. The napkin was cut into small pieces, 10 g of which were put in a flask and filled with 200 mL of distilled water. The extract was allowed to stand at room temperature for 24 hours, then the paper was separated by decantation and the water adjusted to a final volume of 250 mL.

## Results and discussion

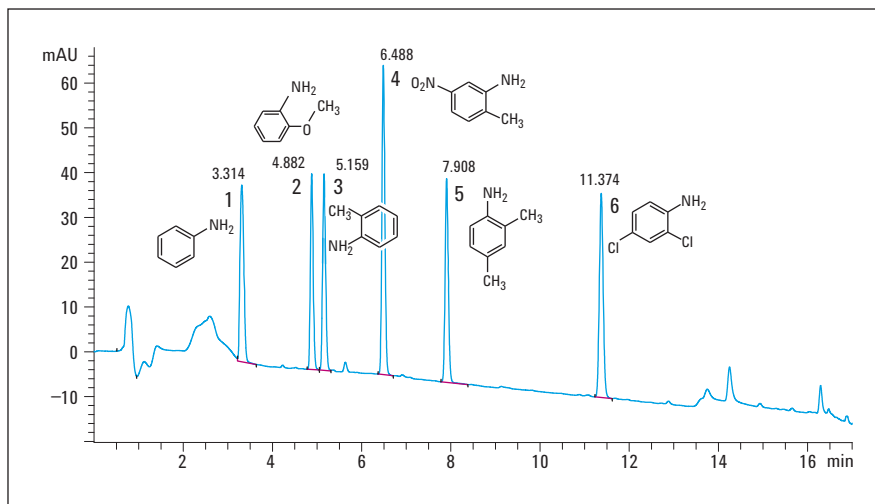
To meet the requirement of highly sensitive UV based detection of PAAs down to an individual level of 1 ppb, two modifications were made to the standard configuration of the Agilent 1290 Infinity LC System.

First, the standard 10-mm Max-Light flow cell in the 1290 Infinity Diode Array Detector was replaced with a 60-mm Max-Light high sensitivity flow cell. Second, the standard 20- $\mu$ L loop in the 1290 Infinity Autosampler was replaced with a 40- $\mu$ L loop by including the 1290 large volume injection kit to inject volumes up to 120  $\mu$ L<sup>1</sup>.

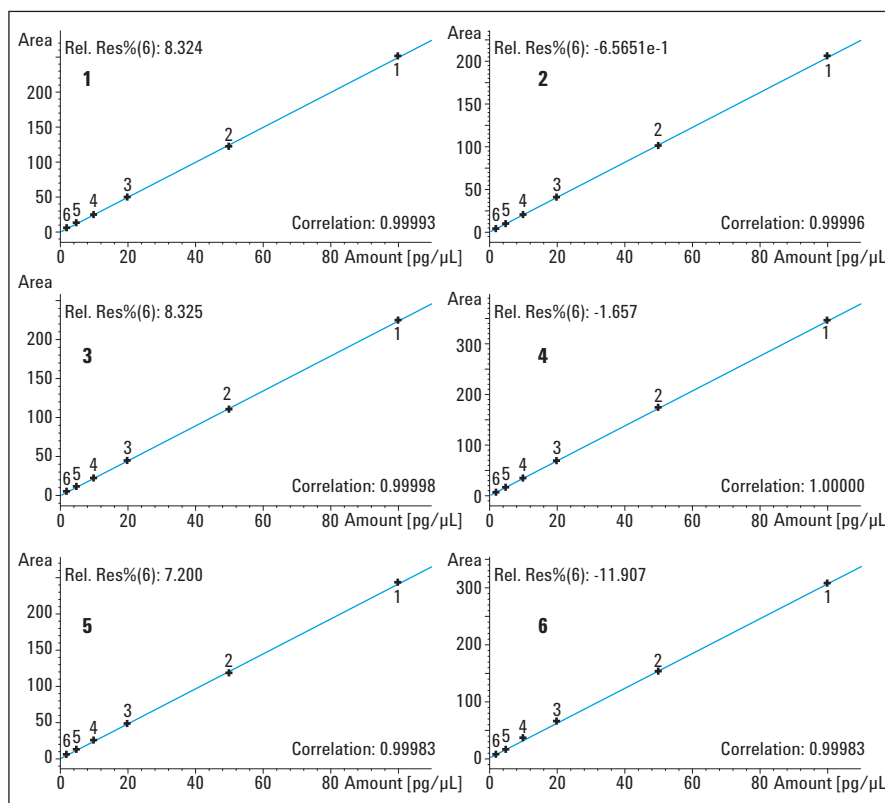
The method that was finally applied was developed by using a mixture of the six PAAs at a concentration of 100 ng/mL each (Figure 1). The method starts with an enrichment step for the first minute followed by a steep increase to the starting conditions at 20% methanol. The gradient separation was done in the following 13 minutes up to 70% methanol.

With the final method, a calibration was done for all PAAs from 100 ng/mL down to a level of 2 ng/mL (2 ppb). All linearity correlation coefficients were above 0.99983 (Figure 2). The concentration level at 2 ng/mL was defined as the limit of quantification (LOQ) because the compounds' signal-to-noise ratio was around 10 at this point. The limit of detection (LOD) was 0.5 ng/mL at a signal-to-noise ratio around 3 for all compounds.

A statistical evaluation was done on the 10 ng/mL level as an example for the lower level concentrations. The relative standard deviation (RSD) of the retention times was between 0.039 and 0.057%, the area RSDs were between 0.5 and 2.7%. The precision of the measured concentrations was in the same range (Table 1). Relative standard deviation of the compound response factors were between 0.004 and 0.017%.



**Figure 1**  
Primary aromatic amines at 100 ng/mL, 1) aniline: 3.314 minutes, 2) o-anisidine: 4.882 minutes, 3) o-toluidine: 5.159 minutes, 4) 2-methyl-5-nitroaniline: 6.488 minutes, 5) 2,4-dimethylaniline: 7.908 minutes, 6) 2,4-dichloroaniline: 11.373 minutes.



**Figure 2**  
Calibration curves 2–100 ng/mL of the used paAs, 1) aniline: Correlation: 0.99993, 2) o-anisidine: Correlation: 0.99996, 3) o-toluidine: Correlation: 0.99998, 4) 2-methyl-5-nitroaniline: Correlation: 1.00000, 5) 2,4-dimethylaniline: Correlation: 0.99983, 6) 2,4-dichloroaniline: Correlation: 0.99983

To test the method, a blank matrix sample produced from a heavily colored napkin was spiked with the six PAAs at various concentrations (Figure 3). All six PAAs could be well separated from the matrix compounds and identified and quantified with the developed method and calibration. However, for some PAAs, a sample cleaning step using SPE prior to the chromatographic analysis might be necessary as indicated by a recovery that was too high, for example, of o-toluidine. This may have been caused by matrix interferences and has to be considered in further method development activities.

## Conclusion

This Application Note shows that the Agilent 1290 Infinity LC System can detect low amounts of primary aromatic amines by using the 60-mm Max-Light high sensitivity cell in the diode array detector, and the 1290 large volume injection kit in the autosampler for an enrichment step. Data are shown which prove an excellent linearity of the calibration down to the LOQ at 2 ppb. The LOD was found at 0.5 ppb. The lower level calibration points show good relative standard deviations for the retention time and the area as well as good precision for the measured concentrations. The PAAs could be detected and quantified in a sample with heavy matrix load at lowest levels.

## Reference

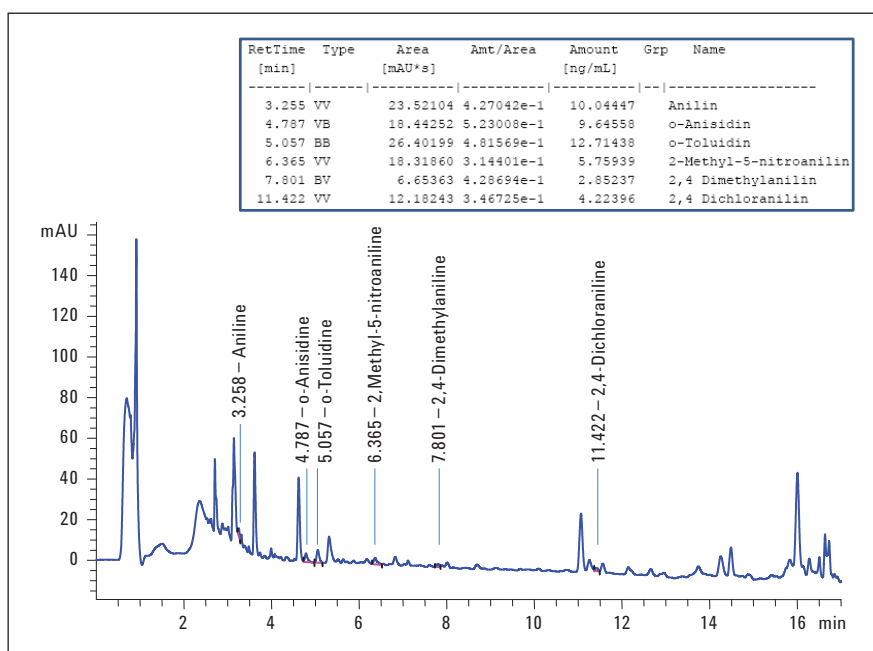
1. *Enhancing the maximum injection volume of the Agilent 1290 Infinity Autosampler*, Agilent Technical Overview, Publication Number 5990-9533EN, 2011.

Compound	Aniline				o-Anisidine				o-Toluidine			
	RT	Area	Amount	Compound response factor	RT	Area	Amount	Compound response factor	RT	Area	Amount	Compound response factor
Average	3.273	22.474	9.610	0.427	4.815	19.131	9.988	0.522	5.084	20.848	10.014	0.480
Standard deviation	0.001	0.117	0.048	7.049E-05	0.002	0.094	0.048	2.870E-05	0.002	0.567	0.271	5.390E-05
RSD (%)	0.039	0.521	0.505	0.016	0.047	0.494	0.489	0.005	0.047	2.722	2.715	0.011

Compound	2-Methyl-5-nitroaniline				2,4-Dimethylaniline				2,4-Dichloraniline			
	RT	Area	Amount	Compound response factor	RT	Area	Amount	Compound response factor	RT	Area	Amount	Compound response factor
Average	6.400	31.729	9.913	0.312	7.827	22.871	9.925	0.433	11.367	28.067	10.050	0.358
Standard deviation	0.004	0.279	0.087	1.298E-05	0.004	0.198	0.086	2.950E-05	0.006	0.321	0.116	6.251E-05
RSD (%)	0.057	0.880	0.880	0.004	0.050	0.869	0.875	0.006	0.049	1.146	1.163	0.017

**Table 1**  
Retention time precision, area precision, concentration precision and compound response factor precision for the six used standard paAs at 10 ng/mL.



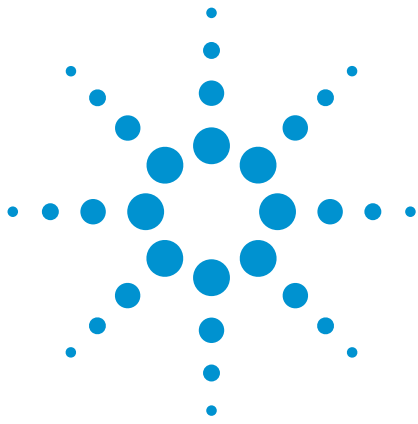
**Figure 3**  
Matrix sample from a heavily colored napkin spiked with the six paAs.

[www.agilent.com/chem/1200](http://www.agilent.com/chem/1200)

© Agilent Technologies, Inc., 2012  
Published in the USA, February 10, 2012  
5990-9751EN



**Agilent Technologies**



# Determination of polymer additives and migration products prevalent in food packaging material

Using the Agilent 1260 Infinity SFC System with the Agilent 6130 Single Quadrupole LC/MS System

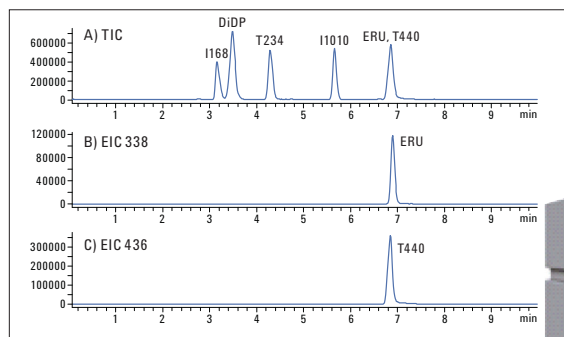
## Application Note

Consumer Product, Food Safety

### Authors

Melissa Dunkle, Gerd Vanhoenacker,  
Frank David, Pat Sandra  
Research Institute for Chromatography,  
President Kennedypark 26,  
8500 Kortrijk, Belgium

Martin Vollmer  
Agilent Technologies Inc.  
Waldbronn, Germany



### Abstract

According to EU directive 2002/72, materials that come into contact with food products should be tested for possible leachables. Supercritical fluid chromatography (SFC) is a complimentary separation technique to HPLC for the analysis and potential detection of polymer additives that might be released out of packaging material. This Application Note demonstrates the applicability of SFC for typical polymer additives using the Agilent 1260 Infinity Analytical SFC System in combination with an Agilent 6130 Single Quadrupole LC/MS System.



**Agilent Technologies**

## Introduction

According to EU Directive 2002/72/EC, materials that are intended to come into contact with food products should be tested for potential leach out of the plastic material<sup>1</sup>. This directive contains a list of additives, along with global and specific migration limits (SMLs). The list contains volatiles, such as acetic acid and monomers (for example, butadiene), semivolatiles (phenols) and nonvolatile components. An additional directive describes four simulants that can be used for migration testing<sup>2</sup>.

Specific migration of solutes is determined by analyzing the simulants. Obviously, different analytical methods are used for these tests. While the volatile solutes can be analyzed by gas chromatography, for example, in combination with headspace sampling, semivolatiles and nonvolatiles require other analytical methods. For some compounds, HPLC can be used. Several additives, however, are quite apolar and have a high molecular weight (> 300 Da). For the analysis of this class of solutes, supercritical fluid chromatography (SFC) is an excellent technique. Since several additives do not contain a chromophore, MS detection is often required.

In this Application Note, the analysis of some typical polymer additives by SFC/MS is demonstrated. Additionally, the potential of the SFC/MS approach is illustrated for the analysis of unknown (non-UV absorbing) solutes that leached out of a polymer intended to be used as food packaging. Based on the SFC/MS analysis, the material was rejected.

## Experimental

### Solutions and sample preparation

A mixture containing six typical polymer additives, belonging to different

classes, was prepared at a concentration of 50 µg/mL in methanol. The solutes are listed in Table 1, with their abbreviation, molecular formula, and molecular weight.

The SFC/MS method was applied to the analysis of solutes released from a polymer intended to be used for food packaging. Approximately 1.5 g of the polymer was weighed and placed in a 20 mL vial; 10 mL of a 85/15 water/ethanol solution was added to the vial, and the vial was placed in an oven at 40 °C for 24 hours. After removal of the polymer, the extract was analyzed as such.

Name	Abbrev.	Formula	MW (g/mol)	Ion APCI (+)	Ion mass	Ion APCI (-)	Ion mass
Diisodecyl Phthalate	DiDP	C <sub>28</sub> H <sub>46</sub> O <sub>4</sub>	446.66	M+H	447	N/A	N/A
Irganox 1010	I1010	C <sub>73</sub> H <sub>108</sub> O <sub>12</sub>	1177.67	M+H+NH <sub>3</sub>	1195	M-H	1176
Tinuvin 440	T440	C <sub>25</sub> H <sub>45</sub> N <sub>3</sub> O <sub>3</sub>	435.64	M+H	436	M-H	434
Tinuvin 234	T234	C <sub>30</sub> H <sub>29</sub> N <sub>3</sub> O	447.63	M+H	448	M-H	446
Erucamide	ERU	C <sub>22</sub> H <sub>43</sub> NO	337.58	M+H	338	N/A	N/A
Irgafos 168	I168	C <sub>42</sub> H <sub>63</sub> O <sub>3</sub> P	646.90	M+H	647	N/A	N/A

**Table 1**  
List of compounds in test mixture.



## Experimental

The analyses were performed on an Agilent 1260 Infinity Analytical SFC System coupled to an Agilent 6130 Single Quadrupole LC/MS System. The system configuration is listed in Table 2. Details on the coupling of the Agilent 1260 Infinity SFC to MS systems can be found in another Agilent publication<sup>3</sup>.

Two normal phase columns of the same stationary phase (Agilent ZORBAX RX-SIL: 4.6 × 250 mm, 5 μm) were coupled together to give a total column length of 50 cm. The modifier used was methanol with 20 mM ammonium formate. Detection was done in positive mode using an APCI source. The experimental conditions are summarized in Table 3.

Agilent 1260 Infinity SFC/MS solution	Part number
1260 Infinity Analytical SFC System consisting of:	G4309A
• 1260 Infinity Degasser	
• Aurora Fusion A5 module	
• 1260 Infinity SFC Autosampler	
• 1260 Infinity SFC Binary Pump	
• 1290 Infinity Thermostatted Column Compartment	
• 1260 Infinity Diode Array Detector VL Plus	
External heating device	Caloratherm heater
1260 Infinity Micro Degasser	G1379A
1100 Series Binary Pump	G1312A (used as make-up flow pump)
6130 Quadrupole LC/MS	G6130B

**Table 2**  
System modules.

Conditions	
Column:	2 × Agilent ZORBAX RX-SIL (4.6 × 250 mm, 5 μm) (p/n 88097-901)
Supercritical fluid:	CO <sub>2</sub>
Modifier:	MeOH w. 20 mM NH <sub>4</sub> COOH
Outlet pressure:	120 bar
Flow rate:	2.0 mL/min
Modifier gradient:	0–10 min: 10–20%
Temperature:	40 °C
Injection volume:	5 μL
Caloratherm heater (*):	60 °C
Make-up flow (*):	Isopropanol at 0.5 mL/min
Detection:	MS scan 200–1200 amu (screening) MS SIM (419 amu) (DiNP quantification)
APCI:	Capillary V ± 3,000 V Corona current = 4.0 μA(+), 15.0 μA(-) Drying gas flow: 8.0 L/min at 325 °C Nebulizer pressure: 50 psig Vaporizer temperature: 350 °C

(\*): Caloratherm heater and make-up flow prevent solute deposition/condensation after the back-pressure regulator<sup>3</sup>.

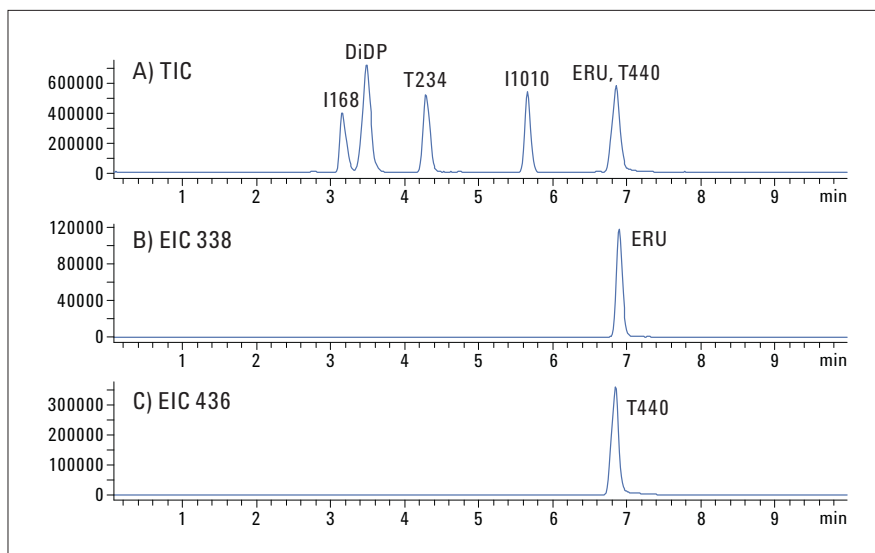
**Table 3**  
Experimental conditions.

## Results and discussion

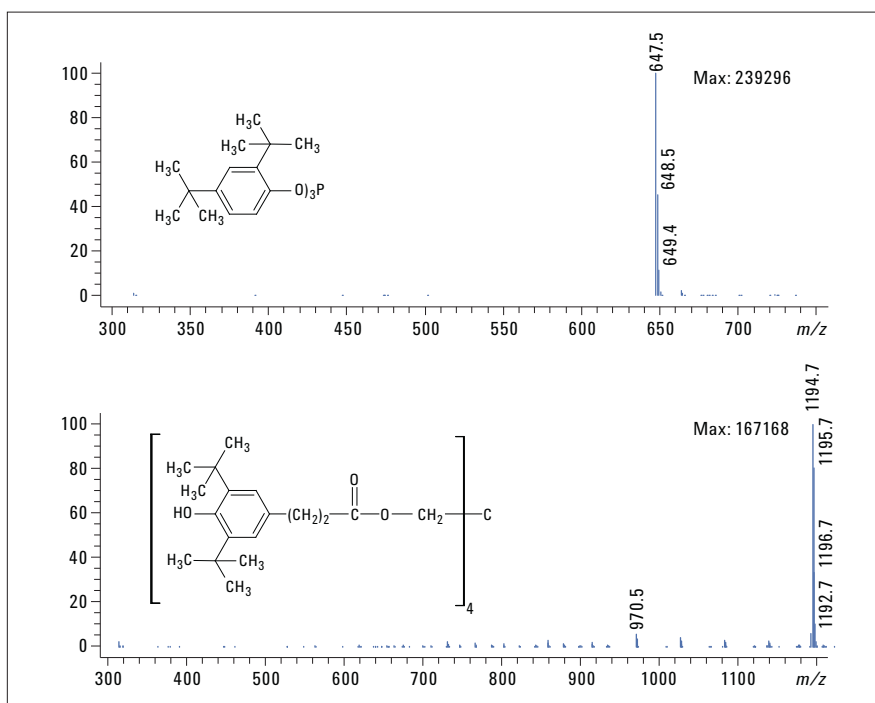
### Analysis of polymer additives using SFC-APCI-MS in positive mode

The test mixture, containing six typical polymer additives, was analyzed using the separation conditions given in Table 3. The separation obtained using these generic SFC conditions in APCI (+) mode is shown in Figure 1. Sufficient resolution between all compounds is achieved in 10 minutes analysis time. The test mixture contains analytes typically added at different steps of the manufacturing process of the packaging material, including diisononylphthalate (a plasticizer), Irgaphos 168 (a tris-arylphosphite processing stabilizer), Irganox 1010 (a sterically hindered phenolic antioxidant), Tinuvin 234, and Tinuvin 440 (hindered amine light stabilizers/UV absorbers) and erucamide (a slip, antistatic, anti-sticking agent). All these compounds can be separated and detected using SFC and good quality mass spectra are obtained, as illustrated in Figure 2 for Irgaphos 168 and Irganox 1010. Typically,  $[M+H]^+$  ions are prevalent, except for Irganox 1010 where an ammonium adduct is detected.

As shown in the TIC trace in Figure 1, erucamide and Tinuvin 440 are not chromatographically separated using the SFC conditions. However, based on their different mass spectrum, peak deconvolution using extracted ion chromatograms, clearly proves the presence of two different compounds as illustrated in Figure 1B (EIC 338 = erucamide) and Figure 1C (EIC 436 = Tinuvin 440).



**Figure 1**  
TIC of the SFC-APCI(+)-MS analysis of the polymer additive test mixture (A) and the EIC of the two coeluting compounds erucamide (B) and Tinuvin 440 (C).



**Figure 2**  
APCI(+)-MS mass spectra of A) Irgaphos 168 giving a clean spectra of the  $M+1$  ion (647) and B) Irganox 1010 giving a spectra of the ammonium adduct (1195). Note that the spectra have different x-axis scales.

Repeatability of the SFC/MS analysis was demonstrated by analyzing the test mixture six times. As illustrated in Table 4, excellent retention time reproducibility was obtained. Peak area repeatability was in the order of 5–10% taking into consideration that this is measured on raw peak areas obtained on extracted ion chromatograms from (APCI) scan acquisition.

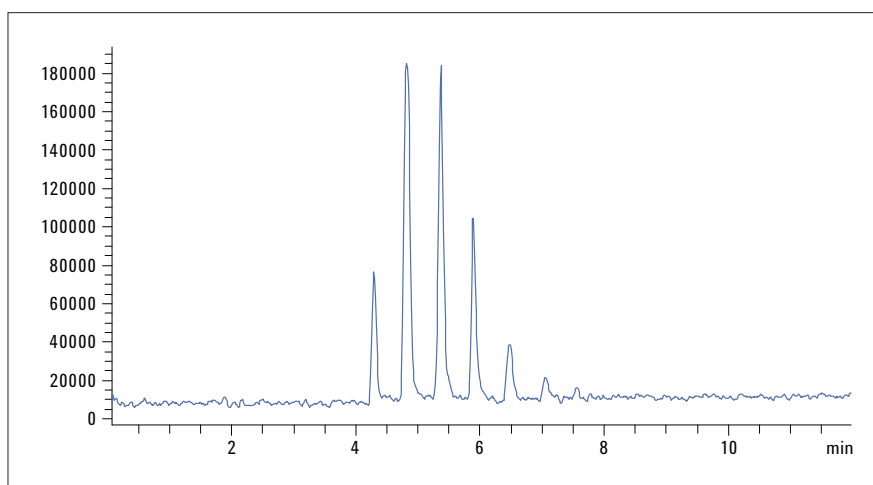
The analysis of the standard mixture of typical polymer additives clearly illustrates that SFC/MS is a useful tool for these type of applications. The described generic SFC/MS method can be applied to different classes of additives. It is also applicable for the analysis of other irganox, tinuvin, phthalate or amide type polymer additives. Since most polymers do not contain very complex cocktails of additives, it is in most cases not necessary to use slower modifier programs which results in increased analysis time.

### Screening of polymer extract

The potential of SFC/MS is also demonstrated by the analysis of an extract obtained from a polymer intended to be used for food packaging. The polymer was extracted in 15% ethanol. After 24 hours at 40 °C, the solution was analyzed. The total ion chromatogram obtained by SFC-APCI(+)MS in scan mode is shown in Figure 5. The first eluting compound was determined as an antioxidant (sterically hindered phenol).

	Ion	Retention time Average	% RSD	Peak area Average	% RSD
I168	647	3.168	0.52	1870000	9.62
DiNP	447	3.489	0.41	4995000	8.23
T234	448	4.296	0.29	3702500	8.08
I1010	1195	5.670	0.22	2417500	7.60
T440	436	6.832	0.27	2622500	8.00
ERU	338	6.899	0.21	599875	7.99

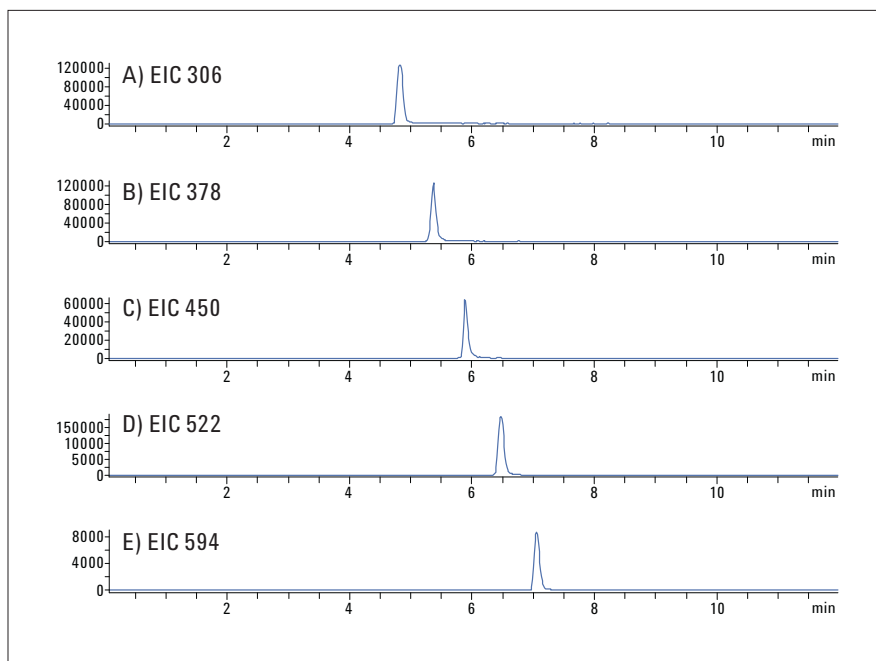
**Table 4**  
Reproducibility data.



**Figure 5**  
TIC of the SFC-APCI(+)MS analysis of ethanol/water extract of polymer.

The mass spectra of the other peaks showed most abundant ions at 306, 378, 450, 522, and 594, as illustrated in the extracted ion chromatograms in Figure 6. The difference between these masses is 72 Da, which most likely corresponds to poly-THF oligomers.

This example clearly illustrates how the SFC/MS system can be used for screening of solutes released from polymers in different simulants. It should also be noted that the extract was also analyzed by GC/MS and HPLC/UV and that neither of these techniques were able to detect all these compounds, either due to lack of volatility or lack of chromophore.



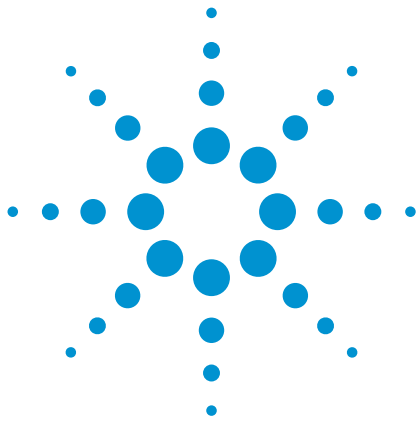
**Figure 6**  
EICs from Figure 5 showing the homologues series with a mass difference of 72 Da.

## Conclusion

The combination of the Agilent 1260 Infinity Analytical SFC System with the Agilent 6130 Single Quadrupole LC/MS System is an interesting tool to screen and quantify polymer additives and solutes that can migrate out of packaging material consisting of polymeric material. Using the SFC/MS conditions described, general screening of a wide range of polymer additives and oligomers (typically in a MW range from 200-1500) SFC/MS is very useful.

## References

1.  
EU Directive 2002/72/EC, Official Journal of the European Communities, L220/18, 15.8, **2002**.
2.  
EU Directive 85/572/EEC, Official Journal of the European Communities, L372/14, 31.12.85, **1985**.
3.  
M. Dunkle, G. Vanhoenacker, F. David, P. Sandra, M. Vollmer, Agilent Technologies Technical Overview, Publication Number 5990-7972EN, **2011**.



# Determination of phthalate migration from toys

Using the Agilent 1260 Infinity Analytical SFC System with an Agilent 6130 Single Quadrupole LC/MS

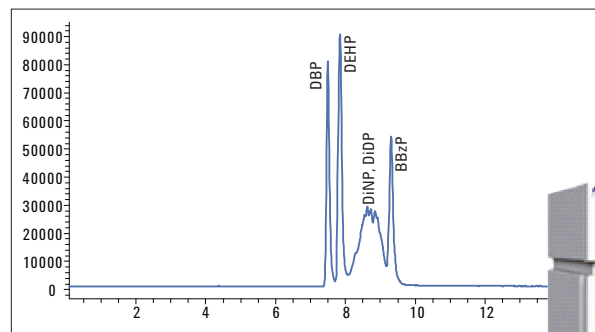
## Application Note

Consumer Products

### Authors

Melissa Dunkle, Gerd Vanhoenacker,  
Frank David, Pat Sandra  
Research Institute for Chromatography,  
President Kennedypark 26,  
8500 Kortrijk, Belgium

Martin Vollmer  
Agilent Technologies, Inc.  
Waldbronn, Germany



### Abstract

Supercritical fluid chromatography (SFC) can be used for the determination of polymer additives such as phthalates that can migrate or leach out of plastics. In this Application Note, the analysis of phthalates in a migration test from PVC toys is performed using the Agilent 1260 Infinity Analytical SFC System in combination with an Agilent 6130 Single Quadrupole LC/MS. The SFC/MS approach facilitated identification and quantification of mixed isomer phthalates in less than 15 minutes analysis time with good repeatability.



**Agilent Technologies**

## Introduction

Phthalates form a group of well known plasticizers that are often applied to soften polymers, such as PVC, in toys. High molecular weight phthalates are used as polymer additives. Phthalates are not chemically bound to PVC and can leach out or evaporate into the environment. It has been shown that, in rodents, phthalates can act as hormone-like compounds. They therefore have to be considered as a potential health risk to humans. Some well known phthalates, such as di(ethylhexyl) phthalate (DEHP), consist of a single isomer; others, such as diisononyl phthalate (DiNP) and diisodecyl phthalate (DiDP), consist of a mixture of isomers with different branching of the alkyl groups. It poses a significant analytical challenge to perform the analysis of these mixed isomer phthalates. Using capillary gas chromatography (GC), a partial separation of the individual isomers (within a sample of diisononyl or diisodecyl phthalate) is obtained, but this separation is not required since quantification is done on the sum of the isomers. Conversely, no GC separation is available, allowing the complete chromatographic separation of all DiNP isomers from all DiDP isomers. Moreover, in GC/MS using electron ionization (EI), all phthalates give very similar mass spectra with a most abundant ion at  $m/z$  149. Differentiation of both mixed isomer phthalates is only possible by using the  $[M\text{-alkyl}]^+$  ion ( $m/z$  297 for DiNP,  $m/z$  307 for DiDP)<sup>1</sup>. In contrast, different HPLC techniques can cover only a portion of leachable polymers, therefore reversed-phase separation and normal phase chromatography have to be used in order to cover the complete polarity range. In addition, leachables are often obtained in apolar solvents, which require solvent exchange prior to analysis if reverse phase separation is the method of choice.

SFC has an advantage because it is useful for a very broad range of analytes from polar to apolar. In addition, the analysis time is significantly lower

than that of HPLC methods due to the superior diffusion characteristics of the mobile phase, and due to the fact that solvent exchange is usually not required.

In this Application Note, the analysis of phthalates by SFC-MS is demonstrated. By using atmospheric pressure chemical ionization (APCI),  $[M+H]^+$  ions are obtained that allow good differentiation of DiNP and DiDP from each other and from other phthalates. The method was applied to the determination of DiNP from a toy, according to a procedure described by the European Commission<sup>2</sup>.

## Experimental

### Samples and extraction procedure

Stock solutions of dibutyl phthalate (DBP), butyl benzyl phthalate (BBzP), DEHP, DiNP and DiDP were prepared at 1,000 ppm in dichloromethane and stored at 4 °C. From these

stock solutions, a 10 ppm mixture was prepared; additionally, a dilution series for DiNP was made from 50 ng/mL–1,000 ng/mL in MeOH.

A plasticized PVC toy was analyzed according to the official procedure<sup>2</sup>. The extraction procedure consisted of cutting two disks from the toy (about 2.5-cm diameter, corresponding to a 10-cm<sup>2</sup> surface taking both sides into consideration). Both disks were placed into a sealable glass vessel with 30 mL of artificial saliva solution and three metal spheres. The container was then sealed and placed on a horizontal shaker for 30 minutes. The metal spheres were added to simulate a child chewing on the toy. The solution was then transferred to a separation funnel, to which 10 mL of cyclohexane were added. The cyclohexane layer was collected, evaporated down, and reconstituted in 1 mL of cyclohexane prior to injection.

Name	Abbreviation	Formula	MW (g/mol)	Ion APCI (+)	Ion mass
Dibutyl phthalate	DBP	C <sub>16</sub> H <sub>22</sub> O <sub>4</sub>	278.34	M+H	279
Benzybutyl phthalate	BBzP	C <sub>19</sub> H <sub>20</sub> O <sub>4</sub>	312.36	M+H	313
Di(2-ethylhexyl) phthalate	DEHP	C <sub>24</sub> H <sub>38</sub> O <sub>4</sub>	390.56	M+H	391
Diisononyl phthalate	DiNP	C <sub>26</sub> H <sub>42</sub> O <sub>4</sub>	418.61	M+H	419
Diisodecyl phthalate	DiDP	C <sub>28</sub> H <sub>46</sub> O <sub>4</sub>	446.66	M+H	447

**Table 1**  
Names, abbreviations, molecular formulae, and MW information of selected phthalates.

Agilent 1260 Infinity SFC/MS solution	Part number
1260 Infinity Analytical SFC System consisting of: <ul style="list-style-type: none"><li>• 1260 Infinity Degasser</li><li>• Aurora Fusion A5 module</li><li>• 1260 Infinity SFC Autosampler</li><li>• 1260 Infinity SFC Binary Pump</li><li>• 1290 Infinity Thermostatted Column Compartment</li><li>• 1260 Infinity Diode Array Detector VL Plus</li></ul>	G4309A
External heating device	Caloratherm heater
1260 Infinity Micro Degasser	G1379A
1100 Series Binary Pump	G1312A (used as make-up flow pump)
6130 Quadrupole LC/MS	G6130B

**Table 2**  
Instrument configuration used in the Agilent 1260 Infinity SFC/MS solution.

## Instrumentation

The analyses were performed on an Agilent 1260 Infinity Analytical SFC System coupled to an Agilent 6130 Single Quadrupole LC/MS System. The system configuration is listed in Table 2. Details on how to couple the Agilent 1260 Infinity Analytical SFC to MS systems are described in another Agilent publication<sup>3</sup>.

Three Agilent ZORBAX SB CN columns (4.6 x 250 mm, 5  $\mu$ m) were coupled together to give a total column length of 75 cm. The modifier was acetonitrile isocratic at 4%, and detection was performed in positive ion mode using an APCI source. The experimental conditions are summarized in Table 3.

## Results and discussion

### Analysis of standard samples

A mixture containing DBP, BBzP, DEHP, DiNP, and DiDP was analyzed using SFC-APCI(+)-MS. The total ion chromatogram of the SIM trace is shown in Figure 1. The peak shapes for DiNP and DiDP are broader than the rest in the phthalate mixture, which is due to the isomers present. As in gas chromatography and liquid chromatography, these phthalates cannot be chromatographically resolved, and DiNP isomers overlap (at least partially) with DiDP isomers. However, DiNP and DiDP can easily be differentiated based on their MS spectra. Using the extracted ion chromatograms at the respective  $[M+H]^+$  ions, the peaks for DiNP and DiDP can be deconvoluted (Figure 2). In comparison to GC/MS analysis, the SFC/MS analysis is faster and deconvolution is easier since the most abundant ion is the  $[M+H]^+$  ion, while in electron ionization (EI) MS, all phthalates have a common  $m/e$  149 as the most abundant ion, which cannot be used for deconvolution.

### Experimental conditions

Column:	Three Agilent ZORBAX SB CN (4.6 x 250 mm, 5 $\mu$ m)
Supercritical fluid:	CO <sub>2</sub>
Modifier:	Acetonitrile (isocratic at 4%)
Outlet pressure:	120 bar
Flow rate:	2.0 mL/min
Temperature:	40 °C
Injection volume:	5 $\mu$ L
Caloritherm heater (*):	60 °C
Make-up flow (*):	Isopropanol at 0.5 mL/min
Detection:	MS in SIM mode, monitoring $[M+H]^+$ ions (Table 1)
APCI:	Capillary V $\pm$ 3000 V, Corona I = 4.0 $\mu$ A
	Drying gas = 8.0 L/min at 325 °C
	Nebulizer = 50 psig
	Vaporizer = 350 °C

(\*): Caloritherm heater and make-up flow prevent solute deposition/condensation before the back-pressure regulator<sup>3</sup>.

Table 3  
Experimental conditions.

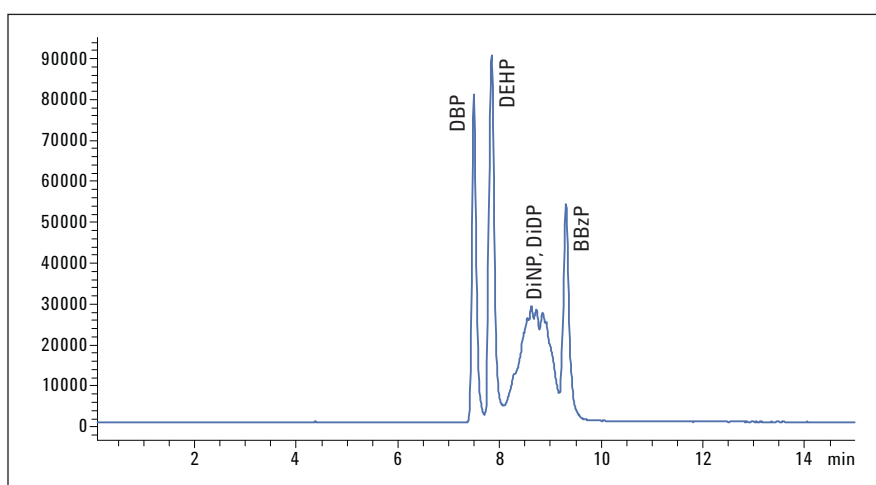


Figure 1  
TIC of the SFC-APCI (SIM) analysis of the phthalate mixture (separation conditions are listed in Table 3).

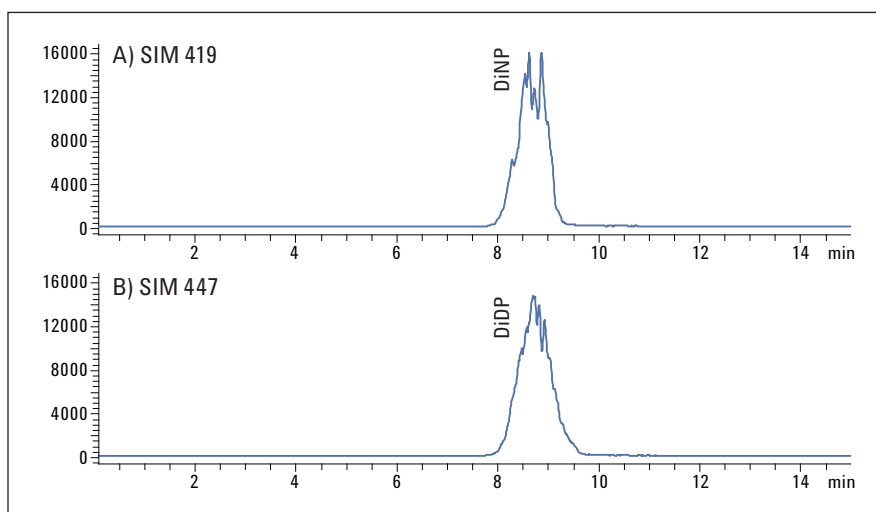


Figure 2  
Extracted ion chromatograms showing the deconvolution of: A) DiNP at 419 amu B) DiDP at 447 amu.



The analytical method was applied to the analysis of a toy made from plasticized PVC. Sample preparation was done according to an official validated procedure, simulating migration of phthalates from the toy into artificial saliva. The extract was analyzed by SFC/APCI(+)MS operated in SIM mode. The chromatogram obtained (extracted ion chromatogram at  $m/z$  419) is shown in Figure 3. In the sample, DiNP was clearly detected.

The concentration of DiNP was determined using a calibration curve obtained for a serial dilution of a DiNP external standard (50 ng/mL – 1,000 ng/mL). The calibration curve showed good linearity ( $R^2 > 0.999$ ). Good repeatability was obtained at low, mid and high levels. These figures of merit and the limit of detection (LOD) at  $S/N > 3$  and limit of quantitation (LOQ) at  $S/N > 10$  are listed in Table 4.

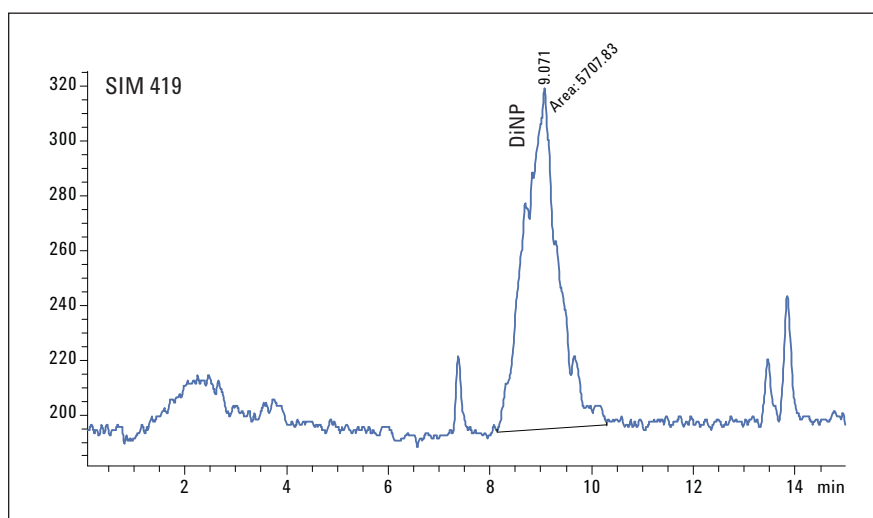
The measured concentration of DiNP in the extract from the toy was 122 ng/mL in the concentrated cyclohexane solution, corresponding to 4.1 ng/mL in the artificial saliva solution. This concentration corresponds to a relatively low DiNP release of 2.1 ng/10 cm<sup>2</sup>/min.

## Conclusion

The Agilent 1260 Infinity Analytical SFC System coupled to an Agilent 6130 Single Quadrupole LC/MS was used for the determination of phthalates in a plasticized PVC toy. The method allowed fast separation and, due to the APCI/MS detection, differentiation between DiNP and DiDP was possible. The method showed good linearity and repeatability and could be applied to measure phthalate migration from the toy into an artificial saliva simulant. The SFC/MS method proved to be a good alternative to GC/MS or LC/MS methods.

Parameter	DiNP
LOD (ng/mL)	12.5
S/N (LOD)	3.2
LOQ (ng/mL)	50
S/N (LOQ)	10.3
Linearity ( $R^2$ ) (50–1000 ng/mL)	0.9995
RSD (%) on peak area, 50 ng/mL level (n=5)	9.68
RSD (%) on peak area, 500 ng/mL level (n=5)	2.85
RSD (%) on peak area, 1000 ng/mL level (n=5)	1.68

**Table 4**  
Figures of merit for DiNP analysed by SFC-APCI-MS.



**Figure 3**  
Extracted ion chromatogram ( $m/z$  419) of the SFC-APCI-MS analysis of the concentrated extract of a plasticizer PVC toy. The separation conditions are the same as in Figure 1.

## References

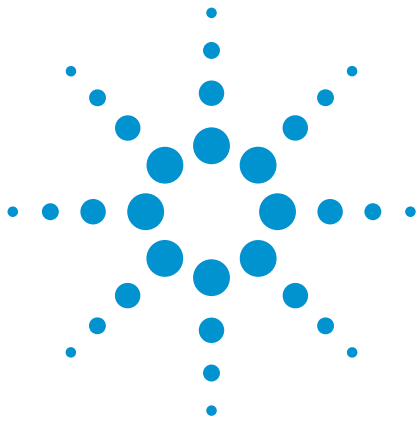
1. F. David, P. Sandra, B. Tienpont, F. Vanwalleghem, and M. Ikononou in Phthalate Esters, The Handbook of Environmental Chemistry, Volume 3 (Anthropogenic Compounds), part Q, Volume editor: C.A. Staples, Editor-in-chief: O. Hutzinger, Publisher: Springer Verlag, Berlin, **2003**, ISBN 3-54000992-2, Chapter 2, pp 9-56.
2. [http://ec.europa.eu/health/archive/ph\\_risk/committees/sct/documents/out113\\_en.pdf](http://ec.europa.eu/health/archive/ph_risk/committees/sct/documents/out113_en.pdf).
3. M. Dunkle, G. Vanhoenacker, F. David, P. Sandra, M. Vollmer, "Agilent 1260 Infinity SFC/MS Solution - Superior sensitivity by seamlessly interfacing to the Agilent 6100 Series LC/MS system", Agilent Technologies Technical Overview, **2011**, Publication Number 5990-7972EN.

[www.agilent.com/chem/SFC](http://www.agilent.com/chem/SFC)

© Agilent Technologies, Inc., 2011  
Published in USA, January 1, 2012  
Publication Number 5990-9597EN



**Agilent Technologies**



Agilent Application Solution

# Analysis of bisphenol A leaching from baby feeding bottles

## Application Note

Consumer Products

### Author

Syed Salman Lateef  
Agilent Technologies, Inc.  
Bangalore, India

### Abstract

Bisphenol A can leach out from the plastic surfaces of food containers and has been detected in various matrices such as plasma, urine and groundwater. Bisphenol A is an endocrine disruptor, which can mimic the body's own hormones such as estrogen and may lead to negative health effects. In this Application Note, we describe a method to quantify bisphenol A and a structurally similar analog bisphenol F extracted from baby feeding bottles. The method was developed on an Agilent 1260 Infinity LC system using an Agilent ZORBAX Eclipse Plus C18 column. Partial method validation was performed to demonstrate linearity, robustness and precision of area and retention time. The dilution series was generated automatically using an Agilent 7696A Sample Prep WorkBench, saving analyst time. The limit of quantitation (LOQ) for bisphenol A was found to be 1.06 ng/mL. During sample recovery studies, 80% recovery was obtained for bisphenol A. The method was transferred to an ultrahigh performance liquid chromatography (UHPLC) method using an Agilent 1290 Infinity LC System. The UHPLC method has the same experimental conditions but showed narrower and higher peaks, better resolution, and improved signal-to-noise response. Both methods can be applied for bisphenol A quantification in quality control of food containers such as baby feeding bottles.



**Agilent Technologies**

## Introduction

Bisphenol A (BPA) is a monomer used to make polycarbonate plastic and epoxy resins. Traces of BPA can leach out of these polycarbonate plastic surfaces under various environmental conditions such as heat or pH changes and eventually are consumed by humans. BPA was detected in various matrices such as urine, groundwater and plasma. Based on the assumption that a threshold exists above which toxic effects are seen, the U.S. Environmental Protection Agency (US EPA) has established 50 µg/kg body weight/day as the reference dose (RfD) for BPA<sup>1</sup>. Baby bottles made of polycarbonate plastic are a potential risk to children. In this Application Note, we used a structurally similar commercially available compound bisphenol F, (BPF), (Figure 1) along with BPA to determine separation efficiency.

Ballesteros-Gomez *et al.*, reviewed various analytical methods used to separate, identify and quantify BPA<sup>2</sup>. Also, the ASTM standard test method, D 7574-09, describes a SPE based offline method for extracting bisphenol A from environmental waters<sup>3</sup>. BPA is a fluorescent compound, and fluorescence detector (FLD) is sensitive to detect BPA concentration in baby bottles. In this Application Note, a method is described to simultaneously quantify BPA and BPF using a SPE based offline extraction procedure with (U)HPLC/FLD detection.

## Experimental

### Instruments and software

An Agilent 1260 Infinity Binary LC system consisting of the following modules was used:

- Agilent 1260 Infinity Binary Pump (G1312B)
- Agilent 1260 Infinity Autosampler and Thermostat (G1367E, G1330B)
- Agilent 1260 Infinity Thermostatted Column Compartment (TCC) (G1316A)
- Agilent 1260 Infinity Fluorescence Detector (G1312B) with 8 µL flow cell

The UHPLC analysis was developed and performed using an Agilent 1290 Infinity LC System consisting of the following modules:

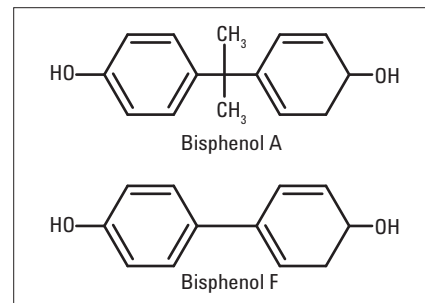
- Agilent 1290 Infinity Binary Pump (G4220A)
- Agilent 1290 Infinity Autosampler and Thermostat (G4226A, G1330B)
- Agilent 1290 Infinity Thermostatted Column Compartment (G1316C)
- Agilent 1260 Infinity Fluorescence Detector (G1312B) with 8 µL flow cell

Software:

- Agilent ChemStation B.04.02

Sample preparation:

- Agilent 7696A Sample Prep WorkBench



**Figure 1**  
Molecular structures of bisphenol A and bisphenol F

## Reagents and materials

All chemicals and solvents used were HPLC grade. Purified water was used from a Milli Q water purification system (Millipore Q-POD Element, USA). Acetonitrile and methanol super gradient were purchased from Lab-Scan (Bangkok, Thailand) and potassium phosphate monobasic was obtained from Fluka (Germany). Standards of bisphenol A and bisphenol F were purchased from Sigma-Aldrich (India). BPA-free baby bottles manufactured in USA and three different brands of polycarbonate baby bottles manufactured locally were purchased.

## Chromatographic parameters

The chromatographic parameters for reverse phase liquid chromatography using Agilent 1260 and Agilent 1290 Infinity LC systems are shown in Table 1.

Parameters	Agilent 1260 Infinity LC system	Agilent 1290 Infinity LC system
Column:	Agilent ZORBAX Eclipse Plus C18 4.6×100 mm 5 µm (p/n 959996 902)	Agilent ZORBAX Eclipse Plus C18 4.6×100 mm 1.8 µm (p/n 959964 902)
TCC temperature:	40 °C	
FLD:	Ex: 230. Em: 316	
FLD acquisition rate, gain:	9.26 Hz, 15	
Sample thermostat:	4 °C	
Mobile phase A:	10 mM monobasic potassium phosphate in water	
Mobile phase B:	100% Acetonitrile	
Gradient:	Time (min)	%B
	0	5
	2	5
	2.1	35
	12.5	35
	12.6	70
	17	70
	18.1	5
	23	5
Flow:	0.9 mL/min	
Injection volume:	20 µL. 5 sec needle wash at flush port for 5 sec, using mobile phase A	

**Table 1**  
Chromatographic parameters used in the Agilent 1260 Infinity LC and Agilent 1290 Infinity LC systems.

## Preparation of standards

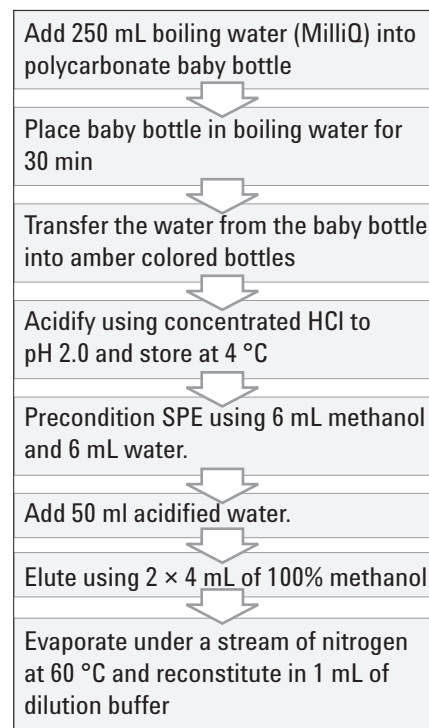
BPA and BPF were accurately weighed out and dissolved in 100% methanol separately to obtain stock solutions of about 300 µg/mL each, which were stored at 4 °C when not in use. A 400 ng/mL solution of BPA and BPF was prepared freshly by diluting the stock solutions using the dilution buffer of 5% acetonitrile and 95% 10 mM monobasic potassium phosphate in water. Linearity levels shown in Table 2, were prepared by subsequent dilution of a 400 ng/mL solution. The Agilent 7696A Sample Prep WorkBench was used to make linearity levels, using serial dilutions. In the first sequence, 400 µL of dilution solution was added to all the vials. In the second sequence, 300 µL of 400 ng/mL solution was added to a Level 7 vial from the first sequence and vortexed for 15 seconds. Serial dilutions were carried out by taking 300 µL from the previous level and added to the next level vial. Note that instead of running two sequences, the steps can also be programmed into one method and running one sequence. The syringe parameters used in the setup of the Agilent 7696A Sample Prep WorkBench are given in Table 3. An Agilent Application Note<sup>5</sup>, describes in detail the set up of 7696A Sample Prep WorkBench<sup>4</sup>.

Linearity levels	Bisphenol A (ng/mL)	Bisphenol F (ng/mL)
LOD	0.195105	0.195105
1	1.06224	1.06224
2	2.478559	2.478559
3	5.783305	5.783305
4	13.49438	13.49438
5	31.48688	31.48688
6	73.46939	73.46939
7	171.4286	171.4286

**Table 2**  
Dilution table for bisphenol A and bisphenol F.

## Sample preparation

BPA from polycarbonate baby bottles was extracted following the schematic shown in Figure 2. An SPE adapter (p/n 12131001) and 3 mm OD tubing (p/n 5062-2483) were used to load the sample onto an Agilent Bond Elut Plexa SPE column, 200 mg, 6 mL (p/n 12109206). An Agilent 20 port vacuum extraction manifold (p/n 12234104) was used for the setup of SPE. We followed the sample handling precautions as described in the ASTM method<sup>3</sup>. The reconstituted solution from the final step (Figure 2) was used directly for sample analysis.



**Figure 2**  
Extraction of BPA from baby bottles and sample preparation using SPE.

	Solvent prewash 1	Dispense wash	Dispense pumps	Dispense settings
Number of pumps or washes	1	1	3	
Wash volume (µL)	50	50	20	
Draw speed (µL/min)	1250	1250	1250	1250
Dispense speed (µL/min)	2500	2500	2500	2500
Needle dept off set (mm)	-2.0	-2.0	-2.0	-2.0
Viscosity delay (s)	0	0	0	0
Turret solvent	A			
Air gap (% syr. vol.)	0			0

**Table 3**  
500 µL syringe parameters used for the Agilent 7696A Sample Prep WorkBench.

## Procedure

The reconstituted extracts from the baby bottles were injected to measure the approximate concentration of BPA before establishing the linearity range. A 20  $\mu\text{L}$  solution of mobile phase A was injected as blank, followed by each linearity level in six replicates. Area and retention time (RT) information for each level was used to calculate the relative standard deviation (RSD) values. The average area of each linearity level in the linearity range was plotted against the concentration to obtain a calibration curve. The limit of detection (LOD) and limit of quantitation (LOQ) for BPA and BPF were established from the lower linearity level injections.

To evaluate the robustness of the method, six critical method parameters were evaluated:

- Flow rate  $\pm 2\%$
- Column temperature  $\pm 2.5\%$
- Injector volume  $\pm 5\%$
- Excitation and emission wavelength  $\pm 3\%$
- Step gradient  $\pm 10\%$
- Buffer concentration  $\pm 10\%$

For each robustness parameter, a standard concentration of 30 ng/mL solution of BPA and BPF was injected in seven replicates.

To perform the recovery studies, we extracted samples from BPA-free baby bottles as described in Figure 2. To 50 mL of this sample, either a low or a higher quantity of BPA and BPF was spiked. Both spiked samples were subjected to SPE. The resulting concentrations of the samples were determined using the calibration curves. The theoretical concentrations were compared against the experimental values to obtain the recovery values.

Finally, three different brands of baby bottles were analyzed to determine the leaching concentrations of the two bisphenols using the standard HPLC method.

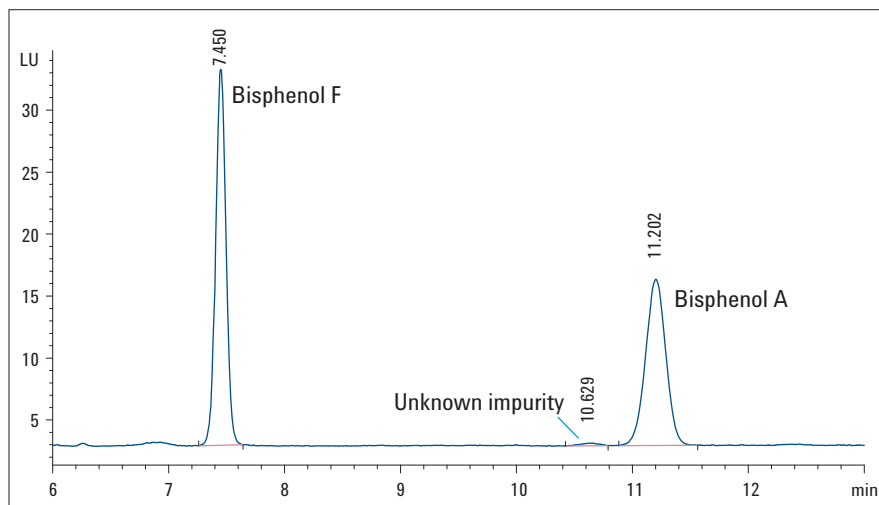
The method was then transferred to an Agilent 1290 Infinity LC system and run on a 1.8  $\mu\text{m}$  column using the same experimental conditions to test resolution and sensitivity of the method. For this method, we also evaluated LOD, LOQ, linearity of each standard and precision of the method by area and RT RSD.

## Results and Discussion

### Separation and detection

The separation of BPA and BPF was tested on C18 columns using acidic and basic mobile phases during method development. Extracted water samples from baby bottles were also tested before finalizing the method.

An Agilent ZORBAX Eclipse Plus C18 column was used for further experiments. A low temperature (35  $^{\circ}\text{C}$ ) of the TCC provided optimal separation of BPA from a closely eluting impurity, however 40  $^{\circ}\text{C}$  was found to be better when analyzing matrix samples. A linear gradient separated the two bisphenols, however a preliminary method robustness study showed large variation when the gradient was modified. A step gradient method was therefore adapted, which gave comparatively robust results. The ASTM method recommended storing bisphenols at low temperature, therefore the auto-sampler was maintained at 4  $^{\circ}\text{C}$  during the analysis. Figure 3 shows a chromatogram separating the two bisphenols using the final method.



**Figure 3**  
Separation of 30 ng/mL solution of bisphenol F and bisphenol A using an Agilent ZORBAX Eclipse Plus C18 column. The chromatogram was collected using FLD settings of excitation at 230 and emission at 316 nm.

## Limit of Detection (LOD) and Limit of Quantitation (LOQ)

The analyte concentration that provides a signal-to-noise ratio (S/N) of > 3 was considered as LOD and the analyte concentration with S/N ratio > 10 was considered as LOQ. A peak-to-peak method was used to calculate noise. Figure 4 shows a chromatogram of BPA at the LOQ level overlaid with a blank (mobile phase) injection. For BPA, the LOD was 0.19 ng/mL with S/N = 4.3 and LOQ was 1.06 ng/mL with S/N = 15.1.

## Linearity

Calibration curves with linearity range (see Table 2) were prepared using an Agilent 7696A Sample Prep WorkBench. The WorkBench automates the sample handling, providing consistent results. Different sets of linearity ranges can be prepared by simply rerunning the program. The linearity levels were established starting from the LOQ level of BPA. LOD and LOQ values, along with the linearity results are included in Table 4. LOD and LOQ values can be further decreased by increasing the injection volume but it was not necessary for this application since the values obtained from baby bottles were found to be within the linearity range.

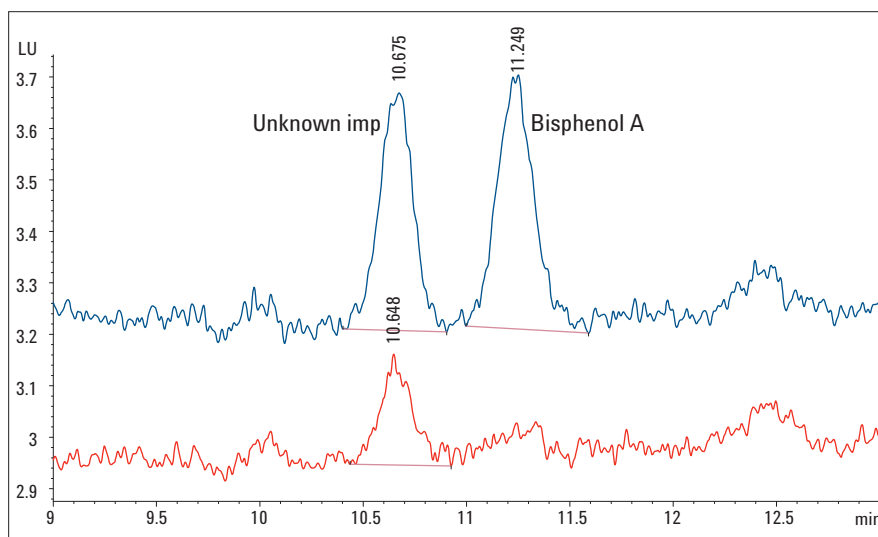
## Precision of retention time (RT) and area

The area precision was measured as RSD(%) across the linearity levels. The maximum RSD value of 5.6% and 7.2% for level 1 (L1) were obtained for BPA and BPF respectively. Similarly, RT precision calculations showed a maximum RSD value of only 0.14% and 0.11% for the BPA and BPF. Graphical representation of area RSD values are shown in Figure 5.

SI no.	Name	LOD ng/mL	S/N	LOQ ng/mL	S/N	Linearity range	R <sup>2</sup> value	No. of levels
1	Bisphenol F	0.19	5.1	0.46	12.4	1.06–171.43	0.99999	7
2	Bisphenol A	0.19	4.3	1.06	15.1	1.06–171.43	0.99998	7

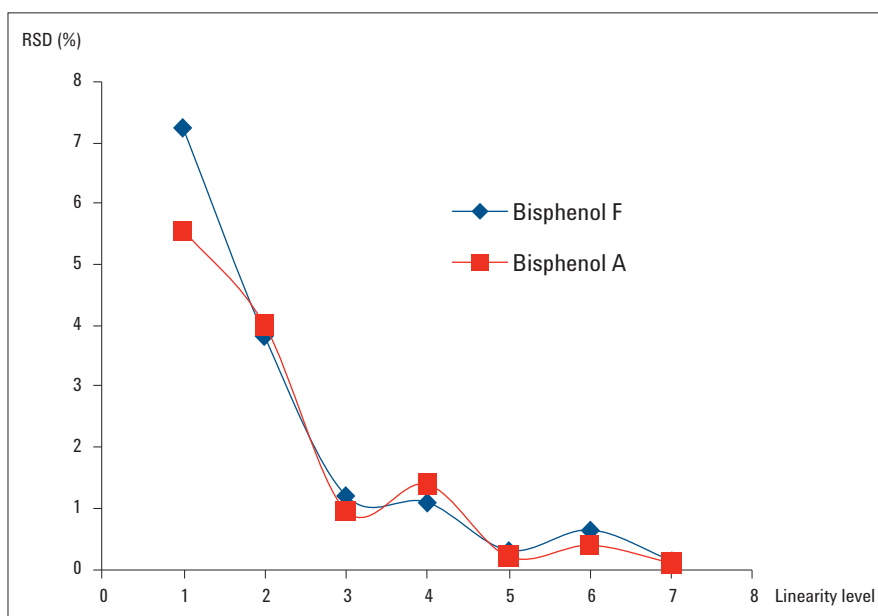
**Table 4**

LOD, LOQ and linearity for BPA and BPF. Samples were prepared using an Agilent 7696A Sample Prep WorkBench. BPA levels found in polycarbonate baby bottles were within the linearity range.



**Figure 4**

A 20  $\mu$ L injection of LOQ level, 1.06 ng/mL (21 pg on column) solution, of bisphenol A overlaid with blank injection. S/N ratio obtained at this concentration was 15.



**Figure 5**

Area precision measured as RSD(%) for six replicates at each concentration level for BPA and BPF.

## Robustness

To test the robustness of the method, a standard solution containing 30 ng/mL of BPA and BPF was used. Six critical method parameters (flow rate, column temperature, injector volume, excitation and emission wavelength, step gradient and buffer concentration) were varied separately and data were collected for seven replicate injections. The compound peak areas from the last six replicates were compared for analysis. The allowed deviation for the area and retention time was set to  $\pm 5\%$  and  $\pm 3\%$  respectively.

The results of the robustness tests are summarized in Table 5. The red numbers indicate where the result exceeded the allowed deviation. A flow rate change of +2% resulted in a decreased area of the two bisphenols. Specifically for bisphenol A, the peak area was found to have the negative deviation caused by 2.5% change in column temperature. The resolution of BPA compared to the impurity (see RT 10.6, Figure 3) showed poor results when the temperature was increased and improved results when the temperature was decreased to 35 °C. A temperature of 40 °C was found to be better for sample analysis. Robustness results show the importance of maintaining the column temperature during the analysis. Setting the FLD excitation at 230 nm and emission at 316 nm was found to be ideal, as it displays the maximum peak area. The emission setting of 316 nm is robust since a variation of 3 nm does not deviate the area percentage from the allowed limit. The excitation wavelength however, needs to be controlled. A change in buffer concentration is also critical as a deviation of 10% decreases the peak area for both BPA and BPF. Robustness results indicate that the method is reliable for normal usage and to a great

extent the performance remains unaffected by deliberately changing method parameters. However, some parameters are critical and must be carefully controlled.

## Recovery from sample matrix

BPA-free baby bottles were used as blank matrix. The recoveries of the BPA and BPF were tested by spiking experiments in duplicates. A low standard spike contained BPA (30 ng) and BPF (30 ng) each spiked into 50 mL water extracts of BPA-free bottles. Another high standard spike consisted of BPA (50 ng), BPF (50 ng) each spiked into a 50 mL water extracts from BPA-free bottles. The analytes were extracted from the water sample as described above. Using the aqueous linearity curve (see section Linearity), the area

was converted to concentration values. The low and high concentration values were compared against the theoretical value. The recovery experiment results are shown in Table 6. BPA shows a recovery value of 80% at the high concentration value. The value of 80% is higher than the value reported in the ASTM method where an average single laboratory results shows a recovery of 70%.

Compound name	Recovery low conc. (%)	Recovery high conc. (%)
Bisphenol F	70.2	75.9
	70.1	74.1
Bisphenol A	76.9	79.6
	75.1	81.1

**Table 6**  
Recovery results from spiking experiments performed in duplicates.

Parameters	Changes	BPF		Resolution of BPA with unknown	BPA	
		% area	% RT		% area	% RT
Flow: 0.9 mL/min $\pm 2\%$	High: 0.92 mL/min	-4.6	-1.2	1.9	-5.1	-1.2
	Low: 0.88 mL/min	0.1	1.9	1.9	-1.9	2.2
TCC: 40 °C $\pm 2.5\%$	High: 41 °C	-4.2	-0.4	1.7	-5.0	-0.6
	Low: 39 °C	-3.1	0.9	2.1	-10.0	1.3
Injector: 20 $\mu$ L $\pm 5\%$	High: 21 $\mu$ L	2.6	0.2	1.9	0.0	0.2
	Low: 19 $\mu$ L	-7.6	0.1	1.9	-9.8	0.1
Wavelength: 230–316 $\pm 3$ nm	233–316	-2.2	0.0	1.9	-5.7	0.0
	227–316	-7.0	0.2	1.9	-4.6	0.2
	230–319	-3.2	0.1	1.9	-4.5	0.1
	230–313	-3.5	0.1	1.9	-3.0	0.1
Step gradient starting point: 2 min $\pm 10\%$	High: 2.2 min	-3.8	2.9	1.9	-4.1	2.0
	Low: 1.8 min	-3.3	-2.4	1.9	-3.8	-1.5
Buffer concentration: 10 mM $\pm 10\%$	High: 11 mM	-4.2	0.2	1.9	-6.0	0.2
	Low: 9 mM	-5.9	0.1	1.8	-9.8	0.1

**Table 5**  
Robustness test method results compared to the standard method at concentration of 30 ng/mL. The red values in the table indicate that the deviations exceeding the allowed limits of 5% for area and 3% for retention time.



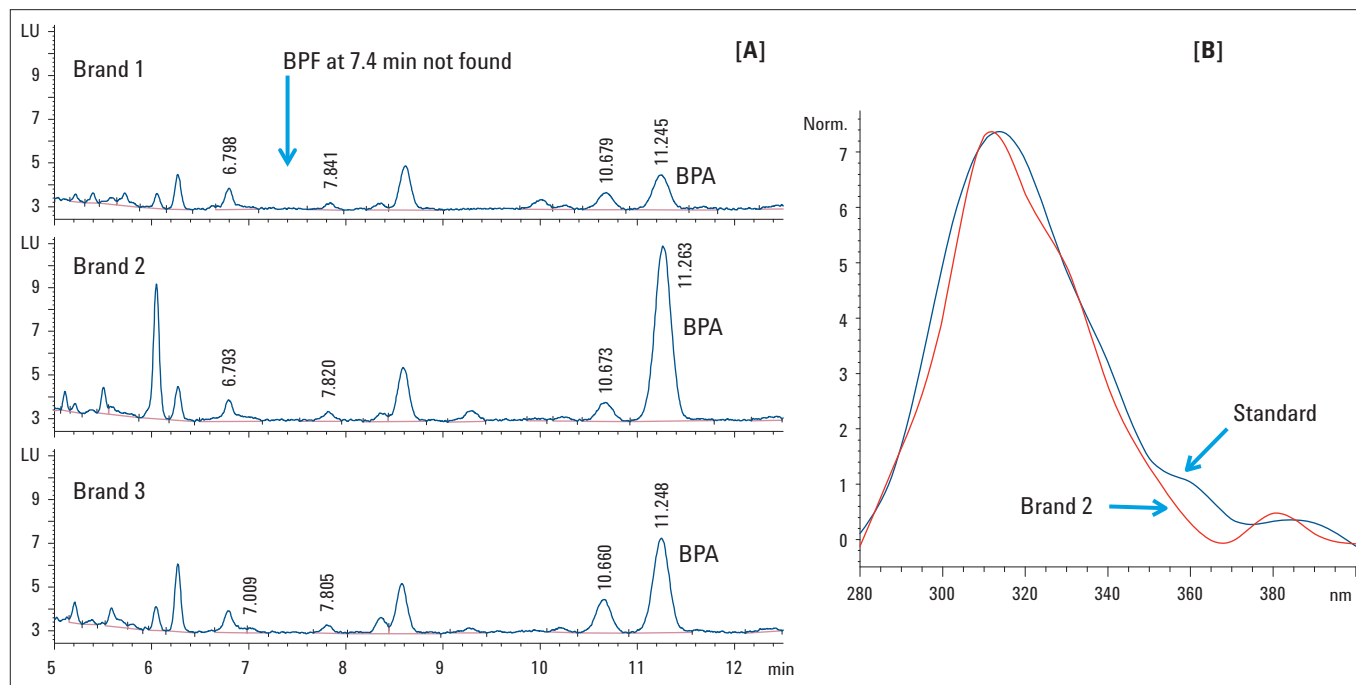
## Sample analysis

The content of BPA and BPF in baby bottles was determined using the extraction procedure and the developed chromatographic method. Baby bottles labeled as brand 1, brand 2, and brand 3, were analyzed in duplicates. The results of the analysis were compared against the calibration curve prepared prior to sample analysis. Blank water samples subjected to SPE did not show BPA, suggesting that no BPA leached out of plastics used in the experiment<sup>3</sup>. Different amounts of BPA were detected in the three brands of baby bottles (see Figure 6A). The BPA emission spectra from the standard was overlaid with the spectra from the sample. A good overlap was observed confirming the presence of BPA (see Figure 6B). Different brand analysis showed a high concentration of 4 ng/mL while a low value of 0.5 ng/mL (see Table 7). These values are consistent with those observed earlier

by Sun *et al.*, who showed a value of 0.6 ng/mL<sup>5</sup>. If a baby of 10 kg were to drink 250 mL from brand 2 baby bottle, the baby would consume 0.1 µg/kg/day of BPA. This value is less than the reference dose of 50 µg/kg/day established by the EPA but is of concern according to some other studies<sup>6</sup>. The results also show that BPF was not detected in any bottle.

Compound name	BPF (ng/mL)	BPA (ng/mL)
Brand 1	0	0.76
	0	0.52
Brand 2	0	4.26
	0	4.46
Brand 3	0	2.08
	0	2.58

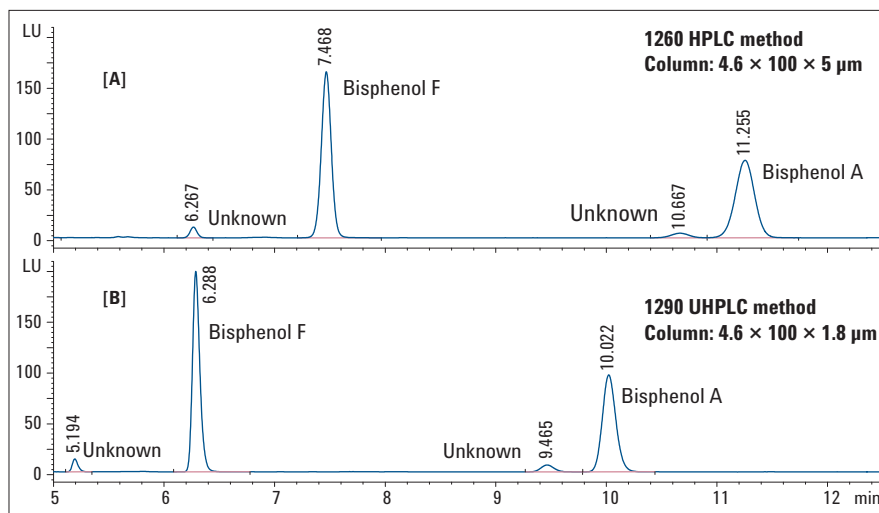
**Table 7**  
Concentration of BPA and BPF extracted in 250 mL water from different brands of baby bottles.



**Figure 6**  
[A] The overlay of chromatogram from three different baby bottles analyzed for BPA and BPF. [B] The overlay of the emission spectrum of BPA from standard and that obtained from brand 2 sample.

## UHPLC method

The HPLC method was transferred to an UHPLC method on an Agilent 1290 Infinity LC system keeping the same run time as shown in Figure 7. The transfer was performed to study the effect on resolution and sensitivity. The UHPLC method used the same mobile phase, gradient, and detector settings. The column dimensions were kept the same but the particle size was reduced from 5  $\mu\text{m}$  to 1.8  $\mu\text{m}$  for the UHPLC method. The peaks in the UHPLC method elute about 1.2 minutes earlier, which is due to the lower delay volume in an Agilent 1290 Infinity LC system. The UHPLC method also showed narrower peaks and better resolution compared to the HPLC method. The peak properties such as peak area, peak height, peak width, resolution and S/N at the lowest linearity level L1 and the highest linearity level L7 are compared in Table 8. The results show that resolution of BPA increased from 1.9 in the HPLC method to 2.5 in the UHPLC method. The S/N ratio almost doubled thereby adding sensitivity and allowing the possibility to redefine the LOQ and LOD levels.



**Figure 7**  
An overlaid chromatogram of the HPLC method [A] and UHPLC method [B] separating the level 7 standards for BPA and BPF on an Agilent ZORBAX Eclipse Plus C18 4.6×100 column. A 5  $\mu\text{m}$  particle size was used for HPLC method while 1.8  $\mu\text{m}$  was used for UHPLC method.

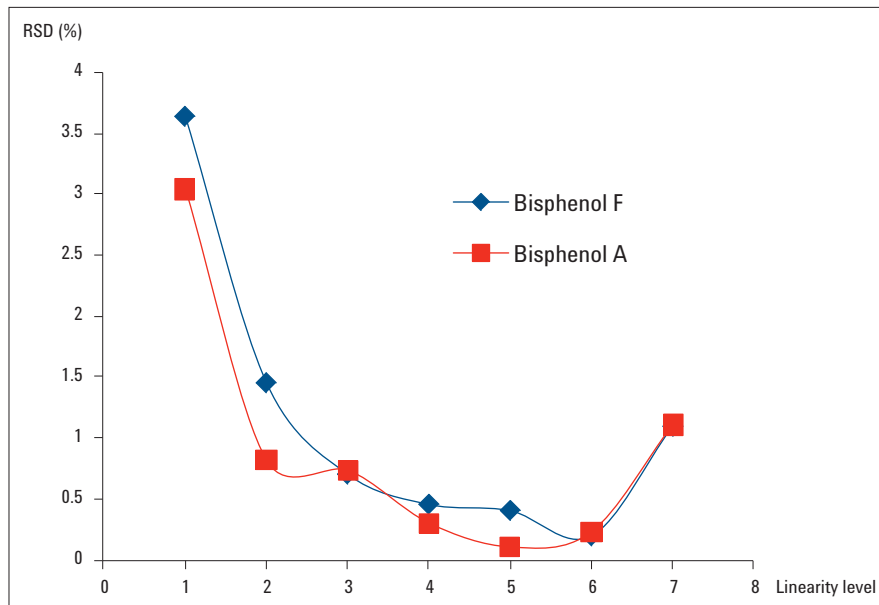
Compound name (Level)	HPLC method					UHPLC method				
	Peak area	Peak width at half height	Peak height	Resolution	S/N	Peak area	Peak width at half height	Peak height	Resolution	S/N
BPF (L7)	1037.0	0.10	163.7	-	3683.0	930.5	0.07	199.6	-	6784.8
BPA (L7)	934.1	0.19	76.3	1.9	1715.7	825.8	0.13	96.4	2.5	3276.7
BPF (L1)	7.5	0.10	1.1	-	27.4	7.2	0.07	1.4	-	42.6
BPA (L1)	8.1	0.20	0.6	1.8	15.1	9.4	0.14	1.0	2.5	31.6

**Table 8**  
Comparison of peak area, peak width at half height, peak height, resolution and S/N ratio between HPLC and UHPLC method from first level and last linearity level. The UHPLC method provides better sensitivity and resolution compared to the HPLC method.

The calibration for BPA and BPF, when using the same calibration levels (see Table 2) was found to be linear -  $R^2$ : 0.99991 for BPF and  $R^2$ : 0.99993 for BPA. RSD(%) deviation on area and RT was calculated for all concentration levels. The results show that RSD(%) on area deviation was comparatively lower in the UHPLC method. As shown in Figure 8, a value of 3.0% was found for level 1 for BPA. The maximum RSD of RT for both BPA and BPF was less than 0.1%.

## Conclusion

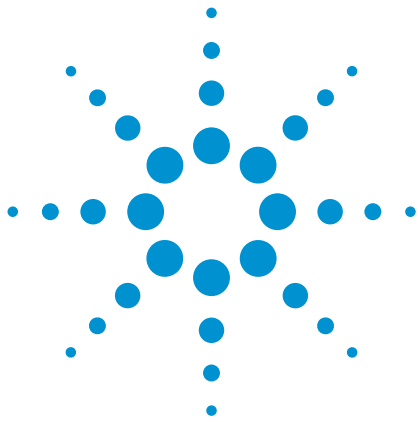
Bisphenol A and bisphenol F were separated and quantified using an Agilent 1260 Infinity LC system and an Agilent ZORBAX Eclipse Plus C18 column. Calibration standards were prepared using the Agilent 7696A Sample Prep WorkBench. A method was developed and partially validated. This method quantifies bisphenol A and bisphenol F from various baby bottles with 80% recovery values. The method can be applied to determine BPA and BPF levels for quality control of baby bottles. A method transfer to an Agilent 1290 Infinity LC system was effectively carried out by keeping the same detector and method conditions. Both HPLC and UHPLC methods were linear and give precise results. The UHPLC method however showed better resolution, S/N ratio, narrower peak width and increased peak height compared to the HPLC method.



**Figure 8**  
Area precision measured as RSD (%) for BPF and BPA with UHPLC. Six replicates at each concentration level were measured.

## References

1. U.S. Environmental Protection Agency (U.S. EPA), Bisphenol A. (CASRN 80-05-7), <http://www.epa.gov/iris/subst/0356.htm>
2. A.Ballesteros-Gomez; S. Rubio; D.Perez-Bendito, "Analytical methods for the determination of bisphenol A in food," *J. Chrom A*, 1216: 449-469, **2009**.
3. ASTM method, "Standard Test Method for Determination of Bisphenol A in Environmental Waters by Liquid Chromatography/Tandem Mass Spectrometry," D7574-09.
4. W.D. Snyder, "Agilent 7696A Sample Prep WorkBench: How to automate Preparation of a Sample Set by Serial Dilution for Measurement of Flame Ionization Detector Performance," Agilent Application note, Publication Number, 5990-6850EN, **2010**.
5. Y. Sun, M. Wada, O. Al-Dirbashi, N. Kuroda, H. Nakazawa, K. Nakashima, "High-Performance Liquid Chromatography with Peroxyoxalate Chemluminescence Detection of Bisphenol A Migrated from Polycarbonate baby bottles using 4-(4,5-diphenyl-1H-imidazol-2-yl) benzoyl chloride as a label," *J.Chrom B*, 749: 49-56, **2000**.
6. S.K. Ritter, "Debating BPA's Toxicity. The Precautionary Principle Serves as a Dividing Line in Arguments Over the Safety of Bisphenol A," *Chemical & Engineering News*, 89: 14-19, **2011**.



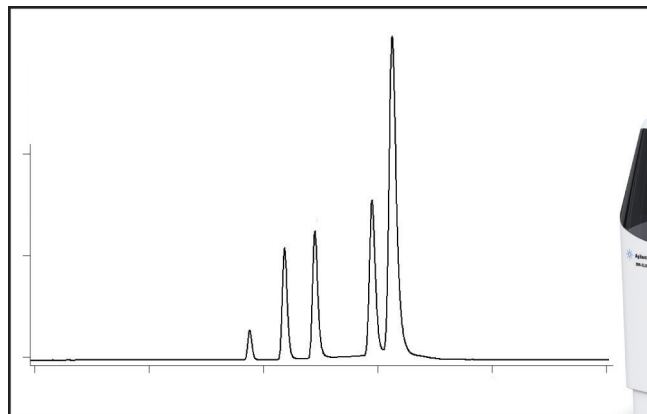
# High sensitivity analysis of phthalates using HPLC with low temperature evaporative light scattering detection

## Application Note

Specialty chemicals, consumer products

### Author

Stephen Ball  
Agilent Technologies, Inc.  
Craven Arms, UK



### Abstract

This Application Note describes how the Agilent 385-ELSD Evaporative Light Scattering Detector can successfully detect highly volatile dialkyl phthalates at very low concentrations. Dialkyl phthalates are a class of widely used industrial compounds selected for their many beneficial chemical properties. Because of their high volatility, dialkyl phthalates have always presented a challenge for evaporative light scattering detection after separation by HPLC. The 385-ELSD has a built-in Peltier cooler and unique gas control to evaporate high boiling solvents at very low temperatures, making it ideal for detection of highly volatile dialkyl phthalates.



**Agilent Technologies**

## Introduction

Agilent evaporative light scattering detectors respond to all compounds that are less volatile than the mobile phase. At higher operating temperatures, semivolatile analytes may evaporate along with the eluent, making detection difficult or even impossible. The Agilent 385-ELSD Evaporative Light Scattering Detector can be operated at very low temperatures (or even ambient temperature) so that losses of semivolatile sample components can be minimized, preserving sample integrity and offering maximum sensitivity.

Dialkyl phthalates are a class of widely used industrial compounds selected for their many beneficial chemical properties. They are used as softeners of plastics, oily substances in perfumes, additives to hairsprays, lubricants, and wood finishers. The smell of newness, which becomes especially noticeable after a vehicle has been exposed to direct sunlight for a few hours, is partly due to the pungent odor of phthalates volatilizing from a hot plastic dashboard. Because of their high volatility, dialkyl phthalates have always presented a challenge for evaporative light scattering detection after separation by HPLC and, therefore, they represent an excellent performance test for the 385-ELSD.

## Experimental

### Instrumentation

Column	Agilent Poroshell 120 EC ZORBAX RRHD Eclipse Plus C18, 30 × 2.1 mm, 3 μm
Detection	Agilent 385-ELSD Evaporative Light Scattering Detector
Nebulizer temp	25 °C
Evaporation temp	25 °C
Gas flow	1.6 SLM

### Materials and reagents

Eluent A	Water
Eluent B	Acetonitrile

### Conditions

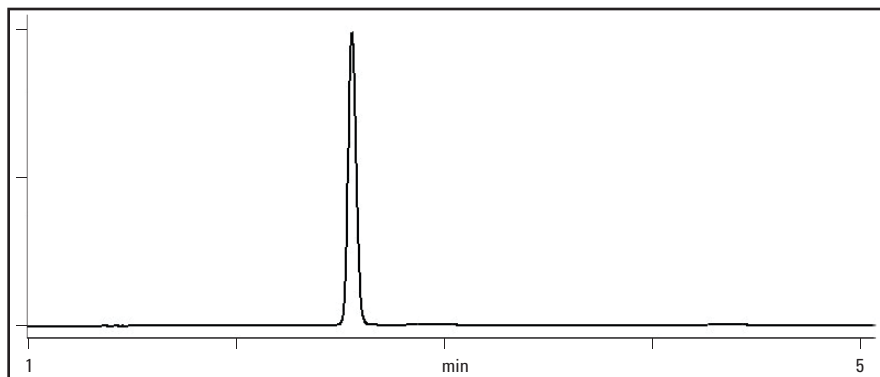
Flow rate	0.5 mL/min
Injection volume	10 μL
Gradient:	0–100% B in 3.1 min, hold for 7 min

## Results and discussion

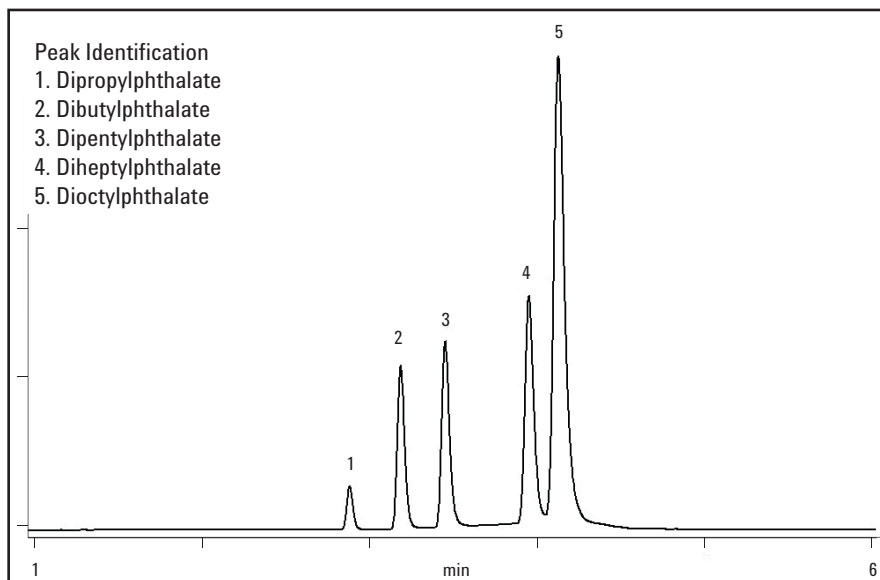
By operating the Agilent 385-ELSD Evaporative Light Scattering Detector at near ambient conditions, it is easily possible to detect diethylphthalate at 1.0 mg/mL as shown in Figure 1, although recovery diminishes at lower concentrations. For longer alkyl chains, phthalates can be detected at much lower concentrations (100 ppm or 0.1 mg/mL), as illustrated for the series shown in Figure 2. The variation in response still reflects differences in volatility but nevertheless, for chain lengths greater than octyl, the response is reasonably uniform.

## Conclusion

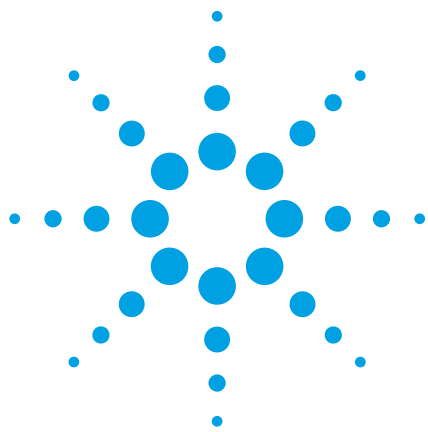
The Agilent 385-ELSD successfully detected highly volatile dialkyl phthalates at very low concentrations. The 385-ELSD surpasses other ELS detectors for low temperature HPLC applications with semivolatile compounds. Its innovative design represents the next generation of ELS detection technology, providing optimum performance across a diverse range of HPLC applications. The unique gas control of the 385-ELSD facilitates evaporation of high boiling solvents at very low temperatures. For example, 100 % water at a flow rate of 5 mL/min can be removed at 30 °C. The novel design of the 385-ELSD achieves superior performance compared to detectors from other vendors for the analysis of semivolatile compounds.



**Figure 1**  
Straightforward detection of diethylphthalate at 1.0 mg/mL under ambient conditions with the Agilent 385-ELSD Evaporative Light Scattering Detector (ELSD).



**Figure 2**  
Long chain phthalates detected at 0.1 mg/mL by the Agilent 385-ELSD Evaporative Light Scattering Detector.



# Agilent 1290 Infinity LC with Agilent Poroshell columns for simultaneous determination of eight organic UV filters in under two minutes

## Application Note

Consumer Products

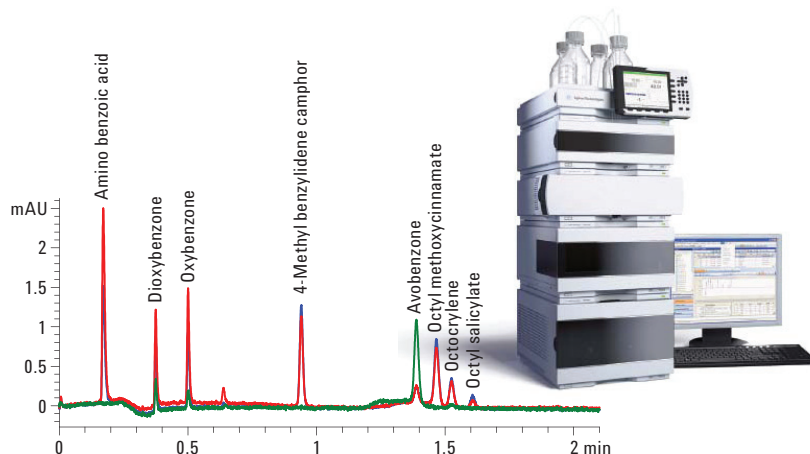
### Authors

Siji Joseph

Agilent Technologies India Pvt. Ltd.  
Bangalore, India

Michael Woodman

Agilent Technologies, Inc.  
2850 Centerville Road  
Wilmington DE 19808  
USA



### Abstract

Levels of UV filters in personal care products are regulated by the FDA and European Pharmacopeia (EP). Liquid chromatographic (LC) methods are widely accepted analytical techniques for the qualitative and quantitative analysis of these UV filters. Most of these traditional LC methods require about 25–50 minutes. In this Application Note, the Agilent 1290 Infinity LC, in combination with Agilent Poroshell columns, were used for development of a short, sensitive, robust and well resolved separation of eight FDA/EP approved active UV filter ingredients in 99 seconds. Standard deviation (SD) and relative standard deviation (RSD) values of retention time for replicate injections confirmed the excellent performance of the Agilent 1290 Infinity Binary Pump. Exceptional performance of the Agilent 1290 Infinity Diode Array Detector was established by minimum area RSD values and a wide linear range with standard organic UV filters in amounts from 0.25 ng to 200 ng on-column. In addition, the method was effectively used to identify active UV filters extracted from six international personal care products.



**Agilent Technologies**



## Introduction

The wavelength of UV rays lies between X-rays and visible light (~ 10 – 400 nm)<sup>1</sup>. Production of melanin, a pigment that causes the darkening of skin, is a natural defense of the human body against UV radiation. Melanin absorbs UV radiation and dissipates the energy as harmless heat, though the response to UV radiation and production of melanin pigmentation depends on skin color and other genetic factors<sup>2,3</sup>. The intensity of UV radiation and length of exposure are the main parameters involved in sunburn, irrespective of skin tone and ability of the skin to produce melanin. The major classifications of UV light are presented in Table 1<sup>4</sup>.

Sunscreens protecting the skin against sunburn contain one or more of the following types of active ingredients:

- Organic chemicals that absorb UV light.
- Inorganic particulates that reflect, scatter, and absorb UV light.
- Organic particulates that have all the above features.

Organic UV filters are usually aromatic compounds conjugated with carbonyl groups. The FDA has approved seven UV-A filter compounds and nine UV-B filter compounds for sunscreen formulations in the United States, while the European Commission has approved the use of ten additional UV filters in European countries<sup>5</sup>.

Though several approved UV filters are available in the market, extensive use of these UV filters may have several

SI No:	Component	Wavelength (nm)	Effects of over exposure on skin
1	UV-A I	340-400	Can cause tanning but has minimal erythema effect. Can cause long term damage. Penetrates deeply. it can contribute to skin cancer via indirect DNA damage.
2	UV-A II	320-340	Slightly erythema contribution
3	UV-B	290-320	Causes sunburn and is a major contributor to skin cancer development.
4	UV-C	100-290	Very energetic radiation. Absorbed by the ozone layer. Direct DNA damage

**Table 1**  
Major classifications of UV radiation.

major concerns. Some sunscreen ingredients have been shown to have carcinogenic properties. Additionally, older and more widespread sunscreen chemicals cannot dissipate the energy of the excited state as efficiently as melanin, therefore the penetration of these sunscreen ingredients into the lower layers of the skin may increase the amount of free radicals and reactive oxygen species<sup>6</sup>. Therefore, extensive testing of sunscreens is advisable to reveal the efficacy of the ingredients. This Application Note discusses a short LC method to separate eight widely used UV filters within 99 seconds. Cosmetic manufacturers can adopt this method to simplify the analysis of sunscreen raw materials and personal care products in product development, regulatory compliance, and quality control to increase the efficiency of analysis.

## Experimental

### Instrument configuration

An Agilent 1290 Infinity LC, controlled by ChemStation (Version B.04.02) and equipped with a binary pump with integrated vacuum degasser, autosampler, thermostatted column compartment

and a diode array detector, was used for data collection. The injection volume was set to 1  $\mu$ L and the needle wash was enabled using acetonitrile for three seconds. The sample thermostat was set at 5  $^{\circ}$ C, while the columns were operated at 55  $^{\circ}$ C. The binary pump was operated at a flow rate of 1 mL/min. The detector was programmed for three different wavelengths (288, 304 and 358 nm) and operated at a sampling acquisition rate of 80 Hz (response time 0.062 seconds, >0.003 min). An Agilent Poroshell 120 EC-C18 column (75 mm  $\times$  2.1 mm, 2.7  $\mu$ m) was used for the chromatographic separation.

### Chemicals and standards

All eight UV filter standards and acetic acid (mobile phase modifier) were purchased from Aldrich (India). Super gradient grade acetonitrile (ACN) was purchased from Lab-Scan (Bangkok, Thailand). HPLC grade water was freshly taken from a Milli-Q water purification system. Six different brands of international sunscreen formulations were purchased locally. The details of organic UV filter standards used in this study are tabulated in Table 2.

Compound number	Compound	Structure	UV Spectra
1	Name: Aminobenzoic acid CAS No: 150-13-0 Mol Formula: $C_7H_7NO_2$ Mol Wt: 137.14 Detection: 288 nm		
2	Name: Dioxybenzone CAS No: 131-53-3 Mol Formula: $C_{14}H_{12}O_4$ Mol Wt: 244.24 Detection: 288 nm		
3	Name: Oxybenzone CAS No: 131-57-7 Mol Formula: $C_{14}H_{12}O_3$ Mol Wt: 228.24 Detection: 288 nm		
4	Name: 4-Methyl benzylidene camphor CAS No: 36861-47-9 Mol Formula: $C_{18}H_{22}O$ Mol Wt: 254.37 Detection: 304 nm		
5	Name: Avobenzone CAS No: 70356-09-1 Mol Formula: $C_{20}H_{22}O_3$ Mol Wt: 310.39 Detection: 358 nm		
6	Name: Octylmethoxycinnamate CAS No: 5466-77-3 Mol Formula: $C_{18}H_{26}O_3$ Mol Wt: 290.397 Detection: 304 nm		
7	Name: Octocrylene CAS No: 6197-30-4 Mol Formula: $C_{24}H_{27}NO_2$ Mol Wt: 361.48 Detection: 304 nm		
8	Name: Octyl salicylate CAS No: 118-60-5 Mol Formula: $C_{15}H_{22}O_3$ Mol Wt: 250.33 Detection: 304 nm		

**Table 2**  
Detailed list of organic UV filter standards used in this study.

## LC parameters

Premixed solutions of 0.1% acetic acid in water and acetonitrile in the ratio 90:10 (A) and 10:90 (B) were used as mobile phase. The gradient used for the study is presented in Table 3. A post run time of 1 minute was set for column re-equilibration.

Time (min)	B (%)
0	50
0.1	70
2	85

**Table 3**  
Gradient used for experiment.

## Standard mix

A premixed solution of acetonitrile and 0.1% acetic acid in the ratio 50:50 was used as the diluent. A stock solution of each standard was prepared individually at a concentration of 1000 ppm (1000 ng/ $\mu$ L). A standard mixture of p-aminobenzoic acid, dioxybenzone, oxybenzone, 4-methyl benzylidene camphor, avobenzone, octyl methoxycinnamate, octocrylene and octyl salicylate, all 100 ppm (ng/ $\mu$ L) each, was prepared by diluting individual standard stock solutions using diluent. For detector linearity analysis, seven more mixed standard solutions with analyte concentrations of 50, 25, 10, 5, 1, 0.5 and 0.25 ng/ $\mu$ L were prepared by subsequent dilution of the higher concentrated standard mix.

## Extraction of UV filters from formulation samples

UV filters from six different locally available international brands were extracted by a simple extraction procedure using acetonitrile. Two hundred fifty milligrams of each formulation were extracted with 5 mL of acetonitrile, sonicated and centrifuged. The supernatant liquid was filtered using 0.2  $\mu$  Agilent syringe filters (p/n 5061-3361). The resulting filtrate was diluted five times with diluent to get a stock solution of extracted sample. A diluted extracted sample for injection was prepared by further diluting the stock solution with equal volumes of diluent and injecting 1  $\mu$ L. Extracted samples spiked with standards were prepared by mixing

equal volumes of 100 ppm standard mix solution and extracted sample stock solution. This spiked sample was used for the confirmation of peak identity in extracted samples by means of retention time and UV spectra.

## Procedure

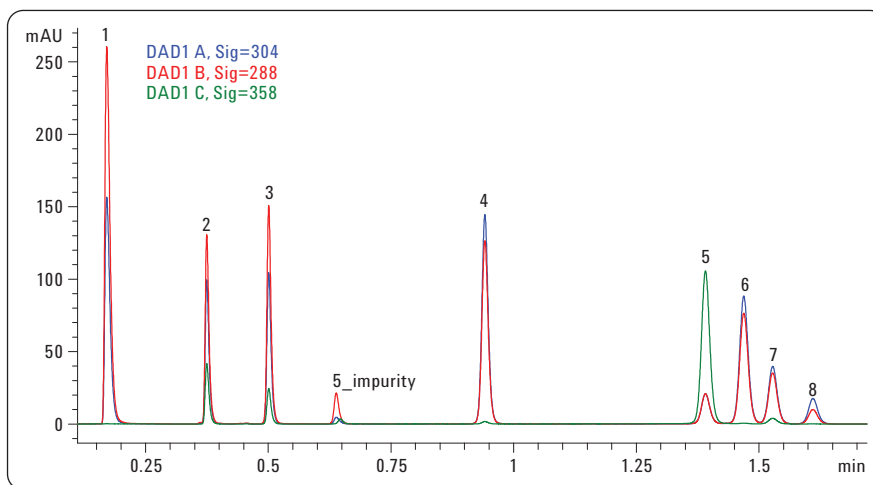
A blank injection was performed in all trials to check the chromatographic interference in the resolution. Standard mix, linearity levels, diluted extracted samples and spiked diluted extracted samples were also injected. The retention time of each standard was confirmed by individual standard injections.

## Results and Discussion

### LC chromatogram of standard mixture

The results showed excellent baseline separation of all eight active sunscreen

ingredients, without chromatographic blank interference. The last peak of the standard mix (octyl salicylate) eluted at 1.62 minutes. A chromatographic representation of the standard mix is as shown in Figure 1. An unknown peak was observed at approximately 0.65 minute, which is an impurity present in the avobenzone standard. A peak purity check by spectral scanning in the range of 200 to 400 nm revealed that all eight compounds eluted without co-elution of any detectable impurities. Three different wavelengths were selected for detection as the maximum absorbance values vary for individual components. The peak width (half height), peak symmetry, USP tailing factor, and resolution values confirm the baseline separation of all the standard analytes in 99 seconds using the Agilent Poroshell 120 EC-C18 column (Table 4).



**Figure 1**  
Chromatographic elution profile of eight organic UV filters in 99 seconds using an Agilent 1290 Infinity LC and an Agilent Poroshell 120 EC-C18 column (three different wavelengths are overlaid).

Comp No:	Name of the compound	Half peak width	Symmetry	USP tail	Resolution
1	Aminobenzoic acid	0.011	0.556	1.438	NA
2	Dioxybenzone	0.008	0.648	1.449	12.662
3	Oxybenzone	0.009	0.720	1.306	8.794
4	4-Methyl benzylidene camphor	0.014	0.862	1.112	22.988
5	Avobenzone	0.018	0.896	1.090	16.456
6	Octyl methoxycinnamate	0.019	0.920	1.070	2.453
7	Octocrylene	0.019	0.912	1.061	1.805
8	Octyl salicylate	0.020	0.910	1.061	2.447

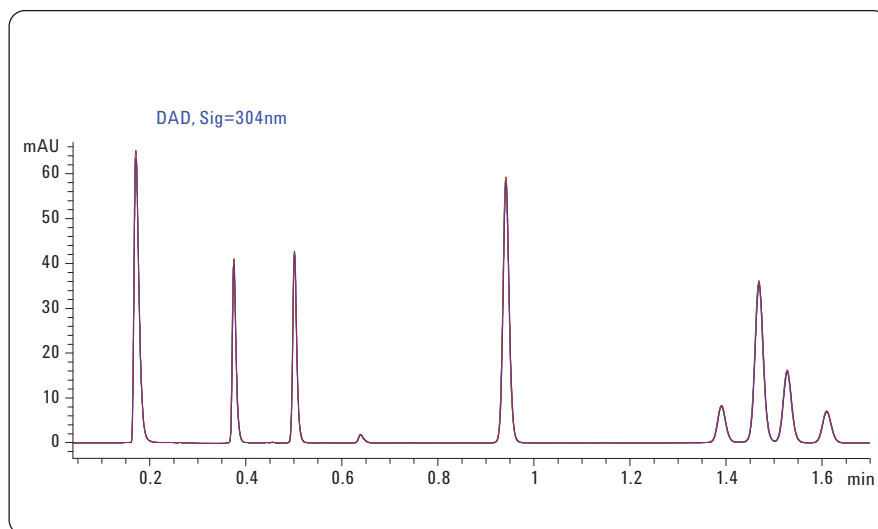
**Table 4**

Peak width (half height), peak symmetry, USP tailing factor, and resolution values of the eight sunscreen ingredient standards in an injection of a standard mix (50 ng) with detection at 304 nm. Injection volume was 1  $\mu$ L.

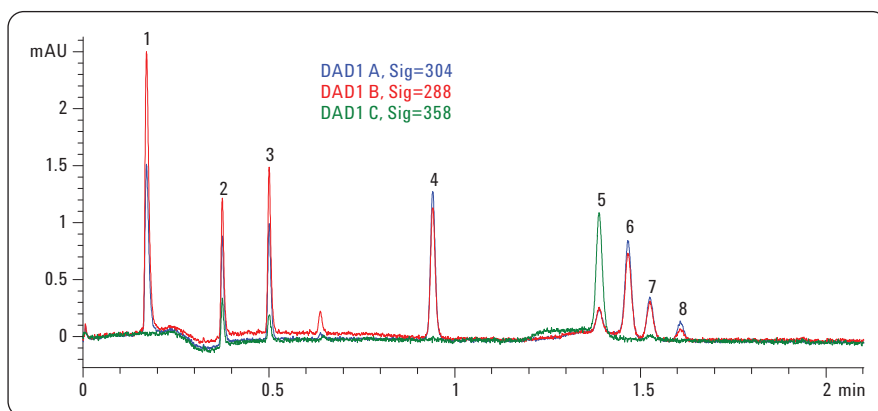
The chromatographic overlay of six replicates at 10 ng/μL confirms the excellent reproducibility of the data (Figure 2). Despite similarities in chemical structures, the components are well resolved within 99 seconds. At this level, the observed standard deviation (SD) value for retention time (RT) was < 0.0005, relative standard deviation (RSD) was < 0.32% and area RSD value was < 1.43%.

### Signal-to-noise ratio

Figure 3 shows the chromatogram of the standard mix where all the analytes were at 0.25 ng on-column concentration. The observed signal-to-noise (S/N) values for each standard is calculated by taking the signal from a readily detectable peak height for each component and noise as absolute noise from the baseline in a compound-free area. The S/N values along with SD, and RSD values are tabulated in Table 5. At this concentration, S/N values for the first six compounds are > 20 and a least S/N value of 5 was observed for octyl salicylate (compound 8).



**Figure 2**  
Chromatographic overlay of six replicates of standard mix injections at 10 ng/μL level.



**Figure 3**  
Chromatogram of standard mix where all the analytes were at 0.25 ng on-column concentration (three different wavelengths are overlaid).

	Comp 1	Comp 2	Comp 3	Comp 4	Comp 5	Comp 6	Comp 7	Comp 8
Injections	288 nm			304 nm	358 nm	304 nm		
3	51.5	26.5	31	36.1	21.1	22.9	10.4	4.6
5	50.3	25.5	28.8	34.7	20.2	22	9.4	4.4
6	56.5	27.3	31.8	34.1	20.8	22	10	4.6
7	50.2	25.6	30	35.1	19.8	21.9	9.5	4.5
8	52.8	26.1	31.4	35.7	19.3	22.2	9.7	4.4
9	50.2	25.3	29.8	35.3	18.6	21.8	9.8	4.5
Average	51.9	26.1	30.5	35.2	20.0	22.1	9.8	4.5
SD	2.47	0.75	1.13	0.71	0.94	0.40	0.36	0.09
RSD (%)	4.75	2.89	3.71	2.02	4.68	1.80	3.71	1.99

**Table 5**  
Signal-to-noise values for each standard at 0.25 ng on-column concentration.

## Linearity

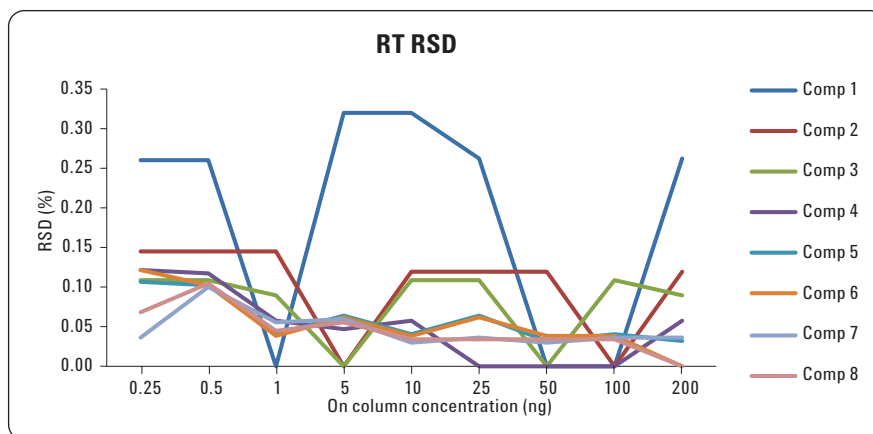
A linearity study was performed in the concentration range of 0.25 ng to 200 ng (nine levels and five replicates) on-column concentration. The levels were 200 ng, 100 ng, 50 ng, 25 ng, 10 ng, 5 ng, 1 ng, 0.5 ng, 0.25 ng. The precision of area and retention time was demonstrated by calculating the SD and RSD values of five replicate injections for each level. The graphical representation of RSD for RT is shown in Figure 4. The observed RSD values are well within the acceptance limit of 1.0% confirming the excellent precision in retention time.

The results show an excellent assurance of area reproducibility above 0.5 ng on-column for all components except octyl salicylate (compound 8). For compound 8, from 1 ng and above, the area RSD values are well within the allowed limit of 2.0%. A smaller peak area showed poor UV response of octyl salicylate compared to other standards. This was the reason for a higher RSD value. The observed area RSD values throughout the linearity levels are tabulated in Table 6.

A calibration graph was constructed by plotting the peak area of each standard against nominal concentrations (0.25 ng, 0.5 ng, 1 ng, 5 ng, 10 ng, 25 ng, 50 ng, 100 ng, 200 ng). The linearity of the relationship between peak area and concentration is established by the correlation coefficients ( $R^2$ ) > 0.9997. The overlaid linearity curves for all standards are shown in Figure 5. Observed  $R^2$  values for individual components are tabulated in Table 7.

## Extracted sample analysis

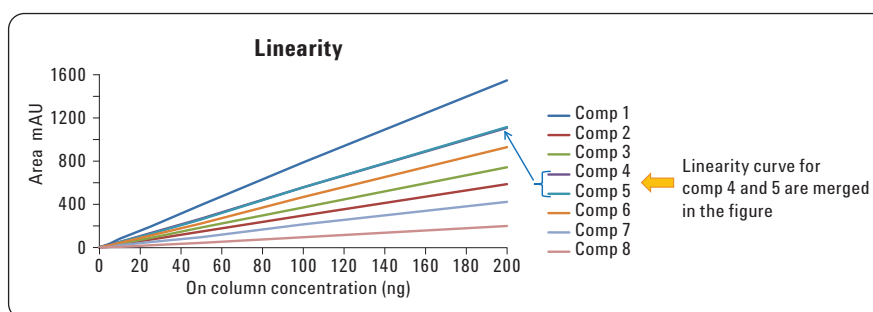
A spectral library was generated for all the standards to confirm peak identities and to provide data for spectral peak purity or the absence of coelution. UV filters from six different international brands were extracted and analyzed. Observed elution patterns for all the samples are overlaid and shown in Figure 6. An unknown peak was



**Figure 4**  
Retention time RSD.

On-column Concentration (ng)	Area RSD values (%)							
	Comp 1	Comp 2	Comp 3	Comp 4	Comp 5	Comp 6	Comp 7	Comp 8
0.25	1.70	4.40	3.57	1.53	1.95	2.80	5.93	9.67
0.5	1.48	1.46	1.48	1.45	0.98	1.46	1.80	4.24
1	0.47	0.55	0.73	0.87	1.00	1.34	1.20	1.94
5	0.22	1.37	0.06	0.09	0.31	0.21	0.20	0.50
10	0.95	1.02	0.96	1.10	1.16	1.29	1.43	1.21
25	0.27	0.45	0.50	0.46	0.55	0.54	0.61	0.53
50	1.11	1.16	1.02	0.98	0.80	0.80	0.70	0.79
100	0.11	0.16	0.20	0.26	0.25	0.29	0.27	0.33
200	0.16	0.24	0.19	0.16	0.19	0.18	0.22	0.11

**Table 6**  
Area RSD values for all compounds at all linearity levels (n=5). Values > 2.0 are marked in red.



**Figure 5**  
Overlaid linearity curves for all standards.

Compound	Name	$R^2$
1	Aminobenzoic acid	0.9999
2	Dioxybenzone	1.0000
3	Oxybenzone	0.9999
4	4-Methyl benzylidene camphor	0.9999
5	Avobenzone	0.9997
6	Octyl methoxycinnamate	0.9998
7	Octocrylene	0.9997
8	Octyl salicylate	0.9998

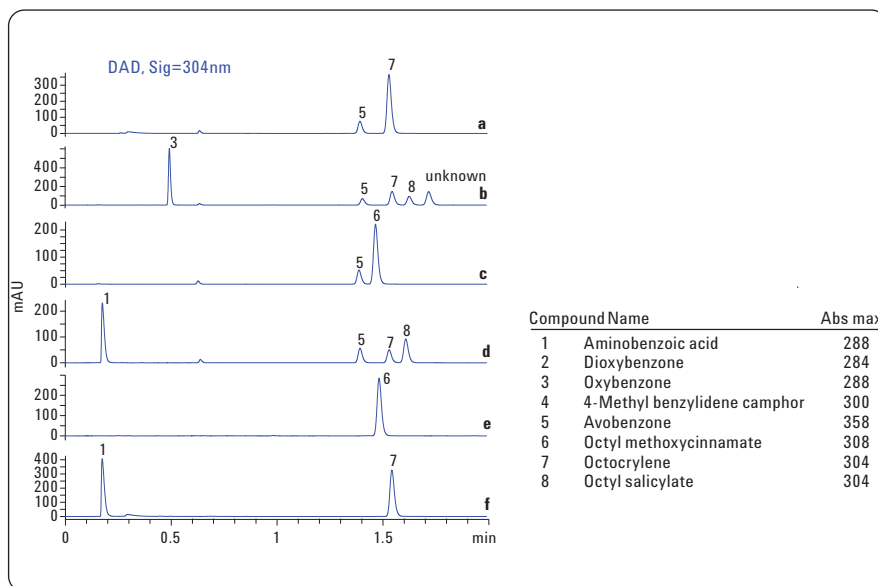
**Table 7**  
Observed  $R^2$  values for individual components.

observed in sample 5 at 1.71 min. Results show that avobenzone and octocrylene are the most widely used UV filter components in the sunscreen personal care products tested. From the extracted sample chromatogram, it is clear that samples b and d provide a broad range of protection against UVA, UVB and UVC rays.

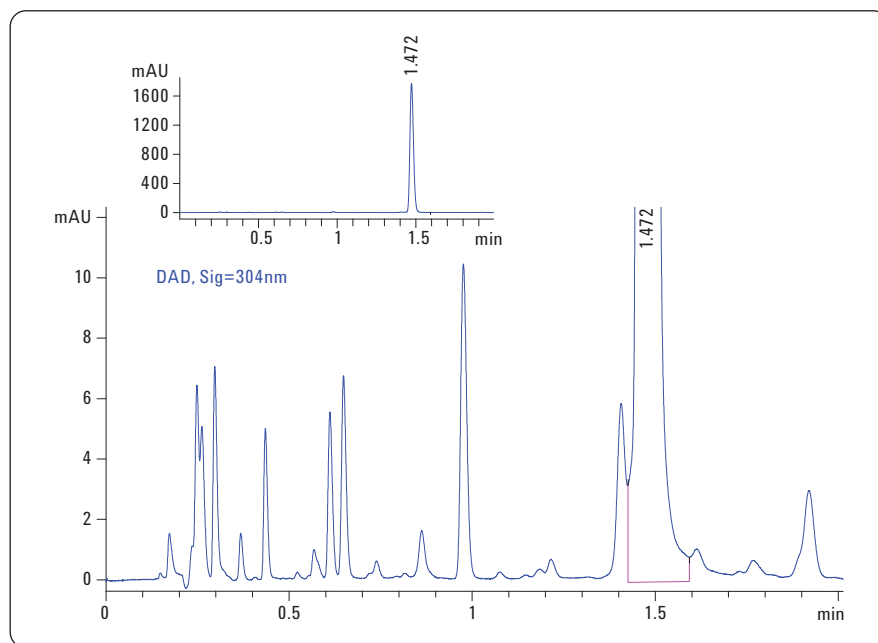
Sunscreen products with higher SPF values may contain higher amounts of sunscreen components and consequently chances are high that these products contain significant amounts of impurities. The Agilent 1290 Infinity LC provides an overall picture of impurity profiles in personal care products in the shortest amount of time, as demonstrated for sample e in Figure 7.

## Conclusions

This Application Note demonstrates the baseline separation of eight FDA/EP approved sunscreen compounds in 99 seconds using the Agilent 1290 Infinity LC and the Agilent Poroshell 120 EC-C18 column. The minimum observed resolution value in the standard mix chromatogram was > 1.8. S/N values for each component at 0.25 ng level (on-column concentration) were demonstrated. Linearity was demonstrated from 0.25 ng to 200 ng on-column for all compounds. The poorest R<sup>2</sup> value is 0.9997 (nine levels and five replicates). Across the linearity levels, the highest observed RT standard deviation value was 0.0018 and the highest observed RT RSD value was 0.32% (n=5). This method can be effectively used to chromatograph UV filters and impurities present in sunscreen and personal care cosmetic products.



**Figure 6**  
Overlay of chromatogram for all six extracted samples.



**Figure 7**  
Full scale and zoomed chromatogram of sample "e", which demonstrates well resolved impurity peaks. These minor unidentified peaks may be parabens or other listed ingredients of the formulations and related impurities.

## References

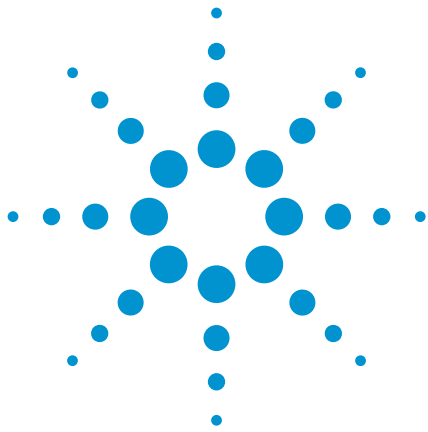
1.  
Dr. James H. Gibson, Senior Research Scientist Director, USDA UVB Monitoring Program Natural Resource Ecology Laboratory Colorado State University.
2.  
Jesus Mercado-Blanco, Fernando Garcia, Manuel Fernandez-Lopez and Jose Olivares, Melanin Production by *Rhizobium meliloti* GR4 Is Linked to Nonsymbiotic Plasmid pRmeGR4b: Cloning, Sequencing and Expression of the Tyrosinase Gene *mepA*, *Journal of Bacteriology*, Sept. 1993, p. 5403-5410.
3.  
David A. Katz, Sunscreens: Preparation and evaluation 2003.
4.  
Ken Klein, Cosmetech Laboratories Inc: Emulsion and sunscreen, (pub date: 2001).
5.  
Marc.S.Reisch C&EN northeast news bureau, *Chemical and Engineering news*, April 11 2005, Volume 83 Number 15, pp 18-22.
6.  
Hanson Kerry M.; Gratton Enrico; Bardeen Christopher J. (2006). "Sunscreen enhancement of UV-induced reactive oxygen species in the skin," *Free Radical Biology and Medicine* 41 (8): 1205–1212.

[www.agilent.com/chem/lc](http://www.agilent.com/chem/lc)

© Agilent Technologies, Inc., 2010  
December 1, 2010  
Publication Number 5990-6861EN



**Agilent Technologies**



# Stable Baselines in the Analysis of Poly(lactide-*co*-glycolide) Polymers by GPC with ELSD

## Application Note

### Authors

Stephen Ball and Greg Saunders  
Agilent Technologies, Inc.

### Introduction

Poly(lactide-*co*-glycolide) copolymers are extensively used in the pharmaceutical and medical industries, for example, as absorbable sutures, surgical clips and staples. The molecular weight distribution of the polymer can affect the properties of the end product, and is therefore of interest in the areas of development and quality control. The copolymer is quite polar in nature, but can be dissolved in several solvents suitable for gel permeation chromatography, notably tetrahydrofuran and chloroform. Low boiling solvents like chloroform can suffer from outgassing effects. When employing refractive index detection, this can lead to chromatograms with noisy or drifting baselines. The Agilent ELSD always delivers baselines that are stable and drift-free. Furthermore, due to its evaporative nature, it provides chromatograms that are free from system peaks around total permeation that are commonly associated with RI detectors. The Agilent ELSD also offers superior sensitivity compared to RI. Poly(lactide-*co*-glycolide) copolymers are relatively low in molecular weight. PLgel 5  $\mu\text{m}$  MIXED-D columns, with their high efficiency (>50,000 plates/meter) and broad resolving molecular weight range (up to 400,000 daltons relative to polystyrene), are the columns of choice for this application.



**Agilent Technologies**



## Instrumentation

Columns: 2 x PLgel 5  $\mu$ m MIXED-D, 300 x 7.5 mm (p/n PL1110-6504)  
Detection: Agilent ELSD

## Materials and Reagents

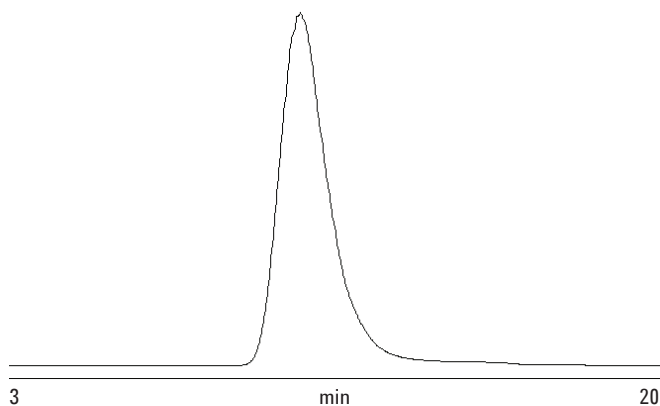
Eluent: Chloroform

## Conditions

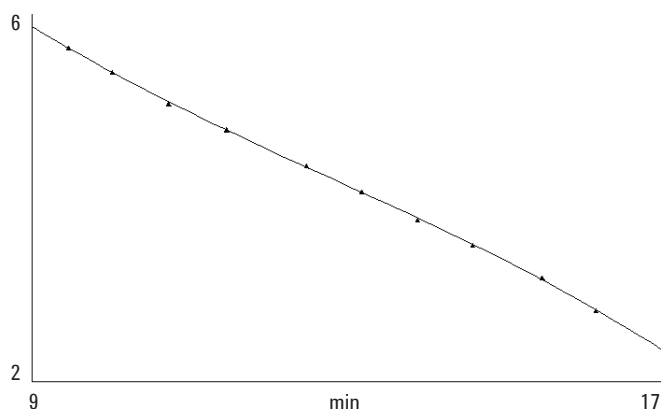
Flow Rate: 1.0 mL/min

## Results and Discussion

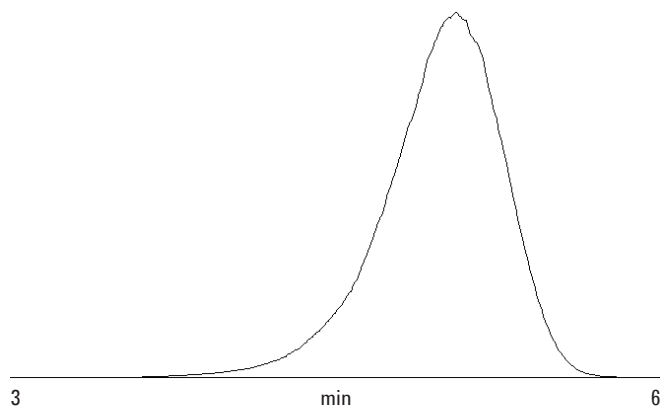
Figure 1 shows a typical raw data chromatogram for a poly(lactide-co-glycolide) sample. The system was calibrated with narrow EasiCal PS-2 polystyrene standards and the calibration curve is presented in Figure 2. The molecular weight distribution plot and calculated molecular weight averages for the sample are illustrated in Figure 3.



**Figure 1. Excellent base line stability in poly(lactide-co-glycolide) analyzed by the Agilent ELSD.**



**Figure 2. System calibration using EasiCal PS-2 standards.**



**Figure 3. Molecular weight averages (Mw 110626 and Mn 70766) of poly(lactide-co-glycolide).**

## Conclusion

PLgel columns and the Agilent ELSD are ideal combinations for the determination of poly(lactide-*co*-glycolide) because of their very low signal to noise ratios and excellent baseline stability.

Mixed pore size PLgel columns offer high resolution over a specific molecular weight range. The robust design of the Agilent ELSD allows the nebulizer and evaporator to operate at very high temperatures, efficiently handling the high boiling point solvents that other ELSDs simply cannot manage.

PLgel columns and the Agilent ELSD are well suited to the separation of compounds that have no chromophores, under isocratic or gradient conditions.

[www.agilent.com/chem](http://www.agilent.com/chem)

This information is subject to change without notice.

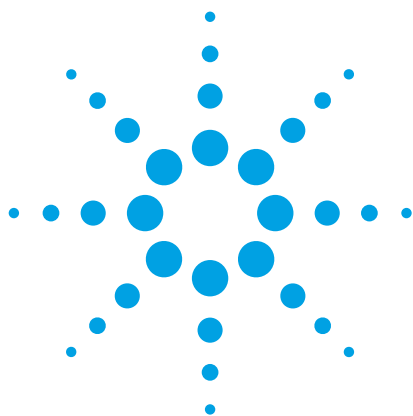
© Agilent Technologies, Inc. 2011

Published in UK, June 9, 2011

5990-8401EN



**Agilent Technologies**



# Analyze Injection-Molding Polymers on Agilent PLgel 5 $\mu$ m MIXED-C by GPC

## Application Note

Materials Testing and Research

### Authors

Greg Saunders and Ben MacCreath  
Agilent Technologies (UK) Ltd  
Essex Rd  
Church Stretton  
SY6 6AX  
UK

### Introduction

Injection-molding thermoplastics are used in a wide variety of applications, including panels for plastic doors, casings for scientific instruments, refrigerator linings, and telephone cases. Ideally, the materials should display excellent weather and impact resistance, good color retention and consistency, resistance to environmental stress, cracking, and high heat resistance. A number of copolymers have been developed that display these properties, such as copolymers of acrylonitrile/styrene/acrylate (ASA) and acrylonitrile/butadiene/styrene (ABS). Typically, these materials are either layered or blended to meet the requirements of a specific application.

This application note describes the analysis of a sample of an ASA/ABS-blended material from a car door panel by gel permeation chromatography (GPC), using Agilent PLgel 5  $\mu$ m MIXED-C columns.

### Injection-Molding Polymer Analysis

Figure 1 shows the blended material that eluted as a single monomodal peak, indicating that the two components of the blend were very similar in molecular size, with an  $M_w$  of 160,000 g/mol and a polydispersity of 2.6.



**Agilent Technologies**

## Conditions

Samples	Blend of ASA and ABS
Columns	2 × Agilent PLgel 5 µm MIXED-C, 7.5 × 300 mm (p/n PL1110-6500)
Eluent	THF (stabilized)
Flow rate	1.0 mL/min
Inj vol	100 µL
Detector	RI
System	Agilent PL-GPC 50

## Conclusions

Gel permeation chromatography with Agilent PLgel 5 µm MIXED-C columns permits the molecular weight distribution of polymers to be assessed, and the size of the molecular components in a polymer blend to be investigated.

## For More Information

These data represent typical results. For more information on our products and services, visit our Web site at [www.agilent.com/chem](http://www.agilent.com/chem).

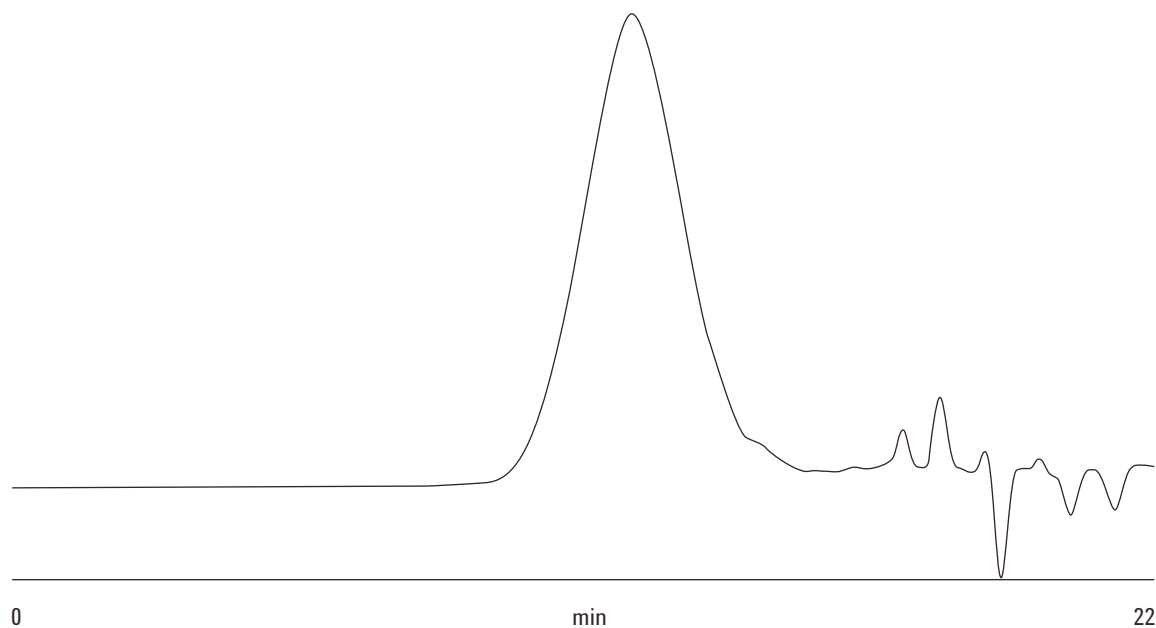


Figure 1. Individual components of an injection-molding polymer elute as a single peak, showing their similarity in molecular size.

[www.agilent.com/chem](http://www.agilent.com/chem)

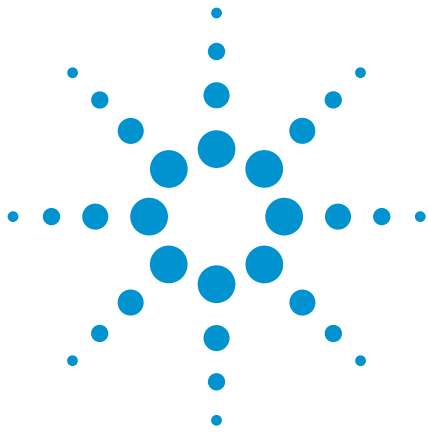
Agilent shall not be liable for errors contained herein or for incidental or consequential damages in connection with the furnishing, performance, or use of this material.

Information, descriptions, and specifications in this publication are subject to change without notice.

© Agilent Technologies, Inc., 2011  
Printed in the USA  
July 8, 2011  
5990-8601EN



**Agilent Technologies**



# Artifact Free Analysis of Lignins by GPC using Agilent PolarGel-M

## Application Note

### Authors

Greg Saunders, Ben MacCreath  
Agilent Technologies, Inc.

### Introduction

Lignin is commonly derived from wood and is one of the most abundant organic compounds on earth, being an integral part of the cell wall of plants. It is a large, cross-linked biopolymer with several unusual but useful properties. For example, wood with a high abundance of lignin is durable and therefore makes a good raw material for construction. However, the presence of lignin is detrimental to the paper making industry and the biopolymer must be removed during the chemical process of pulping the wood to form the paper, an expensive activity. In this chemical pulping - or Kraft – process, the lignin is removed from wood pulp by the breaking down of the cross-links and through sulfonation. The resultant sulfates are considered to be environmentally friendly and have many uses, including forming the bases of many other chemicals such as ethanol and vanillin. They can also be used as additives in agricultural chemicals, as dispersants in water treatment formulations and as textile dyes.



**Agilent Technologies**

## GPC Analysis

PolarGel-M GPC columns are packed with low swell, macroporous copolymer beads that have a surface of balanced polarity, comprising hydrophobic and hydrophilic components. These allow PolarGel-M to be used in the analysis of high polarity polymers that are insoluble in water to give a more accurate representation of the molecular weight distribution of the polymer. If these polar polymers were to be analyzed with traditional styrene/divinyl benzene columns, interactions would cause artifacts in the peak shape and longer retention times, which would translate into apparently much lower molecular weight averages.

## Sample Preparation

Three varieties of lignin from different sources were analyzed to obtain an indication of differences in molecular weight, if any. The samples were made up at 0.2 % (w/v) in DMSO, with 0.1 % LiBr added to reduce sample aggregation, and injected without further treatment.

### Conditions

Columns: 2 x PolarGel-M, 300 x 7.5 mm (p/n PL1117-6800)  
Eluent: DMSO & 0.1 % LiBr  
Flow Rate: 1.0 mL/min  
Injection Volume: 100  $\mu$ L  
Temperature: 50  $^{\circ}$ C  
Detectors: Agilent PL-GPC 50, RI

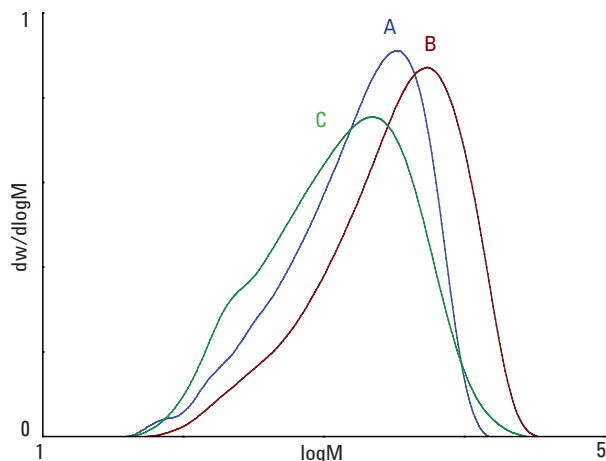


Figure 1. Overlaid molecular weight distributions of the three lignins

## Results

Figure 1 shows overlaid molecular weight distributions of three lignins.

## Conclusion

GPC with PolarGel-M columns allows for the artifact, interaction free analysis of a wide range of high polarity polymers that are difficult to analyze on traditional, organic (PS/DVB) GPC columns.

[www.agilent.com/chem](http://www.agilent.com/chem)

This information is subject to change without notice.

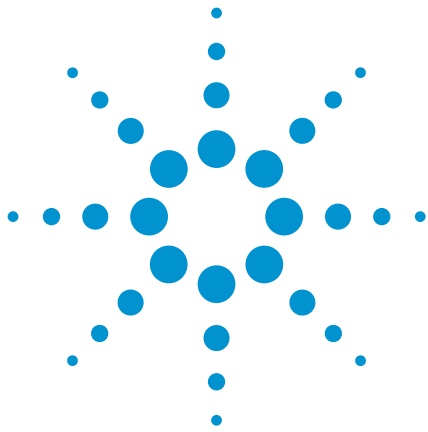
© Agilent Technologies, Inc. 2010

Published in UK, September 2, 2010

SI-00947



Agilent Technologies



# GPC and Agilent PolarGel-M Columns for the True Representation of Novolac Resins

## Application Note

### Authors

Greg Saunders, Ben MacCreath  
Agilent Technologies, Inc.

### Introduction

Novolac resins are thermoplastic materials made with an excess of phenol in an acid catalyzed reaction with formaldehyde. Novolacs are commonly employed as photoresists (light-sensitive materials used to form patterned surface coatings) and in varnishes. They have higher heat distortion temperatures and tend to be more expensive than regular epoxy resins.



**Agilent Technologies**

## GPC Analysis

PolarGel-M GPC columns are packed with low swell, macroporous copolymer beads that have a surface of balanced polarity, comprising hydrophobic and hydrophilic components. These allow PolarGel-M to be used in the analysis of high polarity polymers that are insoluble in water to give a more accurate representation of the molecular weight distribution of the polymer. If these polar polymers were to be analyzed with traditional styrene/divinyl benzene columns, interactions would cause artifacts in the peak shape and longer retention times, which would translate into apparently much lower molecular weight averages.

## Sample Preparation

Two novolac resins were analyzed to obtain an indication of differences in molecular weight, if any. The samples were made up at 0.2 % (w/v) in DMSO, with 0.1 % LiBr added to reduce sample aggregation, and injected without further treatment.

### Conditions

Columns: 2 x PolarGel-M, 300 x 7.5 mm (p/n PL1117-6800)  
Eluent: DMSO & 0.1 % LiBr  
Flow Rate: 1.0 mL/min  
Injection Volume: 100  $\mu$ L  
Temperature: 50  $^{\circ}$ C  
Detectors: Agilent PL-GPC 50, RI

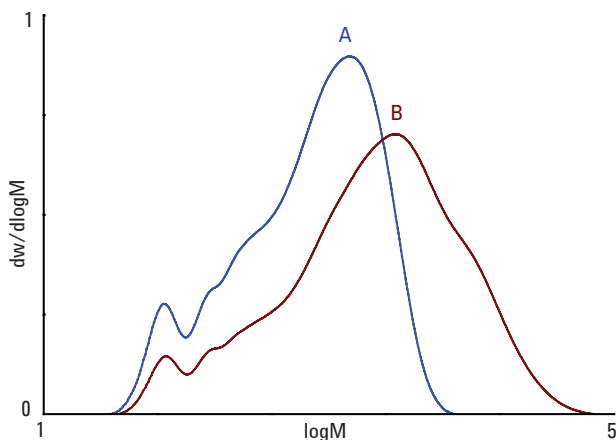


Figure 1. Overlaid molecular weight distributions of two novolac resins

## Results

Figure 1 shows the overlaid molecular weight distributions of two novolac resins.

## Conclusion

GPC with PolarGel-M columns allows for the artifact, interaction free calculation of the composition and molecular weight distributions of novolac resins that are difficult to analyze on traditional, organic (PS/DVB) GPC columns.

[www.agilent.com/chem](http://www.agilent.com/chem)

This information is subject to change without notice.

© Agilent Technologies, Inc. 2010

Published in UK, September 2, 2010

SI-00948



Agilent Technologies





# Analysis of Polysaccharides by GPC Viscometry using the Agilent 390-MDS Multi Detector Suite

## Application Note

### Authors

Greg Saunders, Ben MacCreath  
Agilent Technologies, Inc.

### Introduction

Polysaccharides are complex polymers constructed from sugar units. There is a wide range of polysaccharides, many of which show large structural differences due to the manner in which they are synthesized. This is most commonly seen in the presence of branches on the polymer chains of some polysaccharides, which strongly influences properties such as solution viscosity. Pullulan polysaccharide is composed of maltotriose units in the polymer backbone, produced from starch by the action of a fungus. Pullulan has a linear structure, whereas in contrast dextran is a complex glucan with many differing components manufactured from sucrose by bacterial action that has a highly branched structure. Investigating the structure of polysaccharides is of interest for determining their properties in applications such as their use as food additives.

Gel permeation chromatography (GPC) is a well-known technique for assessing the molecular weight distribution of polymers, a property that influences many of the physical characteristics of these materials. GPC viscometry, employing a viscometer in combination with a differential refractive index detector, has the advantage of allowing the accurate determination of molecular weights for structurally complex polymers and co-polymers regardless of their structure, via the Universal Calibration approach. GPC viscometry also reveals information about the solution viscosity of polymers, a property related to molecular size. Using this information, the branched structure of polymers can be investigated. This application note describes the analysis of two samples of polysaccharide by GPC viscometry, pullulan with a linear structure, and a highly branched dextran.



**Agilent Technologies**

## Methods and Materials

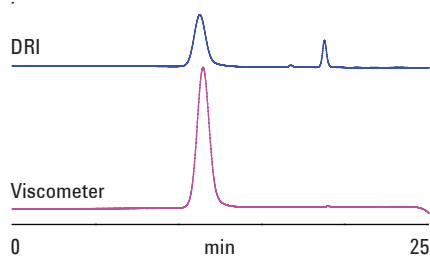
### Conditions

Samples:	Polysaccharides
Columns:	2 x Agilent PL aquagel-OH MIXED-M 8 $\mu$ m, 300 x 7.5 mm (p/n PL1149-6801)
Injection Volume:	200 $\mu$ L
Eluent:	0.2 M NaNO <sub>3</sub> + 0.01 M NaH <sub>2</sub> PO <sub>4</sub>
Flow Rate:	1.0 mL/min
Detector Train:	390-MDS incorporating Viscometer and DRI
Detector Temp:	All detectors set at 40 °C

The 390-MDS was chosen as part of the system as it is capable of multi-detector GPC in aqueous solvents and therefore allows the complex nature of these materials to be investigated.

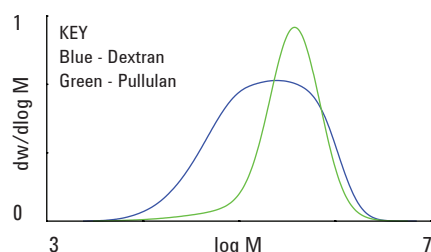
## Results and Discussion

Figure 1 shows an example overlaid multi-detector chromatogram for a sample of pullulan polysaccharide. The material eluted as a broad peak.



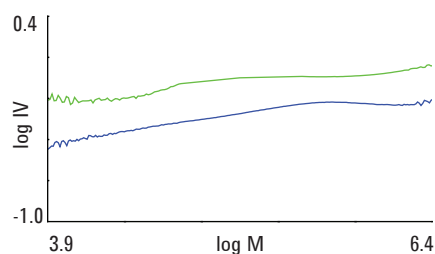
**Figure 1. Overlaid multi-detector chromatogram for an example of pullulan polysaccharide**

Figure 2 shows an overlay of the accurate molecular weight distributions of the two samples under investigation. As can be seen, they have very different molecular weight distributions.



**Figure 2. Overlaid multi-detector molecular weight distributions of two samples of polysaccharide**

Figure 3 shows the overlaid Mark-Houwink plot of log intrinsic viscosity as a function of molecular weight for the two samples. Compared to the pullulan, the dextran shows a marked shift of the Mark-Houwink plot to lower intrinsic viscosity values at any given molecular weight. This indicates that dextran is smaller in solution than pullulan across the molecular weight range, a result of the presence of branching on the dextran molecules. The dextran plot is complex and shows some changes in slope, indicating that the degree of branching varies across the range of molecular weight, as expected for a complex material.



**Figure 3. Overlaid Mark-Houwink plots for the two samples of polysaccharide**

## Conclusion

The data in this application note illustrates how multi-detector GPC employing the 390-MDS can be used to clearly see structural differences between pullulan and dextran with a highly branched structure.

[www.agilent.com/chem](http://www.agilent.com/chem)

This information is subject to change without notice.

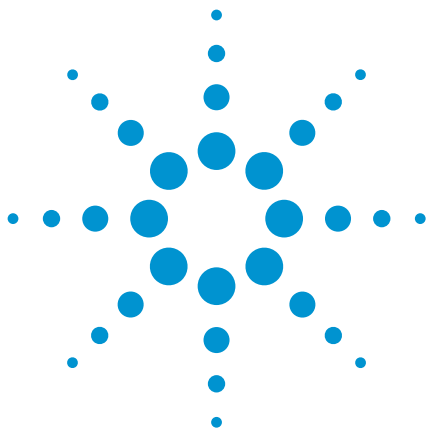
© Agilent Technologies, Inc. 2010

Published in UK, September 13, 2010

SI-02389



**Agilent Technologies**



# Characterization of Block Copolymers Synthesized via Transition Metal Mediated Living Radical Polymerization

## Application Note

### Authors

Greg Saunders, Ben MacCreath  
Agilent Technologies, Inc.

### Introduction

Polymerization reactions mediated by the presence of a transition metal have received much interest in both literature and the commercial world. These processes allow the controlled synthesis of polymers of predetermined molecular weight, polydispersity and well-defined architecture using cheap and synthetically simple procedures. Generation of a carbon radical initiates free-radical polymerization in the presence of a monomer and a suitable solvent. Termination steps are minimized by the reversible nature of the radical formation reaction. Careful tailoring of the relative reaction rates can lead to well-controlled polymerizations where termination steps are sufficiently controlled to allow polymers of polydispersity of 1.1 to be produced from the reaction. These reactions typically follow pseudo-first order kinetics. The ability to readily convert hydroxyl functional groups to active initiator groups ready for polymerization leads to a convenient synthetic pathway for the synthesis of architecturally diverse materials such as stars, blocks and grafts.

One such class of polymer structures that may be prepared using this synthetic process are block copolymers. These copolymers are made up of two or more chains that contain different repeat units that are known as blocks, for example a block of polystyrene connected to a block of polymethyl methacrylate repeat units. The materials are of interest because under certain conditions they facilitate phase separation, forming nanostructures with properties that differ from the equivalent blended material or from random copolymers of the monomers used in the two blocks.

Determining the molecular weight of block copolymers is not straightforward as the composition of the material affects the molecular dimensions, which in turn means that molecular weights determined by conventional GPC using only a refractive index detector are inaccurate. However, using viscometry, it is possible to determine the molecular weights of these materials by the universal calibration approach.



**Agilent Technologies**

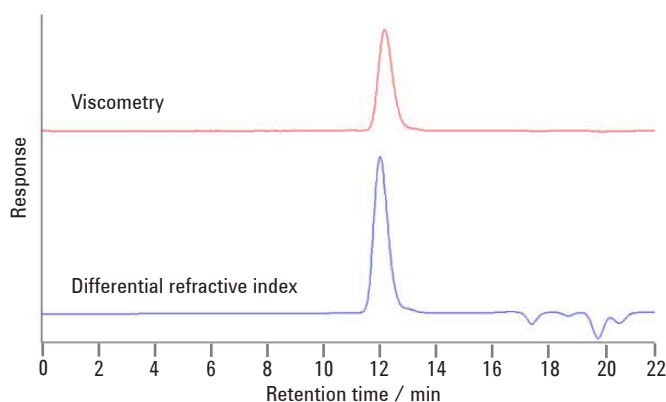
This methodology makes use of the relationship between molecular weight and molecular density, allowing accurate molecular weights to be determined for materials irrespective of their chemistry. This note describes the analysis of a series of five poly(styrene-co-methyl methacrylate) copolymers manufactured with different molecular weights by GPC viscometry.

## Results and Discussion

### Conditions

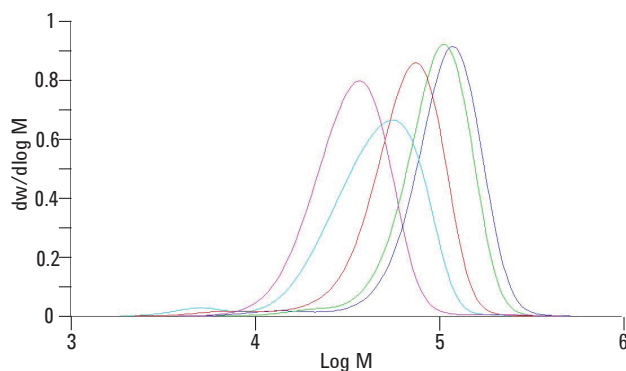
Columns: 2 x Agilent PLgel 5  $\mu$ m MIXED-C, 300 x 7.5 mm (part number PL1110-6500)  
 Eluent: Tetrahydrofuran  
 Flow Rate: 1 mL/min  
 Inj. Vol: 100  $\mu$ L  
 Sample Conc: 2 mg/mL  
 Temp: 40  $^{\circ}$ C  
 Detectors: Agilent 390-MDS Multi Detection Suite comprising a differential refractive index and a four capillary bridge viscometer  
 Calibration Standards: Agilent Polystyrene EasiVials

Figure 1 shows overlaid dual detector raw data chromatograms for a poly(styrene-co-methyl methacrylate) sample showing the data collected from the individual detectors. The polymers all eluted as narrow near-Gaussian peaks.



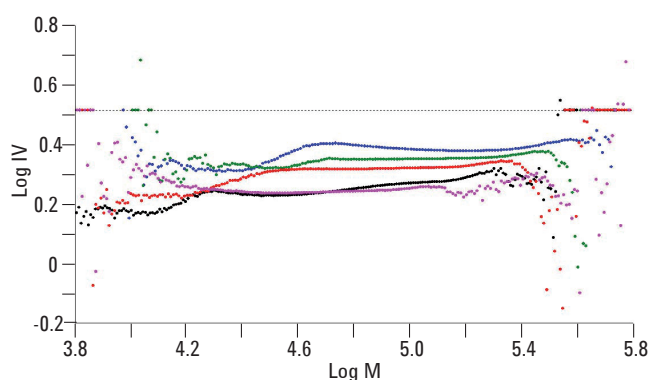
**Figure 1. Overlaid dual detector raw data chromatograms for a block copolymer sample**

The samples were all then analyzed by GPC with viscometry, employing the universal calibration method to determine molecular weights that were not dependent on calibrant chemistry. The overlaid molecular weight distributions are shown in Figure 2.



**Figure 2. Overlaid molecular weight distributions calculated by universal calibration analysis of all samples**

The Mark-Houwink plots for the four materials are shown in Figure 3.

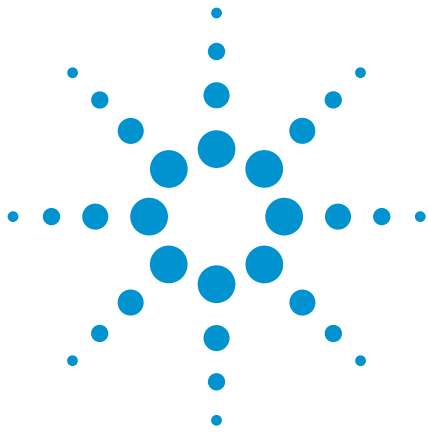


**Figure 3. Overlaid molecular weight distributions calculated by universal calibration analysis of all samples**

The Mark-Houwink relationship describes the scaling behavior of the intrinsic viscosity of polymers as a function of molecular weight. Assuming that materials have the same molecular density, they will follow the same Mark-Houwink plot. In these samples the variations in the block lengths for the different samples have caused shifts in the Mark-Houwink plots.

## Conclusion

The 390-MDS multi detection suite successfully determined the molecular weights of some block copolymers and revealed differences in the block lengths. Viscometry detection delivered by the 390-MDS is a powerful tool for investigating the molecular weight and structural properties of polymers, irrespective of their chemistry.



# Analysis of Biodegradable Polymers by GPC

## Application Note

### Author

Greg Saunders  
Agilent Technologies, Inc.

### Introduction

Polymers have a wide range of uses in society because of their durability and resistance. This durability, however, has its drawbacks, especially when it comes to the disposal of polymers once they are no longer useful. An accumulation of degradation resistant polymers in landfill sites has become a serious problem. The solution is a polymer that can be degraded by natural means without losing the functional properties that make the polymer so useful.

A biodegradable polymer can be broken down into simpler substances by the activities of living organisms and is, therefore, unlikely to persist in the environment. Biodegradable polymers are also used in medicine, for such things as drug and gene delivery or bio-absorbable stents. Polycaprolactones and polylactides are good examples of biodegradable polymers with a wide range of industrial and biomedical applications. Polycaprolactones are fully biodegradable thermoplastic polymers, though they are derived from the chemical synthesis of non-renewable crude oil. Polylactides (PLA) are biodegradable polymers derived from lactic acid. Gel permeation chromatography is an ideal method for the analysis of biodegradable polymers. The approach adopted here employs refractive index and viscometry detection.



**Agilent Technologies**

### Conditions

Sample: Polylactide, polycaprolactone and polylactide-glycolide  
Columns: 2 x Agilent ResiPore, 300 x 7.5 mm (p/n PL1113-630)  
Eluent: THF  
Flow Rate: 1 mL/min  
Temp: 40 °C  
Detector: Agilent PL-GPC 50 Plus (DRI and Agilent PL-BV 400RT)

## Results and Discussion

Figures 1 to 3 show examples of dual detection chromatograms for some biodegradable polymers. Figure 1 shows a polylactide sample, Figure 2 is a polycaprolactone sample and Figure 3 is a polylactide-glycolide.

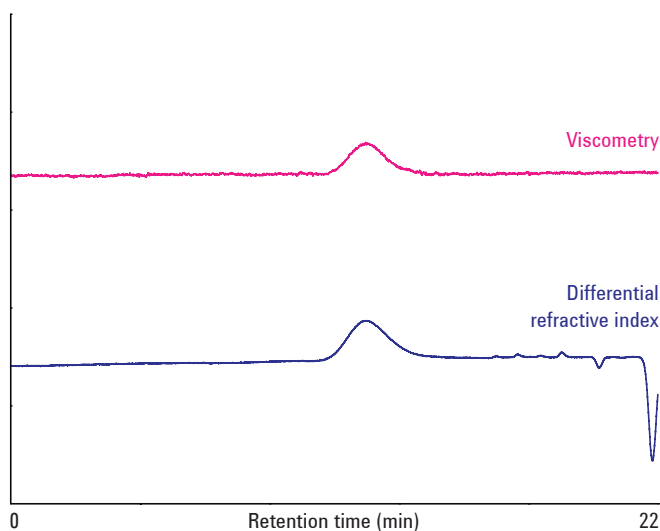


Figure 1. Dual detection chromatograms of a sample of polylactide

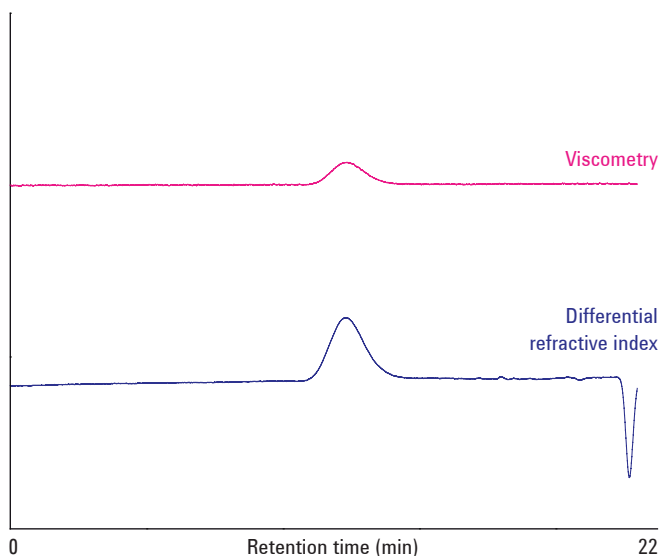


Figure 2. Dual detection chromatograms of a sample of polycaprolactone

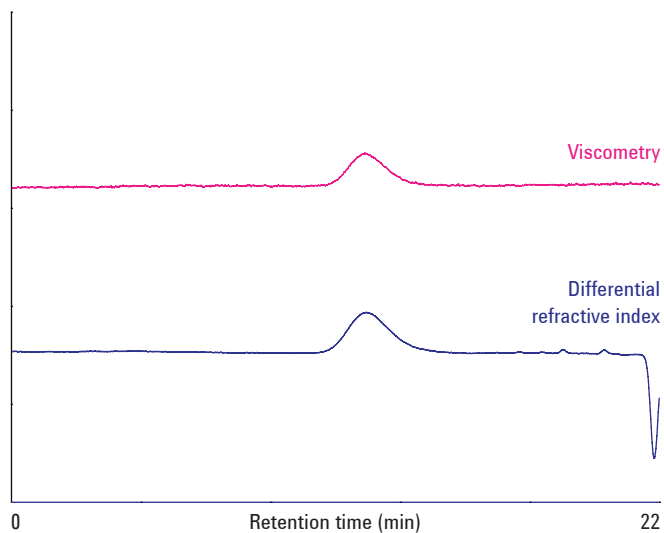


Figure 3. Dual detection chromatograms of a sample of polylactide-glycolide

The overlaid molecular weight distribution plots are shown in Figure 4.

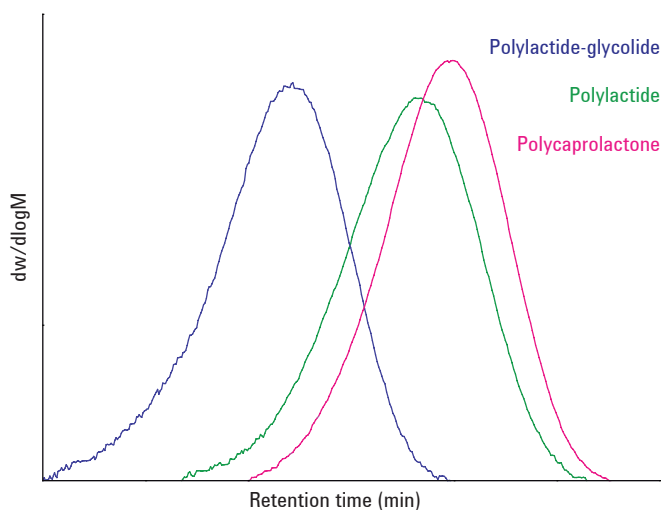


Figure 4. Molecular weight distributions of three biodegradable polymers

The universal calibration curve was generated using linear PS standards with narrow polydispersity (Figure 5).

Based on this calibration, the molecular weight averages and weight average, intrinsic viscosity (IV<sub>w</sub>) was calculated for the biodegradable polymers. The table shows the molecular weight averages for a selection of such polymers.

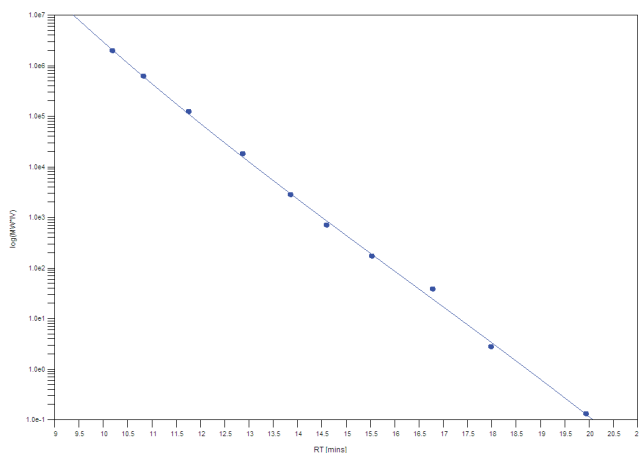


Figure 5. Universal calibration curve

Table 1. Molecular weight averages for a selection of biodegradable polymers

Sample	Molecular Weight Averages $\text{gmol}^{-1}$						PD
	Mp	Mn	Mw	Mz	Mz+1	Mv	
Poly(d,l-lactide)	70,863	42,039	73,904	115,032	160,338	68,604	1.758
	69,596	41,967	74,148	114,767	158,539	68,860	1.7668
Poly(d,l-lactide)-glycolide	72,153	44,926	77,077	118,849	164,761	71,687	1.7156
	70,863	43,821	76,555	118,849	164,761	71,687	1.747
50:50 d,l-PLGA	43,010	24,729	42,860	63,021	84,231	40,121	1.7332
	42,259	24,183	41,822	62,163	83,542	39,774	1.7294
65:35 d,l-PLGA	64,762	36,471	63,183	96,758	133,397	58,812	1.7324
	59,209	33,999	61,212	96,217	135,076	56,698	1.8004
75:25 d,l-PLGA	72,153	43,984	75,487	116,184	160,925	70,231	1.7162
	72,153	42,852	74,164	114,689	158,620	68,914	1.7307
95:5 d,l-PLGA	16,447	9,114	16,488	24,968	33,641	15,339	1.8091
	16,447	9,231	16,280	24,477	32,753	15,167	1.7636
Polycaprolactone	100,091	67,340	105,978	153,033	203,984	99,736	1.5738
	100,091	67,310	105,871	154,173	206,777	99,514	1.5729

## Conclusion

The GPC system successfully characterized some biodegradable polymers. Using RI and viscometer detection, and universal calibration, it was possible to derive the molecular weight distributions of the samples, and calculate several of their characterization parameters.

[www.agilent.com/chem](http://www.agilent.com/chem)

This information is subject to change without notice.

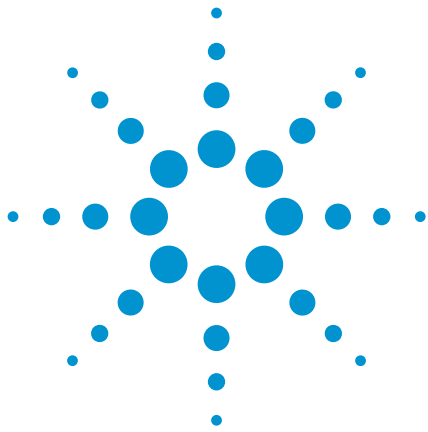
© Agilent Technologies, Inc. 2010

Published in UK, September 3, 2010

SI-01914



**Agilent Technologies**



# Analysis of Poly(styrene/butadiene) Copolymers by Conventional Gel Permeation Chromatography on the Agilent PL-GPC 50 Plus

## Application Note

### Authors

Ben MacCreath, Ian Willoughby,  
Greg Saunders  
Agilent Technologies, Inc.

### Introduction

A poly(styrene/butadiene) block copolymer (SBR) mimics many of the properties of natural rubber and has applications in a wide variety of industrial areas. The characteristics are provided by the hard polystyrene chains being surrounded by a network of rubbery polybutadiene, which provides strength and flexibility over a large temperature range. The copolymer is a thermoplastic elastomer and therefore can easily be used in manufacturing by injection moulding, or blended into an existing product to increase elasticity or impart toughness. The molecular weight distribution is critical, as any homopolymer will significantly affect the resultant end properties.



**Agilent Technologies**



## Methods and Materials

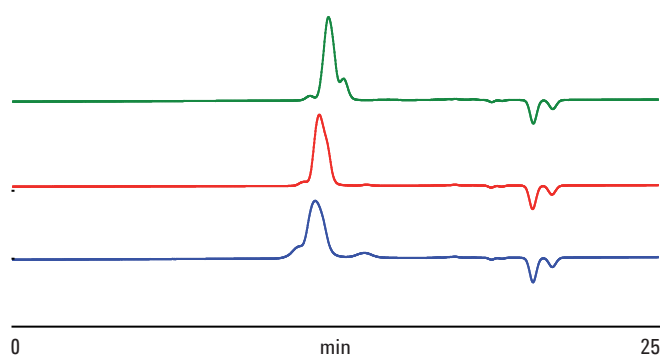
### Conditions

Columns: 2 x Agilent PLgel 5  $\mu$ m MIXED-C, 300 x 7.5 mm  
(part number PL1110-6500)  
Eluent: Tetrahydrofuran (250 ppm BHT)  
Flow Rate: 1.0 mL/min  
Sample Concentration: 2.0 mg/mL  
Injection Volume: 100  $\mu$ L  
Temperature: 40  $^{\circ}$ C  
Calibration Standards: Agilent Polystyrene EasiVial  
Detection: PL-GPC 50 Plus, DRI

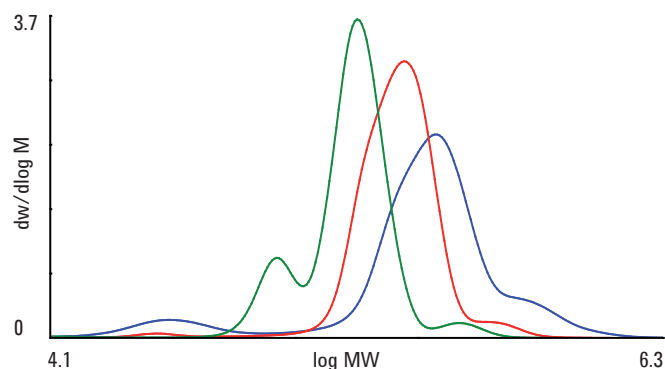
## Results and Discussion

Chromatograms for three poly(styrene/butadiene) block copolymer samples are shown in Figure 1. Figure 2 reveals the copolymer overlaid molecular weight distributions.

Each peak eluted as a relatively narrow main peak indicative of ionic polymerization. The molecular weights of the components of the samples were different, due to a change to the synthesis conditions employed. The main peak of each sample was the block copolymer. However, one of the samples also contained a smaller peak eluting after the main peak, indicating the presence of homopolymer at lower molecular weight. Evidence of high molecular weight termination products is provided by the small peaks eluting before the main peak. The presence of these peaks is a result of imperfections in the polymerization processes used to manufacture the materials.



**Figure 1. Chromatograms for three samples of poly(styrene/butadiene) – each sample eluted as a multi-modal distribution of relatively sharp peaks**



**Figure 2. Overlaid molecular weight distributions for the poly(styrene/butadiene) samples**

## Conclusion

Three samples of poly(styrene/butadiene) were analyzed by conventional gel permeation chromatography on the PL-GPC 50 Plus. Distinct differences were observed arising from presence of homopolymers, along with the anticipated copolymer. This application note demonstrates how GPC may be used to assess the products of complex synthesis reactions to gain mechanistic insights into polymerization processes.

[www.agilent.com/chem](http://www.agilent.com/chem)

This information is subject to change without notice.

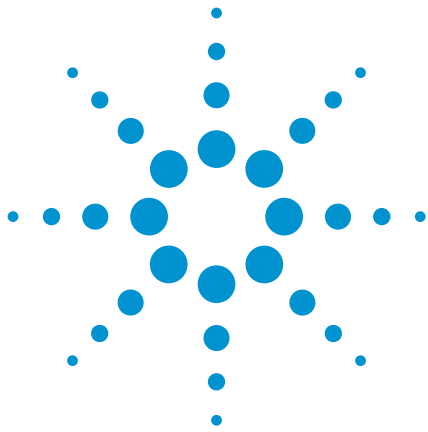
© Agilent Technologies, Inc. 2010

Published in UK, September 9, 2010

SI-02369



**Agilent Technologies**



# Size Exclusion Chromatography for the Analysis of Dental Polymers

## Application Note

### Author

Greg Saunders, Ben MacCreath  
Agilent Technologies, Inc.

### Introduction

Copolymers of vinylmethyl ether and maleic anhydride are widely used in a range of dental applications. These include their use as a denture bioadhesive, as well as a toothpaste additive which helps the toothpaste to remain active between brushing. Batch to batch variations of such copolymer systems strongly influence performance in dental applications. Here, two batches of a commercial copolymer were analyzed by size exclusion chromatography (SEC). One of them had worked well in formulation but the other had failed.



**Agilent Technologies**

## Materials and Methods

A column set comprising 2 x Agilent PL aquagel-OH MIXED 8  $\mu\text{m}$  columns were used for the analysis. These versatile columns offer resolution over a wide range of molecular weight (up to 10,000,000 relative to PEG/PEO), simplifying column selection. Column calibration was achieved using Agilent EasiVial PEG/PEO standards. EasiVials provide a rapid and convenient means of constructing an aqueous SEC column calibration curve over a wide molecular weight range (typically 100 to 1,200,000 g/mol). The samples were made up in sodium nitrate buffer at neutral pH.

### Conditions

Samples: Two samples of dental polymers  
 Columns: 2 x PL aquagel-OH MIXED 8  $\mu\text{m}$ , 300 x 7.5 mm (p/n PL1149-6800)  
 Eluent: 0.2 M  $\text{NaNO}_3$  + 0.01 M  $\text{NaH}_2\text{PO}_4$  at pH 7  
 Flow Rate: 1.0 mL/min  
 Detection: Agilent PL-GPC 50 Plus (DRI)

## Results and Discussion

Figure 1 shows the Agilent EasiVial PEG/PEO calibration curve. Figure 2 shows overlaid raw data chromatograms for the two batches, indicating large differences in molecular weight and molecular weight distribution.

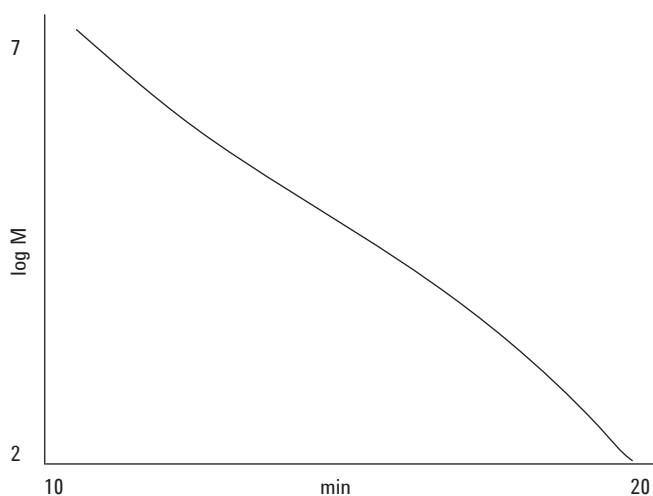


Figure 1. SEC PEG/PEO calibration using EasiVial standards

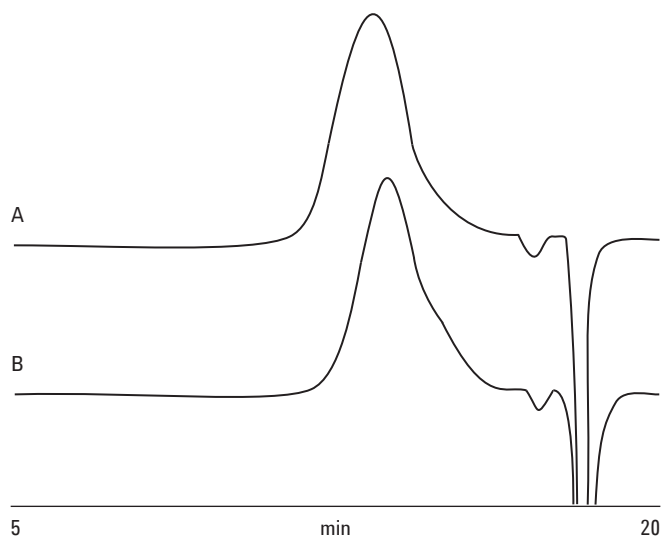


Figure 2. Raw data chromatograms of two dental polymers

The molecular weight distribution plots are presented in Figure 3 and clearly indicate the differences between the two batches.

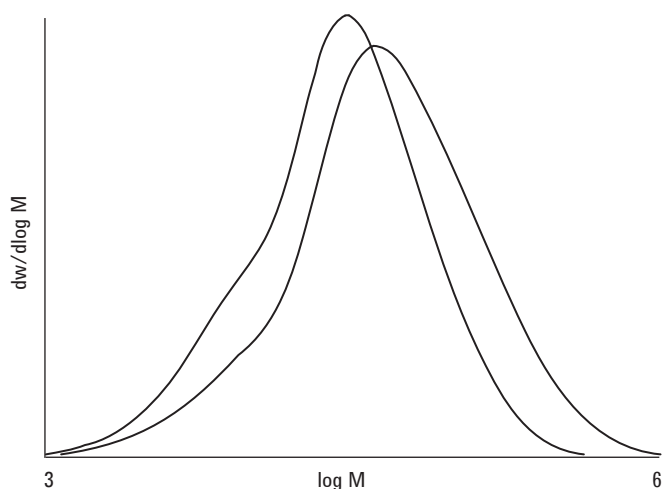


Figure 3. Overlay of the molecular weight distributions of two dental polymers

Table 1.  $M_p$ ,  $M_w$ ,  $M_n$  and polydispersity values for the two dental polymers

Batch	$M_p$	$M_w$	$M_n$	Polydispersity
A	169,330	100,070	258,200	2.6
B	124,100	69,550	152,060	2.2

## Conclusion

Size exclusion chromatography using the PL-GPC 50 Plus in combination with PL aquagel-OH MIXED 8  $\mu\text{m}$  columns was able to distinguish between successful and failed batches of copolymer for a dental application, illustrating the usefulness of the system for the quality control of polymers.

[www.agilent.com/chem](http://www.agilent.com/chem)

This information is subject to change without notice.

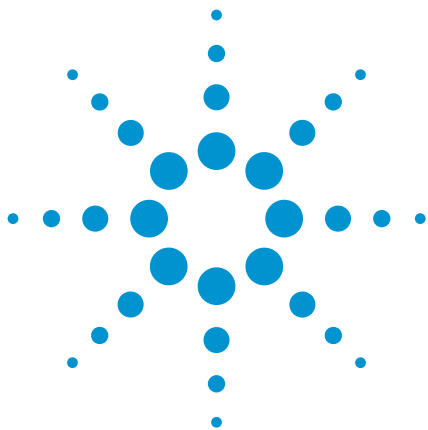
© Agilent Technologies, Inc. 2010

Published in UK, September 7, 2010

SI-01965



**Agilent Technologies**



# SEC Analysis of a Water Soluble Copolymer

## Application Note

### Authors

Greg Saunders, Ben MacCreath  
Agilent Technologies, Inc.

### Introduction

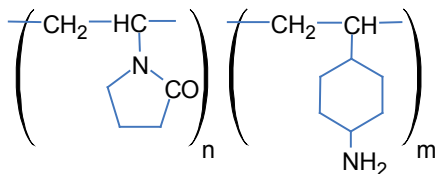
This sample is a copolymer of N-vinyl pyrrolidone / p-amino styrene. It was assessed by aqueous SEC with Agilent PL aquagel-OH 50 8  $\mu\text{m}$  columns. These columns combine high pore volume and high column efficiency (>35,000 plates/meter) for maximum resolution.



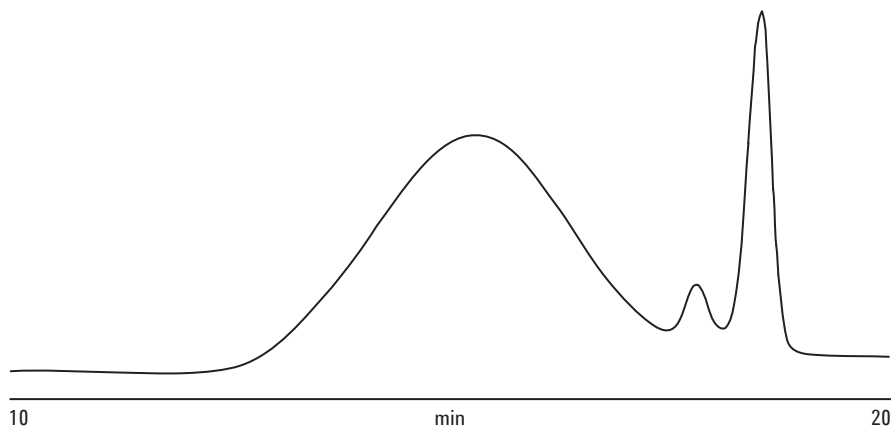
**Agilent Technologies**

### Conditions

Sample: Water soluble copolymer  
Columns: 2 x PL aquagel-OH 50 8  $\mu\text{m}$ ,  
300 x 7.5 mm (p/n PL1149-6850)  
Eluent: 0.2 M  $\text{NaNO}_3$  + 0.01 M  $\text{NaH}_2\text{PO}_4$  at  
pH 7  
Flow Rate: 1.0 mL/min  
Detection: RI



**Figure 1. Raw data chromatogram of poly 2-vinyl pyridine**



**Figure 2. Raw data chromatogram of N-vinyl pyrrolidone / p-amino styrene copolymer**

## Conclusion

Size exclusion chromatography using PL aquagel-OH columns successfully analyzed a sample of water soluble copolymer. Aqueous SEC with PL aquagel-OH columns provides information not only on the molecular weight of the polymer but also on the polydispersity and the shape of the molecular weight distribution. The excellent chemical and mechanical stability of these columns offer high performance with good repeatability and column lifetime.

[www.agilent.com/chem](http://www.agilent.com/chem)

This information is subject to change without notice.

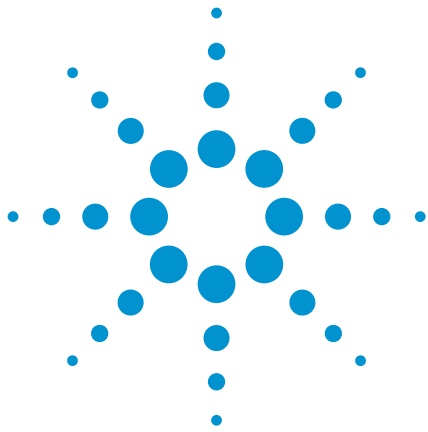
© Agilent Technologies, Inc. 2010

Published in UK, September 2, 2010

SI-01577



**Agilent Technologies**



# SEC Analysis of a Acrylamide Copolymer

## Application Note

### Authors

Greg Saunders, Ben MacCreath  
Agilent Technologies, Inc.

### Introduction

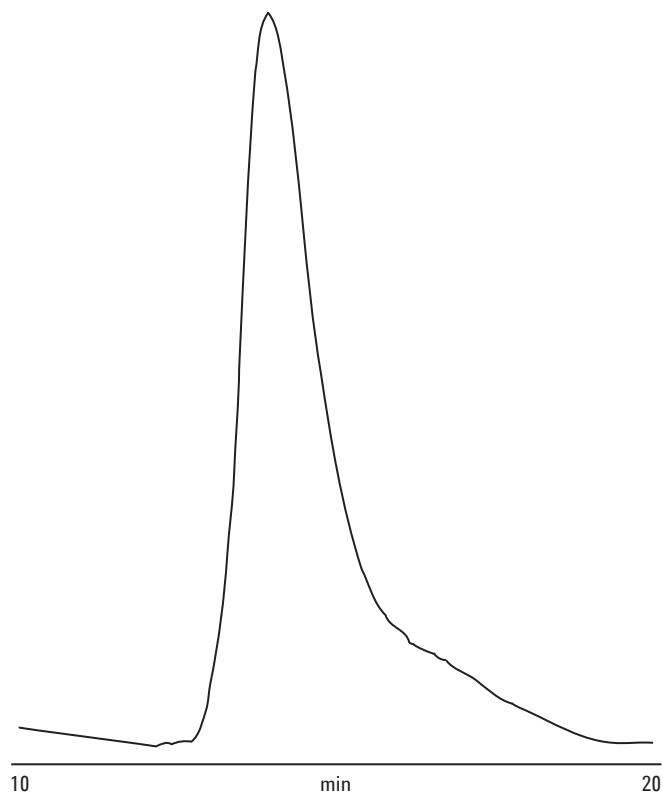
This sample is a copolymer of acrylamide and dimethylaminoethyl acrylate quaternized with methyl chloride. It was necessary to maintain a low sample concentration (0.1 %) to minimize problems of shear with this high molecular weight polymer. The sample was assessed by aqueous SEC with Agilent PL aquagel-OH 40 and 60 15  $\mu\text{m}$  columns. These columns were employed in order to avoid on-column shear degradation, and cover a molecular weight range from  $10^4$  to  $10^7$ .



**Agilent Technologies**

## Conditions

Samples: Sodium polyacrylate  
Columns: 2 x PL aquagel-OH 60 15  $\mu\text{m}$ , 300 x 7.5 mm (p/n PL1149-6260)  
+ 1 x PL aquagel-OH 40 15  $\mu\text{m}$ , 300 x 7.5 mm (p/n PL1149-6240)  
Eluent: 0.2 M  $\text{NaNO}_3$  + 0.01 M  $\text{NaH}_2\text{PO}_4$  at  
pH 7  
Flow Rate: 1.0 mL/min  
Detection: RI



**Figure 1. Raw data chromatogram of an acrylamide co-polymer**

## Conclusion

Size exclusion chromatography using PL aquagel-OH 40 and 60 15  $\mu\text{m}$  columns successfully analyzed a sample of acrylamide copolymer. Aqueous SEC with PL aquagel-OH columns provides information not only on the molecular weight of the polymer but also on the polydispersity and the shape of the molecular weight distribution. The excellent chemical and mechanical stability of these columns offer high performance with good repeatability and column lifetime.

[www.agilent.com/chem](http://www.agilent.com/chem)

This information is subject to change without notice.

© Agilent Technologies, Inc. 2010

Published in UK, September 2, 2010

SI-01578



**Agilent Technologies**